UNIVERSIDAD DE CHILE
FACULTAD DE CIENCIAS FÍSICAS Y MATEMÁTICAS
DEPARTAMENTO DE ASTRONOMÍA

SEARCHING FOR THE SMALLEST PLANETS ORBITING AROUND NEARBY STARS

TESIS PARA OPTAR AL GRADO DE
DOCTOR EN CIENCIAS, MENCIÓN ASTRONOMÍA

MATÍAS RODRIGO DÍAZ MUÑOZ

PROFESOR GUÍA:
CÉSAR ISAÍAS FUENTES GONZÁLEZ

PROFESOR CO-GUÍA:
JAMES JENKINS

MIEMBROS DE LA COMISIÓN:
ROBERT PAUL BULTER
ANDRÉS CRISTÓBAL JORDÁN COLZANI
RICARDO RODRIGO MUÑOZ VIDAL

Este trabajo ha sido parcialmente financiado porCONICYT/PFCHA-Doctorado Nacional-2014 21140646 Chile, Proyecto Basal AFB-170002 y
The Observatories, Carnegie Institution for Science, Pasadena, CA, USA.

SANTIAGO DE CHILE
2022

RESUMEN DE LA TESIS PARA OPTAR
AL GRADO DE DOCTOR EN CIENCIAS, MENCIÓN ASTRONOMÍA
POR: MATÍAS RODRIGO DÍAZ MUÑOZ
FECHA: 2022
PROF. GUÍA: CÉSAR ISAÍAS FUENTES GONZÁLEZ

BÚSQUEDA DE PLANETAS PEQUEÑOS ALREDEDOR DE ESTRELLAS CERCANAS

Esta tesis está basada en cuatro artículos científicos de primer autor. Primero, se discute el estudio de una señal visible en las velocidades radiales que puede ser interpretada como un candidato a planeta orbitando la estrella tipo K HD 26965 con un periodo orbital de 42.364±0.015 días. Nuestra mejor solución es consistente con una super-Tierra con una masa mínima de 6.92±0.79 $M_\oplus$. Se han analizado las correlaciones entre los índices de actividad y las velocidades radiales para cada instrumento. Hemos encontrado moderadas correlaciones que se han incluido en nuestro modelo. Recuperamos una señal de ∼42 días, la que es muy cercana al periodo de rotación estelar de 38 días. A partir de datos independientes de Mt. Wilson HK, encontramos evidencia de una señal de 42 días, estadísticamente significativa. Esto hace dudar de la naturaleza planetaria de la señal encontrada. Concluimos que existen efectos residuales de la rotación estelar que son difíciles de modelar y remover de este set de datos, resaltando las dificultades para separar señales débiles debido a planetas del ruido fotosférico, particularmente cuando los periodos orbitales son similares a los periodos de rotación de la estrella. Este estudio sirve como un excelente caso de prueba para trabajos futuros, cuyos objetivos sean la detección de pequeños planetas orbitando estrellas similares al Sol. Las técnicas aplicadas en este estudio las hemos extendido al resto de nuestro trabajo en objetos adicionales que cuentan con más de 100 velocidades radiales con el objeto de mejorar el censo de pequeños planetas orbitando estrellas cercanas.

Luego se describe un nuevo método para la derivación de espectros libres de Iodine, directamente obtenidos de las observaciones de estrellas con espectrógrafos de alta resolución que utilizan celdas de Iodine. La motivación principal para obtener espectros libres de Iodine es poder usar porciones del espectro que contienen cientos de líneas de absorción superimpuestas, y de esta forma "contaminados" no permitiendo el cálculo, por ejemplo, de índices de actividad estelar en estas regiones lo que resulta útil a la hora de validar candidatos a planetas. El problema se hace más díficil cuando la amplitud de las señales de estos planetas es del orden de unos pocos metros por segundo, por lo que al incluir estos índices en los modelos, ayuda a determinar el origen de estas señales.

La parte final de esta tesis se enfoca en la detección y caracterización de planetas extrasolares. Reportamos el descubrimiento de un nuevo planeta de periodo orbital corto, similar a Neptuno, orbitando la estrella tipo Sol TOI-132 descubierta por el telescopio *TESS*. Luego de una campaña de monitoreo con HARPS, confirmamos el planeta con un período orbital de 2.11 días. Luego, combinando esto con la masa de la estrella, obtenemos una masa absoluta para el planeta de $21.90^{+1.39}_{-1.46}$ $M_\oplus$. Modelando la curva de luz de *TESS*, encontramos un radio de $3.571^{+0.111}_{-0.121}$ $R_\oplus$, obteniendo una densidad de $2.651^{+0.299}_{-0.323}$ g cm^{-3} para el planeta. Finalmente, reportamos la detección de un planeta denso, de tipo Neptuno orbitando a la estrella brillante HD 95338. La detección inicial de la señal de 55 días proviene de una campaña de velocidades radiales con el espectrógrafo PFS. HD 95338 también fue observada por *TESS* como un evento monotránsito. Una búsqueda MCMC nos permitió imponer condiciones muy acotadas en los valores de algunos parámetros orbitales como el tiempo de tránsito, cuyo resultado fue muy similar al calculado con *TESS*. Nuestro modelo produce una masa absoluta $39.43^{+6.04}_{-4.13} M_\oplus$ y un radio de $3.98^{+0.09}_{-0.08}$ $R_\oplus$. Así, obtenemos una densidad de $3.41^{+0.56}_{-0.40}$ g cm^{-3} para el planeta. HD 95338 b es uno de los planetas tipo Neptuno más densos descubiertos a la fecha, indicando un enriquecimiento de elementos pesados del orden del 90%. Este sistema representa una oportunidad única para futuras campañas de seguimiento que puedan ayudar a modelar los planetas gigantes fríos.

RESUMEN DE LA TESIS PARA OPTAR
AL GRADO DE DOCTOR EN CIENCIAS, MENCIÓN ASTRONOMÍA
POR: MATÍAS RODRIGO DÍAZ MUÑOZ
FECHA: 2022
PROF. GUÍA: CÉSAR ISAÍAS FUENTES GONZÁLEZ

SEARCHING FOR THE SMALLEST PLANETS ORBITING AROUND NEARBY STARS

This thesis is based on four first-author refereed papers. First, we discuss the study of a radial velocity signal that can be interpreted as a planetary-mass candidate orbiting the K dwarf HD 26965, with an orbital period of 42.364±0.015 days. Our best solution is consistent with a super-Earth that has a minimum mass of 6.92±0.79 $M_\oplus$. We have analyzed the correlation between spectral activity indicators and the radial velocities from each instrument, showing moderate correlations that we include in our model. We recover a ∼42 day signal, which is very close to the reported stellar rotation period of 38 days. From independent Mt. Wilson HK data, we find evidence for a significant 42 day signal after subtraction of longer period magnetic cycles, casting doubt on the planetary hypothesis for this period. We conclude that the residual effects of stellar rotation are difficult to fully model and remove from this dataset, highlighting the difficulties to disentangle small planetary signals and photospheric noise, particularly when the orbital periods are close to the rotation period of the star. This study serves as an excellent test case for future works that aim to detect small planets orbiting "Sun-like" stars using radial velocity measurements. The techniques we have learned from this work are being applied to ∼ 20 additional candidates that have more than 100 precision radial velocities, in order to help map out the census of small planets orbiting the nearest stars.

We then describe a new method to derive clean, iodine-free spectra directly from observations acquired using high resolution spectrographs equipped with iodine cells. The main motivation to obtain iodine-free spectra is to use portions of the spectrum that are superimposed with the dense forest of iodine absorption lines, to retrieve lines that can be used to monitor the magnetic activity of the star, helping to validate planet candidates. This is key when trying to address the problems that arise when searching for exoplanet signals with amplitudes of only a few meters per second, since including correlations between activity indicators and the radial velocities when modeling the data can help to determine the signal's origin, either Doppler or stellar activity. We provide a straight-forward methodology to derive iodine-free spectra directly from the observations.

The final part of this thesis focuses on planet detection and characterization. We report the discovery of a new short-period Neptune orbiting the solar-type star TOI-132 by *TESS*. Radial velocity follow-up with HARPS confirms the transiting planet with a ∼2.11 d orbital period, which when combined with the stellar mass of 0.97 $M_\odot$, provides a planetary absolute mass of $21.90^{+1.39}_{-1.46}$ $M_\oplus$. Modeling the *TESS* light curve returns a planet radius of $3.571^{+0.111}_{-0.121}$ $R_\oplus$, yielding a density of $2.651^{+0.299}_{-0.323}$ g cm^{-3}. Finally, we report the detection of a transiting dense Neptune orbiting the bright K star HD 95338. Detection of the 55-day periodic signal comes from the analysis of precision radial velocities from the PFS on the Magellan II Telescope. HD 95338 was also observed by *TESS* as a single transit event. A Markov Chain Monte Carlo period search on the velocities allows strong constraints on the expected transit time, matching well the epoch calculated using *TESS*. A joint fit model yields an absolute mass of $39.43^{+6.04}_{-4.13} M_\oplus$ and a radius of $3.98^{+0.09}_{-0.08}$ $R_\oplus$, therefore a density of $3.41^{+0.56}_{-0.40}$ g cm^{-3} for the planet. Given the planet mass and radius, structure models suggest it is fully composed of ices. HD 95338 b is one of the most dense Neptune planets yet detected, indicating a heavy element enrichment of ∼90%. This system presents a unique opportunity for future follow-up observations that can further constrain structure models of cool gas giant planets.

to myself

Acknowledgements

I would like to thank James for his support, knowledge, advice and for being a good friend over these years. Big thanks to Paul for sharing his expertise and for being a great and fun supervisor. I also want to thank Shec for giving me the opportunity to work at a top-class research institution during my graduate fellowship at Carnegie Observatories, always trying to test new ideas, hearing my questions and always giving good advice. Thanks to Irina, Beverly, Becky, Vgee and all the staff at Carnegie Observatories in Pasadena, for all the help and for making me feel at home from the moment I arrived. Thanks to Dante for his support in the early days of my interest of planet hunting.

Thanks to the PFS team: Jeff, Pamela, Fabo, Johanna, Sharon for giving me the opportunity to work among such a talented group.

Thanks to the telescope operators Jorge, Mauricio, Hugo and all the staff at Las Campanas Observatory, in particular to Mauricio N., Víctor, Gabriel, David and Don Héctor. Also thanks to the ESO staff at La Silla Observatory and the TIOs Eduardo, Mauricio, Javier, Pablo, Ariel and Duncan. It wouldn't have been the same without your work, experience and on-site support.

To my friends Grecco, Jorge, Juanpi, Juan, Guus, Blake, Pepe, Seba. Thanks for cursing everyday making Calán a tolerable place. To Sudeep, Dani, Pía, Bica, Richi, Chelo, Nina, Vains, Pablo and Patits for the laughs, tears, drinks, drugs and adventures. Also to Mari for sharing the frustrations with Calán, science, academia and people. Thanks to Marta, Vale, Nelly, Ale and Luis. To Guido and René for finding a place for me and letting me start working at Calán before applying to the Doctoral program. Thanks to Chispa for his friendship from ancient times at PUC.

Thanks to Adrian, Bruce, Dave, Janick, Nicko and Steve for being such an inspiration.

To my family, Pepe, Patty, Patichito, Jai and Maurice for always being there.

To Gaby for her support over these years.

Table of Content

List of Tables

List of Figures

Chapter 1

Introduction

1.1 26 years of exoplanet discoveries

Planets orbiting the nearest stars to the Sun are the most highly prized of all exoplanets, since they represent the most accessible targets for follow-up characterization studies. Developments in instrumentation (Vogt 2002; Pepe et al. 2002b; Crane et al. 2010; Quirrenbach et al. 2016; Pepe et al. 2020) and analysis techniques (Anglada-Escudé et al. 2013; Tuomi et al. 2014b; Feng et al. 2017b) over the past decade have also allowed us to detect rocky planets with masses similar of the mass of the Earth (Mayor et al. 2009; Vogt et al. 2010; Tuomi et al. 2014b).

The measurement of precision radial velocities has allowed us to begin to build up a collection of planets orbiting the nearest stars, while also characterizing their orbital parameters. In particular, discoveries like 51 Peg b (Mayor & Queloz 1995), 47 UMa b (Butler & Marcy 1996), 70 Vir b (Marcy & Butler 1996), HD 143361 b and HD 154672 b (Jenkins et al. 2009), HD 86226 b, HD 164604 b, HD 175167 b (Arriagada et al. 2010), HD 128356 b, HD 154672 b and HD 224538 b (Jenkins et al. 2017), GJ 876 b, c, d, e (Rivera et al. 2010), and υ And b, c, d (Wright et al. 2009; Curiel et al. 2011), among others, have allowed us to explore the wide diversity of gas giant planetary systems.

Until now, detailed studies have been possible for a handful of gas giant worlds. For example, two of the most well-known planets are HD 189733 b (Bouchy et al. 2005) and HD 209458 b (Henry et al. 2000; Charbonneau et al. 2000). HD 209458 b was the first confirmed transiting planet and it was also the first that allowed us to detect elements in its escaping atmosphere, in this case Na and CO (Charbonneau et al. 2002). HD 189733 b also orbits a fairly bright star, and therefore we were able to show that this object has an inflated atmosphere that is in the process of being evaporated due to the close proximity of the host star (Lecavelier des Etangs et al. 2012; Bourrier et al. 2013). From its escaping atmosphere Sodium D absorption has been characterized (Wyttenbach et al. 2015; Salz et al. 2016). Recent studies have revealed water vapor absorption in the planet's atmosphere (Birkby et al. 2013; Alonso-Floriano et al. 2019) and also absorption due to methane (Brogi et al.

2018). Beyond these two planets, we now have a number of transiting gas giants that have revealed their atmospheric make-up (e.g., GJ 3470 b, Nascimbeni et al. 2013; WASP-12 b, Kreidberg et al. 2015; MASCARA-2 b/KELT-20 b, Casasayas-Barris et al. 2019; KELT-9 b, Turner et al. 2020), however many more are needed to fully explore the nature of planet formation and evolution.

Although we have learned a great deal about gas giants, the vast majority of what we know applies only to the hottest subset, those closest to their stars that are heavily irradiated. The equilibrium temperatures of these hot Jupiters are generally >1000 K, and therefore their atmospheric chemistries and physical properties are likely very different to those on longer period orbits, like Jupiter in our solar system. The population of longer period transiting planets is growing (e.g. HATS-17 b, Brahm et al. 2016; Kepler-538 b, Mayo et al. 2019; EPIC 249893012 c & d, Hidalgo et al. 2020), particularly since the introduction of *TESS* that finds transits orbiting significantly brighter stars than *Kepler* or *K2*, and across the whole sky (e.g., HD 1397 b, Brahm et al. 2019; TOI-667 b, Jordán et al. 2019; HD 21749 b & c, Dragomir et al. 2019). However, despite these gains, we have only uncovered a few transiting planets with orbital periods greater than 40 days, orbiting stars bright enough ($V < 9$) for detailed atmospheric characterization.

Once a planet has been confirmed orbiting a nearby star, there exists the ability to perform detailed secondary follow-up studies, like measuring accurate stellar atomic and molecular abundances (Schuler et al. 2015; Meléndez et al. 2017) that could be sign-posts of planetary systems, or searching for transits and secondary eclipses (Baskin et al. 2013; Chen et al. 2014; von Paris et al. 2016). The combination of minimum mass (from the radial velocities) and radius (from any detected transit) measurements allows the density of the planet to be obtained (e.g., BD+20594 b, Espinoza et al. 2016; GJ 1214 b, Valencia et al. 2013; GJ 436 b von Braun et al. 2012; Lanotte et al. 2014; 55 Cnc e, de Mooij et al. 2014; Winn et al. 2011) and from there, model comparisons can be made to infer the bulk composition. Therefore, gaining a better understanding of the population of low-mass planets requires the detection of more of these worlds orbiting bright stars in the solar neighborhood.

The discovery of such planets around nearby stars, e.g., GJ 876 d (Rivera et al. 2010), HD 40307 b, c, d, e, f and g (Mayor et al. 2009; Tuomi et al. 2013a), GJ 581 d (Vogt et al. 2010), GJ 667C b, c and d (Anglada-Escudé et al. 2012, 2013), the candidates orbiting τ Ceti, planets b, c, d, e, and f (Tuomi et al. 2013b; Feng et al. 2017a), recently Proxima Centauri b (Anglada-Escudé et al. 2016a; Suárez Mascareño et al. 2020) and Barnard's star b (Ribas et al. 2018) represent a new population of super-Earth planets not witnessed in the Solar System, and are defined as being small planets with masses ∼2-10$M_\oplus$ that can either be primarily rocky objects or more "fluffy", atmosphere-dominated worlds (Valencia et al. 2007; Kaltenegger et al. 2011).

In comparison to the gas giants, super-Earths seem to have some dramatically different characteristics, likely related to their formation and early evolution. They generally appear to be orbiting on mostly circular orbits (Tuomi & Anglada-Escudé 2013a), come in tightly packed planetary systems (Lissauer et al. 2011; Latham et al. 2011), and do not seem to

follow the same metallicity bias as the gas giants (Buchhave et al. 2012; Courcol et al. 2016). In fact, there may be a lack of low-mass planets orbiting nearby and super metal-rich Sun-like stars (Jenkins et al. 2009, 2013). Models that invoke core accretion as the dominant planet formation scenario predict some of these trends, with mass functions rising heavily toward the lowest masses (Mordasini et al. 2008), also shown by analysis of the radial velocity sample of detected planets (Lopez & Jenkins 2012).

Planetary formation models also predict a damping of the metallicity bias in planet fraction for low-mass objects, since the stellar metallicity is an observational proxy of the dust content in the inner disk when the planets were undergoing formation. However the picture may be less clear, since Mulders et al. (2016) have shown that there might be an increase in the occurrence of small rocky planets around host stars with super-solar metallicities and orbital periods < 10 days. Moreover, Lu et al. (2020) have shown similar results, with stronger dependence for late-type stars.

The *Kepler* space telescope (Borucki et al. 2010) has allowed us to understand the population of small planets ($R_{\rm p} < 4\ R_{\oplus}$) in a real statistical sense for the first time. *Kepler* revealed that the majority of planets are the so-called super-Earths, with an occurrence rate of $\sim$6% of Earth-size planets around Sun-like stars (Petigura et al. 2013) (see Figure 1.1).

Kepler has also unveiled a bi-modality in the radius distribution of such planets (see Figure 1.2, Fulton et al. 2017; Van Eylen et al. 2018), which could be the result of photo-evaporation of the planetary atmosphere due to the intense stellar radiation (Lopez & Fortney 2013; Owen & Wu 2013; Jin et al. 2014; Chen & Rogers 2016). Furthermore, planets in the Neptune regime are also more abundant than the large gas giant planets. It is important to note that the distinction between super-Earths and sub-Neptunes is based on the radius, where the first class is commonly defined as planets with $1\,R_{\oplus} < R_{\rm p} < 2\,R_{\oplus}$ while the latter comprises planets with $2\,R_{\oplus} < R_{\rm p} < 4\,R_{\oplus}$. From *Kepler* statistics, 25-30% of Sun-like stars in our galaxy are found to host at least one small planet ($R_{\rm p} < 4R_{\oplus}$) on a short period orbit ($P < 100\,{\rm d}$) (Batalha et al. 2013; Marcy et al. 2014; Izidoro et al. 2021).

As the transit probability of a planet orbiting a star decreases with increasing orbital period, or star-planet separation, the majority of transiting systems contain planets with orbital periods of less than 10 days. For planets with longer periods, not only does the probability decrease compared with the shorter period counterparts, but they are also much more difficult to detect and confirm logistically, using ground-based transit surveys. Large-scale surveys have been setup to try to target longer period transiting systems (e.g., HATSouth, Bakos et al. 2013; NGTS, Wheatley et al. 2017), but they are generally limited to detection sensitivities that fall off after 12 days, due to the observing window function problem (Bakos et al. 2013). Space-based surveys can bypass this issue, as they are capable of monitoring these targets almost continuously.

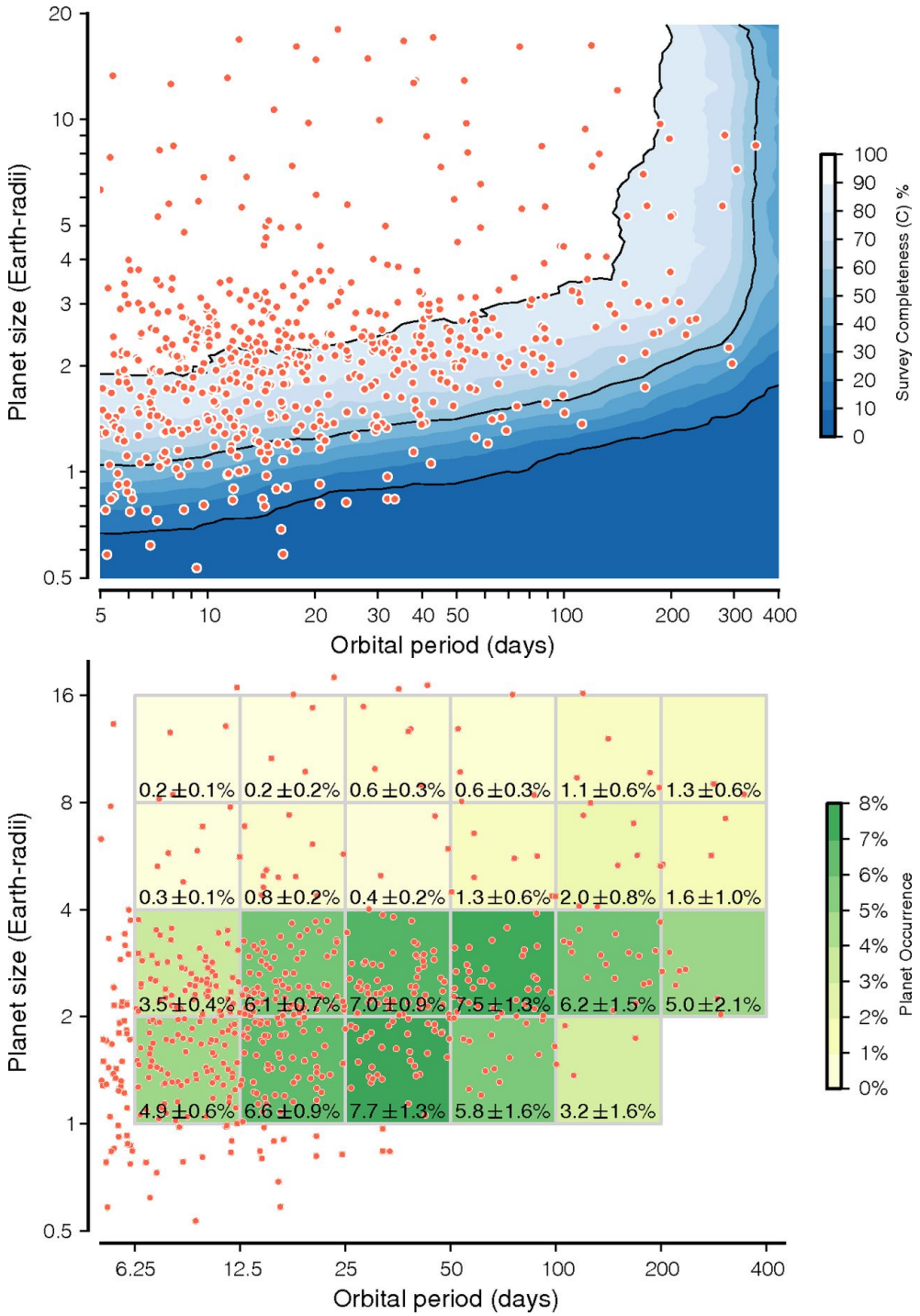

Figure 1.1: Figure from Petigura et al. (2013) based on *Kepler* data. Top plot shows the planetary radius vs orbital period for the 603 planet detected. The color scale shows the completeness of the survey measured by injection and recovery of synthetic planets into real photometry. Most common planets detected have periods shorter than 20 days and radii between 1 and 3 $R_\oplus$. Bottom plot shows the planet occurrence for a given radius and orbital period bin.

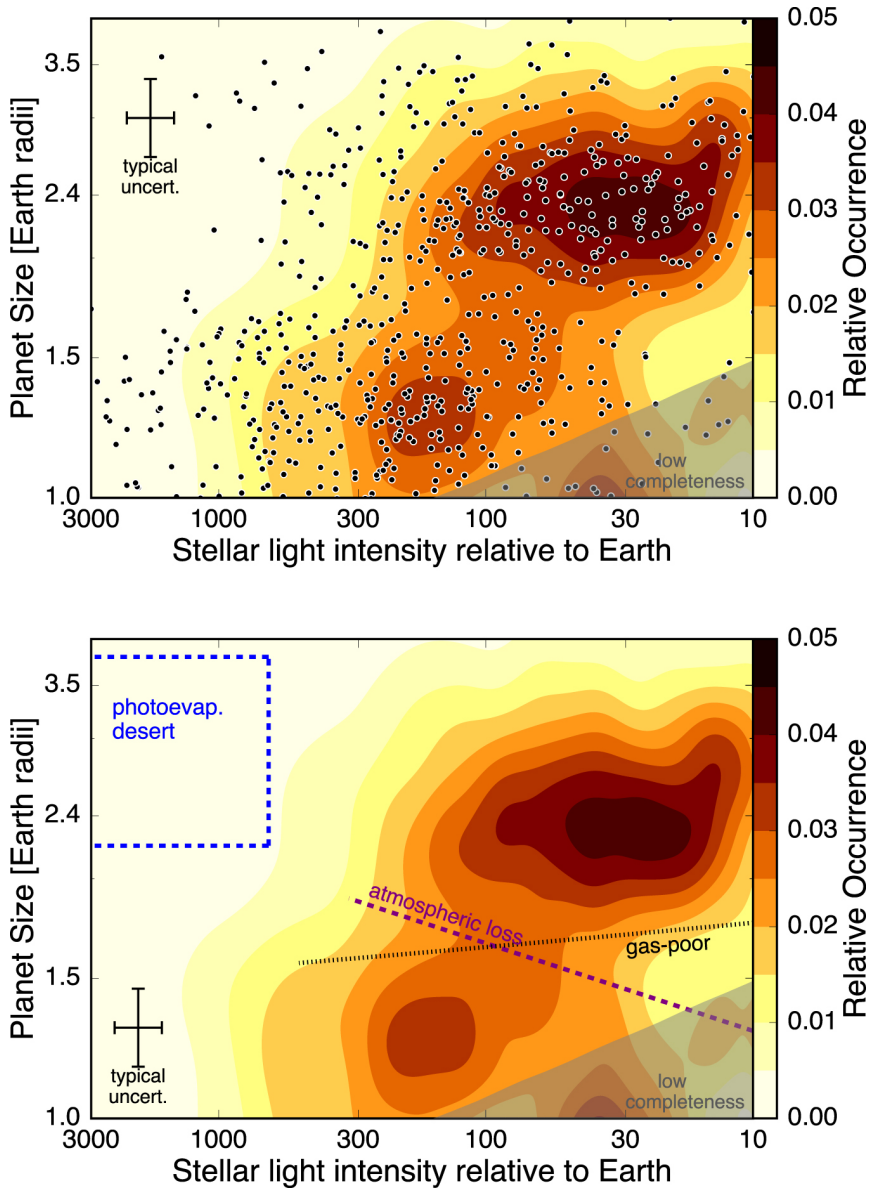

Figure 1.2: Figure from Fulton et al. (2017) showing a bi-modality in the radius distribution of close-in (P<100 d) exoplanets from *Kepler* data (top). One class of planets has typical radii of ∼1.3 $R_\oplus$, while another class of slightly larger planets with radii of ∼2.4 $R_\oplus$. Bottom plot shows the same as top panel, with the detections removed. The region enclosed by the dashed blue lines marks the photoevaporation desert (hot Super Earths). The paucity of planets between 1.5 and 2.0 $R_\oplus$ supports the picture that close-in planets smaller than Neptune are composed of rocky cores measuring 1.5 $R_\oplus$ or smaller with varying amounts of low-density gas that determine their total sizes.

1.2 Transiting Exoplanet Survey Satellite

Following the success of the *Kepler*/K2 mission, NASA launched the MIT-led *TESS* and it has been in operation since April 2018. The spacecraft orbits the Earth in a 2:1 lunar-resonant orbit (Gangestad et al. 2013) and unlike *Kepler*/K2 that stared a single field of 116 deg^2 to produce a statistical sample of exoplanets in its observation "cone", *TESS* focuses on the brightest nearby stars in the sky, which are the most accessible targets, giving the opportunity to get precise ($\sim$ 250 ppm for $T_{\rm mag}$ $\sim$10) observations for interesting targets that could serve as potential candidates for detailed follow-up spectroscopic observations with the next generation of space telescopes to study their atmospheres. The primary goal of the *TESS* mission, is to discover 50 planets with radii ≤ 4 $R_{\oplus}$ transiting stars brighter than V ≤ 12, for which precise masses can be measured using high-precision Doppler spectroscopy (Level 1 Science Requirement).

Each orbit of the spacecraft is 13.7 days, yielding a 27.4-day observing period after which the data is transferred to Earth for further processing and analysis by the *TESS* team. There is an overlapping region of the sectors at the ecliptic poles, with observing periods of 100s of days called the continuous viewing zones (CVZs), where long-period planets could be detected (see Figure 1.3). To date more than 2,000 planet candidates have been identified (Guerrero et al. 2021)[1].

The *TESS* spacecraft consists of a mosaic of four identical cameras, each with a 24×24 degree field of view, a pixel scale of 21 arcseconds/pixel and a wide, red bandpass (600-1000 nm), aligned to cover strips of the sky, the so-called *TESS* sectors covering 24×90 degrees each. Over its two-year Primary Mission, *TESS* observed $\sim$70% of the celestial sphere in 26 observing sectors, consisting of two main data types: the small, summed image subarrays or "postage stamp" also known as Target Pixel Files (TPFs), centered on 20,000 pre-selected targets where the CCDs are read at 2 second intervals; and the full-frame images (FFIs), from each of the four cameras, stacked into 30-minute stamps (see Figure 1.4).

During a typical sector (2 orbits), *TESS* produces over $\sim$19,000 sets of 2-min TPFs and $\sim$1,200 sets of FFIs. The data is then processed into calibrated light curves by two pipelines. The Science Processing Operations Center (SPOC, Jenkins et al. 2016b, 2020a) for 2-min cadence images and the MIT Quick Look Pipeline (QLP, Huang et al. 2020a,b) for the FFIs. These pipelines identify potential transiting events by searching for periodic flux decreases, which are referred to as 'Threshold Crossing Events' (TCEs) in both types of data products. Over the course of the prime mission the SPOC and QLP pipelines have produced timeseriesnlightcurves for more than 200,000 stars and $\sim$16 million stars ($T_{\rm mag}$ >13.5) for the 2-minute cadence and FFIs, respectively (Guerrero et al. 2021).

[1] `https://exoplanetarchive.ipac.caltech.edu/cgi-bin/TblView/nph-tblView?app=ExoTbls&config=TOI`

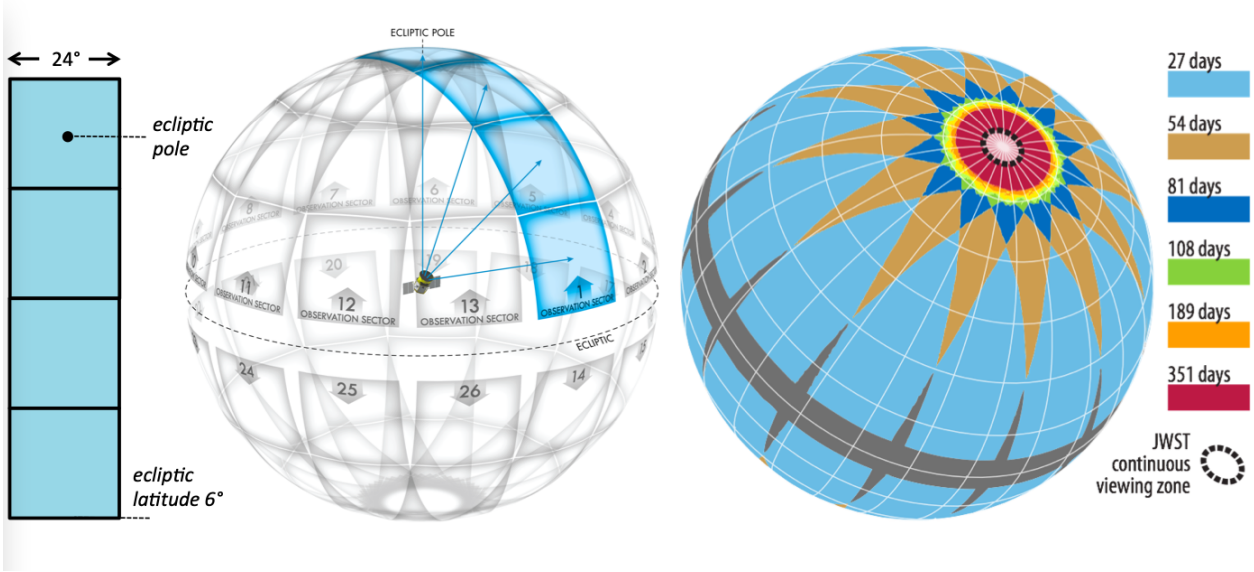

Figure 1.3: Diagram showing the sky coverage of the TESS spacecraft. A sector is composed of the images of the 4 cameras. Each sector overlaps with the previous enabling the detection of planets with periods longer than the 27-day baseline of each sector. Image from Ricker et al. (2015).

The majority of *TESS* exoplanets detected by SPOC are expected to have orbital periods of less than 14 days. Longer-period, cooler candidates are some of the most intriguing targets for atmospheric studies, particularly the lower-mass population. Neptune-sized planets have lower temperatures that could spark marked changes in the expected atmospheric chemistry (Burt et al. 2021).

TESS expanded the number of small planets around cool stars, and combining these results with the detections from *Kepler*, there is a striking planet population that emerge when studying the planet mass vs radius plane. One of the most surprising is the large population of planets with sizes between Earth and Neptune, a population that is completely absent from our Solar System.

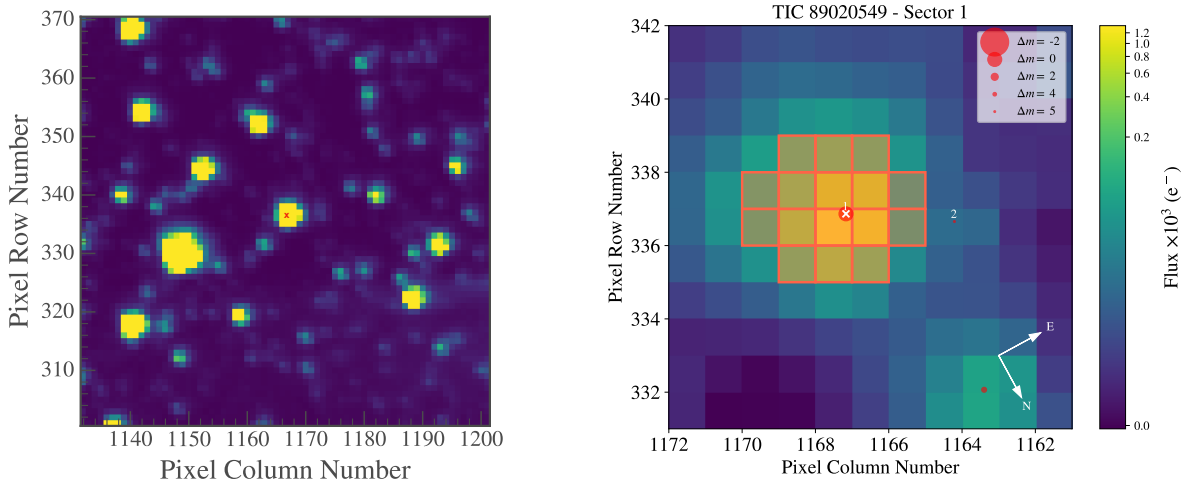

Figure 1.4: TESS data products. Left panel shows a cutout of 70×70 pixels from the FFI centered at the target TIC 89020549 (red cross). Right panel shows the TPF for the same target, including the default aperture used by the reduction pipeline (orange boxes). Nearby sources to the target are marked with red circles, where the size of the symbol represents the difference in magnitude with respect to the object of interest, also known as TOI-132. Plot created using `tpfplotter` (Aller et al. 2020).

1.3 The Neptune Desert

Although Neptune-sized planets orbiting Sun-like stars are fairly abundant (e.g., Espinoza et al. 2016; Luque et al. 2019; Mayo et al. 2019; Palle et al. 2019), at short orbital periods they are very rare. A number of early studies indicated a lack of Neptune-sized planets with periods shorter than 2−4 days (Szabó & Kiss 2011; Benítez-Llambay et al. 2011; Beaugé & Nesvorný 2013; Helled et al. 2016), and the term "Neptune desert" was coined to explain this paucity. The Neptune desert is a region of parameter space with a paucity of such planets, but it is not completely empty (see Figure 1.5). Mazeh et al. (2016) placed this dearth on a statistical footing, whilst providing robust boundaries for the region. Even though the dominant mechanism that produces this desert is currently unknown, models that invoke tidal disruption of a high-eccentricity migration planet, coupled with photoevaporation can explain the triangular shape of the gap described by Mazeh et al. (2016) (also Lundkvist et al. 2016; Owen & Lai 2018).

West et al. (2019) discovered the planet NGTS-4 b as part of the Next Generation Transit Survey (Wheatley et al. 2018) and although the star is fairly faint ($V = 13.14$), making the constraints on the radius and mass more difficult, the planet resides inside the boundaries of the desert defined by Mazeh et al. (2016). *TESS* , during its two first years of mission, has detected a handful of these types of planets, populating the Neptune desert. For example, HD 21966 b, a hot-Neptune that resides in the edge of this region, orbiting around a Sun-like star was detected from data from the first *TESS* sector (Esposito et al. 2019). The mission is also providing unprecedented targets to follow-up to study the Neptune desert, particularly the discovery of the first ultra hot Neptune, LTT 9779 b ($R_{\rm p}$= 4.59±0.23 $R_{\oplus}$, $P = 0.79$ days; Jenkins et al. 2020b). This planet resides well within the Neptune desert, and since the star is bright ($V = 9.76$), detailed follow-up can be performed to shed light on the processes that sculpt the desert. Another extreme example is TOI-849 b (Armstrong et al. 2020), a remnant core of a giant planet due probably to photoevaporation that could provide more information about planetary interiors. While not as extreme as the previous examples, recently the detection of the dense Neptune-like planet TOI-824 b (Burt et al. 2020) currently stands out as the most irradiated small planet that could be followed up for atmospheric studies and detailed characterization. An example of more recent discoveries are TOI-674 b (Murgas et al. 2021) and TOI-532 b (Kanodia et al. 2021), two large and massive super Neptunes detected around M dwarfs. However, more such examples are necessary to populate the desert, in order to uncover the dominant process(es) at play in this region of the mass period plane.

These planets are intrinsically rare, less than 1% of FGK stars host planets with radius between 2-6 $R_{\oplus}$ and P<4 days (Hsu et al. 2019). The origin of these hot Neptunes, however, remains unclear as their radii lie between the terrestrial planets that are thought to form primarily in-situ (Matsumoto & Kokubo 2017) and the giant planets that are believed to experienced inward migration processes (Nelson et al. 2017). These hot Neptunes, much like hot Jupiters, are more likely to be found orbiting metal-rich stars where they are the only transiting planet (Dong et al. 2018; Petigura et al. 2018).

The classical picture of planet formation considers a scenario where planets form within a protoplanary disk, composed 99% of gas and only a 1% of dust, and they grow from pebbles (∼10 cm) to planetesimals (10-1000 km) to planetary cores or embryos (Moon-sized/Mars-sized objects). Observational constraints such as the observed eccentricity distribution of exoplanets (Van Eylen et al. 2018), occurrence rates of certain types of planets (e.g., Jupiter-like vs Super-Earth/Neptunes, Fulton et al. 2017) have been used to refine the models.

A variety of physical processes occur within the protoplanetary disk such as particle drift due to the drag created by the gas in the disk that causes pebbles to drift inward, for example (Raymond & Morbidelli 2022). Clumping of these pebbles can lead to the formation of planetesimals, however when and where this process occurs is not clear. Planetesimals are most likely to grow larger due to drifting pebbles (pebble accretion), as the pebbles are more likely to stick to these larger bodies. Simulations have shown that in the case of an encounter of two planetesimals, they are more likely to bounce off each other than stick together (Lambrechts & Johansen 2012). They have also shown that it takes more time to form a core due to planetesimals than to pebble accretion, and this process can explain how big planet cores could have formed. Pebble accretion is, however, a self limiting process: once the growing core is large enough (∼20 $M_{\oplus}$ on a Jupiter-like orbit) it creates a large density wave out of its orbit that traps the pebbles, shutting the process off. Being able to manoeuvre the "pebble isolation mass", can give rise to quite different planetary system outcomes.

In the rocky regime, embryos can grow from planetesimal collisions. For Neptune-like planets, the picture is not that clear. It has been found that they are more difficult to form (with pebbles of planetesimals) unless they are embedded in disks with large amount of solids (Venturini & Helled 2017). This suggests that Neptune-like planets in low metallicity environments could form through merging of mini-Neptunes (Izidoro et al. 2015). Recent simulations by Izidoro et al. (2021) suggest that the increase in pebble flux could be enough to bifurcate the growth of planetary embryos from one producing super-Earths or hot Neptunes and another producing massive cores that could eventually become gas giants (Lambrechts & Lega 2017).

Migration is often observed in the simulations. When growing planets interact with the disk, they can launch a spiral density wave within it causing the orbit to shrink. The process stops at the inner edge of the disk. This process, called Type I migration, could explain the origin of hot Super-Earths. For bigger planets the process is slower (Type II migration), the planet creates a gap in the disk and the process could be responsible for planet-planet scattering and as a result it produces high eccentric orbits (Raymond & Morbidelli 2022 and the references therein).

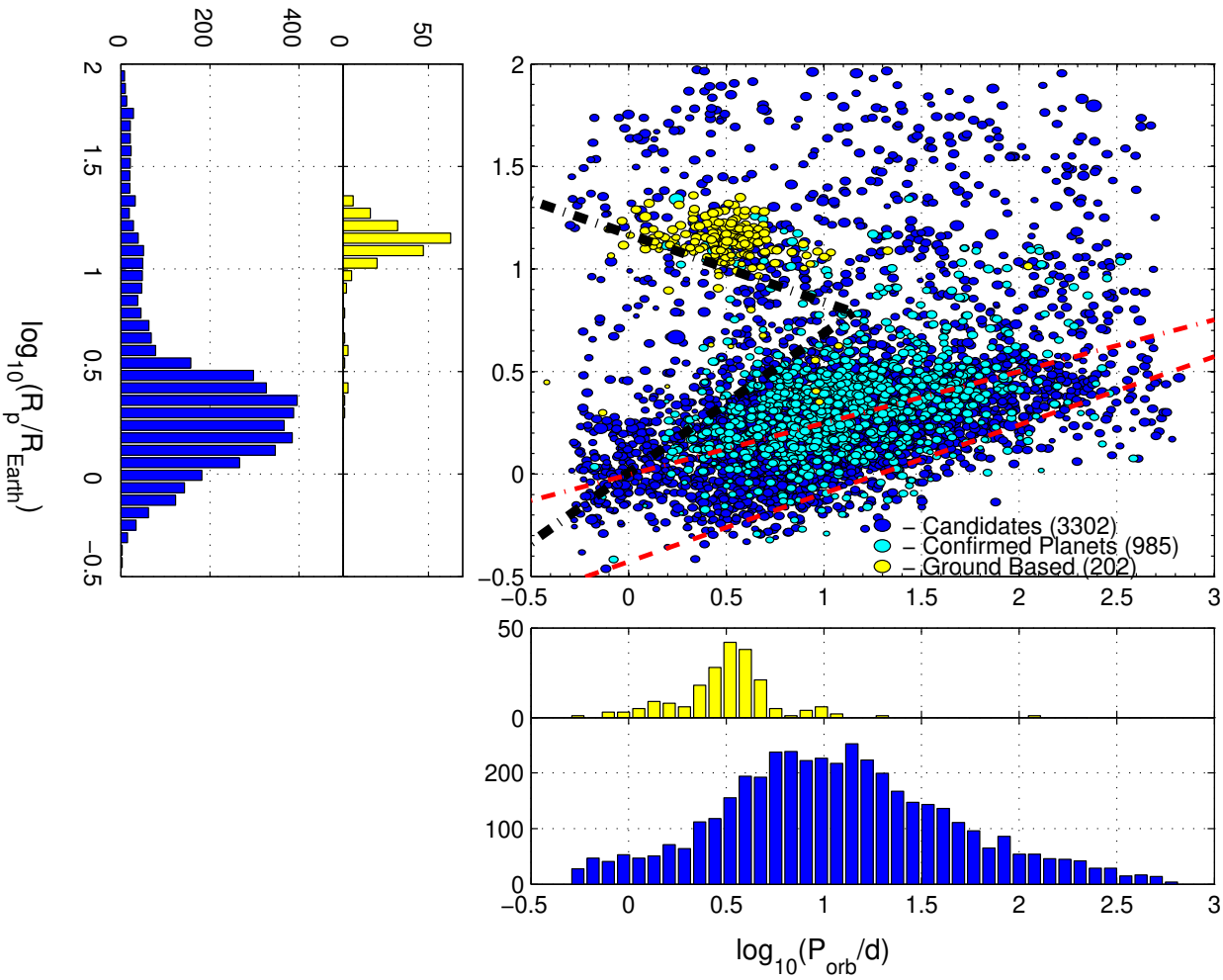

Figure 1.5: Planetary radii vs orbital period from Mazeh et al. (2016), based on ground-based transit searches (yellow points), *Kepler* candidates (blue points) and *Kepler* confirmed planets (cyan points). Black dotted lines defined the boundaries of the Neptune desert. Red dash-dotted line shows the center of the "ridge", a dense region of *Kepler* detected planets. The red dashed line represents the region that is poorly represented, and that it is determined by the S/N of a transit.

1.4 Detection Methods

In the following sections we briefly describe the two most successful methods for detecting planets orbiting around other stars. The transit method has produced the majority of the discoveries to date, in part thanks to the successful *Kepler* space mission (and later K2) and currently being employed by *TESS*, while the radial velocity technique started the field in the early 90s, providing the first batch of discoveries in the following years. There are other methods such as direct imaging, microlensing, transit timing variations, astrometry, but they will not be covered as they are not the subject of this thesis.

1.4.1 Radial Velocities

Detection methods and instrumental techniques have dramatically improved their precision since the detection of the first extrasolar planet in 1995. Doppler spectroscopy has been one of the two most successful detection techniques to search for exoplanets orbiting other stars. This method consists of acquiring spectra to measure the wobble of the star, produced by the gravitational effects of an (unseen) planet orbiting around it. This method gave rise to the first detection of an exoplanet orbiting a sun-like star[2].

Gravitationally linked bodies, such as planets orbiting around their host stars, orbit a common point where the sum of the forces equate to zero. This is known as the barycenter of the system. Due to the fact that the planet is much less massive than the star, the barycenter is closer to the star. Therefore, the presence of a planet orbiting around a star can be inferred by measuring the velocity of the star in the line of sight of an observer located on Earth. When a source is moving, due to the Doppler effect, the light emitted at frequency f will experience a change in frequency, so the observer will measure $f + \delta f$, with δf the change in frequency.

Translating the problem into the wavelength domain, this effect can be measured directly from the acquired spectrum of the star as the light originally emitted at λ_0, will experience a wavelength shift due to the fact that it is moving with respect to the observer.

This change in wavelength can be written according to

$$\lambda = \lambda_0 \sqrt{\frac{1 - v/c}{1 + v/c}} \tag{1.1}$$

where v is the velocity of the moving source and c corresponds to the speed of light.

[2]The very first detection of an exoplanet was, in fact, around the pulsar PSR B1257+12 by Wolszczan & Frail (1992)

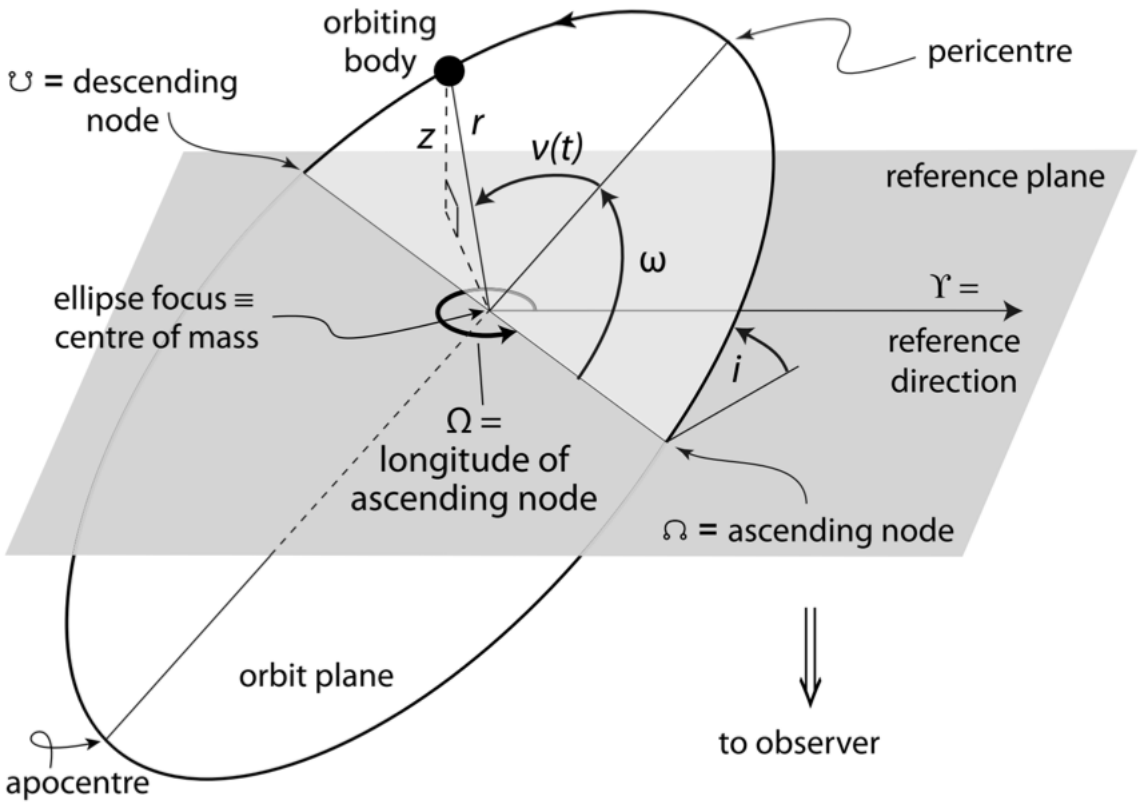

Figure 1.6: Radial velocity orbital diagram showing the orbital elements of a body (planet) moving in an elliptical orbit. Figure from Perryman (2011).

Hence, we rewrite it as

$$\frac{\Delta\lambda}{\lambda_0} = \frac{v}{c} \tag{1.2}$$

Therefore, if the source is moving towards us, the light will be blueshifted. On the other hand, if the source is moving away from the observer, the light will be redshifted, according to Equation 1.2.

Measured radial velocities have to be referred to a non-moving frame (or one with constant motion). Therefore, the Solar System barycenter is commonly adopted. Usually, the NASA JPL ephemeris[3] is used to apply the barycentric correction to the computed radial velocities, as it provides a correction for the time-varying motion of the Earth around the barycenter, including effects due to gravitational perturbations of other planets in the Solar System (Konopliv et al. 2006), for example. A detailed discussion about barycentric correction applied for exoplanet studies can be found in Wright & Eastman (2014).

The standard mathematical representation of the radial velocity is given by

[3] `https://ssd.jpl.nasa.gov/?ephemerides`

$$v_r(t) = K[\cos(\omega + \nu(t)) + \mathrm{e}\cos\omega] + \gamma \tag{1.3}$$

where ω argument of periapsis of the star's orbit with respect to the barycenter, $\nu(t)$ is the true anomaly of the orbit at the time of transit, e is the eccentricity and γ is the systemic velocity (or rest frame velocity) of the system (see also Figure 1.6). K corresponds to the radial velocity semi-amplitude given by

$$K = \left(\frac{2\pi G}{P}\right)^{\frac{1}{3}} \frac{M_{\mathrm{p}}\sin\mathrm{i}}{(M_\star + M_{\mathrm{p}})^{\frac{2}{3}}} \frac{1}{(1-\mathrm{e}^2)^{\frac{1}{2}}} \tag{1.4}$$

Where P corresponds to the orbital period of the planet around the star, $M_\star$ and M_{p} are the mass of the star and the mass of the planet, respectively and i is the inclination of the orbital plane with respect to the line-of-sight (observer).

Following Wright (2018), we can write the dependence of K, with the other quantities of interest:

$$K = 28\ \mathrm{m\,s^{-1}}(1-\mathrm{e}^2)^{-\frac{1}{2}} \left(\frac{P}{\mathrm{yr}}\right)^{\frac{1}{3}} \left(\frac{M_\star}{M_\odot}\right)^{\frac{2}{3}} \left(\frac{M_{\mathrm{p}}}{M_{\mathrm{J}}}\right) \sin\mathrm{i} \tag{1.5}$$

or alternatively,

$$K = 0.64\ \mathrm{m\,s^{-1}}(1-\mathrm{e}^2)^{-\frac{1}{2}} \left(\frac{P}{\mathrm{day}}\right)^{\frac{1}{3}} \left(\frac{M_\star}{M_\odot}\right)^{\frac{2}{3}} \left(\frac{M_{\mathrm{p}}}{M_\oplus}\right) \sin\mathrm{i} \tag{1.6}$$

where we assume, for simplicity, that $M_{\mathrm{p}} \ll M_\star$.

From equations 1.5 and 1.6, we see that the radial velocity depends strongly on the planet candidate's minimum mass and orbital period. A giant, Jupiter-mass planet on a year orbit around a Sun-like star will produce a radial velocity variation (or semi-amplitude) of $\sim$28 m $\mathrm{s^{-1}}$. An Earth-like planet on a 1-day orbit around a Sun-like star will translate to a radial velocity semi-amplitude of 0.64 m $\mathrm{s^{-1}}$. This highlights the instrumental challenge needed to detect these types of planets with the currently available technology.

In order to achieve the radial velocity precision needed to detect companions orbiting other stars, precise wavelength references are needed. Over the years, two main methods have stood out as the best to derive precise radial velocities: one is based on the use of simultaneous calibration within a vacuum temperature and pressure-stabilized echelle platform, by applying two fiber observations to simultaneously record the spectrum of the star and an 'in-house' calibration source (e.g. Thorium-Argon lamp). This method has been improved and new calibration sources such as Fabry-Perot etalons (Wildi et al. 2010) and laser-frequency combs (Steinmetz et al. 2008; Frank et al. 2018), and now it can deliver radial velocities with a precision of less than half a meter per second for the newest generation instruments (e.g. HARPS, Pepe et al. 2002b; ESPRESSO, Pepe et al. 2010). This approach is often used

with the cross-correlation technique on fiber-fed spectrographs and it produced the very first detection of an exoplanet orbiting a solar-type star (Mayor & Queloz 1995). Fibers address the variable illumination of the spectrograph slit and the associated wavelength calibration issues (see e.g., Barden et al. 1981; Heacox 1986). The scrambling inside the fiber, due to the multiple internal reflection, decouples the illumination of the spectrograph optics and CCD from guiding errors and calibration source misalignments (Walker et al. 2003; Spronck et al. 2013; Halverson et al. 2015 and the references therein).

Cross-Correlation technique

The Cross-Correlation Function (CCF) method relies on the creation of a box-shaped numerical mask that contains a set of lines that are representative for a given stellar type (see details in Mayor & Queloz 1995, Queloz 1995, Baranne et al. 1996). This numerical mask consists of 1 and 0 values, with the non-zero values at the positions and widths of the stellar absorption lines. The Doppler information is contained in thousands of lines across multiple orders in the echelle spectra. The problem is then reduced to cross-correlating the numerical stellar template with each of the observations acquired for the target star, and then finding the velocity v_R by building a final CCF:

$$CCF = CCF(v_R) \propto \int S(\lambda) M(v_R)\, \mathrm{d}\lambda \tag{1.7}$$

where the cross correlation function, denoted by CCF, is the result of integrating the product of the observed spectrum, S, multiplied by the stellar mask, M shifted by a velocity v_R. Then, as the Doppler-shifted numerical mask can be expressed as the sum of individual masks, M_i, each containing the stellar absorption line i, the CCF can be re-written as

$$CCF = \int S(\lambda) \sum_\mathrm{i} M_\mathrm{i}(\lambda_{v_R})\, \mathrm{d}\lambda \tag{1.8}$$

$$= \sum_\mathrm{i} CCF_\mathrm{i}(v_R) \tag{1.9}$$

As discussed in Pepe et al. (2002a), a weighted cross-correlation CCF^W is used based on the relative depths of the stellar absorption lines. Lines that are relatively deeper, contain more radial-velocity information than weak lines. This technique can improve the overall velocity scatter, the photon noise of the final radial velocity and the effects produced by contamination of telluric lines. Then, equation 1.9 becomes

$$CCF^W = \sum_{\mathrm{i}} CCF_{\mathrm{i}}(v_R)\, c_{\mathrm{i}} \tag{1.10}$$

$$= \int I(\lambda) \sum_{\mathrm{i}} (M_{\mathrm{i}}(\lambda_{v_R})\, c_{\mathrm{i}})\, \mathrm{d}\lambda \tag{1.11}$$

where $I(\lambda)$ corresponds to the continuum intensity in the spectrum and c_{i} is the relative intensity of the i-th absorption line.

Then, a Gaussian function is fit to this CCF^W, where its centroid allows to find the radial velocity and σ provides the error in the radial velocity.

Iodine cell method

The second way to obtain high-precision radial velocity measurements is done by superimposing a gaseous absorption reference spectrum onto the stellar spectrum, providing a precise wavelength scale that is required for such work. One general benefit of this method is that the gas cell is relatively small and portable, and therefore it can be applied to non-stabilized systems (instead of having a custom-built pressure and temperature-stabilized room) at the expense of losing ∼30% of the light in the beam. It has been found that cells mounted at the entrance of the spectrograph dramatically improved radial velocity precision, going from hundreds of meters per second down to ∼10 meters per second in the late 1980s. The idea, originally discussed in Griffin & Griffin (1973), was improved by Campbell & Walker (1979) by making use of hydrogen fluoride (HF) gas to generate a reference using absorption lines. They achieved a precision at the level of ∼15 meters per second. The main limitation of the method used by Campbell & Walker (1979) is that HF provided few lines over a small wavelength range, besides being poisonous. Later, Marcy & Butler (1992) improved the precision by making use of molecular iodine to generate thousands of sharp reference absorption lines in the stellar spectra. While the initial precision was ∼20 meters per second, further improvements in the technique (Valenti et al. 1995) allowed them to achieve a radial velocity precision of ∼3 meters per second a few years later (Butler et al. 1996).

The iodine cell method brought with it a large number of exoplanet discoveries during the next few years (e.g., Marcy & Butler 1996; Butler & Marcy 1996; Marcy et al. 1999; Butler et al. 1999; Rivera et al. 2005). Given its obvious success in allowing the detection of exoplanets using currently functioning echelle spectrographs, the problem always remained that the spectra were essentially rendered useless for any follow-up work beyond velocity calculations. In particular, it has subsequently been found that chromospheric lines, or indeed other photospheric absorption lines can be used in the modeling process to detect smaller signals, and hence smaller planets, or also to better validate signals as being Doppler in nature (Tuomi et al. 2013b; Jenkins & Tuomi 2014; Tuomi et al. 2014a; Anglada-Escudé et al. 2012, 2016b; Boisse et al. 2011, 2012). An extended discussion of this method is presented in Chapter 3.

1.4.2 Transits

The idea to look for an eclipse (or transit) when observing a star to search for planetary companions around them dates from more than four decades ago (e.g., Rosenblatt 1971; Black 1980, 1981). These early studies discussed this possibility and the features that could be observed in the data in extensive detail, but the precision needed was only achieved during the late 1990s.

A transit occurs when a planet passes between the stellar disk and our line of sight, producing a dimming in the light we receive from the star. Figure 1.7 depicts the basic idea and geometry of a planet transiting in front of its host star (adapted from Winn et al. 2011). The first transiting exoplanet was discovered 20 years ago (HD209458 b, Charbonneau et al. 2000; Henry et al. 2000) and since then efforts have been made using both ground based facilities and space-based missions where now more than 4,000 have been discovered, mostly due to the success of this method.

If radial velocities reveal dynamical information about the system, the transit method reveals physical information, i.e., the size (or radius) of an orbiting companion. This way, from the shape of the lightcurve the depth of the transit, δ, can be related directly with the radius of the planet by

$$\delta = \Delta F = \left(\frac{R_p}{R_\star}\right)^2 \tag{1.12}$$

where ΔF, R_p and $R_\star$ denote the change in flux (contrast) measured in the lightcurve, the radius of the planet and the radius of the star, respectively.

If the mean flux radiated by the star, measured in the light curve is denoted by F, the typical contrast for a Jupiter-sized planet orbiting around a Sun-like ($1\ R_\odot$) star, the contrast would be of order 1% or 0.01 mag. An Earth-like planet around the same star would produce a contrast of order $\sim 8.4 \times 10^{-5}$.

Ground based surveys can find planets with typical contrast ratios of $\frac{\Delta F}{F} \sim 1\%$. On the other hand, space based surveys, in the absence of atmospheric effects, can reach down to $\frac{\Delta F}{F} \sim 10^{-4}$, according to Perryman (2011).

The inclination of the system can be written, based on 1.7 and according to Seager & Mallén-Ornelas (2003)

$$b = \frac{a}{R_\star}\cos \mathrm{i} = \left(\frac{(1-\sqrt{\Delta F})^2[\sin^2(t_F\pi/P)/\sin^2(t_T\pi/P)]\,(1+\sqrt{\Delta F})^2}{1-[\sin^2(t_F\pi/P)/\sin^2(t_T\pi/P)]}\right)^{\frac{1}{2}} \tag{1.13}$$

and we can write the scale parameter $\frac{a}{R_\star}$, as

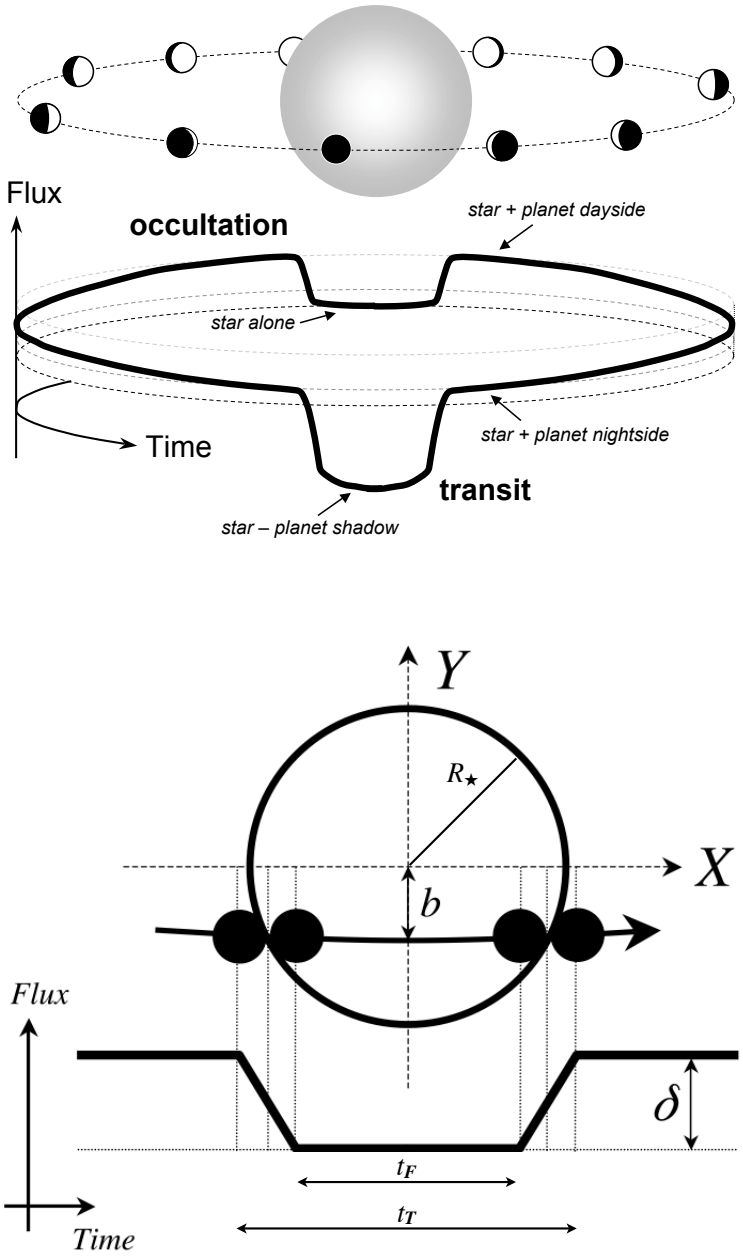

Figure 1.7: Left: Diagram showing the flux variations from a transit (and occultation) around a star. Right: Geometry of a transit light curve showing the depth of the transit δ, the radius of the star $R_\star$, the duration of the transit t_T, the impact parameter b and the duration of the transit between ingress and egress t_F. Figure adapted from Winn (2010).

$$\frac{a}{R_\star} = \left(\frac{(1+\sqrt{\Delta F})^2 - b^2(1-\sin^2)(t_T\pi/P))}{\sin^2(t_T\pi/P)} \right)^{\frac{1}{2}} \tag{1.14}$$

Combining these relations, as shown by Seager & Mallén-Ornelas (2003) an expression for the stellar density, $\rho_\star$, can be found

$$\rho_\star = \frac{M_\star}{R_\star^3} = \left(\frac{4\pi^2}{P^2 G} \right) \left(\frac{(1+\sqrt{(\Delta F)^2 - b^2(1-\sin^2(t_T\pi/P))}}{\sin^2(t_T\pi/P)} \right)^{\frac{3}{2}} \tag{1.15}$$

At this point it is reasonable to consider that the total transit duration and transit duration between ingress and egress, will be both much smaller than the orbital period of the planet, i.e., $t_T\pi \ll P$ and $t_F\pi \ll P$. Therefore, we can rewrite equations 1.12, and 1.13 and 1.14 into more simpler expressions:

$$b = \left(\frac{(1-\sqrt{\Delta F})^2 - (t_F/t_T)^2(1+\sqrt{\Delta F})^2}{1-(t_F/t_T)^2} \right)^{\frac{1}{2}} \tag{1.16}$$

and finally

$$\frac{a}{R_\star} = \frac{2P}{\pi} \frac{\Delta F^{\frac{1}{4}}}{(t_T^2 - t_F^2)^{\frac{1}{2}}} \tag{1.17}$$

and

$$\rho_\star = \frac{32P}{\pi G} \frac{\Delta F^{\frac{3}{4}}}{(t_T^2 - t_F^2)^{\frac{3}{2}}} \tag{1.18}$$

It is important to note that these relations are valid for circular orbits and neglecting the effects of limb-darkening. Limb-darkening is the effect produced by the non-uniform brightness of the stellar disk (Schwarzschild & Villiger 1906) and it can be seen in a transit at the times of ingress and egress. Let $I(\cos\theta)$ be the specific intensity of a star, at an angle θ with respect to the normal to the stellar disk, the limb-darkening is commonly parametrized as:

$$I(\mu) = I(1)[\,1 - u_1(1-\mu)] \qquad \text{linear} \tag{1.19}$$

$$I(\mu) = I(1)[\,1 - u_1(1-\mu) - u_2(1-\mu)^2] \qquad \text{quadratic} \tag{1.20}$$

$$I(\mu) = I(1)[\,1 - u_1(1-\mu) - u_2(1-\sqrt{u})] \qquad \text{square-root} \tag{1.21}$$

with $\mu = \cos\theta$, so $I(1)$ corresponds to the intensity at the center of the disk ($\theta = 0$) and $u_{\rm i}$ are the limb-darkening coefficients. A detailed discussion on the selection of the appropriate limb-darkening law can be found in Espinoza & Jordán (2016). For modeling the transits the parametrization of Kipping (2013) is usually used (see e.g. Espinoza 2018; Espinoza et al. 2019a).

Transits provide enough information to determine most of the orbital parameters of a given system. Therefore, with the help of "follow-up" radial velocities the true mass of the planet can be derived (from $M \sin {\rm i}$) and then we can obtain a value for the planet's density, $\rho_{\rm p}$, serving as a first estimate of the planet's composition.

1.5 Signal Search

1.5.1 Lomb-Scargle Periodogram

Periodograms are an excellent tool to analyze astrophysical time series, as they provide a first approach to find embedded signals in the data. The Lomb-Scargle periodogram (Lomb 1976; Scargle 1982) has been one of the most used tools to search for periodic signals in astronomical, unevenly sampled data. In short, a sinusoidal model is fitted for a given grid of trial frequencies (sampled linearly), and a power spectrum is generated by computing the goodness of the fit of the model for each trial frequency. Therefore, a high power in the spectrum is often related with finding the true period (or frequency) present in the data. A generalized version of this method was introduced by Zechmeister & Kürster (2009) improving one of the most important deficiencies of the original method that assumes the data has a mean given by $\overline{y}$, that is a good estimator of the mean of the series $y(t)$. This is not always true as gaps or poor sampling of the data could lead to aliasing problems. The generalized version of this method includes an additional term that serves as a constant offset for the model proposed in the original formulation of the periodogram, and also it has been shown that it can be more useful in the case of eccentric orbits.

The power spectrum of the Lomb-Scargle periodogram as a function of angular frequency, ω, can be expressed as

$$P_{\rm LS}(\omega) = \frac{1}{2}\left\{ \frac{\left[\sum_j X_j \cos\omega(t_j - \tau)\right]^2}{\sum_j \cos^2\omega(t_j - \tau)} + \frac{\left[\sum_j X_j \sin\omega(t_j - \tau)\right]^2}{\sum_j \sin^2\omega(t_j - \tau)} \right\} \tag{1.22}$$

where τ is defined as

$$\tan(2\omega\tau) = \left(\sum_j \sin 2\omega t_j\right)\left(\sum_j \cos 2\omega t_j\right)^{-1} \tag{1.23}$$

There are a few considerations when choosing the optimal parameters and they are described as follows. First, we need to defined the minimum and maximum frequencies to define the search grid. The maximum frequency, is defined by a pseudo-Nyquist frequency as $\omega_{\rm max} = \overline{\pi/\Delta t}$ with $\overline{1/\Delta t}$ is the median of the inverse time interval between points, following the discussion in Ivezic et al. (2014) and VanderPlas (2018). The minimum frequency, is defined by the baseline of the observations as $\omega_{\rm min} = 2\pi/(t_{\rm max} - t_{\rm min})$, where $t_{\rm min}$ and $t_{\rm max}$ are the first and last time stamp of the series, respectively. Another important parameter is the spacing of the frequency grid. The rule of thumb is that the frequency step has to be small enough to resolve the peaks in the power spectrum. To achieve this one can set $\Delta\omega = 0.1\,\omega_{\rm min}$ according to Debosscher et al. (2007).

In order to assess the statistical significance of the peaks in the resultant Lomb-Scargle power spectrum we used a bootstrap method where we randomly generate a new subset by permutation of the original dataset with replacement, usually 10000 times provides a good balance between accuracy and computational performance.

Unless otherwise noted, all the periodograms in this thesis have been computed following these definitions.

1.5.2 Posterior Samplings and Signal Detection

In the frequentist approach the parameters of a given model are treated as fixed but unknown quantities. However, different data samples give us different estimations for the parameters. In the bayesian approach the parameters are treated as random variables which can be described with a probability distribution. We do not need data to describe the distribution; as probability is our degree of belief about it. Bayesian analysis allows us to update the belief about the parameters based on the results by our experiment (prior x likelihood). The posterior distribution would be equal to the likelihood function when we use uninformative (flat or uniform) priors. More informative priors would have more influence in the posterior and the sample size.

To estimate the posterior probability of the parameters in the model given the observed data we use Bayes' rule:

$$P(\theta \,|\, y) = \frac{P(y \,|\, \theta)\, P(\theta)}{\int P(y \,|\, \theta)\, P(\theta)\, \mathrm{d}\theta} \tag{1.24}$$

$P(y \,|\, \theta)$ corresponds to the probability of observing the data if the hypothesis is true (given the parameters), we refer to this term as the likelihood function. $P(\theta)$ defines our prior knowledge of the hypothesis being true (if the parameter value is θ); this can include, for example, the physical limits or boundaries for some of the parameters and in some cases their distribution (and constraints) according to previous studies (e.g., Tuomi & Anglada-Escudé 2013b; Van Eylen et al. 2019). The denominator in equation 1.24, $\int P(y \,|\, \theta)\, P(\theta)\, \mathrm{d}\theta$, is called the evidence of our model, and it serves as a normalizing constant factor such that it has to integrate to unity over the parameter space. In practice, this term is often not trivial to compute but an approximation can be use by marginalizing, hence we often consider the

marginal likelihood. Then, the left-side term in the equation corresponds to the posterior probability, which updates the belief about the truth of the hypothesis given the data.

1.5.3 MCMC, Metropolis and DRAM algorithms

Monte Carlo methods consist of the generation of random numbers from a given distribution, for example, $\theta \sim \mathcal{N}(0, \sigma)$, a normal distribution with zero mean and an arbitrary standard deviation. When we use a proposal distribution, i.e, normal, the posterior distribution tends to the proposal distribution when the number of samples is large enough. When combined with Bayesian data analysis, we can find the solution of a physical problem by finding the most probable set parameters of a model that best describes the observed data.

A Markov Chain is a sequence of numbers $(x_1, x_2, ..., |x_N)$, where each number in the chain depends only on the previous number in the sequence. Also, for every state there is a positive probability of moving to any other state, and these chains must not get trapped into exhibiting cyclic behaviour (aperiodicity).

Therefore, Markov Chain Monte Carlo (MCMC) methods provide an efficient way to sample points from a given distribution, that may not have an analytical expression, when one wants to infer the cause giving rise to the observed data we usually see in nature, including astronomical problems.

When sampling using MCMC, the distribution approaches the posterior distribution as the number of samples, N, increases. Therefore, the posterior density is not used directly. Instead, samples from the posterior distribution are produced. Each new point, $\theta_{\mathrm{i}+1}$, depends only on the previous point in the chain, θ_{i}.

$$p(\theta_{\mathrm{i}+1}|\theta_{\mathrm{i}}, ..., \theta_3, \theta_2, \theta_1) = p(\theta_{\mathrm{i}+1}|\theta_{\mathrm{i}}) \tag{1.25}$$

- **Random Walk Metropolis**: In the simplest case of MCMC, the samples tend to exhibit a wandering pattern. This is known as the random-walk Metropolis algorithm (Metropolis et al. 1953). The basic idea behind this method is that first, we choose a starting point θ_0, drawn from the normal distribution considered before, for simplicity. The next point will depend on the previous value obtained, e.g., the value drawn from the proposal distribution would be the mean value of the next iteration, and we repeat the process N times. This method has been widely applied but it needs some fine tuning of its parameters by the user to different problems. It is also very dependent on the choice of starting point, θ_0.
- **Metropolis-Hastings**: An improvement to the random walk metropolis was introduced by Hastings (1970) and is it known as the Metropolis-Hastings algorithm. The generalization includes new definitions used to decide which values of θ are accepted or rejected during MCMC sampling. Using Bayes theorem the posterior probability of a given point, θ_{i}, can be estimated. This way, for a new point in the chain, θ_{new}, we compare the new posterior probability with the posterior probability of the previous point, $\theta_{\mathrm{i}-1}$. Recalling 1.24 we can define the ratio of the posterior probabilities of proposed

new point and the current state, θnew and θ_{i-1}, respectively

$$r(\theta_{new}, \theta_{i-1}) = \frac{P(\theta_{new} \mid y)}{P(\theta_{i-1} \mid y)} \tag{1.26}$$

if the posterior probability of the new value is higher than the previous one, then

$$r(\theta_{new}, \theta_{i-1}) > 1$$

and we will always accept the new proposed value. In the opposite case,

$$r(\theta_{new}, \theta_{i-1}) < 1$$

we will not necessarily discard the new value of θ, but instead, we define an acceptance probability

$$\alpha(\theta_{new}, \theta_{i-1}) = \min[\, r(\theta_{new}, \theta_{i-1}), 1] \tag{1.27}$$

Then, we draw a random number

$$u \sim \mathcal{U}(0, 1)$$

and if

$$u < \alpha(\theta_{new}, \theta_{i-1})$$

we set $\theta_i = \theta_{new}$, i.e., accept the new value. In the opposite case, we discard the new value and keep the previous one, $\theta_i = \theta_{i-1}$.

A few issues arise from the Metropolis-Hastings algorithm. Firstly, it strongly depends on the starting values. A good way to overcome this is to discard the initial part of the sample where the chain is still stabilizing and drifting up and down over time. This is generally set arbitrarily and it is known as the burn-in period (for diagnosis examples see Raftery & Lewis 1992). Secondly, due to the nature of the Markov Chain the values of θ are correlated. High autocorrelation could be related with problems in the model (Tuomi & Anglada-Escudé 2013b). To overcome autocorrelation, thinning is usually used, meaning that the MCMC sample size is increased but the samples are drawn at regular intervals, e.g., keeping every n-th value (see, Chapter 7 from Gilks et al. 1995)

- **Adaptive Metropolis and Delayed-Rejection**: Introduced by Haario et al. (2001), the Adaptive Metropolis algorithm is an extension of the original random-walk Metropolis. The modification, also discussed in Mira (2001) consists of adapting the proposal distribution (Gaussian) for the i-th proposed member, done by computing the covariance matrix of the chain, C, based on all the previous i-th states of the the chain. This ensures that the search is more effective at early stages of the simulation, compared with the Metropolis-Hastings. See Haario et al. (2001) and Tuomi (2012) for a detailed definition on how the covariance matrix is defined and updated.

  The Delayed-Rejection Adaptive Metropolis (DRAM) algorithm was proposed by Haario et al. (2006) combining the ideas from Haario et al. (2001) and Mira (2001). The

DRAM algorithm is particularly useful when the acceptance rate is low. The idea is when dealing with a rejected proposal, as in the MH algorithm, instead of retaining the current position as new value, a second stage move is proposed. This process of delaying rejection can be iterated for an arbitrary number of stages. In practice, up to three stages are considered before rejecting a proposed value (see Tuomi et al. 2014b, 2019). So, first we propose a value θ_1 from a proposal density centered typically at the current value, $q_1(\theta_0, \theta_1)$. This first state acceptance probability is identical as in the case of Metropolis-Hastings (eq 1.27), when we use a symmetric proposal density such that $q_1(\theta_0, \theta_1) = 1_1(\theta_1, \theta_0))$. Now, if the new proposed vector θ_1 is rejected, instead of retaining the same current position θ_0, a second candidate vector θ_2 is proposed by using another proposal density $q_2(\theta_0, \theta_1, \theta_2)$, and so on up to a third time and we use the acceptance probability given by Haario et al. (2006)

$$\alpha_{\rm i}(\theta_0, \theta_1, ..., \theta_{\rm i}) = \min \left\{ 1, \frac{P(\theta_{\rm i}|\, y) q_1(\theta_{\rm i}, \theta_{\rm i-1}) q_2(\theta_{\rm i}, \theta_{\rm i-1}, \theta_{\rm i-2}) \cdots q_{\rm i}(\theta_{\rm i}, \theta_{\rm i-1}, ..., \theta_0)}{P(\theta_0|\, y) q_1(\theta_0, \theta_1) q_2(\theta_0, \theta_1, \theta_2) \cdots q_{\rm i}(\theta_0, \theta_1, ..., \theta_{\rm i})} \right.$$
$$\left. \times \frac{[\,1 - \alpha_1(\theta_{\rm i}, \theta_{\rm i-1})\,]\,[\,1 - \alpha_2(\theta_{\rm i}, \theta_{\rm i-1}, \theta_{\rm i-2})\,] \cdots [\,1 - \alpha_{\rm i-1}(\theta_{\rm i}, ..., \theta_{\theta_1})\,]}{[\,1 - \alpha_1(\theta_0, \theta_1)\,] \cdots [\,1 - \alpha_{\rm i-1}(\theta_0, \theta_1, ..., \theta_{\rm i-1})\,]} \right\} \quad (1.28)$$

This is, we sample from a tighter ball around the accepted value, up-to three times before discarding a new proposal.

This algorithm is used, in the case of this thesis, to search for planetary signals in the radial velocity data. DRAM is especially helpful in this situation given that: i) the dimensionality of the problem is high, ii) the parameter space is highly multimodal, therefore the chains could visit all the modes in the posterior regularly so highest maxima are identified with confidence (Tuomi et al. 2014b).

Additional extensions and further applications of these methods include simulated annealing (Hobson & McLachlan 2003), thermodynamic integration (Goggans & Chi 2004) and parallel tempering (Earl & Deem 2005; Jenkins et al. 2019; Vines et al. 2019).

1.6 Stellar Activity

Mitigation of stellar activity is one of the big ongoing efforts in current exoplanet search. In numerous cases, both large and small planet candidates have been challenged as being due to the effects of stellar activity (e.g., HD 166435 Queloz et al. 2001; HIP 13044, Jones & Jenkins 2014; HD 41248, Santos et al. 2014; GJ 581 d, Robertson et al. 2014; Kapteyn b Robertson et al. 2015; α Cen B b, Rajpaul et al. 2016), with most of these challenges leading to counter-claims (e.g. HD 41248, Jenkins & Tuomi 2014; GJ 581 d, Anglada-Escudé & Tuomi 2015; Kapteyn b and c, Anglada-Escudé et al. 2016b). Therefore due care must be taken to ensure any signal has been well inspected for the effects of stellar activity and/or stellar rotation.

Magnetic activity is produced in the interior of stars due to the magnetic fields generated

by the motion fo the plasma (dynamo) (Babcock 1961; Steenbeck & Krause 1969; Raychaudhuri 1972). Stars exhibit different types of mechanisms that are associated to activity and they occur at different timescales: minutes to hours or days or months in the case of rotational-modulated activity, and longer magnetic cycles; and amplitudes that can go from a few cm s^{-1} to a few m s^{-1}. Often, the effects of stellar activity are seen in the spectra and therefore they have an impact on the final computed radial velocity of the star, and if not modeled properly and taken into account, they can give rise to radial velocity variability as they can modify the shape of the absorption lines in the spectra. This spectral line modification can then giving rise to spurious signals with similar amplitudes to that of a planet (see, e.g., Figueira et al. 2010; Haywood et al. 2014; Díaz et al. 2018). Stellar activity can be seen in different flavors such as granulation, spots, faculae, and plage for example.

Pressure mode (p-mode) oscillations typically occur on timescales of minutes, with an average of 5 minutes for solar-type stars (O'Toole et al. 2008). These oscillations can be overcome by observational techniques such as integrating over at least the average of the typical timescales (Udry & Mayor 2008; Dumusque et al. 2011). Others, require more efforts, and can require an extra term, or even approaches such as Gaussian Processes, in the final modelling to be dealt with (see, e.g., Rajpaul et al. 2015).

It is important to discuss how stellar activity can have a significant impact on the radial velocities we measure, and hence in the detection of spurious signals when searching for exoplanets. Since the first discovered exoplanet we have moved from amplitudes of 50 m s^{-1}(with 10 m s^{-1} errors) to $\sim$1 m s^{-1}(with 0.5 m s^{-1} errors or less). This has been possible mainly due to the instrumental advances in the last decade, as discussed above. Despite these improvements and the plethora of known exoplanets to date reaching even lower masses down to a few Earth masses, we are still hunting for a true 'Earth analogue'. For these types of small rocky planets we expect a radial velocity amplitude of order 10 cm s^{-1}. In fact, the signal of an Earth analog would be completely buried within the stellar noise, as stars are not homogeneous static spheres. Instead, we often see them wobbling and changing as they have inhomogeneities on their surface. Therefore, understanding the physics responsible of these processes is key to disentangling stellar activity and planetary signals. The study of the surface of the Sun has provided insights to understanding these phenomena. When we look at the surface of the Sun there is a characteristic corrugated pattern we refer to as granulation. Individual granules on the surface of the star are hot bubbles of gas, so there is a direct link with convection happening where the hot gas is rising up and being blueshifted in the center of the granule, and then as it cools down it falls back towards the center of the star at the edge of the granules, being redshifted with respect to our measurements. As convection produces these cells, moving gas up and down cyclicly, there is a significant cancelling in our velocity measurements, but a net effect exists, since the upward rising hot material is brighter than the downwards falling cool material, which can reach 40 cm s^{-1} according to Meunier et al. (2015).

So how does convection and granulation impact the measured radial velocities? We recall that when we take a spectrum to then obtain radial velocities, if we use the CCF method we cross-correlate the stellar spectrum usually with a binary mask and then we measure the

centroid of the CCF by fitting a Gaussian to it, as explained above. For a true Doppler shift, all the lines move (shift) by the same amount. Now, if there are asymmetries in the line profile we could end up having a spurious velocity shift (i.e. that looks like a true Doppler shift). Asymmetries in the line profile can happen due to the granulation effect explained above, as the granule is blue shifted and the intergranular lane is redshifted (Cegla et al. 2019). A standard way to deal with this is to look for variations in the Bisector (Queloz et al. 2001; Cegla et al. 2019). Newer techniques include the use of Autocorrelation function on the CCF, providing a way to separate Doppler shifts of dynamical origin from variability-induced ones (Collier Cameron et al. 2021).

Convection is also related with the magnetic field of the star, they interplay and are responsible for most of the stellar variability (Noyes et al. 1984; Milbourne et al. 2019). The magnetic field can have an effect by inhibiting the heat transport on the star (mainly through convection on Sun-like stars) and therefore it ends up producing a cooler (darker) area in the surface.This is what we refer to as stellar spot (see for example Giles et al. 2017 and the references therein). Spots are dark regions as they are cool because magnetic fields significantly suppress convection (and also being physically deeper). On the other hand, if there is not enough magnetic field a brighter region appears surrounding the granules, produced by flux evacuation that alters the opacity which allows us to see deeper (and therefore hotter regions) into the star, obtaining what we refer to as faculae/plage. Faculae are seen in the photosphere and plage can be understood as the chromospheric counterpart. Hence, monitoring activity indicators such as H_α and Ca II H&K (Wilson 1978; Saar & Donahue 1997; Saar 1998; Wright et al. 2004; Wright 2005; Jenkins et al. 2008, 2011) provides very useful information about the latter.

1.7 Stars in the sample

The targets observed in this thesis are from a subsample of bright (V_{mag}=5-8), nearby (median distance is 30 pc), chromospherically quiet ($\log R'_{HK} < -4.9$), main sequence stars with FGK spectral types, taken from the Magellan/PFS Exoplanet Planet Search Long-term Survey. This survey makes use of the Carnegie Planet Finder Spectrograph, a high-resolution echelle mounted on the 6.5m Magellan II/Clay telescope located in Las Campanas Observatory in Chile. Since 2010, it systematically monitors hundreds of stars, many of them having common data from older planet searches using other precise spectrographs such as the Hamilton/Lick program, UCLES from the Anglo-Australian Planet Search and the HIRES/Keck program.

The sub-sample includes 20 stars with emerging signals from periodogram analyses, showing peaks in the power spectrum between 1 and 100 days and radial velocity variations of a few meters per second. We applied for telescope time to include high-cadence observations with HARPS, and performed the observations between 2016 and 2019 under the program title “Searching for low-mass planets orbiting nearby stars with HARPS" (P.I. Díaz). The results shown in this thesis have been published in Díaz et al. (2018). Additional targets have been added since the launch of the *TESS* space telescope in 2018. We show the results of two planet detections published in Díaz et al. (2020a) and Díaz et al. (2020b).

1.8 Thesis Outline

Including this introduction, the thesis is comprised of 5 chapters.

Chapter 2 presents a study of a signal detected in the data of the K star HD 26965. According to our findings and modeling, the signal is consistent with a super-Earth on a 42-day orbit. However, upon examination of independent Mt. Wilson activity indicators, we cannot disentangle the weak Doppler signal from the activity of the star as the period found in the activity indices is close to the potential orbital period of the candidate.

Chapter 3 describes in detail a new algorithm to derive iodine-free spectra for observations acquired with high-resolution optical echelle spectrograph in the context of planet searches. Our method provides a fast and straightforward approach to clean each spectrum acquired originally with the iodine cell in place. The applications of this method could be used to derive super high-resolution templates to re-compute radial velocities, with the goal of improving the precision in the final velocities. In addition, the derivation of activity indicators of lines that fall within the iodine region could be derived from the clean spectra.

Chapter 4 presents the confirmation and characterization of a short-period Neptune planet detected by the *TESS* mission abound a solar-type star. HARPS precision velocities confirms and constrains the orbital parameters of TOI-132 b. The planet falls near the edge of the Neptune desert, that now it is being populated as new discoveries emerge. We discuss the properties and possible composition of this Neptune-like planet and the possibilities that studying these *TESS* Level 1 Science Requirement candidates enable.

Chapter 5 presents the confirmation of HD 95338 b, a Neptune mass planet orbiting around a K star on a 55-day orbit. The detection comes from 10 years of data acquired with PFS at Magellan. Additional HARPS data is consistent with the same signal. Recent data from *TESS* shows a single transit event. Combining the spectroscopic and photometric data we conclude the planet has a high density and it is most likely composed of ices. In addition the heavy element fraction is unusually high for a planet in its mass range so future observations and detailed studies are needed to fully explain the planet's origin.

The conclusions and future work are presented at the end of this thesis.

Chapter 2

Difficulties disentangling weak Doppler signals from stellar activity

Based on the results published in Díaz, M. R., et al., *The test case of HD 26965: difficulties disentangling weak Doppler signals from stellar activity*, 2018, ApJ, 155, 3.

In this chapter we discuss the study of a radial velocity signal that can be interpreted as a planetary-mass candidate orbiting the K dwarf HD 26965, with an orbital period of 42.364±0.015 days. Our best solution is consistent with a super-Earth that has a minimum mass of 6.92±0.79 $M_{\oplus}$. We have analyzed the correlation between spectral activity indicators and the radial velocities from each instrument, showing moderate correlations that we include in our model. We recover a ∼38 day signal, which matches the reported stellar rotation period. From independent Mt. Wilson HK data, we find evidence for a significant 42 day signal after subtraction of longer period magnetic cycles, casting doubt on the planetary hypothesis for this period. We conclude that the residual effects of stellar rotation are difficult to fully model and remove from this dataset, highlighting the difficulties to disentangle small planetary signals and photospheric noise, particularly when the orbital periods are close to the rotation period of the star. This study serves as an excellent test case for future works that aim to detect small planets orbiting "Sun-like" stars using radial velocity measurements. Here we present data from a 16 year precision radial velocity monitoring campaign, using multiple high resolution optical spectrographs, of the nearby (∼5 pc) K0.5 star HD 26965.

2.1 HD 26965 - Stellar properties

HD 26965 (HIP 19849, GJ 166A) is classified as a K0.5V star (Gray et al. 2006) with a visual magnitude of V=4.43 and an optical color of $B-V$=0.82. An activity index of $\log R'_{\rm HK}$=−4.99 is reported by Jenkins et al. (2011). This value is also consistent with measurements found in other sources in the literature (e.g., -5.09, Gray et al. 2006; -4.97, Murgas et al. 2013) and a comparison with the Sun's mean activity value of $\log R'_{\rm HK\odot}$=−4.91 (Mamajek & Hillenbrand 2008) tells us that HD 26965 is a chromospherically quiet star.

The remaining stellar parameters were estimated using the **S**pectroscopic **P**arameters and atmosphe**E**ric **C**hem**I**stri**E**s of **S**tars code (SPECIES; Soto & Jenkins 2018). SPECIES derives the

effective temperature, surface gravity, metallicity, microturbulence, macroturbulence and rotational velocity, mass, age and chemical abundances for 11 elements in a self-consistent and automatic manner. The parameters were derived using high-resolution, high signal-to-noise spectra as input for the code, where in this particular case, we have used spectra from HARPS to derive the stellar parameters with SPECIES. The first four parameters were found by measuring the equivalent widths (EWs) for a set of iron lines using the ARES code (Sousa et al. 2007). These values, along with a stellar atmosphere model (Kurucz 1993), were then input to MOOG (Sneden 1973a), which solves the radiative transfer equation by imposing excitation and ionization equilibrium. Following on from this, we then derived the chemical abundances, measuring the EWs of a set of lines for each element. Macroturbulence and rotation velocity were computed by measuring the broadening of spectral lines using a Fourier analysis. Finally, mass and age were found by fitting isochrones (Dotter et al. 2008) using the luminosity and temperature of the star. Figure 2.1 shows the final distributions for the stellar mass, age and log g using a Markov chain Monte Carlo (MCMC) method within SPECIES. More details about this code, in particular on the treatment of correlations between parameters and uncertainties, can be found in Soto & Jenkins (submitted).

We found HD 26965 to have a metallicity [Fe/H] of -0.29 $\pm$ 0.13 dex, consistent with previously reported values (e.g., -0.28 dex Gray et al. 2006; Valenti & Fischer 2005; Turnbull 2015), and significantly poorer in metals than the Sun. SPECIES finds a rotational velocity of $v \sin i$=1.23 $\pm$ 0.28 km s^{-1}, which is in agreement with the values of 1.1 $\pm$ 1.0, 1.4 $\pm$ 0.8, 1.6 $\pm$ 0.8 km s^{-1} reported by Glebocki & Gnacinski (2005) calculated via cross-correlation, calibrated line full width at half maximum (FWHM), and convolution with rotational broadening profiles, respectively.

The $v \sin i$ value we report is consistent with the old age of the star found by SPECIES if we consider that stars on the main sequence spin-down with time due to the loss of angular momentum from winds and the increase in stellar radius with time that is required to maintain hydrostatic equilibrium as the core changes due to nuclear burning. The Sun has a rotational velocity of only 1.6 $\pm$ 0.3 km s^{-1} (Pavlenko et al. 2012) and we classify it as a slow rotator. In summary, the values found for the parameters make HD 26965 a good candidate for radial velocity planet search since it can be considered a quiescent and slowly rotating star. The properties and derived parameters for HD 26965 are summarized in Table 2.1.

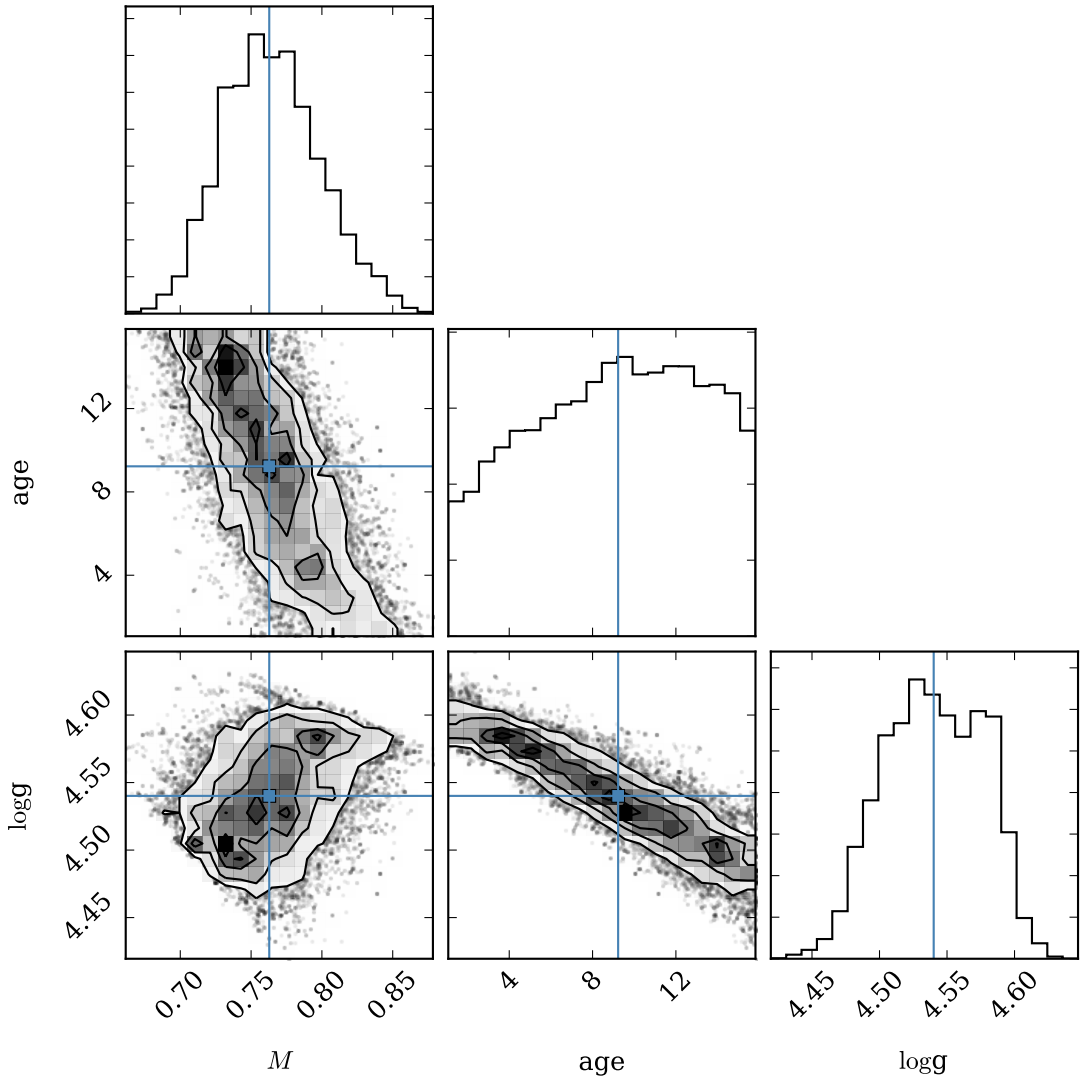

Figure 2.1: Corner plot showing the one and two dimensional projections of the posterior probability distributions for the mass, age and log g parameters estimated via MCMC samples with SPECIES. The plot has been generated using the Python package `corner.py` (Foreman-Mackey 2016).

Table 2.1: Stellar Parameters of HD 26965

Parameter	Value	Source
R.A. (J2000)	04:15:16.32	SIMBAD
Dec. (J2000)	-07:39:10.34	SIMBAD
m_V	4.43	SIMBAD
B-V	0.82	SIMBAD
Distance (pc)	4.98 ± 0.01	van Leeuwen 2007
Spectral type	K0.5V	Gray et al. 2006
Mass ($M_\odot$)	0.76 ± 0.03	This work (SPECIES)
Age (Gyr)	9.23 ± 4.84	This work (SPECIES)
Luminosity ($L_\odot$)	0.44	Anderson & Francis 2012
$T_{\rm eff}$ (K)	5151 ± 55	This work (SPECIES)
[Fe/H]	-0.29 ± 0.12	This work (SPECIES)
log g	4.54± 0.04	This work (SPECIES)
v sin i (km s^{-1})	1.23 ± 0.28	This work (SPECIES)
log R'_{HK}	-4.99	Jenkins et al. 2011

Table 2.2: Summary of instrumental and observational parameters for the different instruments.

Instrument	Resolution	<SNR>/Res. element	$<t_{\rm exp}>$ (s)	$<\sigma_{\rm RV}>$ (m s^{-1})	$N_{\rm obs}$	Baseline (yrs)
HIRES	45,000	270 × 4 exp	11	1.2	230	12
PFS	80,000	235 × 4 exp	40	1.0	65	5
CHIRON	95,000	120 × 3 exp	300	1.6	259	2
HARPS	115,000	150 × 4 exp	100	0.4	437	10

2.2 Spectroscopic Observations

High-precision Doppler measurements of HD 26965 were carried out using 4 different spectrographs: The High Resolution Echelle Spectrograph (HIRES) installed on the 10 m Keck Telescope in Hawaii, the Carnegie Planet Finder Spectrograph (PFS) mounted on the 6.5 m Magellan II (Clay) telescope at Las Campanas Observatory, CHIRON mounted on the 1.5 m telescope from the Small to Moderate Aperture Research Telescopes (SMARTS) consortium in Cerro Tololo Interamerican Observatory and the High Accuracy Radial velocity Planet Searcher (HARPS) installed on the 3.6 m ESO telescope at La Silla Observatory.

2.2.1 HIRES Observations

The full HIRES (Vogt et al. 1994) dataset comprises 229 individual Doppler measurements with an observational baseline of almost twelve years, between November 22nd 2001 and August 25th 2013. These individual radial velocities have been binned nightly to produce 90 measurements. One outlier point with a velocity value more than 3-σ away from the mean of the series has been rejected as it was acquired under poor weather conditions.

HIRES uses the iodine cell method to deliver high precision radial velocities. The method employs a cell containing molecular gaseous iodine (I_2) that is mounted before the slit of the spectrograph so that the incoming starlight is imprinted with thousands of I_2 absorption lines, between ∼4800Å and ∼6200Å that are used for both very precise wavelength reference points and also in the determination of the instrumental point spread function (PSF).

The HIRES spectrograph covers a wavelength range of 3700-8000Å. For most of the observations the B5 Decker (0.86"×3.5") was used, delivering a spectral resolving power of R ∼45,000. The C2 Decker (0.86"×14", R ∼45,000) was also used for a smaller number of observations. I_2-free template observations were carried out with the B3 Decker (0.574"×14") at R ∼60,000.

For the template observations we acquire multiple shots (typically 3) of the target star without I_2 with the narrow slit and we bracket these observations with the spectra of a bright, fast rotating B star observed through the I_2 cell. These I_2-free shots are then combined to create a high signal-to-noise, high resolution spectrum of the star that is later used for the computation of the radial velocities following the spectral synthesis procedure explained in Butler et al. (1996), where the I_2 region is divided into ∼700 chunks of about 2Å each to produce an independent measure of the wavelength, PSF, and Doppler shift. This procedure is also carried out for PFS and CHIRON observations.

Exposure times varied with nightly weather conditions, but we obtained a formal mean[1] uncertainty of $\sigma_{\rm BIN}$= 1.21 m s^{-1} and σ=1.18 m s^{-1} for the binned nightly and unbinned radial velocities, respectively, with this spectrograph.

From individual HIRES spectra we have calculated the S-indices from the Ca II H and K line cores (at 3968.47Å and 3933.66Å, respectively) following the prescription of Duncan et al. (1991) also described in Arriagada (2011). S-indices can be used for chromospheric activity analysis of the stars (Arriagada 2011; Boisse et al. 2011) since they are known to be correlated with spot activity on the surface of the star that can mimic planetary signals, or at best, introduce noise into the data.

[1]Weighted means using the radial velocity uncertainties as weights; $w_{\rm i} = 1/\sigma_{\rm i}$

2.2.2 PFS Observations

Observations were carried out using PFS (Crane et al. 2006, 2008, 2010) between October 18th 2011 and March 5th 2016. We obtained a total of 65 individual radial velocity measurements, translated into 19 binned velocities. PFS is also equipped with an I_2 cell for precise radial velocity measurements and it delivers a resolution of R ∼80,000 in the I_2 region when observing with the 0.5"×2.5" slit. I_2-free template observations were acquired with the 0.3"×2.5" slit at a resolution of R ∼127,000.

We routinely expose for a typical signal-to-noise ratio of ∼300 per spectral resolution element required to achieve a level of ∼1-2 m s^{-1} radial velocity precision. For bright targets, such as HD 26965, we take consecutive multiple exposures -usually 4 or 5- within a timespan of 5 minutes, to both average over the strongest stellar p-mode oscillations (∼5 min for solar-type stars; Leighton et al. 1962; Evans & Michard 1962; Ulrich 1970) and avoid saturation. For monitoring the stellar activity, S-indices were derived using individual spectra using the same approach described for HIRES.

We report a mean uncertainty of σ=0.97 m s^{-1} from this instrument. Mean uncertainty for the nightly binned data is $\sigma_{\rm BIN}$= 0.98 m s^{-1}.

2.2.3 CHIRON Observations

All observations with the fiber-fed high-resolution echelle spectrograph CHIRON (Tokovinin et al. 2013) were performed in service mode at R ∼95,000 using the '*Slit*' mode and 3×1 pixel binning. CHIRON is installed in a thermally controlled space that allows the instrument to be stabilized to temperatures drifts of ± 2 K.The spectrograph covers a fixed wavelength range between 4150Å and 8800Å which, unfortunately, does not allow any measurement of calcium lines to monitor the chromospheric activity. CHIRON also employs an I_2 absorption cell for wavelength calibration. The CHIRON team provides reduced data corresponding to wavelength calibrated spectra (Brewer et al. 2014). We also acquired higher resolution I_2-free templates taken in '*Narrow*' mode at R ∼136,000 with the same pixel sampling as in '*Slit*' mode. Then we used our pipeline to compute the final Doppler shifts with a modified routine similar to the ones used in the PFS and HIRES reduction.

In 2014 we started a high-cadence campaign using this instrument to monitor nearby bright FGK stars with V≤6. When observing with CHIRON, we have found that the linearity regime for the CCD ends once the counts per pixel reach ∼30,000, so we have routinely exposed every target up to a maximum level of 25,000 counts to avoid reaching this non-linearity regime. Since this target is a bright star, we use the same observational strategy that was used on both PFS and HIRES, meaning we take multiple short single exposures of the star that are combined into a single high-precision measurement.

Previous work by Jones et al. (2016) have shown precision of ∼5 m s^{-1} using the high efficiency slicer mode to look for planets orbiting around giant stars, at a lower resolution of R ∼79,000 and for targets fainter than V=6. Recent results by Zhao et al. (2018) using the same observing mode we describe in this work have also shown consistent short-term (nightly) radial velocity precision on the ∼1 m s^{-1} level for the very bright stars. They obtain a mean error of 1.1 m s^{-1} and 1.2 m s^{-1} for α Centauri A (V=-0.01) and B (V=1.13), respectively.

Results from our analysis give a mean radial velocity error for this bright star of σ=1.60 m s^{-1} for the unbinned dataset consisting of 258 velocities taken between October 11th 2014 and January

15th 2016. The mean radial velocity error for the nightly binned velocities is $\sigma_{\rm BIN}$=1.62 m s^{-1}.

2.2.4 HARPS Observations

We used public data obtained with the HARPS spectrograph (Mayor et al. 2003) available from the ESO HARPS archive[2]. All the data have been processed with the HARPS-Data Reduction Software (hereafter DRS) Version 3.5 pipeline which performs all the required reduction steps from bias, flat fielding and wavelength calibration of the high resolution spectra. HARPS is a pressure and temperature stabilized spectrograph that covers a wavelength range between 3800Å and 6900Å with a spectral resolving power of R ∼115,000. We note that HARPS does not make use of an I_2 cell for precise Doppler spectroscopy. Instead, exposures of a Thorium-Argon lamp are taken at the same time as each observation to get a precise wavelength reference for the science spectra (one spectrum on each of the two fibers that feed the instrument). Radial velocities are a product of a post-reduction analysis consisting of cross-correlating each echelle order with a binary mask that is chosen depending on the spectral type of each star. This produces cross-correlation functions (CCF) for each order that are then combined to obtain a mean-weighted CCF. This mean-weighted CCF is then used to generate the radial velocities. For HD 26965 we found 483 useful public Doppler measurements between October 27th 2003 and December 5th 2013 available from ESO HARPS archive. The DRS pipeline and further post-reduction analysis produced 437 radial velocity measurements with a mean error of σ=0.43 m s^{-1}, and yielded a set of 65 binned radial velocities with a mean uncertainty of $\sigma_{\rm BIN}$=0.42 m s^{-1}. HARPS vacuum enclosure was opened in 2015 as part of an upgrade on the fibers. We refer to the pre-upgrade data as HARPS OLD. We include 82 post-upgrade HARPS velocities between September 9th 2015 and March 27th 2016. This post-upgrade data is labeled HARPS NEW.

For all the analyses, the unbinned data from each instrument is used and is treated separately with their corresponding independent velocity offset and noise (jitter) properties.

In the case of the spectrographs equipped with an I_2 cell (HIRES, PFS, CHIRON), the reported velocities are the weighted mean of the velocities of the individual chunks while the uncertainties correspond to the standard deviation of all the chunk velocities about that mean. For HARPS, where the observations were carried out using simultaneous Thorium exposures, the RV uncertainty is provided by the DRS and it is estimated directly from a Gaussian fit to the CCF (Bouchy et al. 2001).

The 1111 radial velocity measurements are shown from Table 2.7 to Table 2.11.

[2] `http://archive.eso.org/wdb/wdb/eso/repro/form`

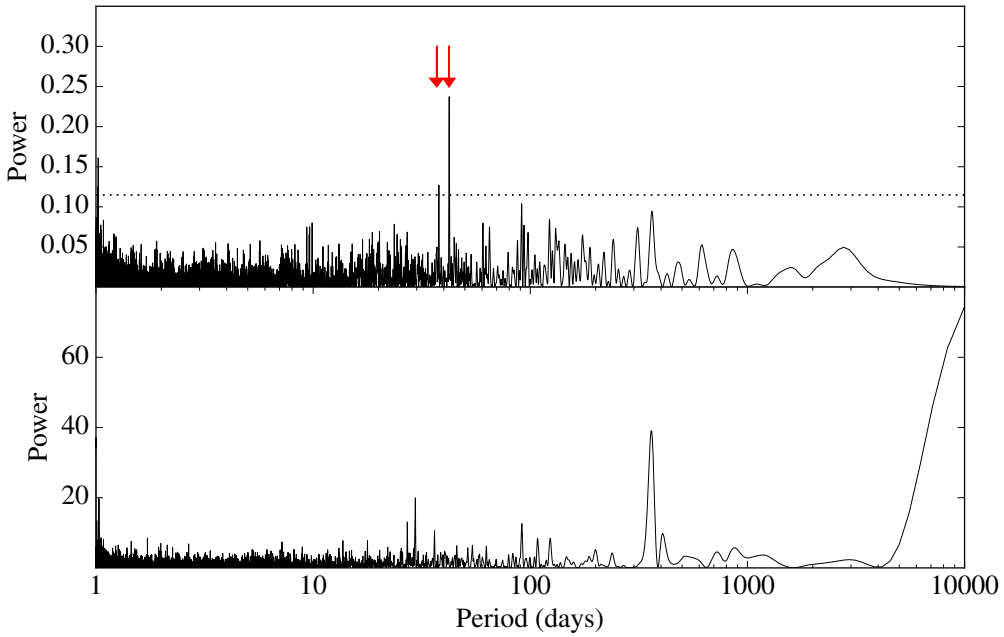

Figure 2.2: *Top:* Generalized Lomb-Scargle periodogram of the unbinned combined velocities. The highest power is found at a period of 42.43 days. The vertical red arrows mark the position of the stellar rotation period and the period found in the time series. The dotted line shows the 0.1% significance level, determined by 1,000 bootstrap resamplings. *Bottom:* Periodogram of sampling (window function) for the combined data.

2.3 Periodogram Analysis

We started to examine the radial velocity data by using the traditional periodogram analysis approach to look for any periodicities embedded in the data. We used the generalized version (Zechmeister & Kürster 2009) of the Lomb-Scargle periodogram (Lomb 1976; Scargle 1982, hereafter GLS) where we set up a minimum period of 1 day and a maximum period of 10,000 days for the search, with 80,000 trial periods evenly spaced in the frequency domain.

Figure 2.2.4 (top panel) shows the GLS periodogram of the combined radial velocities of HIRES, PFS, CHIRON and HARPS. The velocities have been mean subtracted. A maxima at 42 days (marked with a red arrow) clearly exceeds the power threshold of 0.1% significance level. There are also two power maxima close to the 0.1% significance threshold at ∼38 days and at ∼360 days. In the bottom panel of Figure 2.2.4 we show the periodogram of the sampling (window function) of the combined radial velocities. The secondary power spectrum peak at 360 days found in the periodogram of the velocities is also present here, and therefore can be attributed to the frequency of sampling. However, the peak at 38 days is not present and therefore further investigation is required to determine the origin of this possible signal, which we discuss below as being due to the rotation period of the star.

2.4 Bayesian Analysis

In addition to the traditional periodogram analysis we have performed an MCMC search for periodic signals embedded in the data. We modeled the radial velocities of HD 26965 following the statistical model defined in Tuomi et al. (2014b) and also applied in Jenkins & Tuomi (2014) where we include the following elements:

1. A function describing a k-Keplerian planet model
2. A linear trend term
3. A red-noise model consisting of a p-th order moving average - MA(p) - model with an exponential smoothing
4. Linear correlations with the stellar activity indicators

We write the statistical model as follows

$$y_{\mathrm{i},j} = \gamma_j + \dot{\gamma} t_\mathrm{i} + f_k(t_\mathrm{i}) + \varepsilon_{\mathrm{i},j} + \sum_{n=1}^{q_j} c_{n,j} \xi_{n,\mathrm{i},j} + \sum_{l=1}^{p} \phi_{j,l} \exp\left\{\frac{t_{\mathrm{i}-l} - t_\mathrm{i}}{\tau_j}\right\} r_{\mathrm{i}-l,j} \tag{2.1}$$

where $y_{\mathrm{i},j}$ corresponds to the observation at time t_i for the j-th instrument, γ_j is the velocity offset for the j-th dataset, $\dot{\gamma}$ is a linear trend term, and $r_{\mathrm{i},j}$ denotes the residuals after subtracting the model from the measurement. The function f_k is a superposition of k-Keplerian signals,

Table 2.3: Prior selection for the model parameters

Parameter	Prior Type	Range
Semi-amplitude	Uniform	$K \in [\,0, K_{\rm max}]$
Period	Jeffrey's	$P \in [\,1, 2P_{\rm obs}]$
Eccentricity	$\mathcal{N}(0, \sigma_{\rm e})$	${\rm e} \in [0, 1)$
Long. of Pericenter	Uniform	$\omega \in [\,0, 2\pi]$
Mean Anomaly	Uniform	$M_0 \in [\,0, 2\pi]$
Jitter	Uniform	$\sigma_J \in [0, K_{\rm max}]$
Smoothing time scale	Constant	τ_j=4

$$f_k(t_{\rm i}) = \sum_{m=1}^{k} K_m[\,\cos(\omega_m + \nu_m(t_{\rm i})) + {\rm e}_m \cos(\omega_m)] \tag{2.2}$$

where K_m is the velocity semi-amplitude, ω_m is the longitude of pericenter, ν_m is the true anomaly and ${\rm e}_m$ is the eccentricity. ν_m is also a function of the orbital period and the mean anomaly $M_{0,m}$. Hence, f_k is fully described by K_m, ω_m, ${\rm e}_m$, $M_{0,m}$ and P_m , $m \in \{1, ..., k\}$.
The white noise term is denoted by the additive random variable $\varepsilon_{{\rm i},j}$. We assume that there is an excess white noise in each data set with a variance of σ_j such that

$$\varepsilon_{{\rm i},j} \sim \mathcal{N}(0, \sigma_{\rm i}^2 + \sigma_j^2) \tag{2.3}$$

with $\sigma_{\rm i}$ the uncertainty associated with the measurement $y_{{\rm i},j}$ and σ_j is the excess white noise or jitter for the j-th dataset, that is treated as a free parameter in the model.

The remaining terms define the rest of the noise model, including the red-noise component: the first term with parameters $c_{n,j}$ describes the linear correlations with q stellar activity indicators $\xi_{n,{\rm i},j}$ for the n-different instruments. The second term is the MA(p) component with smoothing over a timescale $\tau_j = 4$ days and $\phi_{j,l}$ with a value between -1 and 1 to quantify the correlation between measurements. The smoothing timescale is set to 4 days for simplicity (Tuomi et al. 2013b). We assume the noise is correlated in this timescale although with higher cadence smaller timescales would likely be more appropriate (Tuomi et al. 2013b; Feng et al. 2016).

The posterior probability density of the parameters in the model is computed by following Bayes' rule (see equation 1.24).

In our model we chose the priors for the orbital and instrumental parameters as listed in Table 2.3.

In order to investigate the signal initially found with GLS periodogram of the combined radial velocities we use our Bayesian detection method where we sample the parameter space using the Delayed-Rejection Adaptive-Metropolis (DRAM) algorithm (Haario et al. 2006) based on the Adaptive-Metropolis (AM) algorithm (Haario et al. 2001), applied in Tuomi et al. (2014a) and Jenkins & Tuomi (2014). DRAM and AM are both methods for improving the efficiency of the Metropolis-Hasting algorithm (Metropolis et al. 1953; Hastings 1970). The idea behind using DRAM

is that when the posterior of a parameter is multimodal, such as the orbital period in the case of Keplerian fits to radial velocity datasets, and a new state for the chain is rejected (see full details in Tuomi et al. 2014b), a new proposed state is drawn centered on the last one. Up to three rejections are allowed before that part of the posterior is finally discarded as a region of low probability. This has the benefit of sampling more heavily the posterior phase space, at the cost of a longer run-time.

Tempered samplings are also performed when searching for signals. We include a β parameter following Tuomi et al. (2014b), such as $\beta \in (0, 1)$, meaning we use $P(\theta \mid y)^{\beta}$ instead of the standard posterior probability density, $P(\theta \mid y)$. This way we can define the "temperature" of the chain simply as $T = 1/\beta$ and so a "hot" chain is defined when $T > 1$ and a "cold" chain is where $T = 1$. When $T > 1$ the relative height of the maxima in the posterior probability density are decreased to prevent the chains from getting stuck in regions of high probability, allowing them to visit the entire period parameter space. The typical length of a chain is set to be between $10^6 - 10^7$ for the search run and 10^6 for the initial burn-in period.

We performed a first run for a zero-planet model to determine the observational baseline, and the instrumental noise and stellar noise parameters for each set of radial velocities. We then searched for a signal in the radial velocity data considering a 1-planet model. The search was initially done by setting the temperature for the chain hot enough to let the chain explore the entire parameter space. This is especially helpful when the parameter space is highly multimodal. Our tolerance threshold for the acceptance rate is based on the optimal acceptance rate of the Metropolis-Hastings algorithm which is $\sim$0.234 (Roberts et al. 1997). A lower threshold for the chain to be accepted was set to 10%, so hot chains with lower acceptance rates were discarded. From these runs we found a strong signal was present with a period of 42 days. The signal identified from the maximum of the posterior probability density distribution is shown in Figure 2.4.1, left panel.

We repeated this process by adding additional signals to the model, but we found no more statistically significant periods in the distribution of the posterior probability densities. Finally, to constrain the detected signal, we performed parameter estimations via the AM algorithm by setting a cold chain (β=1) with the parameters initially set as a small ball around the parameters found previously by the hot chain run with DRAM. This gave rise to the posterior histograms shown in Figure 2.4.1, where the period, amplitude, and minimum mass distributions show nice Gaussian forms centered on their respective values, and the eccentricity distribution is consistent with zero. Table 2.4 summarizes the final set of values for the parameters from our analysis.

Table 2.4: Solutions for HD 26965 b. Final set of orbital and instrumental parameters. 1σ errors.

Parameter	HD 26965 b
P (days)	42.364 ± 0.015
K (m s^{-1})	1.59 ± 0.15
e	0.017± 0.046
ω (rad)	0.31 ± 1.93
M_0 (rad)	4.92 ± 1.92
a (AU)	0.215 ± 0.008
$m \sin i$ ($M_\oplus$)	6.91 ± 0.79
$\gamma_{\rm PFS}$ (m s^{-1})	0.13 ± 0.80
$\gamma_{\rm HIRES}$ (m s^{-1})	0.50 ± 0.57
$\gamma_{\rm CHIRON}$ (m s^{-1})	0.43 ± 0.79
$\gamma_{\rm HARPS,old}$ (m s^{-1})	0.17 ± 0.50
$\gamma_{\rm HARPS,new}$ (m s^{-1})	0.45 ± 0.78
$\dot{\gamma}$ (m s^{-1} year^{-1})	-0.031 ± 0.037
$\sigma_{\rm PFS}$ (m s^{-1})	1.54 ± 0.20
$\sigma_{\rm HIRES}$ (m s^{-1})	2.38 ± 0.15
$\sigma_{\rm CHIRON}$ (m s^{-1})	1.78 ± 0.15
$\sigma_{\rm HARPS,old}$ (m s^{-1})	1.11 ± 0.05
$\sigma_{\rm HARPS,new}$ (m s^{-1})	0.69 ± 0.07
$\phi_{\rm PFS}$	0.82 ± 0.10
$\phi_{\rm HIRES}$	0.61 ± 0.07
$\phi_{\rm CHIRON}$	0.62 ± 0.06
$\phi_{\rm HARPS,old}$	0.81 ± 0.04
$\phi_{\rm HARPS,new}$	0.90 ± 0.08
$c_{\rm S\,PFS}$ (m s^{-1})	61.1± 14.0
$c_{\rm S\,HIRES}$ (m s^{-1})	53.1 ± 15.0
$c_{\rm BIS\,HARPS,old}$	0.086 ± 0.046
$c_{\rm FWHM\,HARPS,old}$	1.8 ± 4.5
$c_{\rm S\,HARPS,old}$ (m s^{-1})	1.6 ± 2.6
$c_{\rm H_\alpha\,HARPS,old}$ (m s^{-1})	-12.1 ± 8.9
$c_{\rm HeI\,HARPS,old}$ (m s^{-1})	-76 ± 34
$c_{\rm BIS\,HARPS,new}$	0.27 ± 0.11
$c_{\rm FWHM\,HARPS,new}$	0.089 ± 0.018
$c_{\rm S\,HARPS,new}$ (m s^{-1})	105 ± 36
$c_{\rm H_\alpha\,HARPS,new}$ (m s^{-1})	76 ± 125
$c_{\rm HeI\,HARPS,new}$ (m s^{-1})	23 ± 141

Table 2.5: Logarithm of Bayes factors comparing a k=0, k=1 and k=2 Keplerian models with and without activity correlations

Bayes Factor ln $B_{k,k-1}$	**Activity Correlations**	**No Activity Correlations**
ln $B_{1,0}$	43.38	35.44
ln $B_{2,1}$	0.61	2.96

2.4.1 Model Selection

It is important to define a robust methodology that allows us to compare the results for two given models in order to address the statistical significance of one model with respect to the other.

The probability of a model $\mathcal{M}$, containing the best-fit parameters for the observed data y, is given by

$$P(\mathcal{M} \,|\, y) = \frac{P(y \,|\, \mathcal{M})P(\mathcal{M})}{\sum_{\mathrm{i}=1}^{k} P(y \,|\, \mathcal{M})P(\mathcal{M})} \tag{2.4}$$

In particular, we want to know if the model containing one planet is more probable than a zero-planet model and so on for the k-planet model with respect to a $k-1$-keplerian model. To solve this, we compute the probability of a given model by using the corresponding value of the Bayesian Information Criterion (BIC). A complete and detailed discussion can be found in Tuomi & Jones (2012) and Feng et al. (2016). To compare the $\mathcal{M}_k$ model with a previous $\mathcal{M}_{k-1}$ model, we simply compute the logarithm of the Bayes factor, ln $B_{k,k-1}$, defined via

$$\ln B_{k,k-1} = \ln P(y|\mathcal{M}_k) - \ln P(y|\mathcal{M}_{k-1}) \tag{2.5}$$

Furthermore, the model containing the best-fit parameters that support the signal has to fulfill the detection criteria described in Tuomi (2012). It must hold that

$$P(y|\mathcal{M}_k) = sP(y|\mathcal{M}_{k-1}) \tag{2.6}$$

where $s > 10^4$. Hence using the Bayes factor defined in equation 5.6, we require that the $\mathcal{M}_k$ model describing the k-keplerian signal has to be more statistically probable than the $\mathcal{M}_{k-1}$ model associated with the $k-1$-keplerian signal. Following the conservative threshold from Tuomi et al. (2014b), we define that the evidence ratio should be

$$\ln B_{k,k-1} > 9.2 \tag{2.7}$$

which translates posterior odds of 10,000:1 that the k model is selected over the k-1 model, in order to satisfy our detection criteria. Table 2.5 shows the Bayes factors for $k = 0, 1, 2$-planet models with and without activity correlation terms.

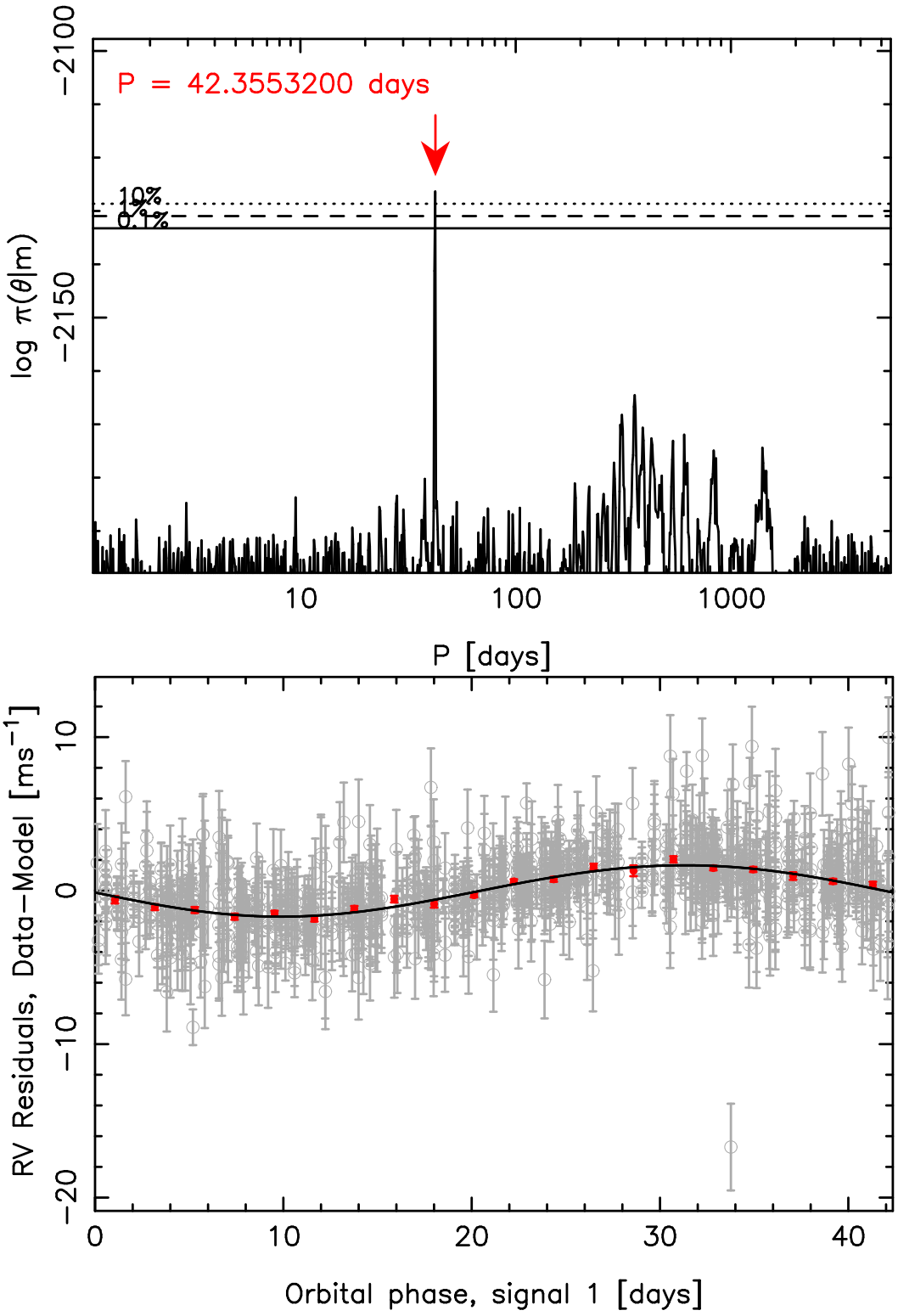

Figure 2.3: *Top:* Posterior probability densities as output from our Bayesian code for a 1-planet model. *Bottom:* Phased-folded radial velocity curve.

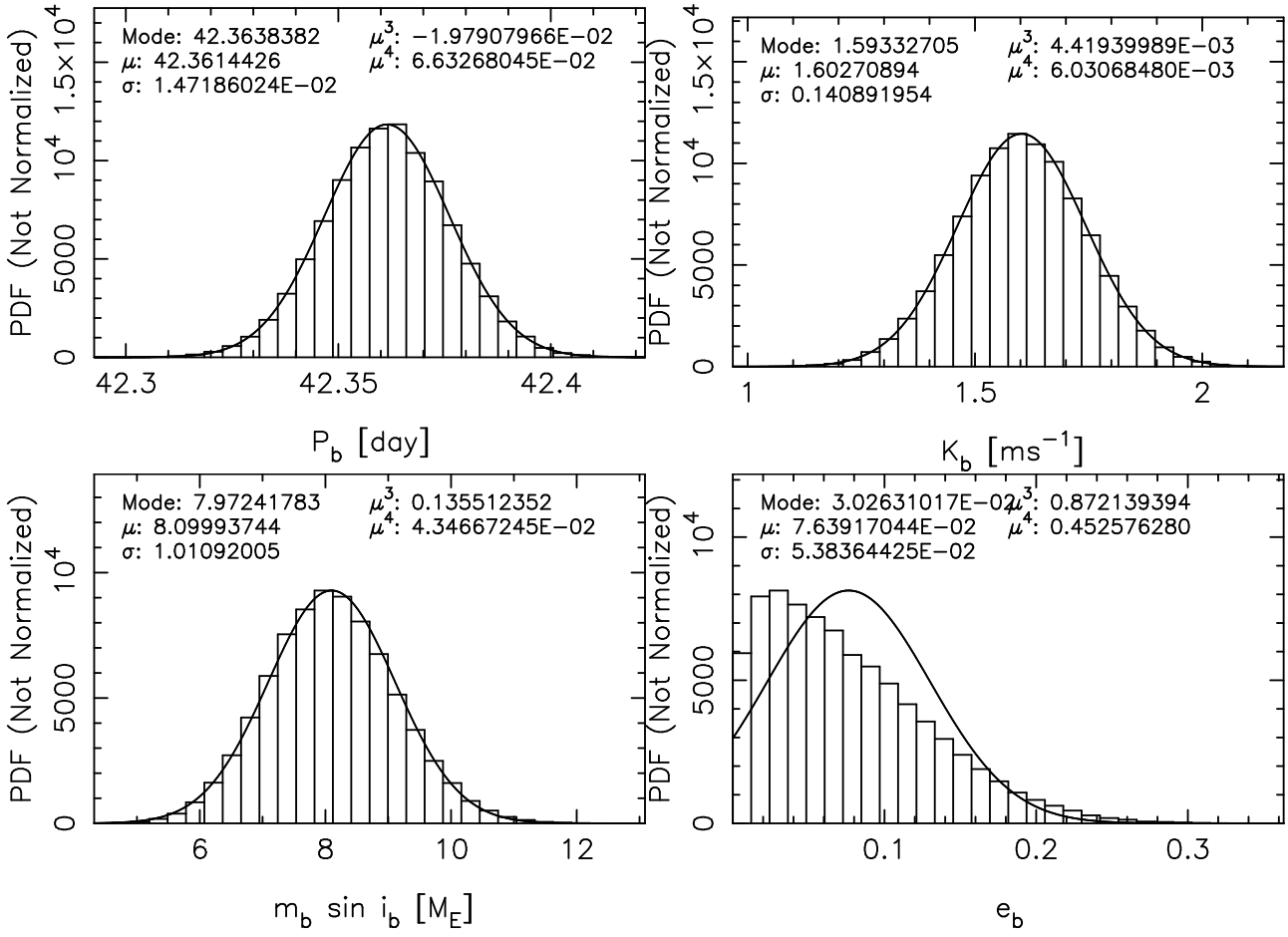

Figure 2.4: *Left to Right, Top to Bottom:* Final distribution of period, semi-amplitude, minimum planetary mass and eccentricity resulting from a cold-chain Adaptive Metropolis run. The numbers at the top of each figure correspond to the mode, mean, variance, skewness and kurtosis, respectively. The solid line represents a Gaussian curve with same mean and variance.

Figure 2.4.2 shows the minimum mass detection thresholds for additional planets orbiting around HD 26965. The green-filled area represents the liquid-water habitable zone estimated according to Kopparapu et al. (2013a,b). The thresholds are calculated following the methods in Tuomi et al. (2014b). From this figure we can say that planets with minimum masses in excess of Neptune in the habitable zone can be ruled out meaning if there are HZ planets orbiting HD 26965, they would likely be super-Earths or smaller. The red circle represents the planet candidate, barely, but significantly above the detection threshold.

2.4.2 Signal injection

As an additional test to investigate if the signal was supported for each instrument we performed a signal injection on the individual datasets. We use the best-fit parameters (i.e. P, K, ω, M_0, e) of the putative signal by using a Keplerian function described in equation 2.2. The hypothesis is the following: if the 42-day signal is injected in a given dataset and we run our usual Bayesian analysis we should, in principle, easily detect it. If the signal is indeed present in the dataset we should recover ∼twice the best-fit radial velocity semi-amplitude as it has been boosted by the injection. On the other hand, if the recovered velocity semi-amplitude is significantly lower than our best-fit values, that would suggest the actual data is not supported by the instrument, or in other words, the precision of the instrument plus the current number of observations do not allow the signal to be detected. When boosting our signal, we recover the candidate period for HARPS OLD, HIRES and CHIRON datasets. For CHIRON, however, the expected peak at 42-days in the GLS is not unique, although it is above the 0.1% significance level, as can be seen from the periodograms shown in Figure 2.4.2. In the case of PFS data, we did not recover the candidate period. Instead, we found a strong power at ∼5 days. This could be caused by the sparse sampling and lower number of observations available from this instrument.

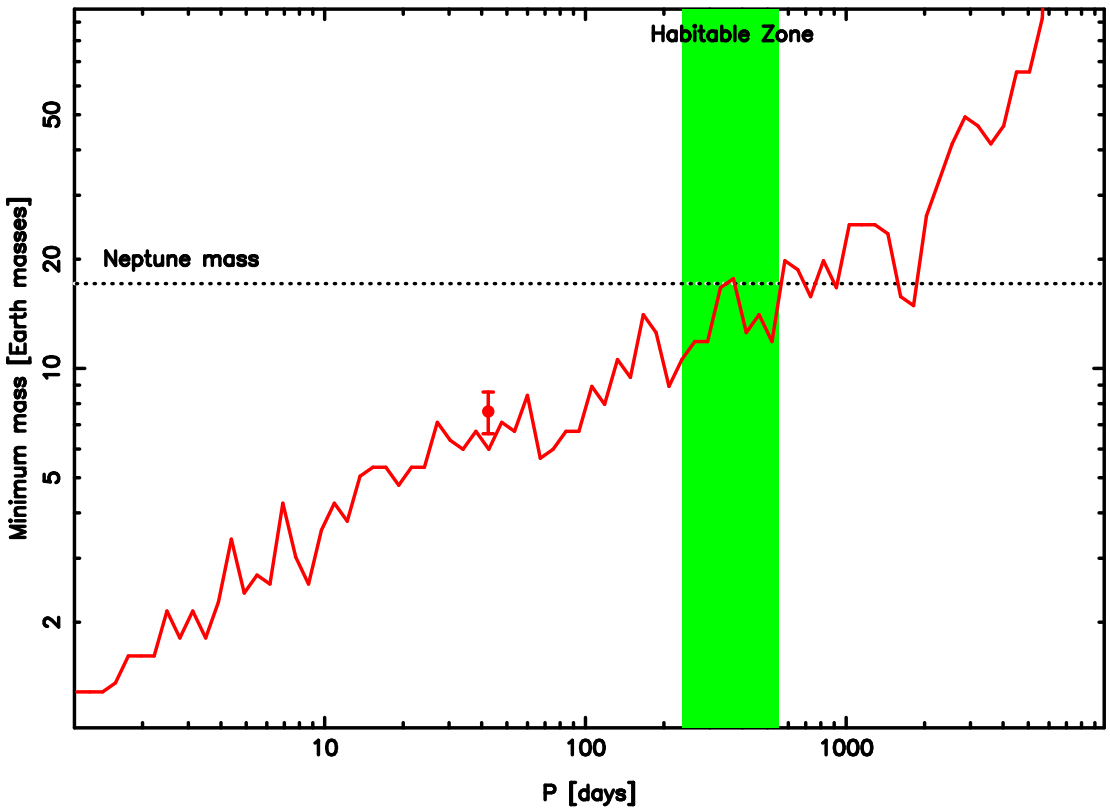

Figure 2.5: Minimum mass detection thresholds for additional planets orbiting around HD 26965 for periods between 1 and 10,000 days. The green-filled area highlights the habitable zone for this K dwarf.

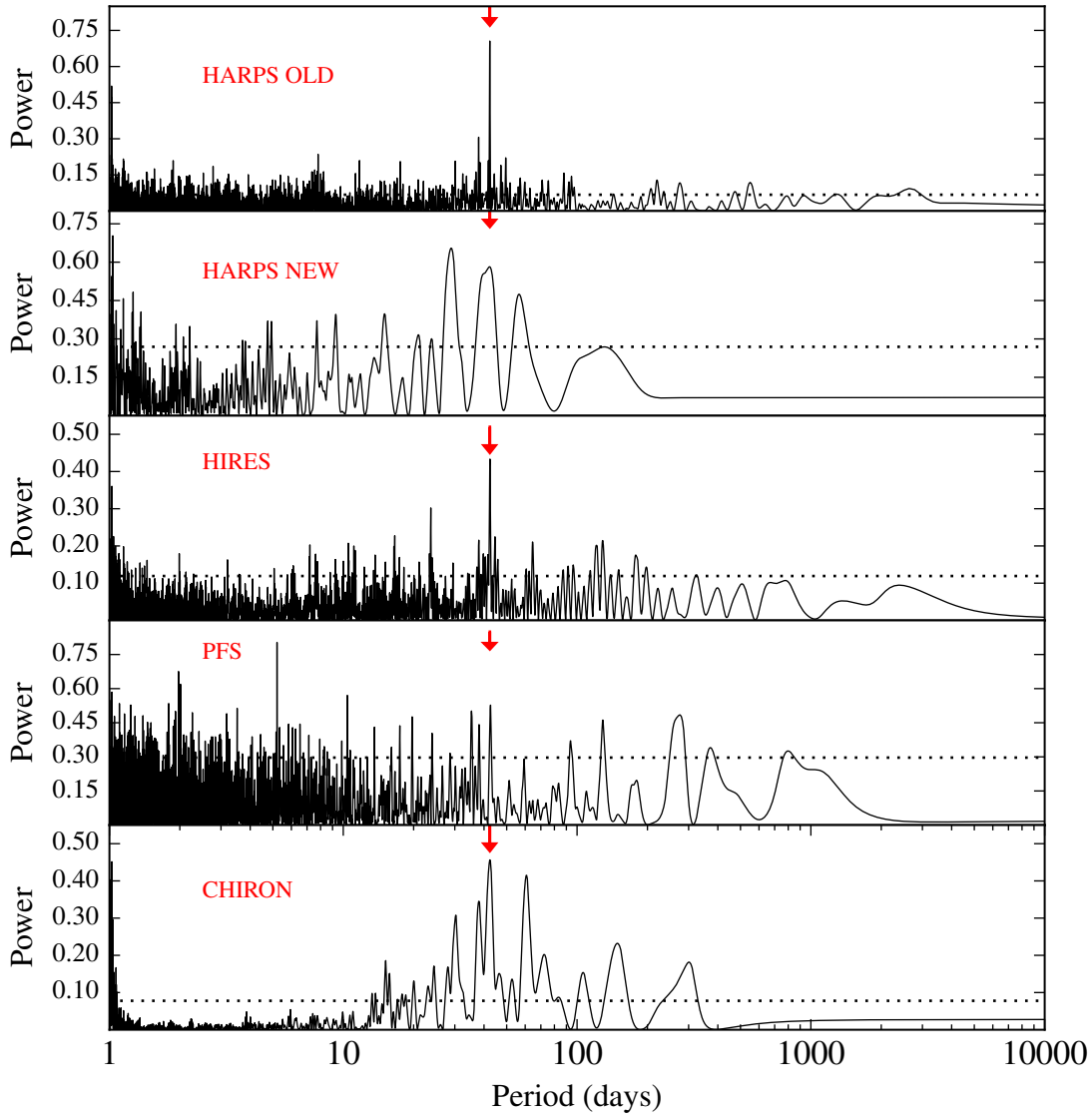

Figure 2.6: *Top:* Generalized Lomb-Scargle periodogram for each dataset where a 1-planet model with the best-fit orbital parameters has been injected into the original measurements. Red arrows mark the candidate period found in the original time series. The dotted lines show the 0.1% significance level, determined by 1,000 bootstrap resamplings.

Table 2.6: Pearson Rank test coefficients. Correlation between activity indicators and radial velocities

Activity Indicator	Pearson r
BIS_{HARPS}	-0.02 ± 0.04
$FWHM_{HARPS}$	0.74 ± 0.04
S_{HARPS}	0.14 ± 0.04
$H_{\alpha\,HARPS}$	0.05 ± 0.04
He I_{HARPS}	-0.04 ± 0.04
S_{PFS}	0.48 ± 0.12
S_{HIRES}	0.44 ± 0.07
$S_{COMBINED}$	0.23 ± 0.03

2.5 Stellar Activity and RV correlations

To investigate the nature of the detected 42 day signal, we perform a similar analysis as in Santos et al. (2014) on the activity indices available from each instrument. First we searched for periodicities present in the activity indices themselves, again using the GLS, and we show these results in Figure 2.5. There are no statistically significant peaks associated with the 42 day signal we detect in the radial velocities. However, the periodogram of the HARPS S-indices shows an emerging peak at 38 days, which is very close to the signal we detected in the radial velocities. Interestingly, this was the period found for the rotation of the star from previous analysis of Ca II lines Saar & Osten (1997) which also agrees with the period inferred from ROSAT measurements (37.1 days; Pizzolato et al. 2003).

Figure 4.2 shows the correlations between radial velocity and activity indicators for HARPS, PFS and HIRES. The combined S-indices we show have been mean subtracted and then combined together. We have computed the Pearson Rank test coefficients to determine the correlation between these quantities. Results are listed in Table 2.6 where we also list the uncertainties associated with each coefficient. To calculate these uncertainties we ran 10,000 bootstraps and created a distribution of r coefficients for every activity index, where the standard deviation of the distribution gave us a measurement of the uncertainty on the coefficients. We note that the correlations are not significant within these uncertainties, given the standard statistical limits for claiming a weak (r <0.5), a moderate ($0.5 \leq r \leq 0.7$), and a strong correlation (r >0.7), therefore we can conclude that the stellar activity indicators do not argue against a Doppler origin for the signal, yet the correlations indicate we must consider them in our full statistical model. Indeed, the correlations suggest there is a weak impact of the stellar noise on the velocities, and we confirm this since the probability of our statistical model is higher when we include these correlations, compared to when we exclude them (see Table 2.5).

2.6 Testing variability and stability of the period and amplitude

Following a similar approach as in Jenkins & Tuomi (2014), we tested the variability and stability of the signal of our candidate. For this analysis we only considered the HIRES and HARPS OLD

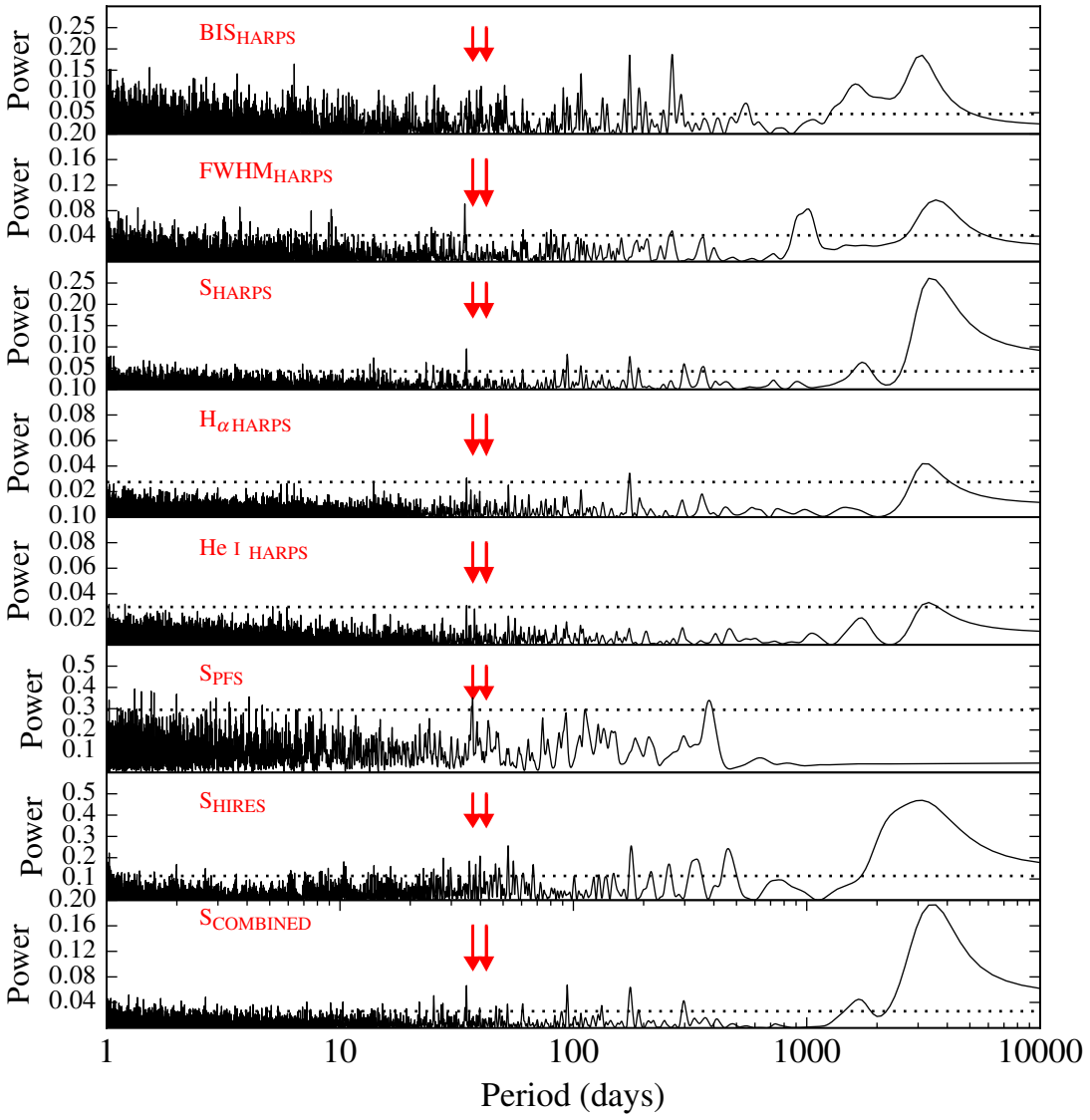

Figure 2.7: Generalized Lomb-Scargle periodogram of the activity indicators available from the different spectrographs. From top to bottom: $\mathrm{BIS_{HARPS}}$, CCF $\mathrm{FWHM_{HARPS}}$, $\mathrm{S_{HARPS}}$, $\mathrm{H_{\alpha\,HARPS}}$, He $\mathrm{I_{HARPS}}$, $\mathrm{S_{PFS}}$, $\mathrm{S_{HIRES}}$ and $\mathrm{S_{COMBINED}}$. The arrows mark the position of the signal found at 42.37 days in the radial velocity series and the reported stellar rotation period of 37.1 days from Saar & Osten (1997). The dotted lines show the 0.1% significance level, determined by 1,000 bootstrap resamplings. There are no statistically significant power in the activity indicators matching the radial velocity period.

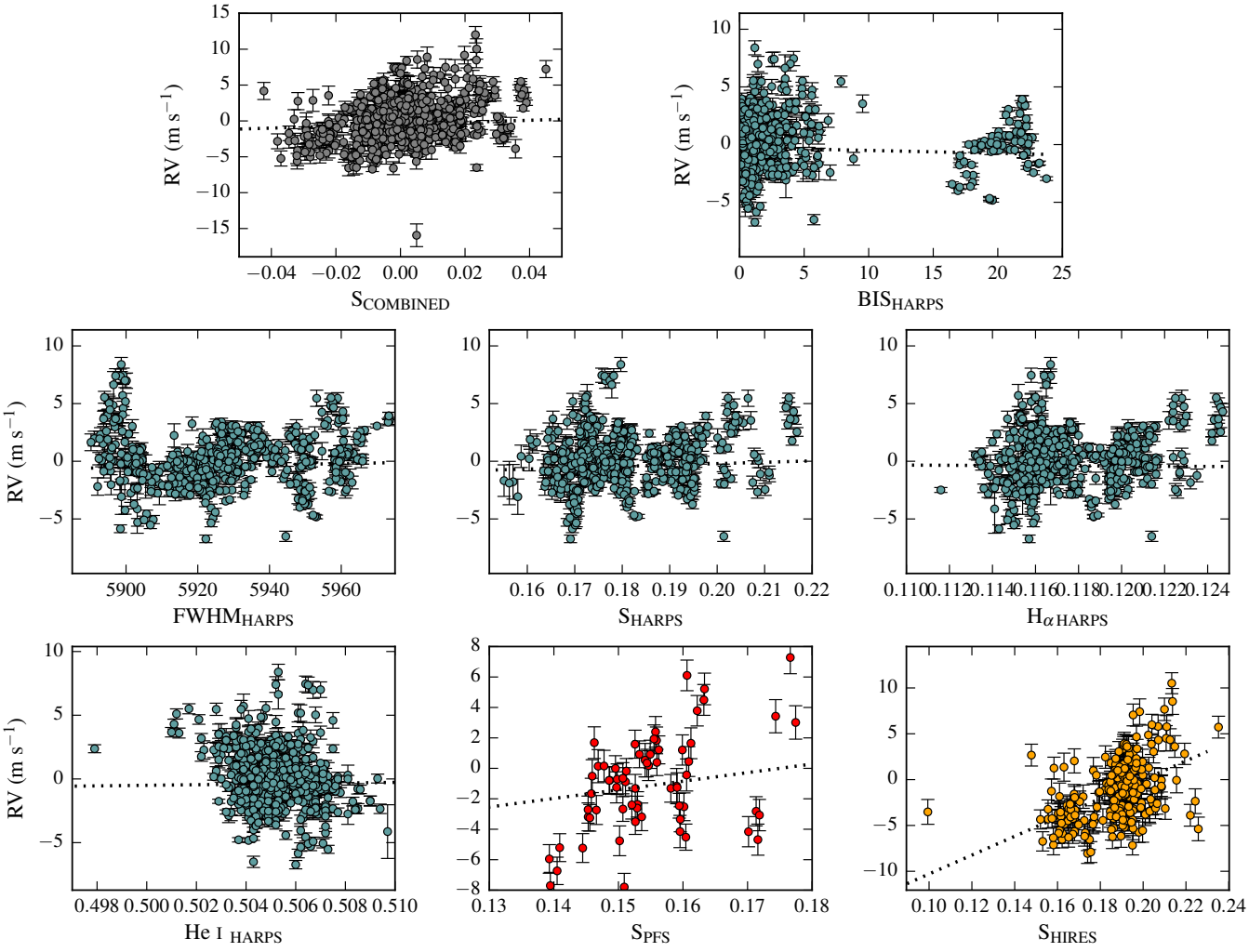

Figure 2.8: Radial velocity correlations with respect to the seven different activity indicators: BIS_{HARPS}, CCF $FWHM_{HARPS}$, S_{HARPS}, $H_{\alpha\,HARPS}$, He I $_{HARPS}$, S_{PFS}, S_{HIRES}. We also include the combined S-indices. The dotted lines mark the 1:1 relationships.

datasets, since both of them have a fairly continuous sampling of Doppler measurements along the ∼16 years of observational baseline. The measurements include a total of 662 unbinned velocities, and we chose JD_s=2454600 as the point to split the data, since this was close to the center of the time baseline of the observations and also produced a well balance between HARPS and HIRES data (i.e., not biased to an instrument in particular). The data prior to JD_s contained 408 data points and the dataset after the split point contained 254 measurements.

We performed the Bayesian analysis on these 2 subsets of velocities independently, running cold chains to constrain the orbital parameters of a 1-Keplerian model. We found the signal is detected with values in agreement within uncertainties for the two baselines tested, as well as for the full data set described above. This shows us that the signal is not varying in time and thus the period and amplitude of our planetary candidate is stable over the tested observational baseline, another strong argument against an activity origin since activity processes should be quasi-static, varying over a few rotation periods of the star.

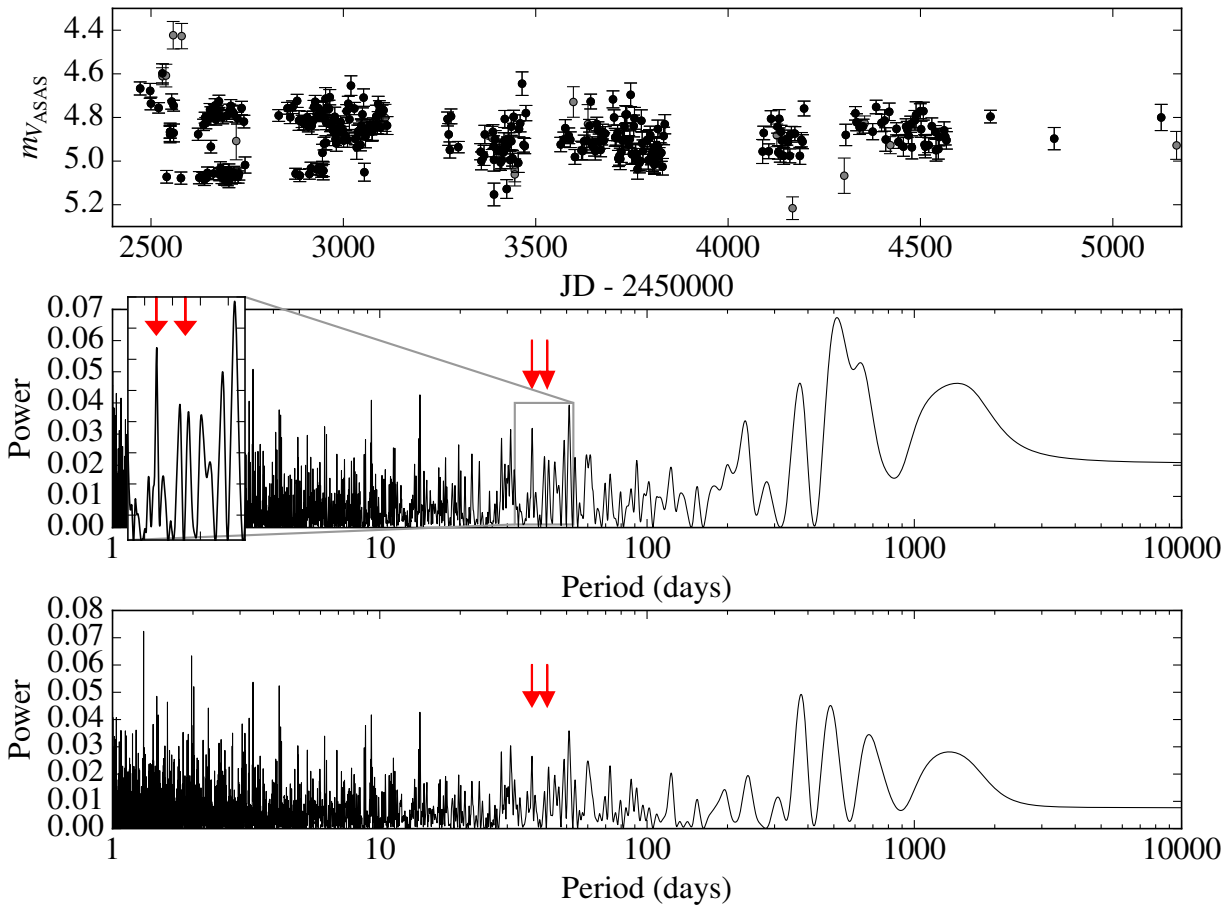

Figure 2.9: *Top:* Photometric measurements from ASAS. Grey circles show the complete set of photometry while black-filled circles are those that meet the criteria as robust points described in the text. *Middle:* Generalized Lomb-Scargle periodogram of the ASAS photometry. Red arrows mark the position of the planetary candidate signal at 42.37 days and the stellar rotation period reported by Saar & Osten (1997) of 38.7 days. No significant powers near the period - or an integer multiple of it - are found in the periodogram. The highest power is seen at 515 days. *Bottom:* Periodogram of the residuals after removing the 515 day period signal.

2.7 ASAS Photometry

To complement the analysis we gathered photometric data available from the All-Sky Automated Survey (ASAS) Catalog (Pojmanski 1997) to investigate if any periodic signal could be seen in light curves, particularly the rotational period of the star. As mentioned above, the literature values were reported by Noyes et al. (1984) and Saar & Osten (1997), where they found $P_{\rm rot}$ ∼37.10 days for this old star. We show the ASAS photometric measurements in Figure 2.6. From the five different apertures available, we selected aperture 1 as its MAD[3] value of 0.219 mag was the smallest. The mean uncertainty in the V-band photometry is $\sigma_{\rm ASAS}$= 0.036 mag. Grey circles correspond to the entire photometry set of 568 useful points acquired from 2000 to 2009. However, we excluded the data with poor quality (those not marked "A" or "B" in the catalog) and also those measurements that deviated more than 3-σ with respect to the mean value of the time series. The highest quality data (316 points) are shown as black circles in the top panel of Figure 2.6. The bottom panel in Figure 2.6 again shows the GLS for the ASAS photometry. We sample the period space starting at a minimum period of 1 day and up to 10,000 days, performing 80,000 period samples. Considering just the data before JD=2452300 tends to favor peaks with higher power towards high frequencies (periods ∼1 day) but without any significant period (or an integer multiple) near the period associated with the 42 day signal of the reported planetary candidate. We also ran the periodogram analysis on the full photometric dataset with no significant periods found. Following the relations in Hatzes (2002), we found that a filling factor of f=0.15 would be required to induce the RV amplitude of 1.6 m s^{-1} of the signal found in the combined data. If we consider the spots on the surface of the star to be opaque, for the sake of simplicity, the ratio between the stellar flux and the flux considering spots covering 0.15% of the surface of the star would be 0.9985. This means, the loss of light due to spots on the stellar surface can be translated into a Δm= 1.64 mmag. Given the precision of the ASAS photometry for this star, we conclude it is insufficient to be informative.

2.8 Mount Wilson HK measurements

Given that we find some moderate correlations between the spectral activity indicators and the radial velocities, we supplemented our activity analysis by studying the original Ca II H&K data from the Mount Wilson Observatory HK Project (Wilson 1978). The Project data are publicly available from the NSO archive[4] and include more than 2,000 stars observed from 1966 to 1995. There are 1,155 HK observations for HD 26965 from JD=2439787.8 to 2449771.7. The processed data do not include associated uncertainties to the calibrated S-values. According to Duncan et al. (1991), the uncertainties in the Mount Wilson S-values can be calculated using the weights, W, included in the data that are derived from the photon counts of the measurements. The uncertainty in the S-index measurements is simply defined as $\sigma_S = S\,(\sqrt{W})^{-1}$. We applied this formula to the reported weights to provide proper uncertainties for the measurements of this star. All HK values for HD 26965 can be found in Table 2.13.

We proceeded to run the same periodogram analysis as for the radial velocities and the photometric time-series from ASAS. A clear long-term variability of ∼4,100 days can be identified (see top and second top panels in Figure 2.8), providing evidence for a long-period magnetic activity cycle, similar to the long-period solar cycle. After removing this signal by modeling it with a sinusoidal function, a second period of ∼715 days is found in the periodogram (second bottom panel in the

[3]Median Absolute Deviation = median($x_{\rm i}$ - median(x))
[4]http://www.nso.edu/node/1335

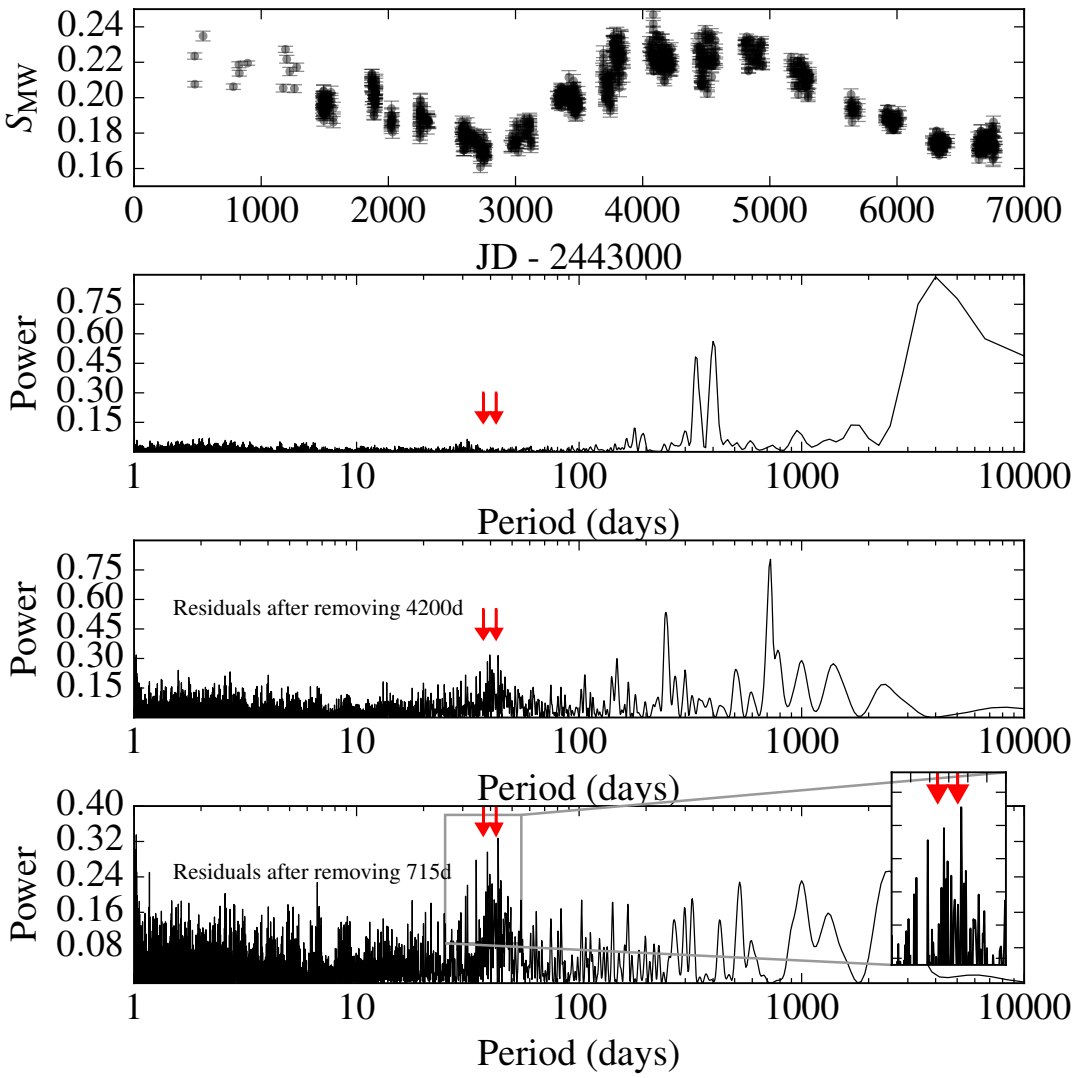

Figure 2.10: *Top:* Mount Wilson S-values for HD 26965. Second, Third & Bottom Panels: Periodogram of the Mount Wilson S-values, periodogram of residuals after removing ∼4100 days and periodogram of residuals after removing ∼715 days, respectively. Red and black dashed lines mark the position of the possible rotation periods of ∼37 and 43 days, respectively.

figure), likely representing another, shorter period magnetic cycle. Finally, the bottom panel in the figure shows the periodogram of the Mount Wilson S-values after removing the 4,100 and 715 day period signals from the data. In this residual periodogram a signal of ∼42.3 days remains in the data. This is most likely the value reported in Baliunas et al. (1996).

The peak is clearly not unique, casting some doubt on its reality, but given that it matches the detected signal in our radial velocity data sets, and rotation periods are known to be quasi-period due to differing spot patterns, changing stellar activity levels, and differential rotation, we must entertain the real possibility that this is actually the rotational period of the star, and not the 38 day period that we found in the measured spectroscopic activity indices. If this is the reality, then HD 26965 represents a case where most of the current suite of tests that we employ to detect planets using radial velocity analyses, fail to remove the noise introduced by the rotation of the star, meaning that we now require better methods to be employed on stars where there are clear correlations between the radial velocities and various activity indicators if we want to detect planets that induce amplitudes at the ~ 1 m s^{-1} level.

Table 2.7: HIRES Radial Velocities of HD 26965

BJD	RV (m s^{-1})	σ RV (m s^{-1})	S (dex)
2452235.83300	-1.415	1.2524	0.1792
2452236.85549	-1.805	1.3973	0.1887
2452237.89810	2.040	1.3150	0.1679
2452307.73757	-2.992	1.4854	0.1785
2452536.99956	-1.836	1.4599	0.1609
2452601.99297	-4.451	1.2644	0.1812
2452856.13402	1.361	1.5298	0.1630
2452856.13536	-3.705	1.3752	0.1605
...	...	...	...

Table 2.8: PFS Radial Velocities of HD 26965

BJD	RV (m s^{-1})	σ RV (m s^{-1})	S (dex)
2455852.81626	0.5372	1.0975	0.1541
2455852.81753	-1.1678	1.1564	0.1590
2455852.81876	-4.1496	1.0584	0.1595
2455852.82000	-0.4344	1.0524	0.1606
2456175.89728	-0.8868	0.9314	0.1511
2456285.67699	-3.5075	0.8318	0.1526
...	...	...	...

Table 2.9: CHIRON Radial Velocities of HD 26965

BJD	RV (m s^{-1})	σ RV (m s^{-1})
2456941.80711	0.7180	1.5175
2456941.81054	1.9459	1.4766
2456941.81463	0.9758	1.6280
2456942.79556	2.0399	1.4729
2456942.79920	0.6670	1.5552
2456942.80289	0.7219	1.4767
2456943.75367	1.8081	1.5570
2456943.75739	1.0934	1.7136
...	...	...

Table 2.10: HARPS OLD Radial Velocities of HD 26965

BJD	RV ($m\ s^{-1}$)	σ RV ($m\ s^{-1}$)	BIS ($m\ s^{-1}$)	FWHM ($m\ s^{-1}$)	S (dex)	H_α (dex)	He I (dex)
2452939.80613	-42200.4336	0.519	1.254	5896.904	0.1753	0.1161	0.5067
2452939.80685	-42199.7695	0.512	1.279	5897.505	0.1742	0.1163	0.507
2452939.80756	-42200.3672	0.572	1.387	5901.748	0.1747	0.1163	0.505
2452939.80827	-42199.8242	0.524	1.720	5898.172	0.1759	0.1153	0.5061
2452939.80899	-42197.6953	0.954	3.537	5899.064	0.1726	0.1152	0.5039
2452939.80969	-42198.8086	0.612	1.192	5899.194	0.1722	0.1163	0.5075
2452940.76906	-42203.6300	0.378	0.184	5898.594	0.175	0.1157	0.5076
2452945.76432	-42203.3750	0.353	2.281	5896.436	0.171	0.1153	0.5067
...	...	...	...	...	...	...	...

Table 2.11: HARPS NEW Radial Velocities of HD 26965

BJD	RV ($m\ s^{-1}$)	σ RV ($m\ s^{-1}$)	BIS ($m\ s^{-1}$)	FWHM ($m\ s^{-1}$)	S (dex)	H_α (dex)	He I (dex)
2457274.86039	-42165.4141	0.1828	18.5315	5951.1924	0.1777	0.1170	0.5055
2457274.86304	-42165.3086	0.1852	18.4779	5951.7017	0.1768	0.1171	0.5059
2457274.86566	-42164.8438	0.2041	18.6366	5951.8066	0.1777	0.1174	0.5059
2457274.86845	-42164.9454	0.2026	18.1923	5951.7324	0.1778	0.1173	0.5051
2457277.84809	-42164.8516	0.2189	18.9974	5950.3081	0.1763	0.1179	0.5056
2457277.85019	-42165.0626	0.2209	18.6706	5950.1743	0.1777	0.1176	0.5049
...	...	...	...	...	...	...	...

Table 2.12: ASAS Photometry of HD 26965

HJD -2450000	Mag 4	Mag 0	Mag 1	Mag 2	Mag 3	Mer 4	Mer 0	Mer 1	Mer 2	Mer 3	Grade	Frame
1953.5693	29.999	29.999	29.999	29.999	29.999	0.028	0.063	0.050	0.034	0.029	C	9642
2172.7745	5.375	5.451	5.324	5.361	5.374	0.033	0.054	0.035	0.027	0.029	A	32848
2206.7643	29.999	29.999	29.999	29.999	29.999	0.030	0.084	0.057	0.037	0.031	C	37541
2227.6900	5.274	4.831	4.866	5.055	5.187	0.030	0.046	0.041	0.031	0.032	A	39837
2230.6884	5.235	4.866	4.942	5.091	5.179	0.038	0.107	0.090	0.063	0.050	D	40329
2234.6770	5.263	4.766	4.821	5.023	5.175	0.032	0.046	0.040	0.032	0.035	A	40805
2236.6731	29.999	29.999	29.999	29.999	29.999	0.034	0.046	0.039	0.031	0.036	C	41118
2501.9039	29.999	29.999	29.999	29.999	29.999	0.033	0.044	0.044	0.035	0.038	C	16126
2529.7900	4.598	3.968	4.145	4.378	4.523	0.044	0.060	0.052	0.043	0.046	B	19144
2549.7769	4.867	5.224	4.976	4.923	4.875	0.028	0.060	0.056	0.040	0.033	B	20837
2553.7667	4.727	4.377	4.445	4.585	4.681	0.035	0.049	0.052	0.043	0.041	B	21379
2558.7711	29.999	29.999	29.999	29.999	29.999	0.028	0.052	0.039	0.028	0.027	C	22103
2655.5941	4.934	6.289	5.861	5.440	5.139	0.029	0.036	0.037	0.027	0.029	A	35213
2954.7503	4.916	5.227	5.076	4.981	4.927	0.032	0.032	0.037	0.028	0.029	A	79986
...	...	...	...	...	...	...	...	...	...	...	...	...

Table 2.13: Mount Wilson HK Project measurements of HD 26965

S_{MW}	JD - 2444000	W
0.223	-523.2	15956.8
0.207	-522.2	16877.2
0.234	-457.2	7264.7
0.206	-219.2	17620.2
0.218	-175.2	17201.9
0.213	-172.2	17475.1
0.219	-107.2	34054.6
0.205	172.8	8716.2
0.227	190.8	17363.2
0.221	200.8	10277.2
0.214	224.8	8639.2
0.205	260.8	8593.6
0.217	278.8	8700.7
0.194	482.9939	3409.7
...	...	...

Chapter 3

Iodine-free spectra for high-resolution spectrographs

Based on the results published in Díaz, M. R., et al., *Deriving Iodine-free spectra for high-resolution spectrographs*, 2019, ApJ, 157, 204.

In this chapter we describe a new method to derive clean, iodine-free spectra directly from observations acquired using high resolution spectrographs equipped with iodine cells. The main motivation to obtain iodine-free spectra is to use portions of the spectrum that are superimposed with the dense forest of iodine absorption lines, to retrieve lines that can be used to monitor the magnetic activity of the star, helping to validate candidate planets. This is key when trying to address the problems that arise when searching for exoplanet signals with amplitudes of only a few meters per second, since including correlations between activity indicators and the radial velocities when modeling the data can help to determine the signal's origin, either Doppler or stellar activity. We provide a straight-forward methodology to derive iodine-free spectra directly from the observations. We note the existence of previous works in an attempt to correct or use clean spectra from iodine-observations, as described in Niedzielski et al. (2009) and Nowak et al. (2010) where they cleaned the spectra using a numerical mask constructed by a sum of delta functions centered in the position of selected iodine lines. The approach we present herein differs on previous efforts as we use our forward model to provide a full iodine-cleaned spectrum for every single observation.

3.1 The iodine cell method for precise radial velocity measurements

The advantage of the iodine cell is that several thousands of absorption lines are superimposed onto the stellar spectrum at the time of the observation, providing a precise wavelength calibration that is required to achieve $\sim$1 m s^{-1} radial velocity precision to search for small exoplanets around other stars. Compared to other gas cells, the iodine is not toxic nor corrosive and it has a strong line absorption coefficient and only a few cm are needed of path length. Despite all these benefits, the main drawback of this method is that by placing the absoprtion cell in the light beam, there is a net loss of light of around 20-30%.

Table 3.1: Instrumental parameters of echelle spectra.

Instrument	Resolution ($\lambda/\Delta\lambda$)	Total Number of orders[a]	Total Number of chunks	Chunks per order[b]	Chunk width (pixels)
PFS	80,000	26	818	34	120
HIRES	60,000	14	718	48	80
UCLES	50,000	20	944	48	50

[a] Effective number of orders in the iodine region used for the computation of radial velocities.

[b] For PFS, HIRES and UCLES, the first order is divided into 18, 31 and 32 chunks, respectively.

As the precision has been improving over the last 20 years, new challenges have arisen when trying to search for small signatures of exoplanet candidates, mainly because the precision of the measurements are now reaching below the intrinsic stellar noise, often referred to as stellar jitter, of even the most quiescent stars. Efforts have been made to not only understand how the star varies with time, i.e., monitoring its activity with spectral indices that quantify the chromospheric activity, but to also 'correct' for this additional noise effect.

Several stellar absorption lines serve as proxies to determine the activity of a star. One well-known example is the Mount Wilson S-indices derived from the Ca II H & K lines (Duncan et al. 1991), which have been considered as one standard proxy for monitoring stellar chromospheric activity. Also, Hα lines are used as diagnostics to analyze the stellar activity as a function of time. Radial velocity searches have also made use of these stellar activity indicators, as it is crucial to estimate rotation periods and stellar jitter (Tinney et al. 2002; Wright 2005; Jenkins et al. 2006, 2008, 2011; Arriagada 2011) and in some cases to validate the true nature of a planetary candidate (see e.g., Queloz et al. 2001; Jenkins & Tuomi 2014; Santos et al. 2014; Díaz et al. 2018; Paneque-Carreño & Jenkins 2019). All these activity indices are still used with iodine-cell spectrographs, since they fall outside the iodine forest.

Given that iodine provides a dense forest of lines from ~5000Å to ~6300Å, every stellar line within this region is blended with several iodine lines, rendering the calculation of spectral indices and bisectors a useless task.

3.1.1 Fundamentals of Iodine Observations

All the fundamentals of the iodine-cell method are described in Butler et al. (1996), but in this section we recall the basic idea behind this technique. In particular, we rewrite the notation for an observed spectrum of a star through the iodine cell. That spectrum is modeled as follows

$$S(x, v) = \kappa \left[T_{I_2}\lambda(x) I_\star(\lambda(x)/(1 - v/c))\right] \otimes \mathrm{LSF}(x) \tag{3.1}$$

where the observation is modeled as the product of two functions: the intrinsic stellar spectrum, $I_\star$, and the transmission function of the iodine, T_{I2}, and then convolved with the point spread function (PSF) of the instrument. In our case, we work with extracted spectra so it is more accurate to use the term Line Spread Function (LSF) instead. The constant κ is a normalization factor and v corresponds to the Doppler shift, i.e, the radial velocity we will later fit as a free parameter. We

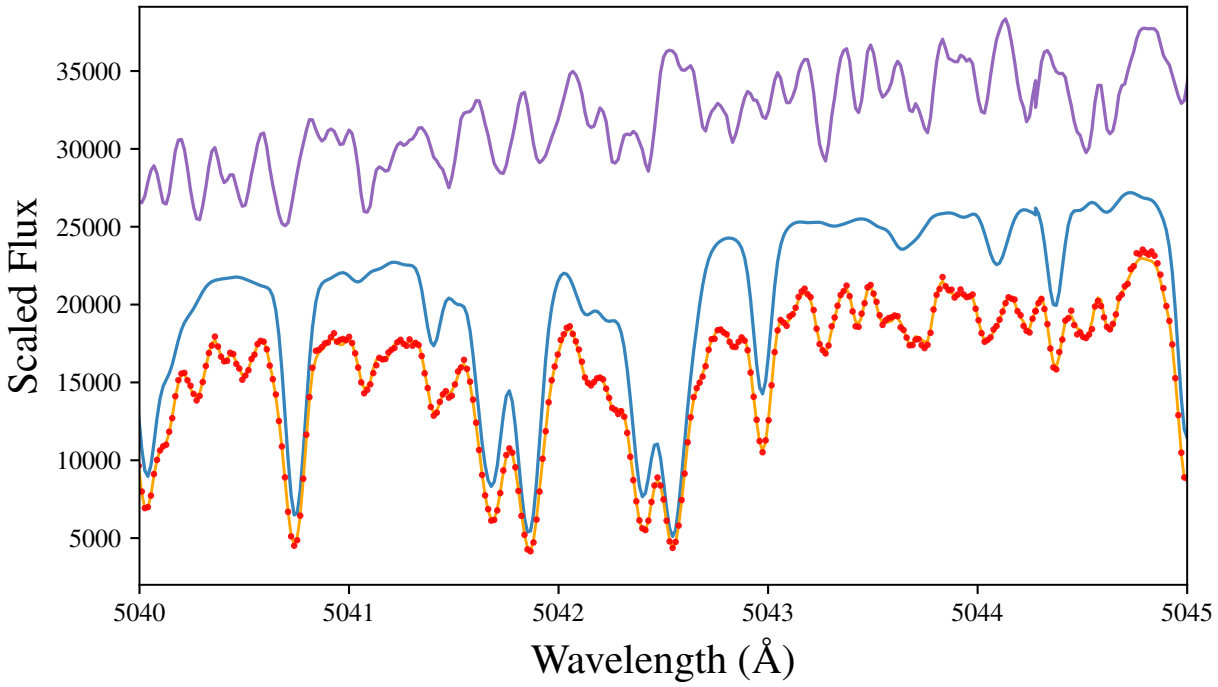

Figure 3.1: Forward modeling process showing a 5Å portion for an observation of the star τ Ceti observed with PFS. From top to bottom: Iodine spectrum convolved with the LSF (purple), intrinsic spectrum of the star, observed without iodine convolved with the LSF (blue), observation of the star through the iodine cell (red points), forward model of the observations (orange line). Note the scale in the y-axis, each spectrum is multiplied by some arbitrary factor for comparison only.

note the use of a slightly different nomenclature to that in Butler et al. (1996). Here we denote our forward model of the observations by $S(x)$ rather than I_{obs}. The latter, in our case, represents the observed spectrum, i.e., the actual data we record in the detector of the instrument that we here denote as S_x. The transmission function of the iodine spectrum, T_{I2}, has to be obtained from external measurement by scanning the iodine cell itself using the Fourier Transform Spectrum (FTS) method described in Valenti et al. (1995), where the instrumental profile of the spectrograph can be determined. The method relies on the acquisition of a high-resolution (R $\sim 10^6$), high signal-to-noise (S/N$\sim$1000) spectrum of the iodine that will provide an extremely precise (10^{-8}) vacuum wavelength scale. The intrinsic stellar spectrum is obtained by observing the star without the iodine cell in place. However, this observed spectrum is not precisely $I_\star$, instead, this spectrum carries the smearing due to the instrumental profile, so $I_\star \otimes$LSF is obtained.

In order to correct for the LSF smearing effect, a rapidly rotating, bright (V$\sim$3) B-type star is normally observed through the iodine cell before and after the observation of the stellar reference spectrum. Given the lack of spectral features for B-type stars, their spectrum is essentially continuum, therefore they serve as incandescent lamps shining through the iodine absorption cell, allowing to accuratelly trace the instrument's LSF. Then a modified version (Gilliland et al. 1992; Butler et al. 1996) of the original Jansson deconvolution procedure (Jansson 1984) allows this instrumental LSF to be deconvolved from the intrinsic stellar spectrum.

We generate a model of the observations, four times oversampled, by convolving the resultant deconvolved stellar spectrum with the instrumental profile and with the same sampling as the observations (see Figure 3.1). Figure 3.2 shows the deconvolution results for two chunks of spectrum for the star τ Ceti acquired with PFS. Red points correspond to the observations of the star without the iodine cell in place. The deconvolved stellar spectrum model is shown with an orange solid curve. The purple points represent 10 pixels on each of the edges of a chunk. Due to the LSF, each pixel is the smeared average of the nearby pixels. In the center of a given chunk this is not a problem. At the edges, however, it is necessary to include some extra pixels from outside the current chunk for the deconvolution routine to able to deal with the edge of the chunk. From the difference plot in the bottom panels of Figure 3.2 we note that the deconvolution is only very slightly different than the observation. The regions where the deconvolved spectrum is different compared with the observed data are mostly the depth of the lines and the difference is less than $\sim$5%.

3.1.2 Determining the LSF, wavelength solution and Doppler shift

We implement the description of the LSF by the sum of 13 Gaussians where the central one is fixed and the other 12 are allowed to vary in amplitude, as explained in Valenti et al. (1995). We define

$$LSF(x) = \sum_m G_m(x) \tag{3.2}$$

where

$$G_m(x) = A_m \, \mathrm{e}^{(x-x_{0,m})^2/2\sigma_m^2} \tag{3.3}$$

The process of generating a LSF prescription involves finding a single fixed central Gaussian, G_1. The half-width of this central Gaussian, σ_1, is found by trial and error. Once the central Gaussian is chosen the additional Gaussians, are placed at fixed positions, $x_{0,m}$, on either side of the central Gaussian such that their half-widths, σ_m overlap, to enforce smoothness. The number of additional Gaussians, and their widths, are found by trial and error, and they are different for each instrument.

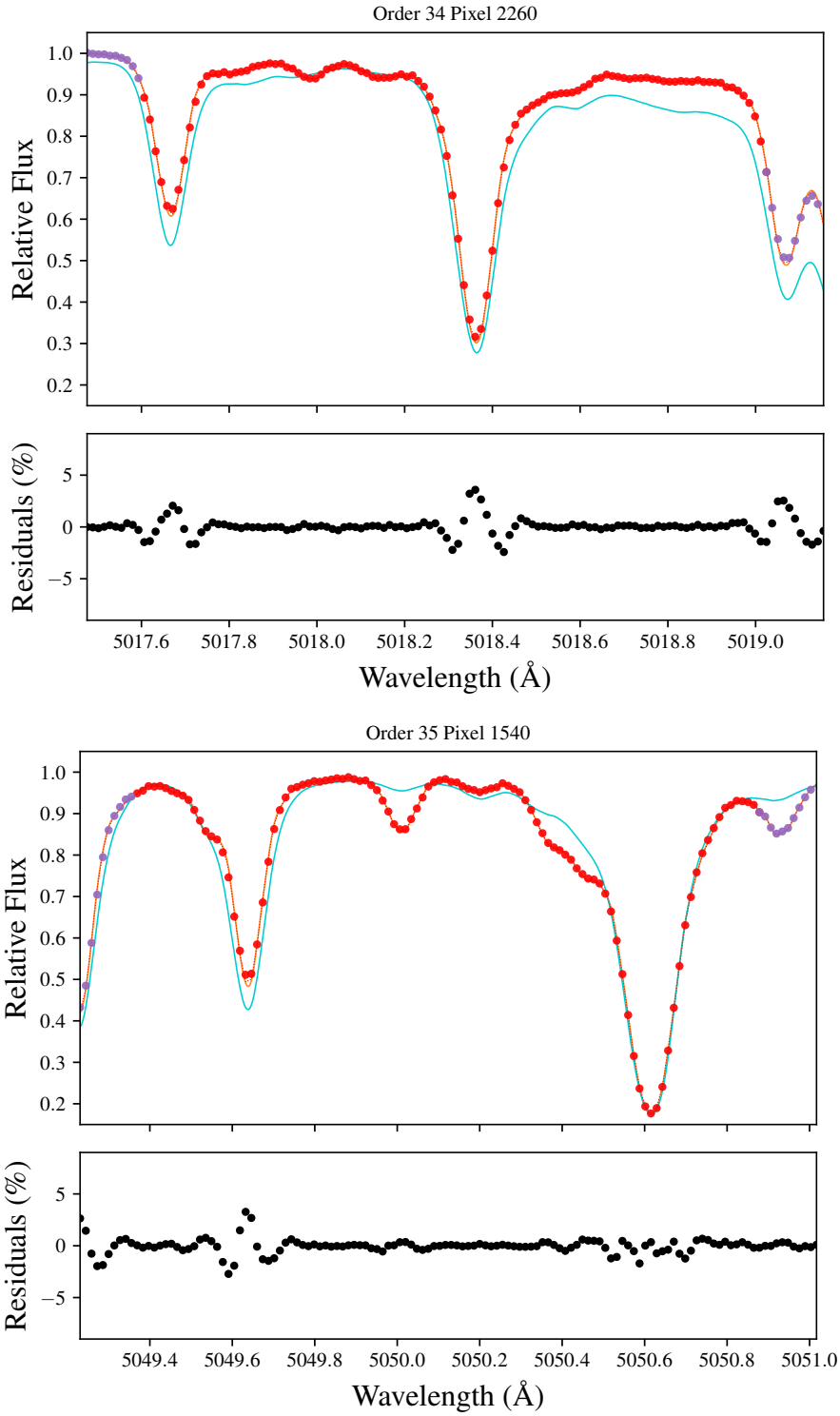

Figure 3.2: Left Panel. Top: 2Å chunk of the star τ Ceti to illustrate the generation of a deconvolved stellar spectrum. Red points correspond to the observation. The deconvolved model of the observation is shown as a dashed-red curve (apparent on top of the solid orange curve). The deconvolved stellar spectrum is shown as a solid orange curve. The solar spectrum binned to the resolution of the observations is plotted in cyan as comparison. Bottom: Residual between the data and the deconvolved stellar spectrum, binned to the same resolution of the observations. Right Panel: Same as in left panel, but for another 2Å chunk.

The goal is to build a LSF prescription with the fewest number of free parameters, but with sufficient flexibility to deal with the variations due to the instrument and the input image on the entrance slit.

The wavelength scale is described by two parameters as follows

$$\lambda_{\rm i} = \lambda_0 + b\, x_{\rm i} \tag{3.4}$$

where λ_0 refers to the wavelength zero-point, b corresponds to the linear dispersion, and i corresponds to the pixel index on the jth chunk, i $= 0, ..., n_{\rm pix} - 1$, where $n_{\rm pix}$ and corresponds to the chunk width and $j = 0, ..., n_{\rm chunk}$ (see Table 3.1).

The initial guess for the wavelength scale is determined from an exposure of iodine and a quartz lamp as part of the nighlty calibrations, but the final wavelength solution will be determined by a nonlinear least squares minimization process that uses the Marquardt gradient-expansion technique (Valenti et al. 1995; Bevington & Robinson 2003).

The radial velocity is defined by only one parameter

$$z = \frac{\Delta\lambda}{\lambda} = \frac{v}{c} \tag{3.5}$$

The barycentric correction is calculated with our own package that makes use of the JPL ephemeris. This correction is subtracted from the derived Doppler shift.

In this way, 16 parameters are needed to fully describe our spectral modeling process: κ, λ_0, b, v and $\sim$12 amplitudes for the Gaussians. We perform three iterations to derive the best-fit parameters that satisfy the model (equations 3.4 to 3.5). In the first pass, all the parameters are allowed to vary. In a second iteration, the linear dispersion is fixed. In a final pass, the linear dispersion and the LSF are fixed and the wavelength zero-point and the Doppler shift are allowed to vary. The fixed LSF is a weighted average of LSF in a given chunk and the nearest adjacent chunks.

3.2 Iodine-free spectra derivation

The primary motivation for deriving iodine-free spectra is to recover the stellar spectrum so that stellar activity indicators from lines that fall within the iodine wavelength region can be measured. We have defined all the elements involved in the calculation of radial velocities from observations of a star acquired through the iodine cell. Now, we extend this idea to describe a straightforward approach to remove the iodine spectrum directly from each observation.

From equation 3.1, we recall that $S(x)$ represents the forward model of observed star through the iodine cell. Now, we define

$$S_\star(\lambda) = \kappa\, I_\star(\lambda) \otimes LSF \tag{3.6}$$

where $I_\star(\lambda)$ is the intrinsic stellar spectrum and $S_\star(\lambda)$ is what we would expect to observe if there was not any iodine.

Then, we introduce the following definition

$$S_{I2} = S(\lambda) - S_\star(\lambda) \tag{3.7}$$

where S_{I_2} corresponds to the intensity of the iodine spectrum in the model of the data.

From equations 3.1, 3.6 and 3.7 we can write

$$S_{\star,x} = S_\star(x) - S_{I2} \tag{3.8}$$

So, the iodine-free spectrum can be described by

$$S_{\star,x} = S_x - S(\lambda) + S_\star(\lambda) \tag{3.9}$$

Another way of understanding this method is by considering S_x - $S(\lambda)$, this corresponds to the data minus the forward model of the observation. This expression can also be understood as the residuals between the data and the model. Then, $S_\star + (S_x - S(\lambda))$ will represent the template spectrum, without iodine, with the observed LSF plus some residuals between the data and the model (see Figure 3.4).

In order to derive the iodine-free spectra we perform the following steps.

1. First, the parameters that describe the LSF are defined: the pixels at which the Gaussians are centered, $x_{0,m}$, and the widths, σ_m, with $m = 1, ..., 13$ for the instruments listed in Table 3.1. We then retrieve the information from the deconvolved stellar spectrum (template) of the star of interest and the information is stored in our database that consists of an `IDL` data structure. Each one of these structures contain all the observations for that particular star, the name of the original files, the best-fit parameters from the modeling process. All the steps are carried out relative to the template, chunk by chunk. There are 818 chunks in the 26 iodine orders of the PFS spectra, for instance (see Table 3.1).

2. We start on the first pixel from the first order of the deconvolved stellar spectrum and we generate a wavelength scale based on the parameters from the template: λ_0 and b from equation 3.4. From the observation, we retrieve the radial velocity from the data structure. This, by definition, corresponds to the shift between the observed spectrum compared with the template, as we do not compute absolute radial velocities.

3. Next, we read the iodine FTS spectrum atlas and we bin it to the same resolution of the observation. After this, we construct a weighted average LSF within a pre-specified domain (adjacent chunks) on the echelle format of the spectrograph. This averaged LSF is then used to convolve the binned iodine spectrum, the template spectrum and the forward model of the observations.

4. The iodine intensity in the observation is obtained by subtracting the template plus iodine and LSF from the forward model (equation 3.7). Finally, we obtain the iodine-free spectrum by subtracting the iodine intensity from the observation, as shown in equation 3.9.

5. This process is repeated for every consecutive chunk, then by pasting each chunk we generate a reconstructed iodine-free spectrum for each one of the orders. These products are saved and the process is repeated for the next observation of the star. Once all the observations for a given star are completed, we move to the next target.

The implementation of the code is written in `IDL`, and the motivation to do so is to interact with the existing libraries and codes that our group currently uses for Doppler analysis. The iodine-free code is currently working on the instruments that we describe in the following subsections. The iodine-free derivation process is analogous for these instruments with minor differences that take into account each instrument's parameters (see Table 3.1). Figure 3.3 shows a simplified flowchart with the main steps of the code.

3.2.1 PFS

The Planet Finder Spectrograph (PFS, Crane et al. 2006, 2008, 2010) is a temperature-controlled, high-resolution echelle spectrograph mounted at the *Magellan* II/Clay-6.5m telescope at Las Campanas Observatory in Chile. The main purpose of this spectrograph is to search for exoplanets using the iodine cell method. The portion of the spectrum that is used to compute radial velocities consists of 26 orders covering the iodine region from ∼5011 Å to ∼6337 Å. Each image has a format of 4096 × 4096 pixels, with a pixel size of 15 μm. Science observations with PFS typically make use of a 0.5" slit that delivers a resolving power of ∼80,000. For the acquisition of the template, stellar spectra are acquired using a narrower 0.3" slit, achieving a higher resolution of ∼130,000. For the computation of the radial velocities, each order is divided into 34 smaller chunks of 120 pixels width that represent ∼2 Å of spectra.

3.2.2 HIRES

The High Resolution Echelle Spectrometer (HIRES, Vogt et al. 1994) is mounted on the 10m Keck I telescope at the W. M. Keck Observatory in Mauna Kea, Hawai'i. The spectrograph delivers a resolution of ∼65,000. The HIRES detector is composed of a 3-chip CCD mosaic covering the 300-1100 nm range. We refer to these chips as red, green and blue. For RV measurements, the iodine spectrum is collected in the green CCD. A spectrum obtained through the iodine cell consists of 14

orders between ∼4460 Å and ∼6500 Å . In the procedure where the radial velocities are computed, each order in the echelle format is divided into 32 smaller chunks, each of 80 pixels width that are equivalent to ∼2 Å in the spectra.

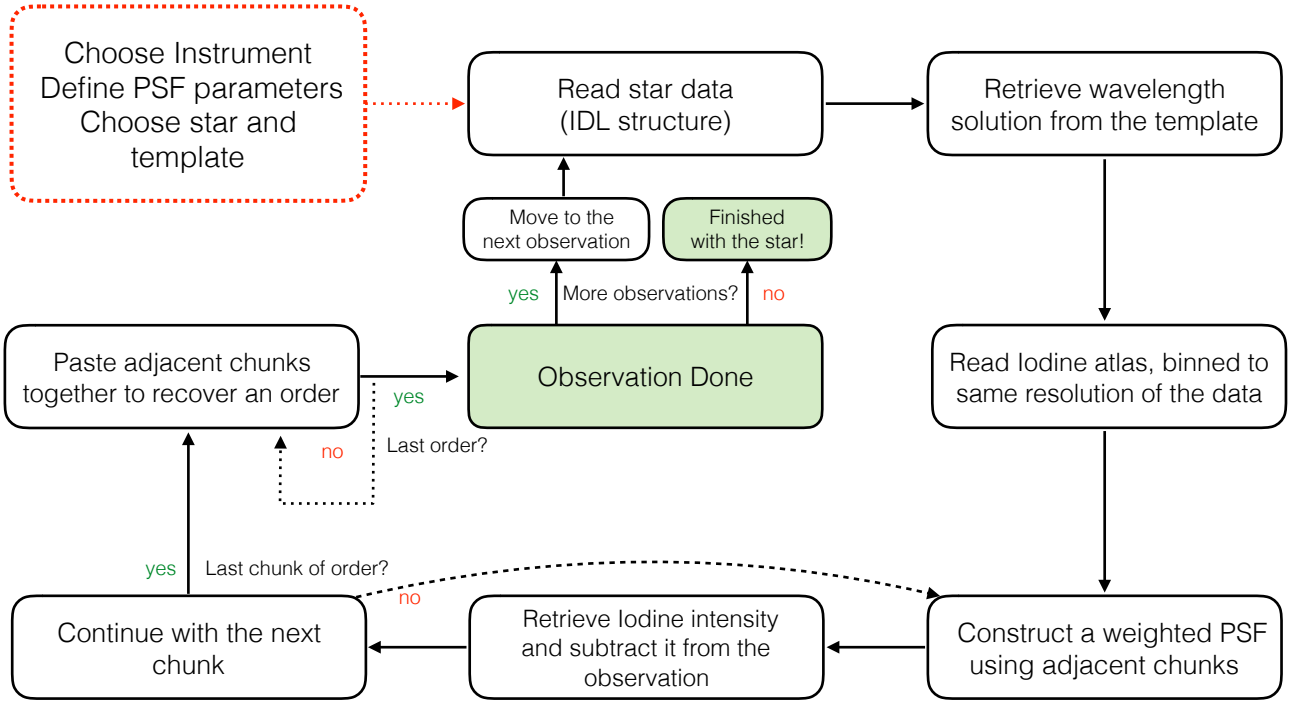

Figure 3.3: Flowchart showing the main steps in the code for the derivation of the clean spectra.

3.2.3 UCLES

The University College London Echelle Spectrograph (UCLES, Diego et al. 1990) was mounted on the 3.9m Anglo-Australian Telescope at the Australian Astronomical Observatory. The instrument offers a resolving power of R ∼50,000 when operated in its 31 lines/mm mode and making use of a 1 arcsec slit. The UCLES detector is a 2K × 4K CCD that covers the wavelength range between 300-1100 nm. The iodine region consists of 20 orders, where each order is divided into 48 chunks of 55 pixels width, equivalent to ∼2 Å in the spectra. Recently decomissioned, this instrument was used to carry out the Anglo-Australian Planet Search (AAPS) project for 18 years. We derived iodine-free spectra from the data available from the AAPS survey for the star τ Ceti as well.

3.3 Results

In figure 3.4 we show two 5 Å portions of the spectra acquired with PFS where the iodine-free spectrum (orange line) is shown on top of the template spectrum of the star τ Ceti and the original observation through the iodine cell (red). In figures 3.5 to **??**, 3.9 to 3.10 and 3.11 to 3.13 we show the iodine-free derived spectra for each order, for observations of the same star acquired with PFS at *Magellan*, HIRES at Keck and UCLES at the AAT, respectively. This star has a magnitude of V=3.5, providing excellent, high signal-to-noise spectra for testing purposes. At this time, we have collected 205 observations of τ Ceti, where the median signal to noise for observations is ∼192, with a typical exposure time of ∼10s. The total computation time needed for one observation consisting of 25 orders divided into 818 chunks is less than one second per chunk, totaling less than 2 minutes to derive and save an iodine-free spectrum in the same format as the observation: an `IDL` structure that can be easily read in both `IDL` and `Python` for further analysis, or indeed a range of other programming languages. Each one of these data structures contains the wavelength scale, template, observation, model, iodine spectrum and iodine-free derived spectrum.

From figures 3.5 to 3.11 (bottom panels) we also show the residuals after subtracting our derived iodine-free spectrum from the original iodine-free template observation of τ Ceti, as a function of chunk. $(S_x - S(x))/S(x)$. The overall scatter is found to be at the sim1.3%-1.5% level, obtained by computing the rms for the resultant residual spectrum for a given order. For each order, σ represents the scatter of the residual of the residual spectrum to highlight the cases where the deconvolution fails due to cosmetics such as pax pixels or columns in the chip, and the iodine free spectrum carries these high-frequency-like patterns for some chunks (e.g., orders 39, 46, 48). When this happens, the whole chunk is not affected, i.e. these patterns are not visible across the whole chunk, but on localized regions that span 20-50 pixels across a few columns in the CCD. We note here that during the raw reduction process of the images we perform cosmic ray removal. However, cosmics and outliers do remain in the spectra. Since each observation produces a velocity for each chunk, we are left with 700 velocities for each observation. We recall that in our Doppler analysis procedure, weights are defined by the estimated variance of each chink. The radial velocity for a given observation is then the weighted mean of the chunks. The chunks that produce velocities at the tail of the distribution are automatically discarded from the velocity analysis. The final error is computed by taking into account these weights as discussed in (Butler et al. 1996).

Throughout the process of developing this algorithm, we encountered a number of artifacts in each of the spectra, artifacts that must be precisely removed. In particular, if we look at the PFS instrument, located, for example, at ∼5245 Å in order 39, there is a defect that needs to be dealt with in a future revision of code. Checking the raw images and comparing them with a smoothed version of a flat field image, we identified bad regions that span several pixels wide and across a few columns on the detector for the orders where we see large residuals after our procedure. These defects are not smoothed away after performing flat fielding, and then when the deconvolution routine tries to reproduce the observed spectrum, it still carries these bad regions into the template by adding systematics that are not stellar features. These problematic regions of the spectra were never fixed since the radial velocity code performs an iterative rejection of deviant chunks based on high χ^2 values for each chunk. In this way, a chunk where the fit of the model is not good, will be removed and will not be considered in the final computation of the velocities, meaning they will not affect the precision too negatively.

Despite the latter, trying to overcome and fix these erroneous regions will be important to deal with in the future. In total we found 15 parts of the HIRES detector that introduced noisy features, along with ∼30 chunks for PFS and ∼10 for UCLES.

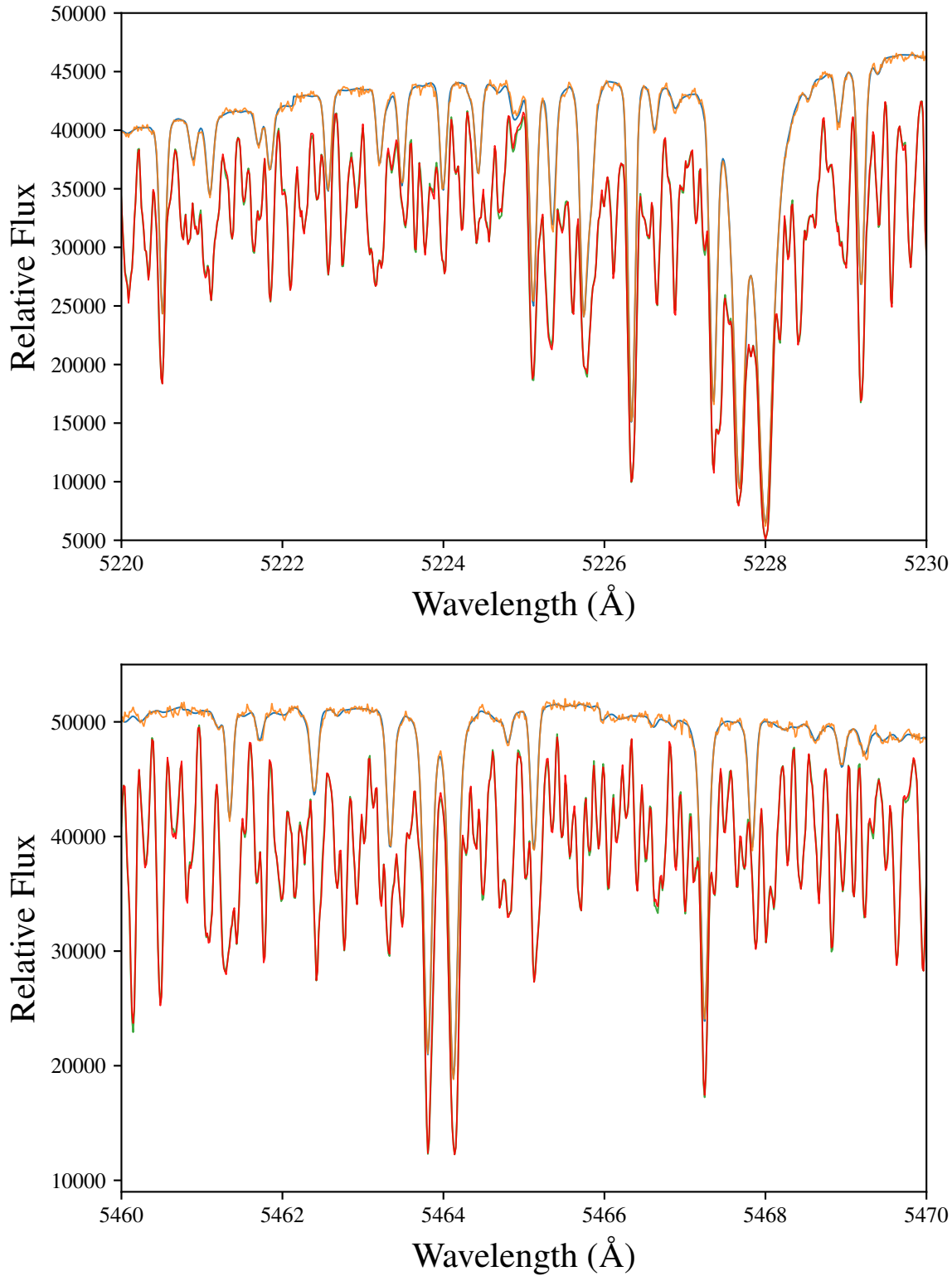

Figure 3.4: 10Å of PFS spectra for orders 40 and 45. The red spectrum, S_x shows the observation of the star τ Ceti taken through the iodine cell. The blue spectrum corresponds to the intrinsic stellar spectrum, without iodine, convolved with the LSF, denoted by $S_\star(\lambda)$. The green spectrum represents the forward model of the observations, $S(x)$. The orange spectrum on top of the template represents the iodine-free spectrum, $S_\star, x$ derived using the method described in Section 3.2.

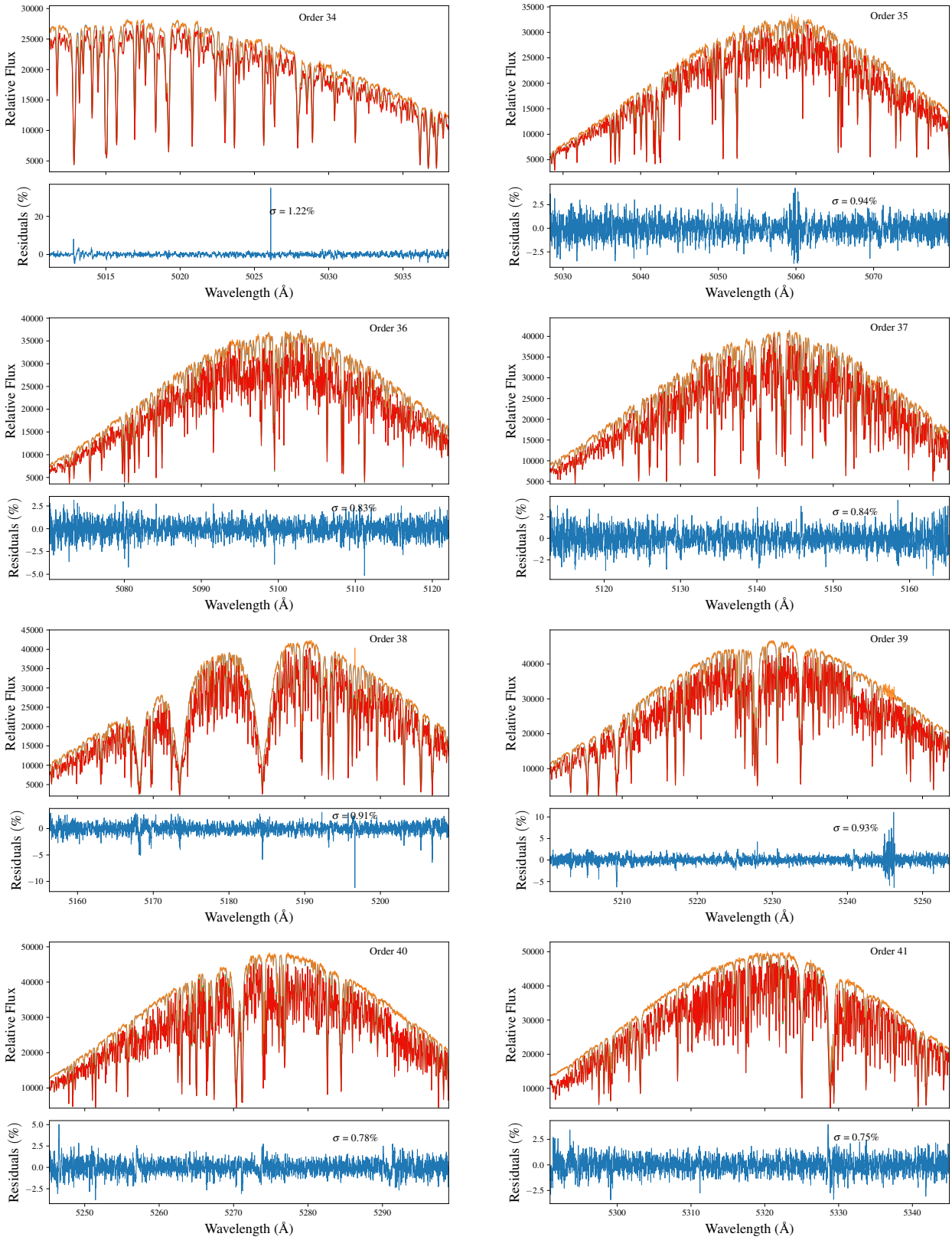

Figure 3.5: Results of the iodine-free derivation for the star τ Ceti. We show the 26 orders from the iodine region of PFS. On each plot, we show the observation through iodine (red), the template observation without iodine (blue), the forward model of the observations through iodine (green) and the recovered iodine-free spectrum (orange). Bottom panels on each plot show the level of precision of the recovered spectrum compared with the template (in %).

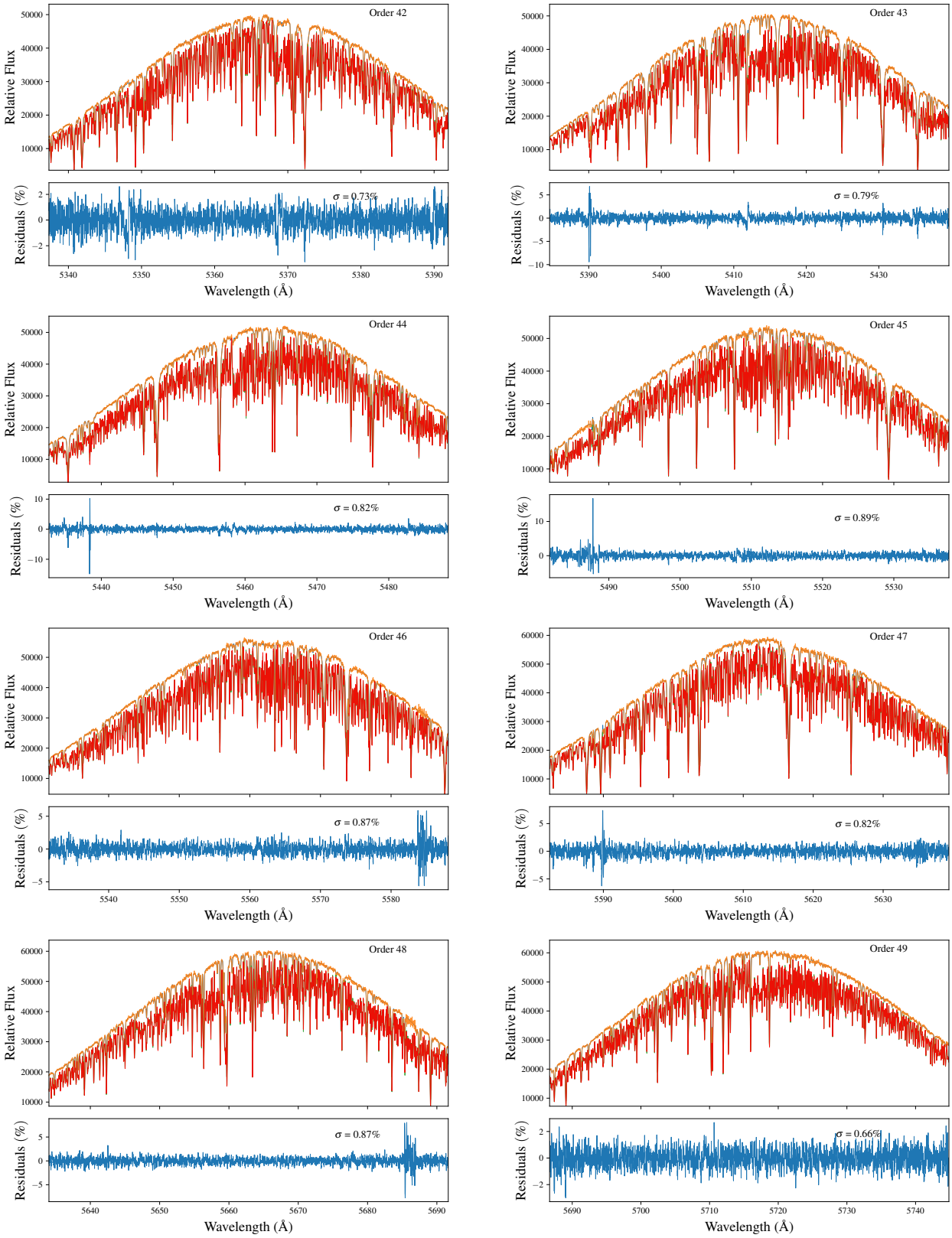

Figure 3.6: Results of the iodine-free derivation for the star τ Ceti. We show the 26 orders from the iodine region of PFS. On each plot, we show the observation through iodine (red), the template observation without iodine (blue), the forward model of the observations through iodine (green) and the recovered iodine-free spectrum (orange). Bottom panels on each plot show the level of precision of the recovered spectrum compared with the template (in %).

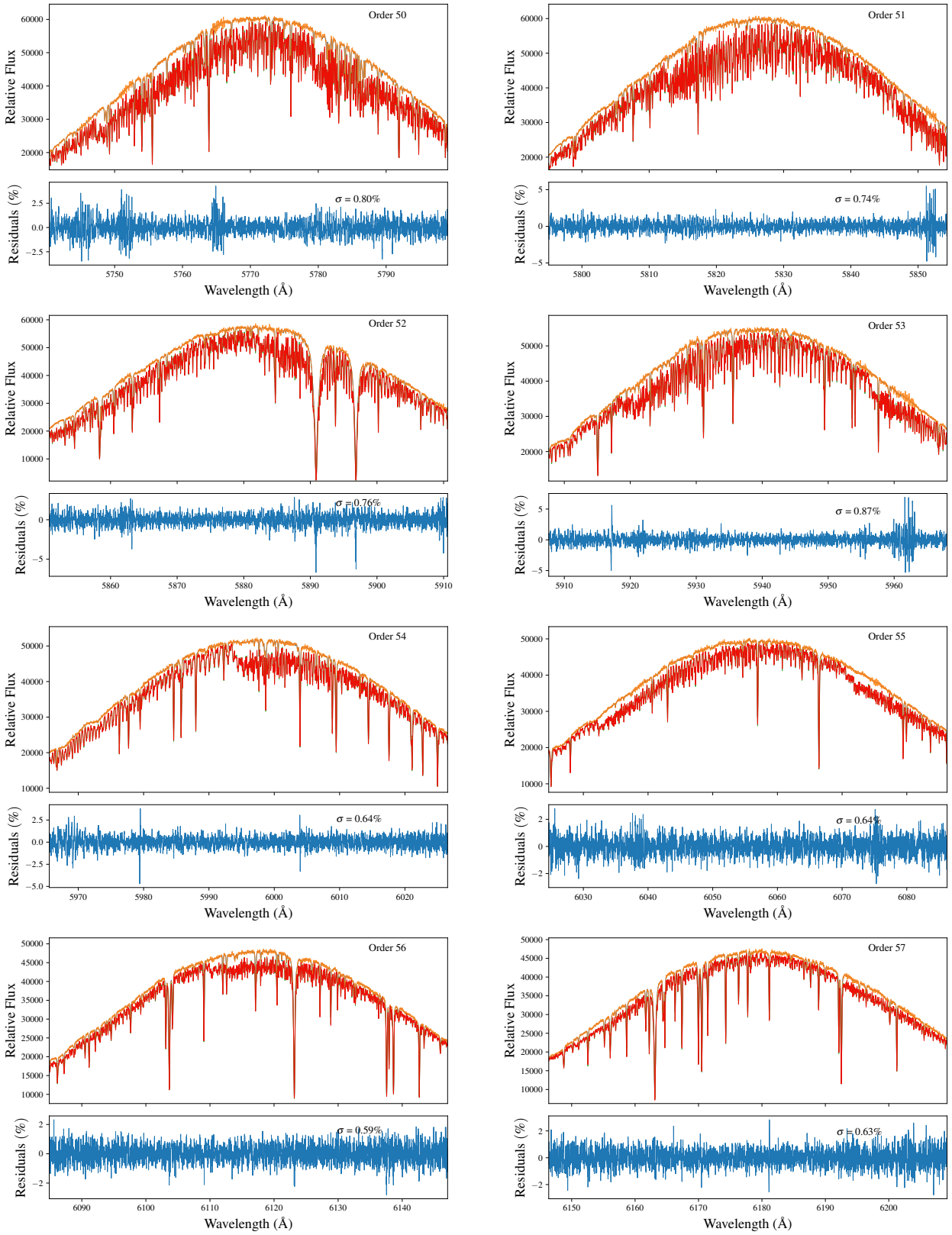

Figure 3.7: Results of the iodine-free derivation for the star τ Ceti. We show the 26 orders from the iodine region of PFS. On each plot, we show the observation through iodine (red), the template observation without iodine (blue), the forward model of the observations through iodine (green) and the recovered iodine-free spectrum (orange). Bottom panels on each plot show the level of precision of the recovered spectrum compared with the template (in %).

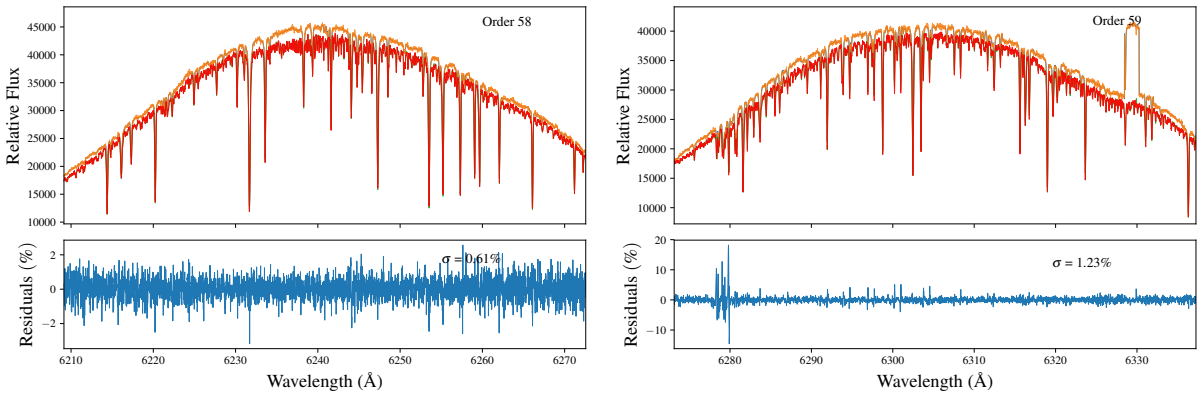

Figure 3.8: Results of the iodine-free derivation for the star τ Ceti. We show the 26 orders from the iodine region of PFS. On each plot, we show the observation through iodine (red), the template observation without iodine (blue), the forward model of the observations through iodine (green) and the recovered iodine-free spectrum (orange). Bottom panels on each plot show the level of precision of the recovered spectrum compared with the template (in %).

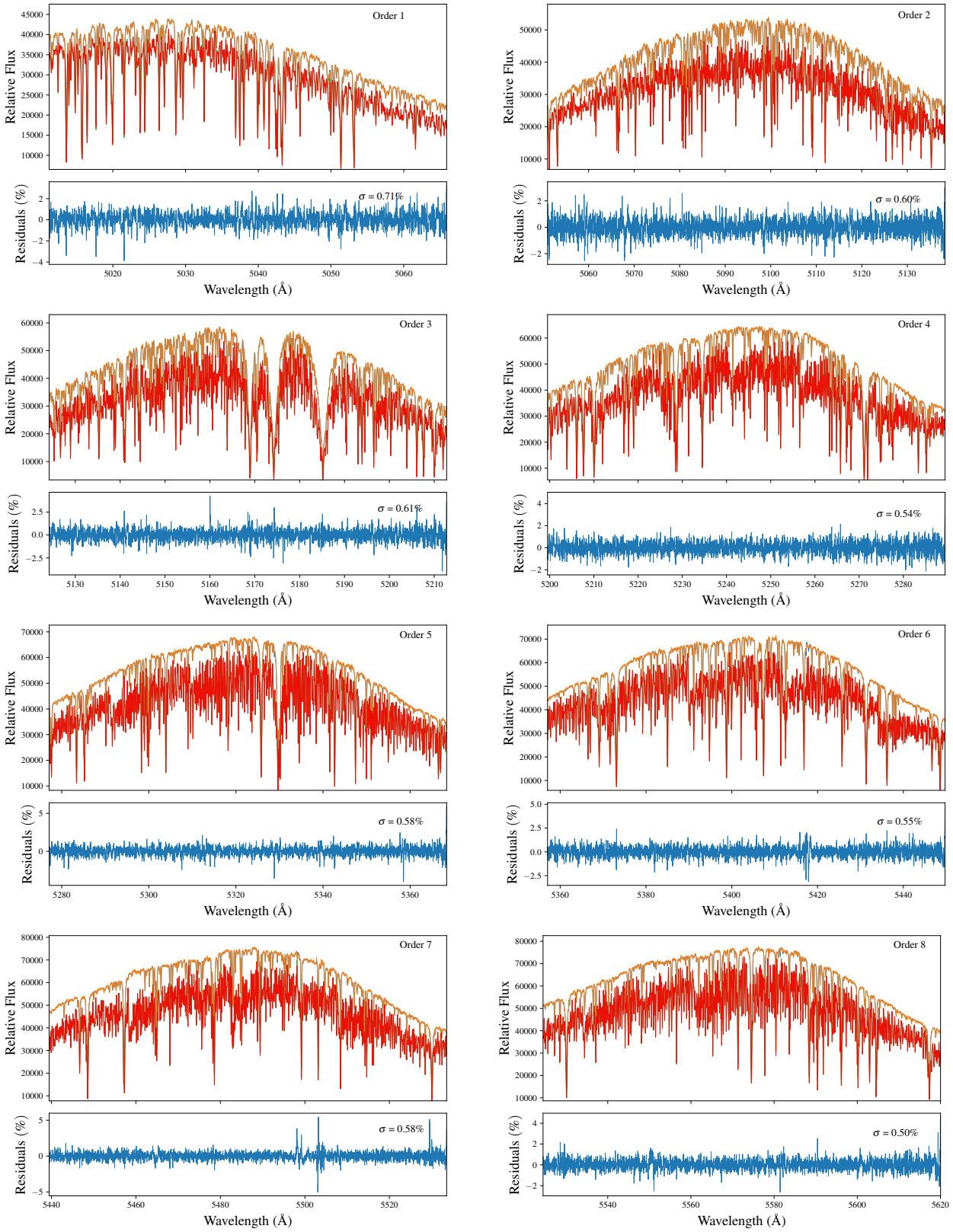

Figure 3.9: Results of the iodine-free derivation for the star τ Ceti. We show the 14 orders from the iodine region of HIRES. On each plot, we show the observation through iodine (red), the template observation without iodine (blue), the forward model of the observations through iodine (green) and the recovered iodine-free spectrum (orange). Bottom panels on each plot show the level of precision of the recovered spectrum compared to the template (in %).

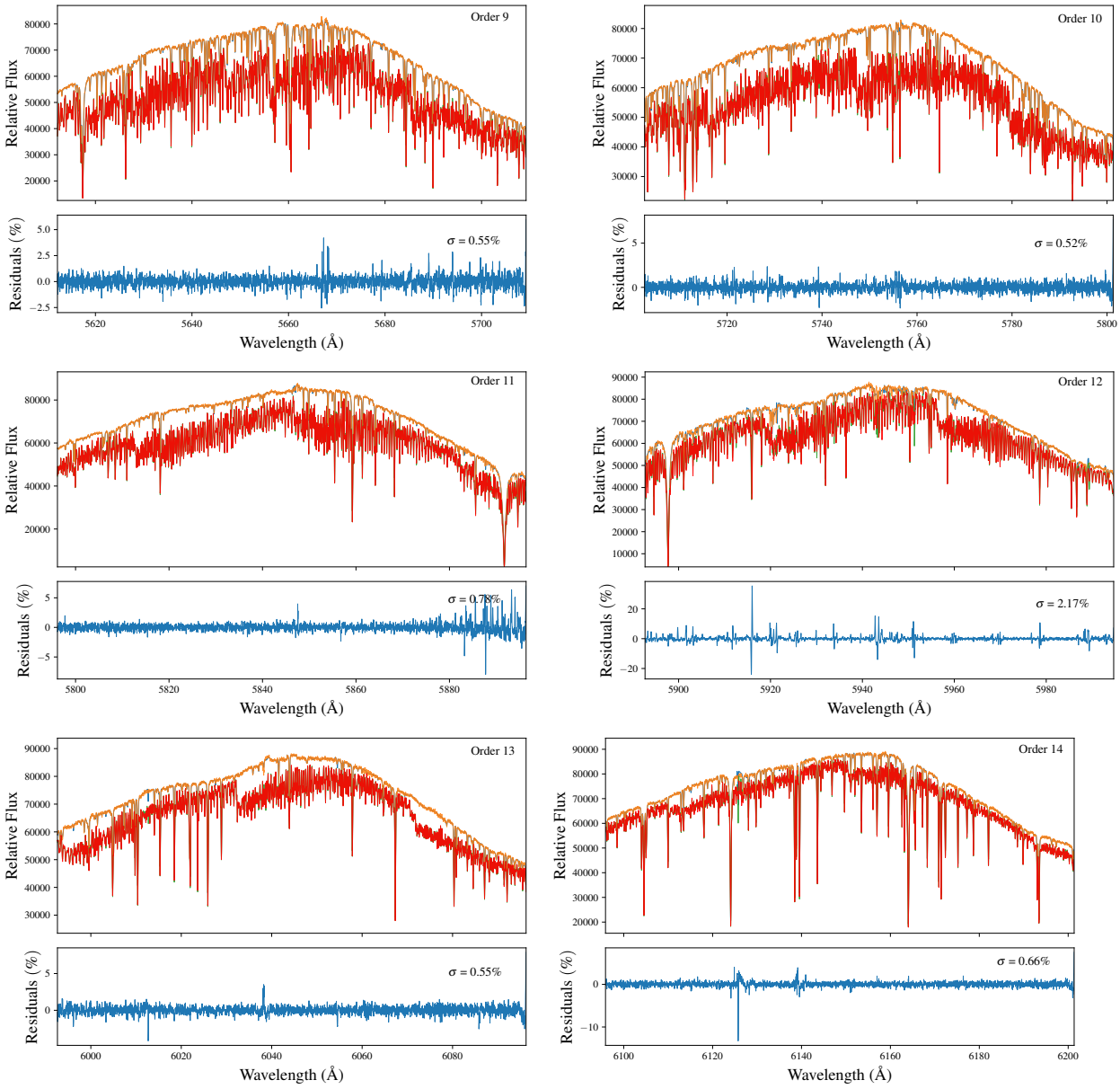

Figure 3.10: Results of the iodine-free derivation for the star τ Ceti. We show the 14 orders from the iodine region of HIRES. On each plot, we show the observation through iodine (red), the template observation without iodine (blue), the forward model of the observations through iodine (green) and the recovered iodine-free spectrum (orange). Bottom panels on each plot show the level of precision of the recovered spectrum compared to the template (in %).

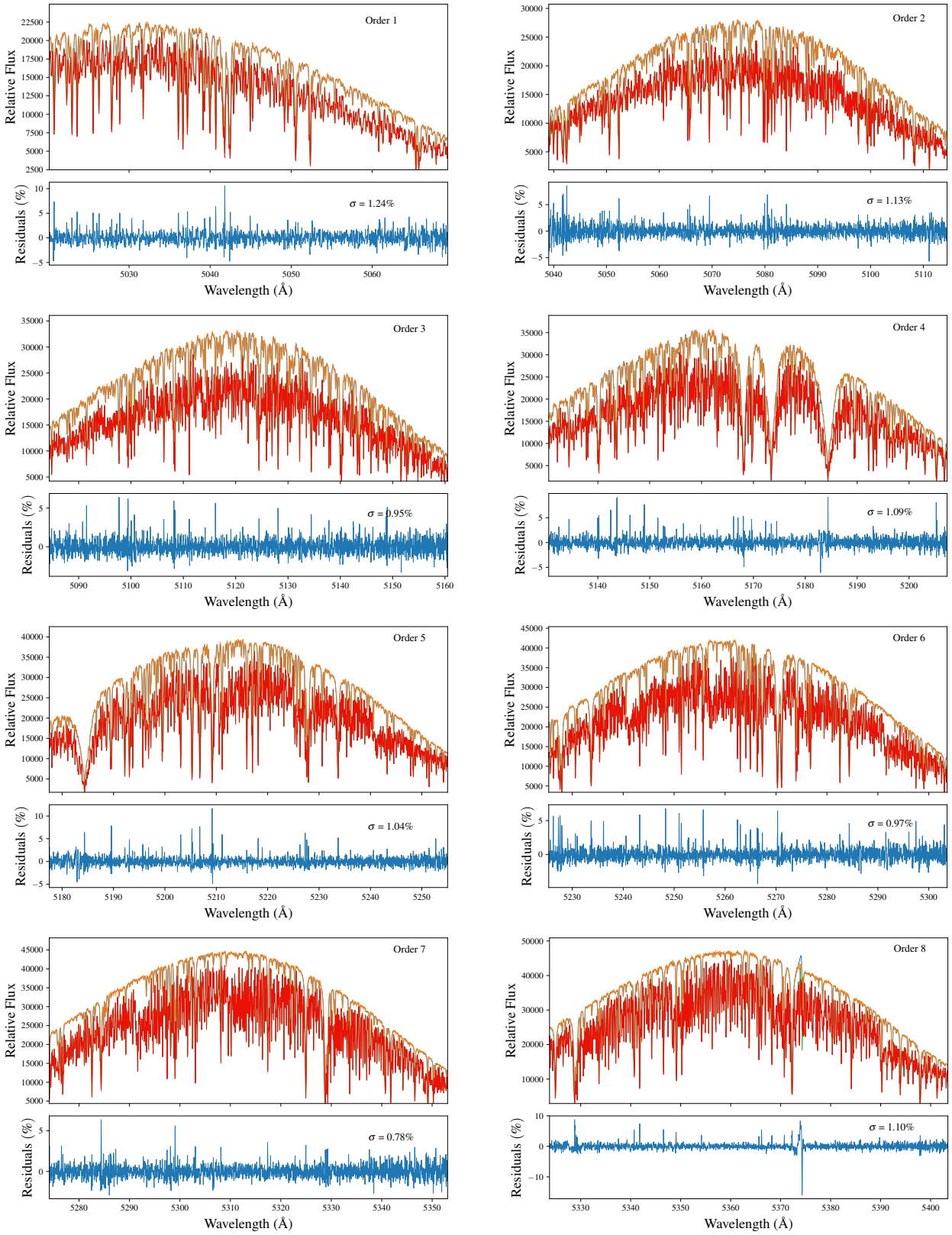

Figure 3.11: Results of the iodine-free derivation for the star τ Ceti. We show the 20 orders in the iodine region from UCLES. On each plot, we show the observation through iodine (red), the template observation without iodine (blue), the forward model of the observations through iodine (green) and the recovered iodine-free spectrum (orange). Bottom panels on each plot show the level of precision of the recovered spectrum compared to the template (in %).

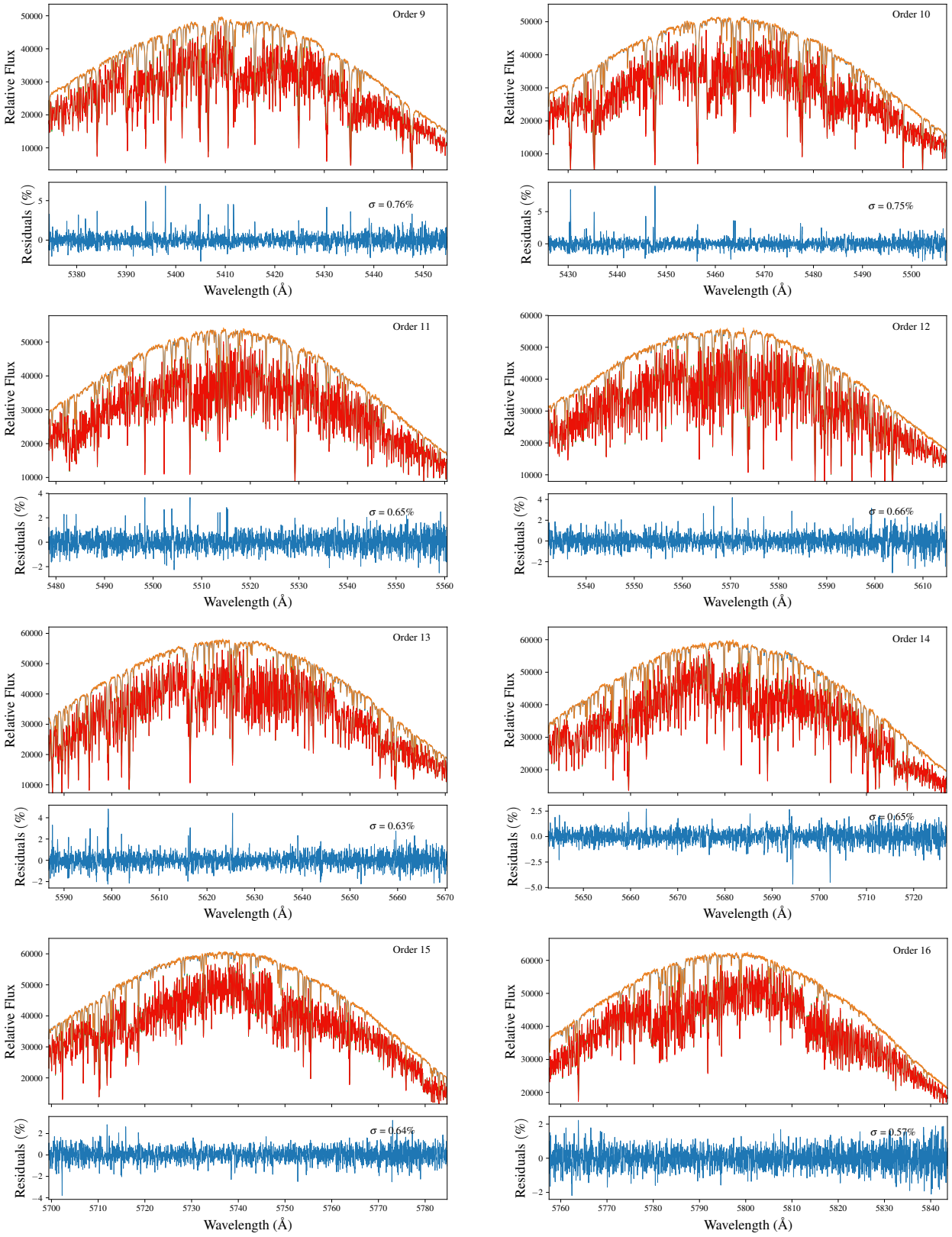

Figure 3.12: Results of the iodine-free derivation for the star τ Ceti. We show the 20 orders in the iodine region from UCLES. On each plot, we show the observation through iodine (red), the template observation without iodine (blue), the forward model of the observations through iodine (green) and the recovered iodine-free spectrum (orange). Bottom panels on each plot show the level of precision of the recovered spectrum compared to the template (in %).

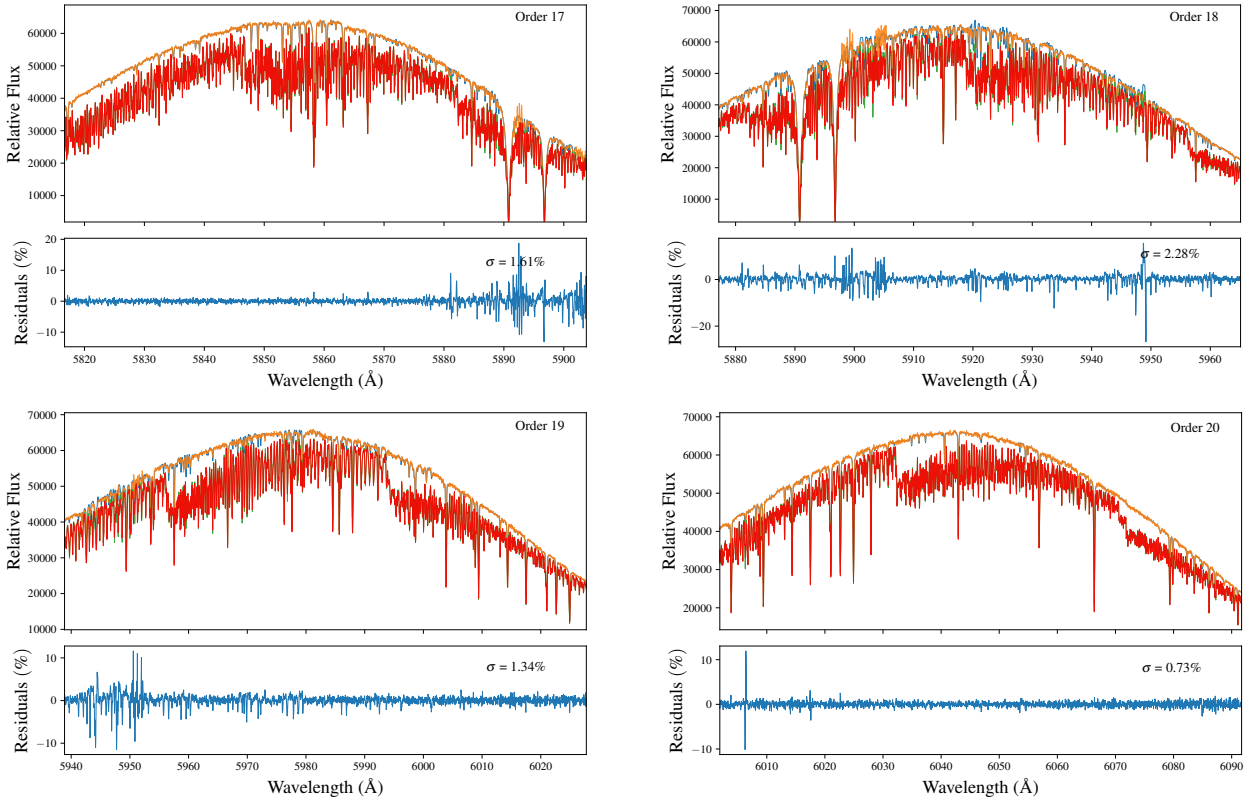

Figure 3.13: Results of the iodine-free derivation for the star τ Ceti. We show the 20 orders in the iodine region from UCLES. On each plot, we show the observation through iodine (red), the template observation without iodine (blue), the forward model of the observations through iodine (green) and the recovered iodine-free spectrum (orange). Bottom panels on each plot show the level of precision of the recovered spectrum compared to the template (in %).

3.4 Direct Applications and Future Work

One immediate application for this method is to derive stellar activity indicators for absorption lines that lie within the iodine region, mostly between 5000 Å and 6300 Å. As future work, we plan to derive activity indicators using the iodine-free spectra, as we now can use portions of the spectra that were originally 'contaminated' with the iodine spectrum. This means, generating activity indicators for lines such as the Sodium D doublet (Na D, λ=5889.95 Å, λ=5895.92 Å), or a host of other lines like Fe I or Mg I that fall within the iodine region of the spectrum Wise et al. (2018). It should also be possible to carry out diagnostic analyses, by computing line-bisectors and so on, in an attempt to correlate the velocities for the effects of rotation, or at least to identify the observations which are questionable because of such effects. At this point, it is important to note that the iodine-free spectrum has an LSF which is variable and depends on the optical aberration of the spectrograph and on the slit illumination. Therefore, the use of bisectors to trace line asymmetries is possible if they are larger compared with the LSF variations. Line equivalent widths and activity indices obtained by integrating flux can be useful, as they are independent of the LSF. The use of the LSF information derived from the iodine lines as part of the forward model is outside the scope of this work and will be the subject to future work.

The idea of creating so called super templates has also been a major motivation to build this code. A similar idea has been proposed and successfully implemented by Gao et al. (2016) for near-infrared observations. In our case, we would take out the distorting effect of the iodine cell on the spectrum for each individual spectrum, and then combine them altogether, after sorting for their mutual velocity offsets, to provide a single, high signal-to-noise and high-resolution template observation. Since this template would be constructed using the individual spectra themselves, the signal-to-noise ratio is only limited by the number of observations considered (assuming the individual spectra are also considered high signal-to-noise). This method can potentially provide higher precision radial velocities to be calculated, given that the new super-templates can allow an increase in the stability of the measurements. They will also provide us with an excellent spectrum to use in the calculation of the stellar parameters like $T_{\rm eff}$, $\log g$, [Fe/H], mass, radius, etc (e.g. Soto & Jenkins 2018).

Another direct application of this method consists of deriving iodine-free spectra for spectroscopic observations of transits. In particular, many spectra of transiting planets can be taken when the planet is blocking the stellar light as it passes in front of the star, with the express aim of measuring the spin-orbit alignment of the planet through the Rossiter-McLaughlin effect (RM, Rossiter 1924; McLaughlin 1924). When studying the RM effect, observations are acquired both outside the transit and in-transit. Hence, removing the iodine from both sets of observations enables the possibility of performing differencing, and hence tracing some elements that could be present in an planet candidate's atmosphere, which otherwise could not be possible when having the iodine spectrum superimposed on the stellar spectrum. Hence, this method could allow possible transmission spectroscopy to be performed, or planetary reflected light studies. It should be noted however, that the precision to which this method can be considered accurate, depends on observing a high-quality template. Also, defects on the CCD can also impact the derived iodine-free spectrum, specifically they can negatively impact the deconvolved stellar spectrum. As future work, the plan is to implement this method for other spectrographs that use the iodine cell method, such as the Automated Planet Finder (APF; Vogt et al. 2014), Ultraviolet and Visible Echelle Spectrograph (UVES: Dekker et al. 2000), and CHIRON echelle spectrograph (Tokovinin et al. 2013).

Chapter 4

A short-period Neptune orbiting the G-type star TOI-132

Based on the results published in Díaz, M. R., et al., *TOI-132 b: A short-period Neptune orbiting a V∼11 G star delivered by TESS*, 2020, MNRAS, 493, 973.

The Neptune desert is a feature seen in the radius-period plane, whereby a notable dearth of short period, Neptune-like planets is found. In this chapter we present discovery of a new short-period planet in the Neptune desert, orbiting the G-type dwarf TYC 8003-1117-1 (TOI-132). *TESS* photometry shows transit-like dips at the level of ∼1400 ppm occurring every ∼2.11 days. High-precision radial velocity follow-up with HARPS confirmed the planetary nature of the transit signal and provided a semi-amplitude radial velocity variation of $11.38\ ^{+0.84}_{-0.85}$ m s^{-1}, which, when combined with the stellar mass of $0.97 \pm 0.06\ M_{\odot}$, provides a planetary mass of $22.40^{+1.90}_{-1.92}\ M_{\oplus}$. Modeling the *TESS* light curve returns a planet radius of $3.42^{+0.13}_{-0.14}\ R_{\oplus}$, and therefore the planet bulk density is found to be $3.08^{+0.44}_{-0.46}$ g cm^{-3}. Planet structure models suggest that the bulk of the planet mass is in the form of a rocky core, with an atmospheric mass fraction of $4.3^{+1.2}_{-2.3}$%. TOI-132 b is a *TESS* Level 1 Science Requirement candidate, and therefore priority follow-up will allow the search for additional planets in the system, whilst helping to constrain low-mass planet formation and evolution models, particularly valuable for better understanding the Neptune desert.

4.1 Photometry

4.1.1 *TESS* Photometry

TYC 8003-1117-1 (also known as TIC 89020549, TOI-132) was observed by *TESS* in Sector 1 on Camera 2 in short-cadence mode ($T_{\rm exp} = 2$ minutes). The total time baseline of the observations is 27.87 days, spanning from July 25th to August 22nd 2018. TOI-132.01 was identified as a potential transiting planet signature by the Science Processing Operations Center (SPOC) in the transit search run on Sector 1 (Jenkins 2002; Jenkins et al. 2010) and promoted to TOI status by the *TESS* Science Office based on the SPOC Data Validation (DV) reports (Twicken et al. 2018; Li et al. 2019).

The target was selected from the *TESS* alerts website[1], based on the magnitude of the star (V=11.2 mag) and period of the candidate, since it presented a good opportunity to be confirmed relatively quickly with HARPS. In addition, from the DV report for TOI-132.01, we note the planetary signature passed all of the diagnostic tests conducted by DV, including the odd/even depth test, the weak secondary test, the ghost diagnostic test, the difference image centroid shift test.

We retrieved the photometry provided by the *TESS* SPOC pipeline (Jenkins et al. 2016a), and accessed the data from the simple aperture photometry (`SAP_FLUX`) and the Presearch Data Conditioning simple aperture photometry (`PDCSAP_FLUX`, Smith et al. 2012; Stumpe et al. 2014), which contains systematics-corrected data using the algorithms previously used for *Kepler* (Jenkins 2017). The median-normalized `SAP_FLUX` photometry is shown in the top panel of Figure 4.1. Bottom panel shows the `PDCSAP_FLUX` photometry, divided by its median value and after applying a 4-σ clipping rejection with the transits masked out. This light curve is used throughout all the analyses in this chapter. The gap in the middle of the time series occurred when the observations were stopped to allow for the data down-link. Finally, in order to avoid any bias in our analysis, we excluded the photometric measurements between (BJD - 2457000) 1347.5 and 1349.3 (gray shaded area) given that the spacecraft pointing jitter was higher than nominal, as described by Huang et al. (2018) and also noted in recent *TESS* discoveries (see, e.g., Espinoza et al. 2019b). A total of 11 transit events were considered for further analysis in the present work. Magnitudes and stellar parameters for TOI-132 are shown in Table 4.1 (see also Section 4.3).

We also performed a time-frequency analysis (Mathur et al. 2010) and computed the auto-correlation function for the *TESS* lightcurve to look for signatures of rotation modulation following the methodology described in García et al. (2014), Ceillier et al. (2017) and Santos et al. (2019). However, no significant signal was found. The length of the data is too short to find a periodicity larger than 9 days as we require to observe at least three periods.

4.1.2 Ground-based time-series photometry

We acquired ground-based time-series follow-up photometry of TOI-132 as part of the *TESS* Follow-up Observing Program (TFOP) to attempt to rule out nearby eclipsing binaries (NEBs) in all stars that could be blended in the *TESS* aperture as potential sources of the *TESS* detection. Furthermore, we attempt to i) detect the transit-like event on target to confirm the event depth and thus the *TESS* photometric deblending factor, ii) refine the *TESS* ephemeris, iii) provide additional epochs of transit center time measurements to supplement the transit timing variation (TTV) analysis, and iv) place constraints on transit depth differences across filter bands. We used the `TESS Transit Finder`, which is a customized version of the `Tapir` software package (Jensen 2013), to schedule our transit observations.

We observed TOI-132 continuously for 443 minutes on UTC 2018 September 09 in R_c band ($\sigma \sim 1.8$ mmag) from the Perth Exoplanet Survey Telescope (PEST) near Perth, Australia. The 0.3-m telescope is equipped with a 1530×1020 pixels SBIG ST-8XME camera with an image scale of 1.2" pixel^{-1} resulting in a $31' \times 21'$ field of view. A custom pipeline was used to calibrate the images and extract the differential photometry using an aperture with radius 8.2". The images have typical stellar point spread functions (PSFs) with a full width at half maximum (FWHM) of ∼4". The data rule out NEBs in stars within 2.5' of the target star that are fainter by as much as 6.4 magnitudes in R_c band.

[1] `//https://tev.mit.edu/data/`

Table 4.1: Stellar parameters of TOI-132

Parameter	Value	Source
TESS Names	TIC89020549 (TOI-132.01)	
RA (hh:mm:ss)	22:33:35.8683	*Gaia*
Dec (dd:mm:ss)	-43:26:11.9167	*Gaia*
μ RA (mas yr^{-1})	35.553 ± 0.043	*Gaia*
μ (mas yr^{-1})	-53.055 ± 0.054	*Gaia*
Parallax (mas)	6.08 ± 0.04	*Gaia**
Distance (pc)	164.47 ± 27.32	*Gaia*
SpT	G8V	This work
Photometry		
B_T	12.07 ±0.17	Tycho-2
V_T	11.29 ± 0.07	Tycho-2
g	11.85 ± 0.02	APASS
r	11.24 ± 0.01	APASS
i	11.08 ± 0.02	APASS
TESS	10.80 ± 0.02	Stassun et al. (2018b)
Gaia	11.2935 ± 0.0003	*Gaia*
J	10.14 ±0.02	2MASS
H	9.76 ± 0.02	2MASS
K_s	9.65 ± 0.02	2MASS
W_1	9.61± 0.02	WISE
W_2	9.69± 0.02	WISE
W_3	9.60±0.04	WISE
W_4	8.72±0.42	WISE
Derived Parameters		
$T_{\rm eff}$ (K)	5397 ± 46	This work
$\log g$ (cm s^{-2})	4.48 ± 0.23	This work
[Fe/H] (dex)	0.16 ± 0.10	This work
$L(L_\odot)$	0.60 ± 0.05	This work
R ($R_\odot$)	0.90 ± 0.02	This work
M ($M_\odot$)	0.97 ± 0.06	This work
$v\ sin$(i) (km s^{-1})	3.00 ± 0.30	This work
$v_{\rm mac}$ (km s^{-1})	1.74 ± 0.20	This work
$\rho_\star$ (g cm^{-3})	1.89 ± 0.15	This work
$\log R_{HK}$ (dex)	−5.02 ± 0.13	This work
Age (Gyr)	$6.34^{+0.42}_{-2.35}$	This work
(U,V,W) (km s^{-1})	18.4 ± 0.2, -32.6 ± 0.4, 16.5 ± 0.4	This work

*Correction of +82 μas from Stassun & Torres (2018) applied to *Gaia*.

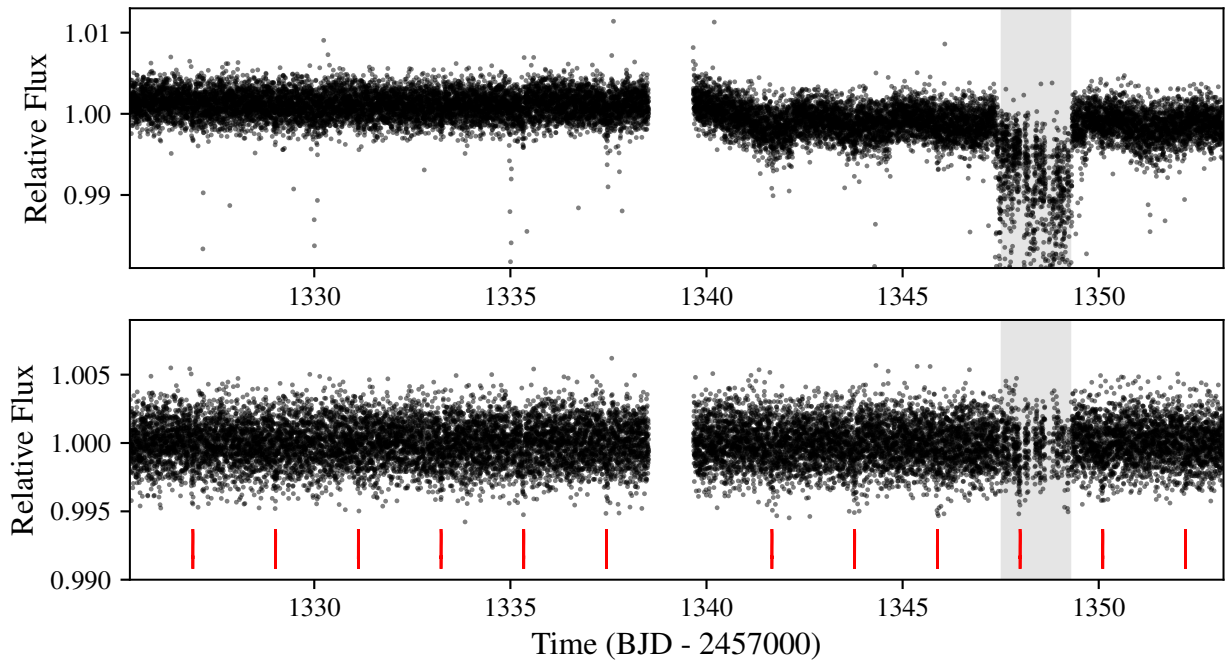

Figure 4.1: *TESS* light curve of TOI-132. Top panel shows the Simple Aperture Photometry (`SAP_FLUX`). Bottom panel shows the systematic-corrected `PDCSAP_FLUX` photometry after normalizing by the median and rejecting 4σ values. Red vertical lines show the position of the 12 transits identified in the *TESS* alert from Sector 1. The gray shaded area highlights the photometric measurements removed from the analysis due to an increase in the spacecraft pointing jitter.

We also observed full predicted transit durations of TOI-132 continuously in z-short band on UTC 2018 November 14, UTC 2019 June 19, and UTC 2019 July 06 from the Las Cumbres Observatory Global Telescope (LCOGT) 1.0 m telescopes (Brown et al. 2013) at Cerro Tololo Inter-American Observatory for 277, 335, and 283 minutes, respectively. Another full transit was observed continuously for 232 minutes in B-band on UTC 2019 August 02 from an LCOGT 1.0 m telescope at Siding Spring Observatory. The 4096 × 4096 LCOGT SINISTRO cameras have an image scale of 0.389" pixel^{-1} resulting in a $26' \times 26'$ field of view. The images were calibrated by the standard LCOGT BANZAI pipeline (McCully et al. 2018) and the photometric data were extracted using the `AstroImageJ` (`AIJ`) software package (Collins et al. 2017), yielding a mean error of 800 ppm for the z-short band data we include in our analysis.

The November data rule out NEBs in all stars within $2\farcs5$ of the target star that are fainter by as much as 8.7 magnitudes in z-short band, which includes all known *Gaia* DR2 stars that are blended in the *TESS* aperture. The June observation confirmed a ∼1400 ppm deep ingress on target arriving ∼80 minutes late relative to the original TOI ephemeris. The follow-up ephemeris was adjusted to account for the 80 minute offset. The July observation confirmed an on-time arrival of a ∼1400 ppm deep full transit relative to the adjusted ephemeris, indicating that the transit timing is consistent with a linear ephemeris. The images have stellar PSF FWHMs of $\sim 2\farcs0$, and the transit signal is reliably detected on target using a follow-up aperture with radius as small as $1\farcs5$. Therefore, the aperture is negligibly contaminated by the nearest *Gaia* neighbor $10\farcs5$ south. Systematic effects start to dominate the light curve for smaller apertures. The August B-band observation confirmed an on-time arrival of a ∼1400 ppm deep full transit, indicating that the transit-like event does not show a filter dependent depth in B and z-short bands, which photometrically strengthens the case for a transiting exoplanet orbiting around TOI-132.

4.2 HARPS Spectroscopic Follow-up

TOI-132 was observed using HARPS (Pepe et al. 2002b) spectrograph mounted at the 3.6-m ESO telescope at La Silla observatory, during seven consecutive nights between April 2 and 9 2019, as part of the observing program 0103.C-0442. The exposure time was set to 1200-1800 sec, which allowed us to achieve a mean signal-to-noise (S/N) ratio of ∼35 per pixel at 5500 Å in the extracted spectra giving rise to a typical error of ∼1.9 m s^{-1}. Upon examination of the radial velocities and after performing a 1-planet model fit to the *TESS* period, we found it necessary to acquire more observations to improve the phase coverage. Therefore, 13 additional radial velocities were taken in two runs between May and July 2019, as part of the observing program 1102.C-0923, covering the initial gaps in the orbital phase from the observations in April. We set the exposure time to 1800-2100 sec, leading to a mean S/N ratio of ∼40 and a mean uncertainty of ∼1.5 m s^{-1}.

We reduced the spectra using the HARPS online data reduction software (DRS) (Bouchy et al. 2001). The data products include the extracted spectra, both in *echelle* and order-merged spectra, the cross-correlation functions[2] (CCF, Baranne et al. 1996; Pepe et al. 2002b) and a measurement of the full-width at half maximum (FWHM) of the CCF profile, and the bisector inverse slope (BIS, Queloz et al. 2001).

[2]Obtained using a G2 numerical mask.

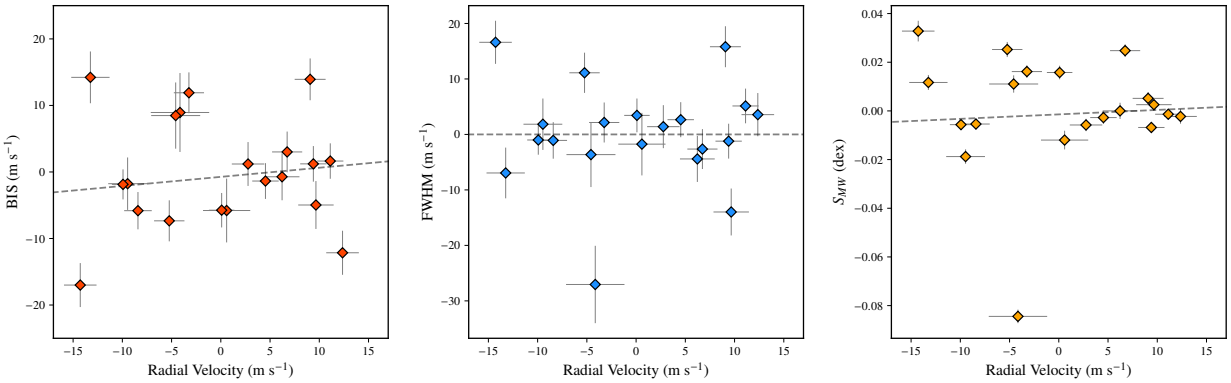

Figure 4.2: Left to right: correlations between BIS, cross-correlation function FWHM, S-index and radial velocities after subtraction of their mean, respectively. The first two are obtained from DRS and the latter is derived from the HARPS spectra using the HARPS-TERRA algorithm. On each plot, the dashed line represents a linear fit between the activity index and radial velocity. All three plots shows no strong evidence for correlation, although outliers are seen in the FWHM and S_{MW}.

We extracted the radial velocity measurements using the HARPS-TERRA package (Anglada-Escudé et al. 2012). The algorithm creates a high signal-to-noise template by combining all the observed spectra, based on their signal-to-noise ratio, and then it recomputes the radial velocity of a given observation by matching each individual spectrum with the template. One advantage for choosing HARPS-TERRA is that RVs are computed for every echelle order so it is relatively easy to find the orders with most of the RV information, discarding contaminated or low S/N orders. In this case, we rejected the 22 bluest orders, and considered only from order 23 to 72 as they produced lowest errors and smallest RMS in the RVs. The software does not compute the BIS nor FWHM of the CCF, which are taken directly from the DRS using a G2 mask. TERRA does compute activity indicators in the form of S-indices directly from each observed spectrum. The S-index is measured from the cores of the Calcium II H & K lines ($\lambda_H = 3933.664$ Å, $\lambda_K = 3968.470$ Å) and compared with the flux on adjacent chunks in the continuum, following the prescription from Lovis et al. (2011) and it is calibrated to the Mt. Wilson system (S_{MW}), serving as a direct proxy to monitor the chromospheric activity of the star. Uncertainties in BIS are taken as twice the internal RV errors and the FWHM error are 2.35 times the RV uncertainties (see Zechmeister et al. 2013; Santerne et al. 2015). The results are shown in Table 4.2.

Figure 4.2 shows the correlations between radial velocities and activity indicators, BIS, FWHM CCF and S_{MW}, from left to right, respectively. No significant correlations are seen between the radial velocities and the activity indicators. However, we note one outlier point in the FWHM and S-index, which was related with an observation acquired under poor weather conditions at the beginning of the observing run in April 2019.

We computed the Generalized Lomb-Scargle periodogram[3] (GLS; Zechmeister & Kürster 2009) of the HARPS Doppler measurements and activity indicators. As shown in Figure 4.3, the GLS periodogram of the HARPS RVs shows a significant peak at the orbital period of the transiting planet (2.11 d) with a false-alarm probability FAP $< 0.1\%$. We note that the secondary peak with FAP $< 1\%$ (P=0.7d) is the alias of the orbital period due to the sampling frequency. The periodograms of the HARPS activity indicators show neither a significant peak matching the one found in the RVs, nor any other significant peaks (Figure 4.3).

4.3 Stellar Parameters

We first estimated the stellar parameters[4] by combining the HARPS spectra into a high-S/N ratio spectrum and fed that into the spectral classification and stellar parameter estimation software package `SPECIES` (Soto & Jenkins 2018). For a more detailed explanation and outputs from this code, the reader is referred to Díaz et al. (2018) and Soto & Jenkins (2018).

We also analyzed the combined HARPS spectrum using both Spectroscopy Made Easy (`SME`, version 5.22; Valenti & Piskunov 1996a,b; Piskunov & Valenti 2017), and the empirical package `SpecMatch-Emp` (Yee et al. 2017). We followed the same procedures outlined in, e.g., Fridlund et al. (2017), Persson et al. (2018, 2019), Gandolfi et al. (2019). The two methods provide consistent results within 1–2 σ, which are also in agreement with those obtained with `SPECIES`. In particular, the age of the star was determined by isochrone fitting according to the method described in `SPECIES`.

[3] `astropy.timeseries.LombScargle()`,`https://docs.astropy.org/en/stable/timeseries/lombscargle.html`.

[4] Including $v\,sin$(i) and $v_{\rm mac}$

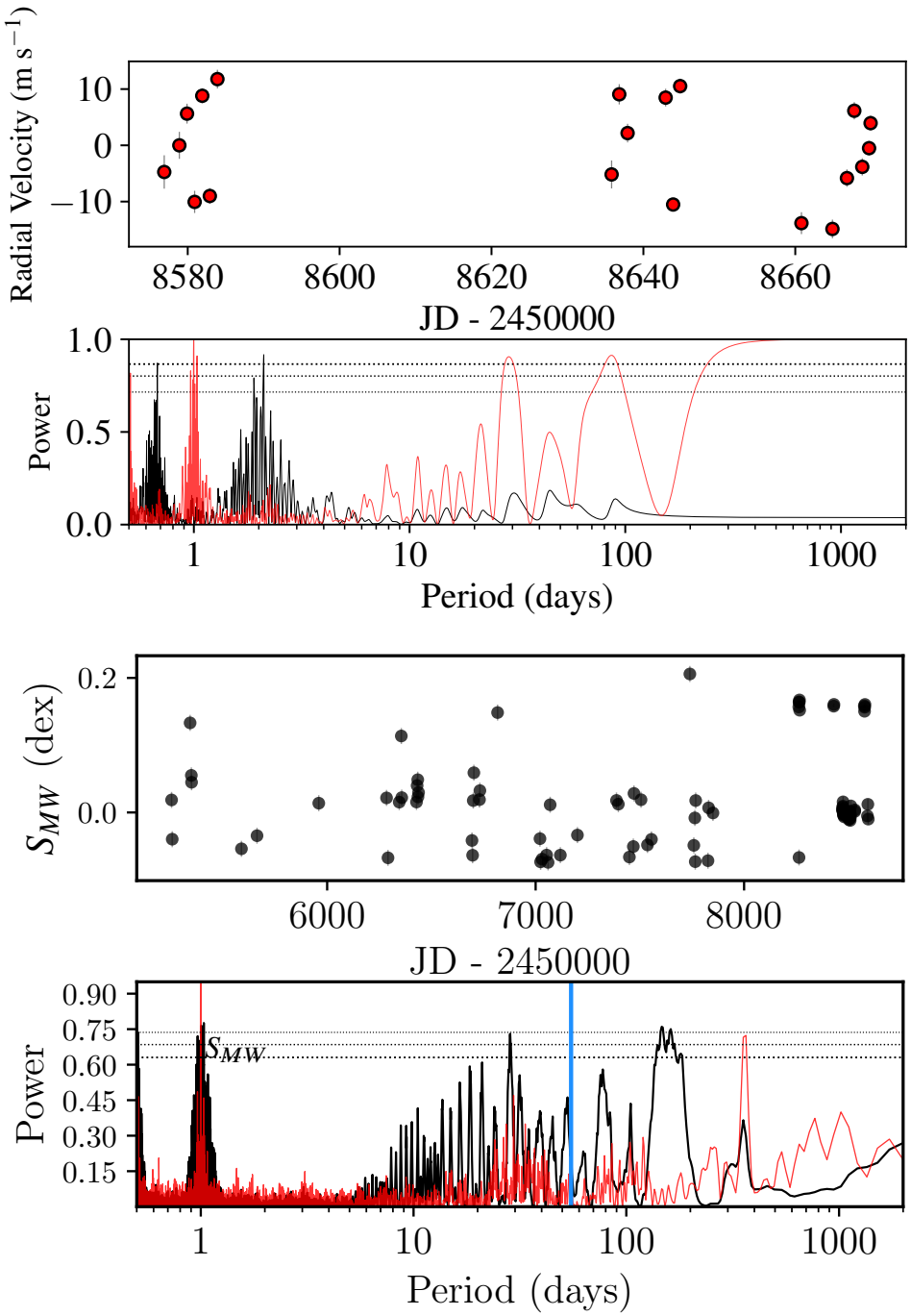

Figure 4.3: Top panels: Time series showing the radial velocities from the HARPS follow-up observations. Generalized Lomb-Scargle periodogram of the radial velocities. Red power spectrum shows the window function. Bottom panels: Same as top panel but for the activity indices obtained with HARPS: BIS, FWHM and S-index, respectively. Horizontal lines, from bottom to top on each periodogram, represent the 10, 1 and 0.1% significance levels estimated via 5000 bootstrap samples. Vertical line on each plot marks the position of the 2.11-day planet candidate signal present in the radial velocity.

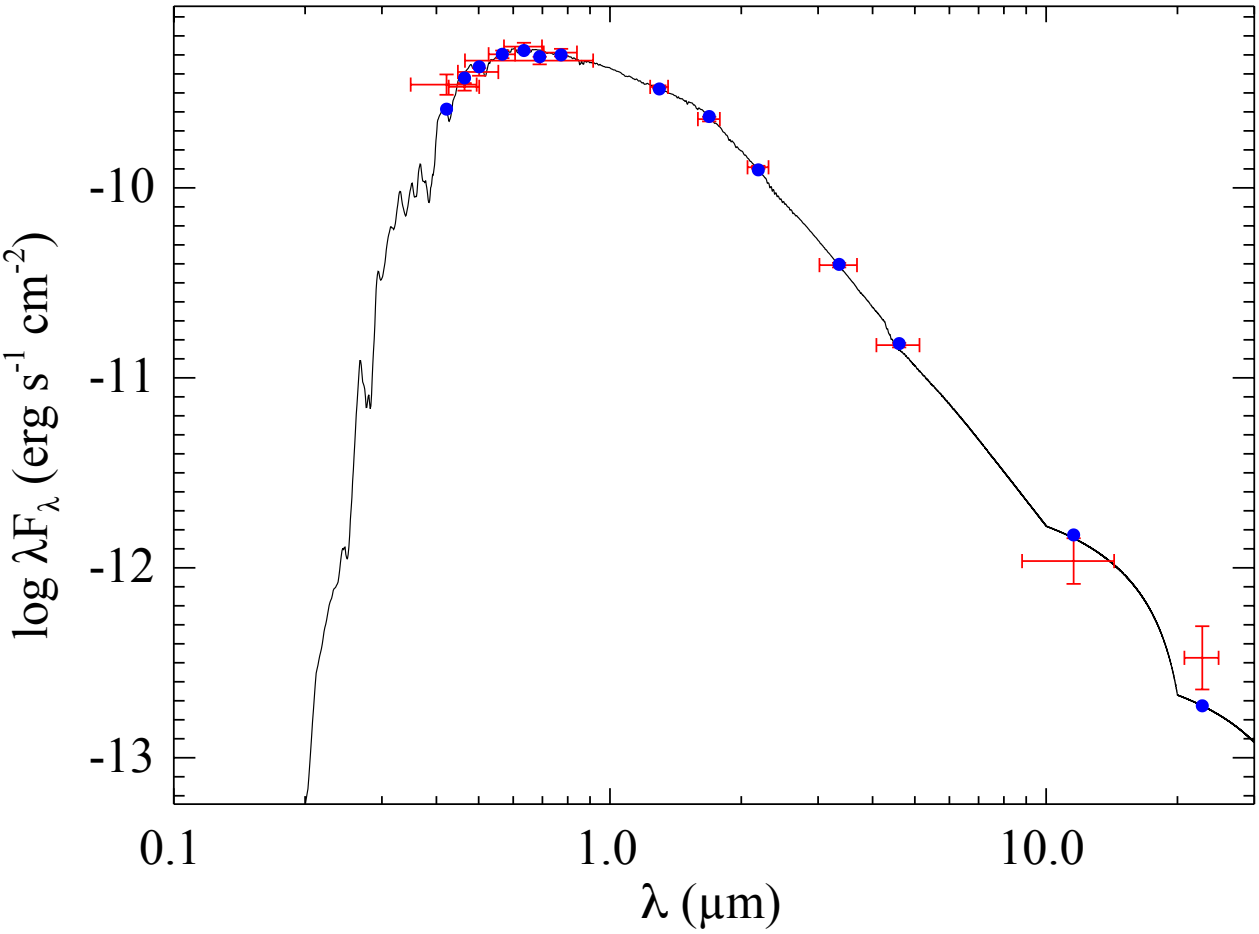

Figure 4.4: Spectral energy distribution of TOI-132. The blue points are the predicted integrated fluxes and the red symbols are the observed values at the corresponding passbands, where the horizontal bars represent the effective width of the passband and the vertical errors represent the 1σ uncertainties. The best-fit Kurucz atmospheric model for TOI-132 is shown by the black solid line.

Table 4.2: HARPS Radial Velocities and spectral activity indices of TOI-132

BJD	RV	σRV	S_{MW}	σS_{MW}	FWHM	σFWHM	BIS	σBIS
(- 2450000)	(m s^{-1})	(m s^{-1})	(dex)	(dex)	(km s^{-1})	(m s^{-1})	(m s^{-1})	(m s^{-1})
8576.90725	-4.737	2.967	0.056	0.003	6.885	16.180	2.967	5.933
8578.89655	0.000	2.398	0.128	0.004	6.911	16.240	2.398	4.797
8579.90764	5.631	1.765	0.140	0.003	6.908	16.234	1.765	3.531
8580.90988	-10.056	1.972	0.121	0.003	6.914	16.248	1.972	3.943
8581.91433	8.808	1.338	0.133	0.002	6.911	16.241	1.338	2.675
8582.91045	-9.005	1.402	0.135	0.002	6.911	16.241	1.402	2.803
8583.90870	11.771	1.656	0.138	0.003	6.916	16.252	1.656	3.312
8635.81477	-5.174	2.488	0.151	0.004	6.909	16.235	2.488	4.977
8636.82174	9.069	1.800	0.143	0.003	6.898	16.211	1.800	3.599
8637.91868	2.175	1.649	0.134	0.003	6.914	16.247	1.649	3.297
8642.93057	8.481	1.571	0.145	0.003	6.928	16.281	1.571	3.142
8643.91730	-10.522	1.129	0.134	0.002	6.911	16.242	1.129	2.257
8644.84072	10.526	1.331	0.139	0.002	6.917	16.256	1.331	2.662
8660.81222	-13.834	1.945	0.152	0.003	6.905	16.228	1.945	3.891
8664.89377	-14.864	1.652	0.173	0.004	6.929	16.283	1.652	3.305
8666.80357	-5.826	1.542	0.165	0.003	6.923	16.270	1.542	3.084
8667.76863	6.145	1.530	0.165	0.003	6.910	16.238	1.530	3.061
8668.82036	-3.829	1.534	0.156	0.003	6.914	16.249	1.534	3.067
8669.71698	-0.505	1.294	0.156	0.003	6.916	16.252	1.294	2.588
8669.91776	3.943	1.344	0.137	0.003	6.915	16.250	1.344	2.687

Table 4.3: Below are the priors used for TOI-132 for the *final* joint analysis fit using `juliet`. As a reminder, $p = R_p/R_*$ and $b = (a/R_*)\cos(\mathrm{i}_p)$, where R_p is the planetary radius, R_* the stellar radius, a the semi-major axis of the orbit and i_p the inclination of the planetary orbit with respect to the plane of the sky. e and ω are the eccentricity and argument of periastron of the orbits. The prior labels of $\mathcal{N}$, $\mathcal{U}$, and $\mathcal{J}$ represent normal, uniform, and Jeffreys distributions. See text for explanations about other parameters.

Parameter name	Prior	Units	Description
Parameters for planet b			
P_b	$\mathcal{N}(2.10937, 0.001)$	days	Period.
$T_{0,b} - 2458000$	$\mathcal{N}(337.451, 10)$	days	Time of transit-center.
$r_{1,b}$	$\mathcal{U}(0, 1)$	—	Parametrization for p and b[1].
$r_{2,b}$	$\mathcal{U}(0, 1)$	—	Parametrization for p and b[1].
a_b	$\mathcal{U}(4.5, 7.0)$	—	scaled semi-major axis.
K_b	$\mathcal{U}(1, 100)$	m s^{-1}	Radial-velocity semi-amplitude.
e_b	$\mathcal{U}(0, 1)$	—	eccentricity.
ω_b	$\mathcal{U}(0, 359)$	deg	argument of periastron.
Parameters for *TESS*			
D_{TESS}	1.0 (Fixed)	—	Dilution factor for *TESS*.
M_{TESS}	$\mathcal{N}(0, 1)$	ppm	Relative flux offset for *TESS*.
$\sigma_{w,\mathrm{TESS}}$	$\mathcal{J}(0.1, 100)$	ppm	Extra jitter term for *TESS* lightcurve.
$q_{1,\mathrm{TESS}}$	$\mathcal{U}(0, 1)$	—	Quadratic limb-darkening parametrization.
$q_{2,\mathrm{TESS}}$	$\mathcal{U}(0, 1)$	—	Quadratic limb-darkening parametrization.
Parameters for LCOGT			
D_{LCOGT}	1.0 (Fixed)	—	Dilution factor for LCOGT.
M_{LCOGT}	$\mathcal{N}(0, 1)$	ppm	Relative flux offset for LCOGT.
$\sigma_{w,\mathrm{LCOGT}}$	$\mathcal{J}(0.1, 100)$	ppm	Extra jitter term for LCOGT lightcurve.
$q_{1,\mathrm{LCOGT}}$	$\mathcal{U}(0, 1)$	—	Quadratic limb-darkening parametrization.
$q_{2,\mathrm{LCOGT}}$	$\mathcal{U}(0, 1)$	—	Quadratic limb-darkening parametrization.
Parameters for HARPS			
μ_{HARPS}	$\mathcal{N}(-0.6, 1.)$	m s^{-1}	Radial velocity zero-point (offset).
$\sigma_{w,\mathrm{HARPS}}$	$\mathcal{J}(0.1, 10)$	m s^{-1}	Extra jitter term for HARPS radial velocities.

We note that, while there is no reason to prefer one set of spectroscopic parameter estimates over the others, we adopted the results derived with `SPECIES` for the subsequent analyses presented in this work.

We performed an analysis of the broadband spectral energy distribution (SED) of the star together with the *Gaia* DR2 parallaxes (adjusted by +0.08 *mas* to account for the systematic offset reported by Stassun & Torres 2018), in order to determine an empirical measurement of the stellar radius, following the procedures described in Stassun & Torres (2016) and Stassun et al. (2017, 2018a). We retrieved the $B_T V_T$ magnitudes from *Tycho-2*, the $BVgri$ magnitudes from APASS, the JHK_S magnitudes from *2MASS*, the W1–W4 magnitudes from *WISE*, and the G magnitude from *Gaia*. Together, the available photometry spans the full stellar SED over the wavelength range 0.2–22 μm (see Figure 5.1).
We performed a fit using Kurucz stellar atmosphere models, with the effective temperature ($T_{\rm eff}$) and metallicity ([Fe/H]) and surface gravity ($\log g$) adopted from the spectroscopic analysis of `SPECIES`. The only free parameter is the extinction (A_V), which we restricted to the maximum line-of-sight value from the dust maps of Schlegel et al. (1998). The resulting fit shown in Figure 5.1, gives a reduced χ^2 of 2.4 and best-fit $A_V = 0.03 \pm 0.01$. Integrating the (unreddened) model SED, it gives the bolometric flux at Earth, $F_{\rm bol} = 7.492 \pm 0.087 \times 10^{-10}$ erg s^{-1} cm^{-2}. Taking the $F_{\rm bol}$ and $T_{\rm eff}$ together with the *Gaia* DR2 parallax, gives the stellar radius, $R_\star = 0.90 \pm 0.02\, R_\odot$. Finally, we can use the empirical relations of Torres et al. (2010) and a 6% error from the empirical relation itself to estimate the stellar mass, $M_\star = 0.97 \pm 0.06\, M_\odot$; this, in turn, together with the stellar radius provides an empirical estimate of the mean stellar density $\rho_\star = 1.89 \pm 0.15$ g cm^{-3}. We note the small errorbars on both stellar mass and radius come directly from propagation of uncertainties in $T_{\rm eff}$, $F_{\rm bol}$, and parallax. In this case, the fractional errors are of order $\sim$1%, $\sim$ 1% and $\sim$0.5%, respectively. Then, the uncertainty in stellar radius is dominated by the $T_{\rm eff}$ error, in this case that implies an error of $\sim$2% (see Table 4.1).

4.4 Speckle Imaging

The relatively large 21-arcsec pixels of *TESS* can result in contamination from companion stars or nearby sources. The additional light from these can dilute the planetary transit, resulting in an underestimated planet radius. We searched for nearby sources with speckle imaging with HRCam on the 4.1-m Southern Astrophysical Research (SOAR) telescope (Tokovinin et al. 2018) on 2018 September 25 UT. From these observations, a potential companion star was detected at low-significance. The purported star was located near the first diffraction ring of the primary star, at 0.079 arcsec (and a projected distance of $\sim$12 AU), a similar position as optical ghosts which can occasionally appear in the speckle imaging during periods of low wind. This triggered a warning as the flux contamination due to the companion (Δm$\sim$2.6 mag) would have not been negligible for the spectroscopic observations given that the diameter of the fibers on HARPS is $\sim$1 arcsec, meaning that the suspected companion was inside the aperture of the fiber. Upon visual inspection of the CCF and the individual spectra, we could not see evidence for such a contamination. The system was observed again on 2019 May 18 UT in excellent conditions, and the possible companion star was not detected. The 5-σ detection sensitivity and auto-correlation function of the later observation are shown in Figure 4.5.

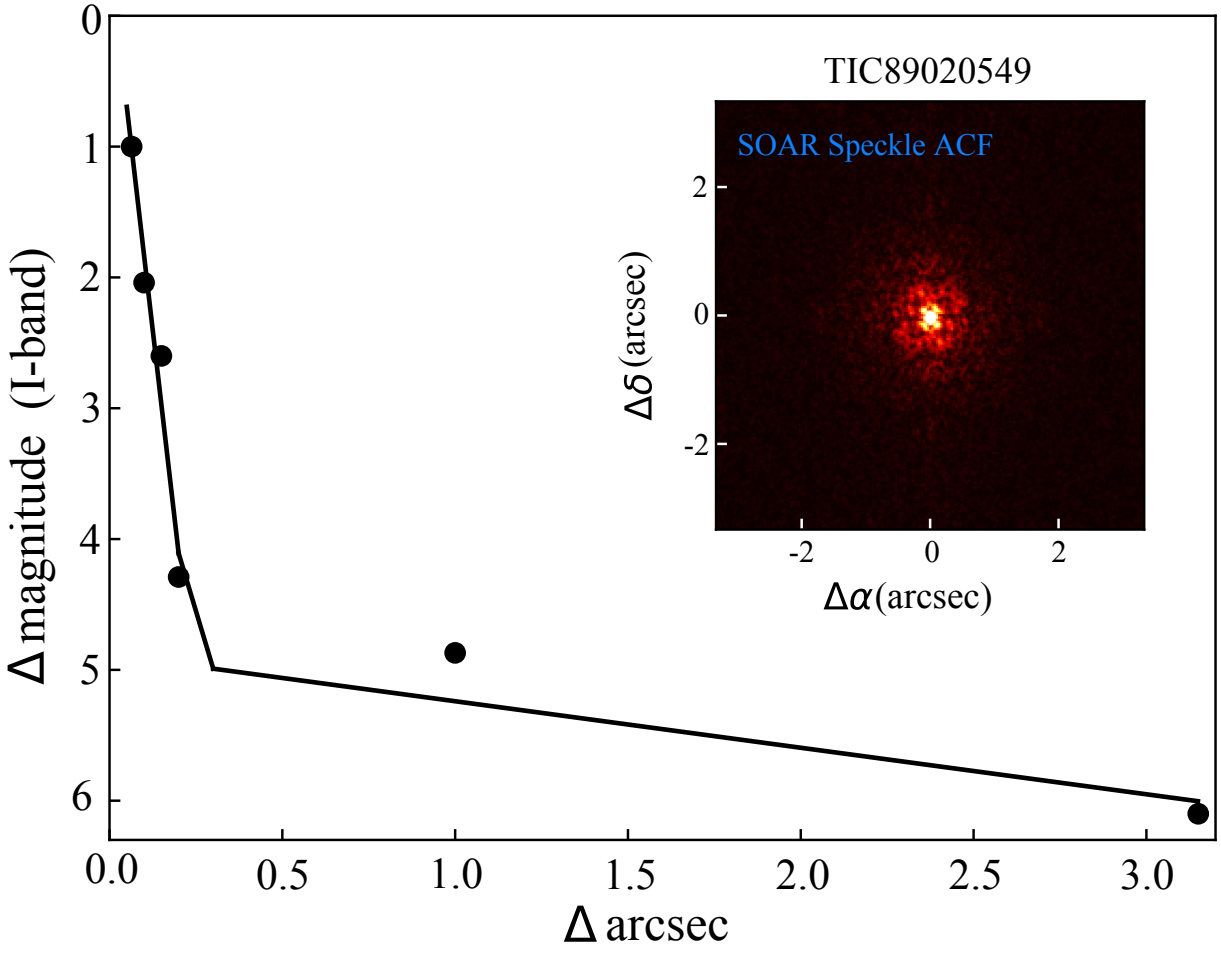

Figure 4.5: Speckle image of TOI-132 obtained with SOAR. Inset on the top right corner shows a preview of the ACF.

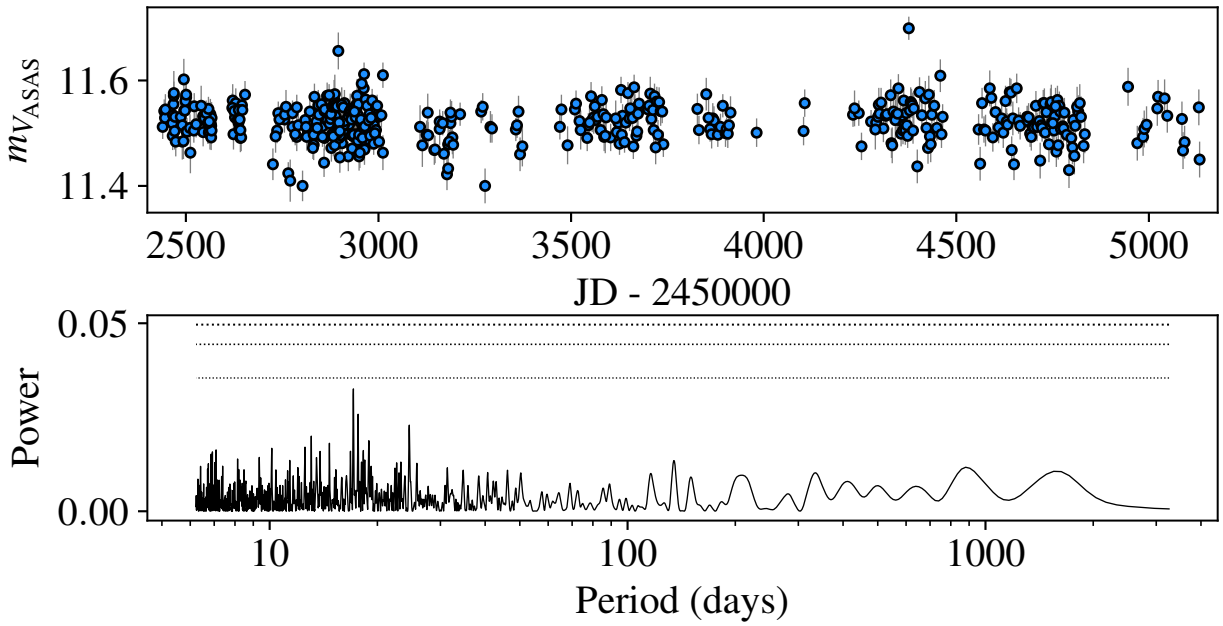

Figure 4.6: ASAS V-band photometry of TOI-132 to search for additional sources of periodicity in the star. The bottom plot shows the Generalized Lomb-Scargle periodogram of the time series. Horizontal lines, from bottom to top, represent the 10, 1 and 0.1% significance levels estimated via 5000 bootstrap samples.

4.5 ASAS Photometry

We analyzed photometry from the All-Sky Automated Survey (ASAS, Pojmanski 1997) to search for stellar rotational periods. There are 694 available photometric measurements spanning 8.9 years, from November 2000 to December 2009. The selection of the best aperture was made choosing the time series with the lowest Median Absolute Deviation (MAD). We discarded 129 points that were flagged as bad datapoints, including only 565 measurements with either "A" or "B" quality. Figure 5.8 shows the photometric time series after removing outliers and bad data and the GLS.

From the power spectrum in the periodogram the highest power is found to be at 17.138 days. We estimated the 10, 1 and 0.1% significance level by running 5000 bootstrap samplings using the implementation available in the PYTHON module `astropy.stats.false_alarm_probability()`[5]. Although the highest peak in the GLS periodogram is noticeable and unique, its significance is below the 10% level, as seen from the bottom panel in the figure. We note that the highest cadence in the photometry is ∼1 day, however the sampling of the time series is very sparse, making the detection of rotation periods on short time scales of ∼10-20 days difficult.

4.6 Joint Analysis

We modeled the radial velocities and the photometry using the `juliet`[6] package (Espinoza et al. 2019a). Table 5.7 shows the priors used in the analysis. We set up the initial priors for the period of the candidate and the time of transit (T_0) using the reported values in the *TESS* DV report document for TOI-132.

Preliminary analysis was done by making use of `Systemic Console v2` (Meschiari et al. 2009). We analyzed the radial velocities only to get an initial rough estimate of both instrumental and orbital parameters of the system such as the velocity semi-amplitude, eccentricity and minimum mass of the planet. The period and transit time were constrained using the updated values provided by *TESS*. Initial results for a 1-planet model with eccentricity fixed at zero, yields an RMS∼2.7 m s^{-1}. Letting eccentricity and argument of periastron as free parameters the best-fit model RMS goes down to ∼2.5 m s^{-1} and e∼0.17.

We then performed further analyses considering two scenarios (circular and eccentric) with `juliet`. This package has been proven to be an excellent tool for analyzing both photometry and radial velocities using a joint model (see e.g., Brahm et al. 2019; Espinoza et al. 2019b; Kossakowski et al. 2019). In short, the code uses `batman` (Kreidberg 2015) to model the transit data and `radvel` (Fulton et al. 2018) to model the radial velocities, and in order to estimate the Bayesian log-evidence, ln$Z$, for model comparison we used the option of the Dynamic Nested Sampling algorithm that the `dynesty` (Speagle & Barbary 2018; Speagle 2019) package provides. We note that, while `juliet` has the option to include Gaussian Processes to model the lightcurve, radial velocities or both, we did not set this option as there was no evidence of additional variability in the `PDCSAP_FLUX`-corrected lightcurve (see Figure 4.1).

We also used the parametrization described in Espinoza (2018) that allows an efficient way to sample the impact parameter, b, and the planet-to-star radius ratio, p, where only values that are

[4] MAD = median($|X_i - \bar{X}|$)/0.6745

[5] `https://docs.astropy.org/en/stable/timeseries/lombscargle.html`

[6] `https://github.com/nespinoza/juliet`

physically plausible in the (p, b) plane are sampled via the r_2 and r_2 coefficients (Espinoza 2018). For the limb-darkening coefficients, we use the parametrization of Kipping (2013) for two parameter laws. Speckle images obtained for TOI-132 rules out the possibility of significant nearby sources of light. Therefore, we fixed the dilution factor to a value of 1 for the photometric datasets. The priors and boundaries for the parameters used in the joint analysis are listed in Table 5.7.

We set up two different runs, first by fixing eccentricity to zero, and another treating it (along with ω) as free parameter. Comparing the evidences from the circular ($\ln Z$=89705.63) and eccentric model ($\ln Z$=89706.85) we obtain $\Delta \ln Z = 1.22$ which suggests weak evidence the latter is preferred over the circular model according to the model selections criteria and thresholds described in Espinoza et al. (2019a). The joint model results are shown in Figure 4.8 and the best-fit, or most probable parameters given the data are listed in table 5.8. The quoted values are the median value from the posterior distribution.

As a sanity check, we also performed an independent joint analysis using the PYTHON/FORTRAN software suite `pyaneti` (Barragán et al. 2019a). Results are consistent with those obtained with `juliet` well within the nominal error bars.

Using the luminosity of the host star, we could retrieve the incident flux on TOI-132 b by using the semi-major axis from our joint model. We estimated that the insolation of TOI-132 b is $S_{\rm p} = 860\, S_{\oplus}$.

In order to estimate the average equilibrium temperature of the planet, considering the physical properties of TOI-132 b we assumed a Bond albedo of $A_B = 0.31$, that corresponds to the value accepted for Neptune. Then

$$T_{\rm eq} = T_* \sqrt{\frac{R_*}{2a}} (1 - A_B)^{\frac{1}{4}} \tag{4.1}$$

yields an equilibrium temperature of $T_{\rm eq} = 1395^{+52}_{-72}\, K$ for the planet.

Table 4.4: Planetary Properties of TOI-132 b

Property	Value
Fitted Parameters	
P (days)	$2.1097019^{+0.000012}_{-0.000011}$
T_0 (BJD - 2450000)	$8333.23095^{+0.00094}_{-0.00096}$
a/R_*	$6.362^{+0.413}_{-0.627}$
b	$0.533^{+0.124}_{-0.137}$
K (m s^{-1})	$11.38\ ^{+0.84}_{-0.85}$
$\mathrm{i_p}$ (deg)	$85.03^{+1.30}_{-1.84}$
e	$0.059^{+0.050}_{-0.037}$
ω (deg)	$125.88^{+57.23}_{-38.05}$
Derived Parameters	
M_p ($M_\oplus$)	$22.40^{+1.90}_{-1.92}$
R_p ($R_\oplus$)	$3.42^{+0.13}_{-0.14}$
a (AU)	$0.026^{+0.002}_{-0.003}$
ρ_p (g cm^{-3})	$3.08^{+0.44}_{-0.46}$
T^1_eq (K)	1395^{+52}_{-72}
Instrumental Parameters	
M_TESS (ppm)	$-0.000069^{+0.000011}_{-0.000012}$
$\sigma_{w,\mathrm{TESS}}$ (ppm)	$10.58^{+27.14}_{-8.14}$
$q_{1,\mathrm{TESS}}$	$0.361^{+0.344}_{-0.242}$
$q_{2,\mathrm{TESS}}$	$0.331^{+0.342}_{-0.223}$
M_LCOGT (ppm)	$-0.000057^{+0.000060}_{-0.000057}$
$\sigma_{w,\mathrm{LCOGT}}$ (ppm)	$462.35^{+72.73}_{-73.70}$
$q_{1,\mathrm{LCOGT}}$	$0.426^{+0.309}_{-0.262}$
$q_{2,\mathrm{LCOGT}}$	$0.284^{0.296}_{-0.186}$
μ_HARPS (m s^{-1})	$-0.18^{+0.51}_{-0.55}$
$\sigma_{w,\mathrm{HARPS}}$ (m s^{-1})	$2.00^{+0.72}_{-0.64}$

[1]Estimated using a Bond albedo of 0.31 (see text).

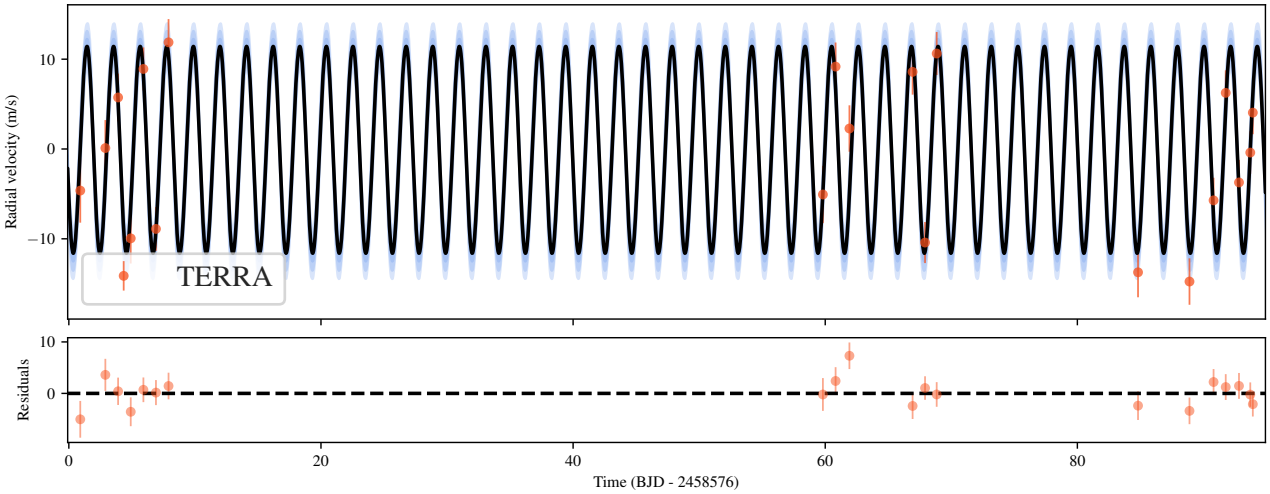

Figure 4.7: Results from the joint fit for the 1-planet model. HARPS-TERRA radial velocities and best-fit Keplerian model (solid curve) the bands around it show 68%, 95% and 99% posterior credibility bands.

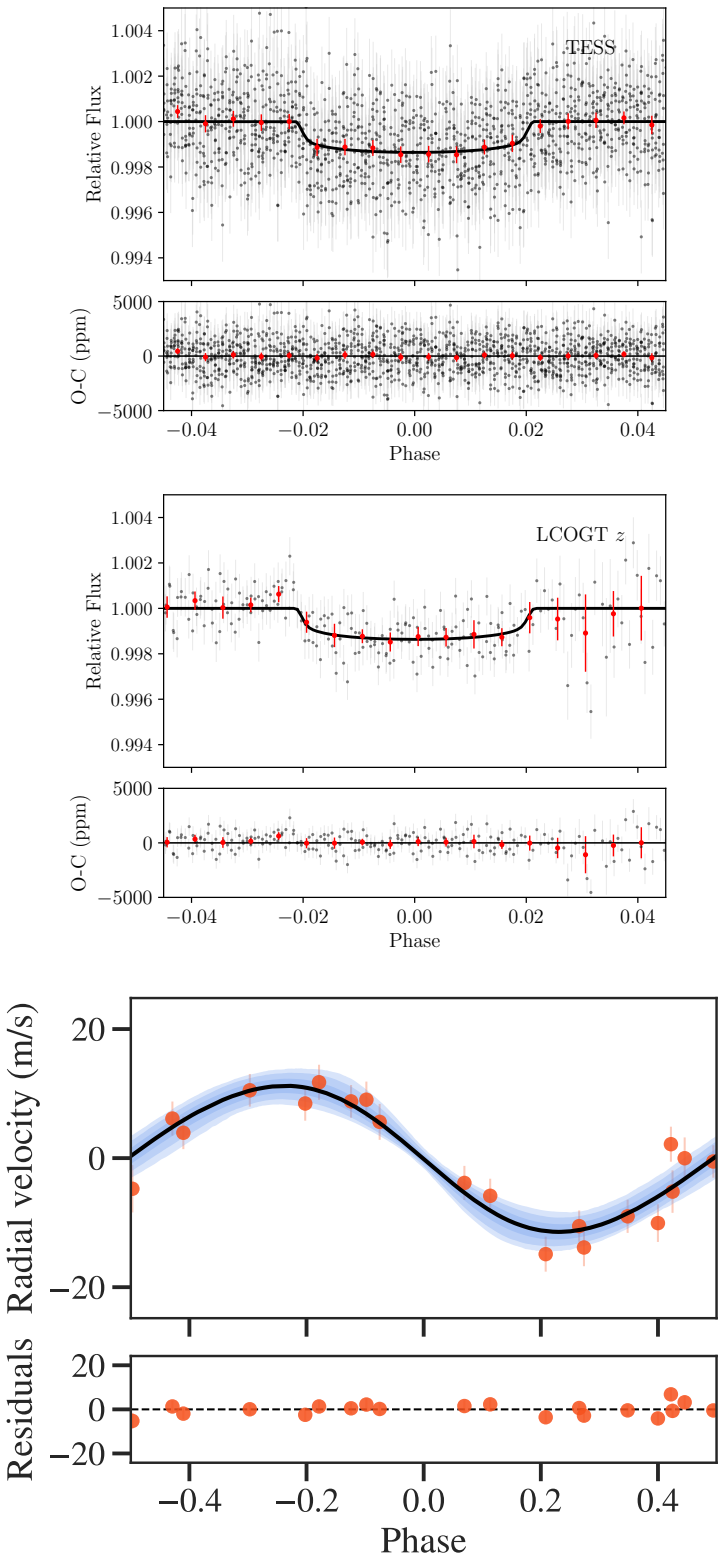

Figure 4.8: Results from the joint fit for the 1-planet model. *Top panels: TESS* photometry (left) and LCOGT z-short photometry (right) phase-folded to the 2.109 d period of TOI-132 b along with best-fit transit model from the joint fit. Red points show the binned photometry in phase bins of 0.005. *Bottom panel:* phase-folded RVs from HARPS. The black line shows the model. Credibility bands are shown in the same way as in top panel. Best-fit parameters are the most probable parameters given the data and the quoted values are the median value from the posterior distribution. The error bars of both photometry and RV data include their corresponding jitter.

4.7 TTV Analysis

In order to search for possible Transit Timing Variations in TOI-132 b, we computed the individual transit time of each light curve using the `EXOFASTv2` code (Eastman et al. 2013; Eastman 2017). `EXOFASTv2` uses the Differential Evolution Markov chain Monte Carlo method (DE-MCMC) to derive the values and their uncertainties for the stellar, orbital and physical parameters of the system.

So as to obtain the transit time of each light curve, we fixed the stellar and orbital parameters to the values obtained from the global fit performed by `juliet`, except for the transit time and their baseline flux. If a planet follows strictly a Keplerian orbit, the transit time of a given epoch $T_c(E)$ is a linear function of the orbital period P:

$$T_c(E) = T_0 + P \times E \tag{4.2}$$

Where T_0 is a reference transit time and E is the number of epochs since T_0. The best-fit values for equation 4.2 from `juliet` are shown in Table 5.8 along with the planetary parameters fixed to compute the individual transit time.

Considering the theoretical and the observed transit times of the light curves, we obtained the TTV values for TOI-132 b presented in Figure 4.9. Even though the larger variation is about 22 minutes, we found no evidence of a clear periodic variation in the transit time. This outlier is probably induced by a gap in the light curve of epoch 5. The RMS variation from the linear ephemeris is $\sigma = 8.03$ min, however, the reduced chi-squared for this model is $\chi^2_{red} = 1.37$. This is an indicator that the transit times, considering their errors, fit well with the proposed linear ephemeris.

The lack of an additional RV signal as well as no evidence of a TTV signal for our given time-span of our transit data, suggest that there is no other close-in companion of TOI-132 b. These results also rule out additional planets in low-order resonant configurations with TOI-132 b. Nevertheless, further ground-based follow-up will be required to unveil the possible existence of companions in TOI-132.

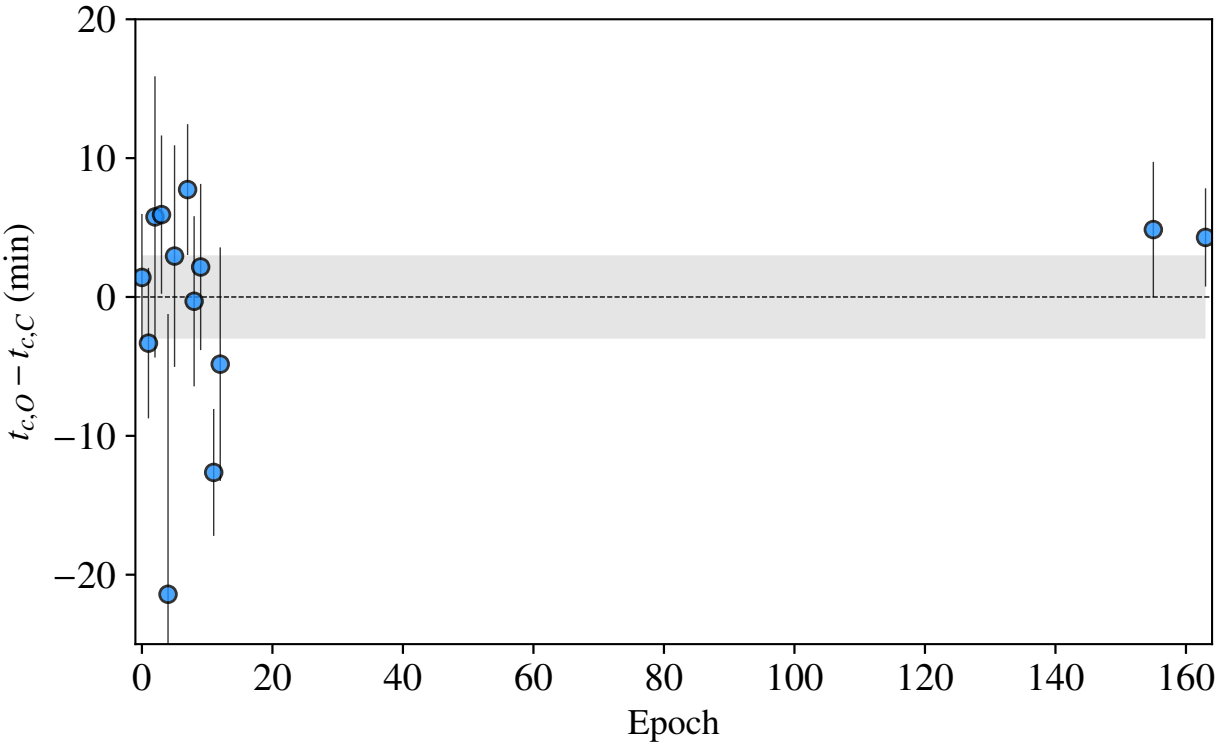

Figure 4.9: Observed minus computed mid-transit times of TOI-132 b . The residuals (TTV) of the transit times are shown considering the proposed linear ephemeris. The dashed line corresponds to zero variation and the grey area is the propagation of 1σ uncertainties, considering the optimal transit time from `EXOFASTv2`, and the period from `juliet`. The epoch 0 is the first transit observed by *TESS* and it is also the corresponding epoch of the optimal transit time. The TTV values shown in this plot fit accordingly with the proposed linear ephemeris ($\chi^2_{red} = 1.37$)

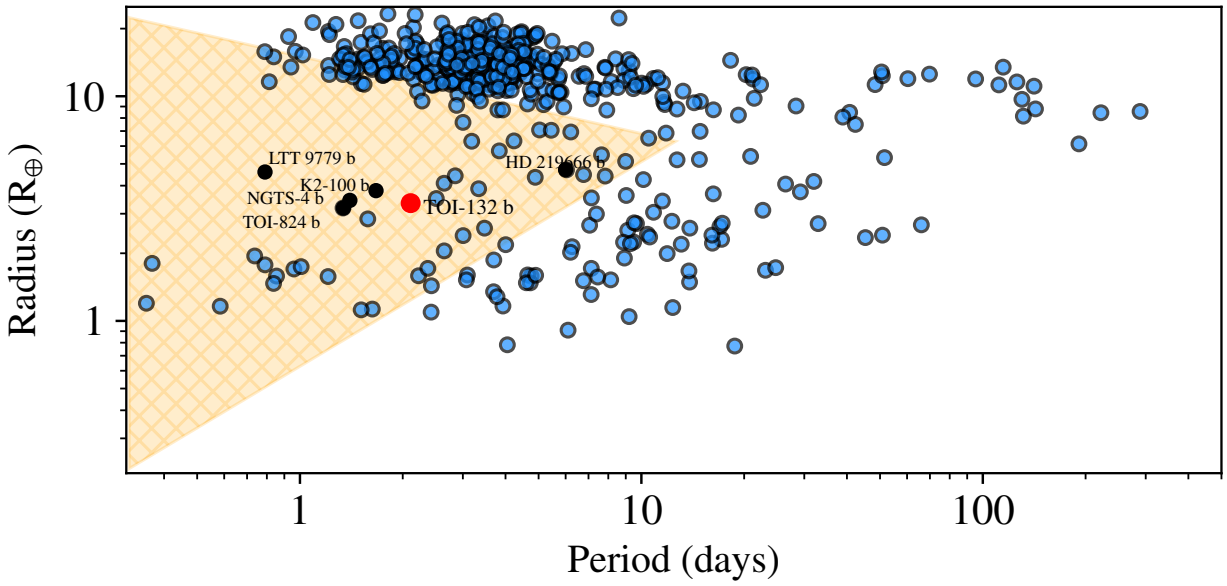

Figure 4.10: Period-radius diagram for planets whose radius has been measured with a precision better than 5%. We have included recent *TESS* discoveries (Burt et al. 2019, Nielsen et al. 2019, private communication). The shaded area indicates the Neptune-desert where the edges are defined by Mazeh et al. (2016). TOI-132 b is highlighted with a red circle, near the edge of the desert.

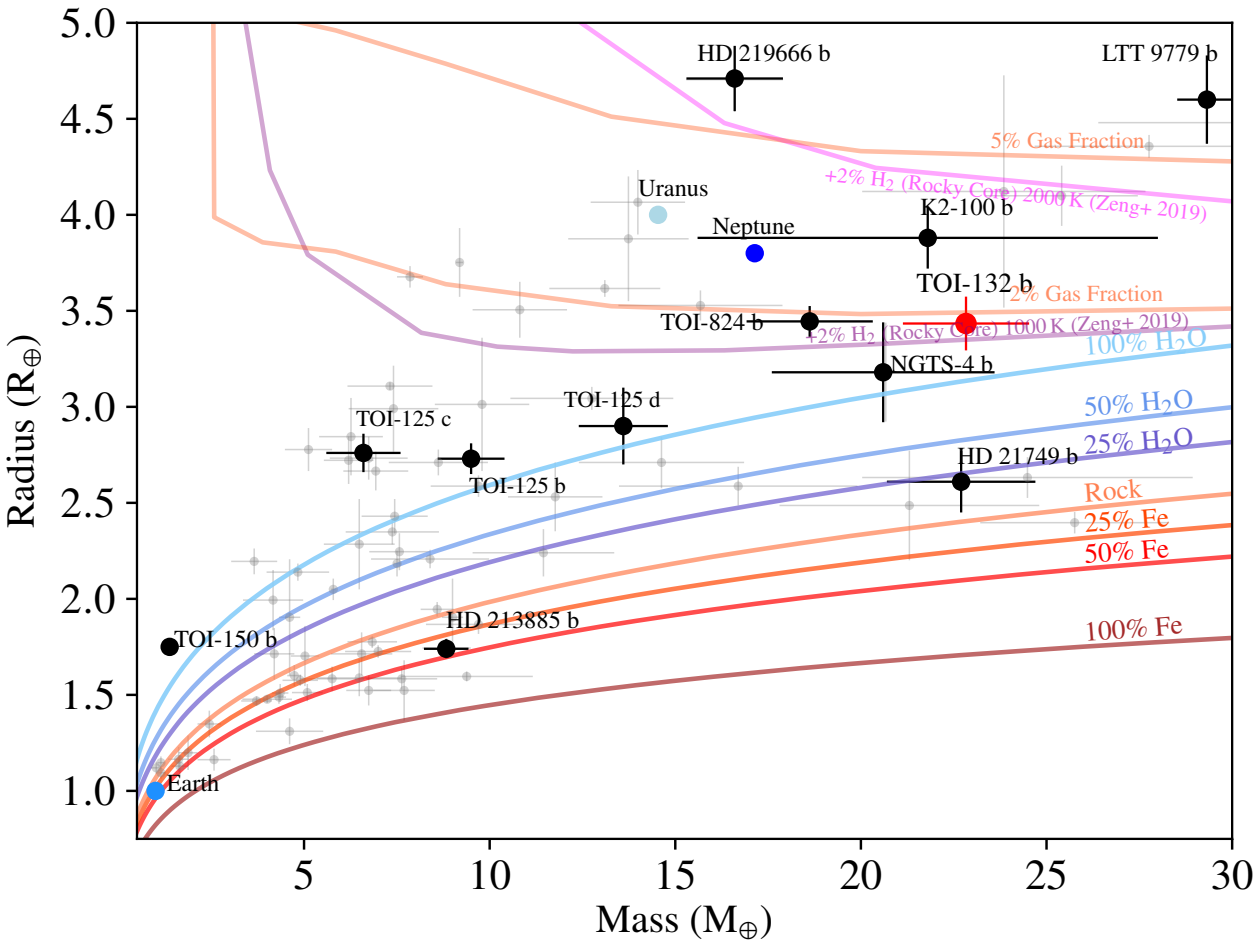

Figure 4.11: Mass-radius diagram for planets whose mass and radius have been measured with a precision better than 25% (gray circles) in the range $R_p < 5R_\oplus$ and $M_p < 30M_\oplus$, retrieved from the transiting planets catalog `TEPCat` (available at `https://www.astro.keele.ac.uk/jkt/tepcat/`, Southworth 2011). Black points show recent discoveries from *TESS*. TOI-132 b is shown with a red circle. Solid, colored lines show models for different compositions from Zeng et al. (2016) ranging from 100% iron core planet to 100% H_2O planet. Also two-layer models from Zeng et al. (2019) are shown for 2% H_2 envelopes at different temperatures (magenta, purple). Extended models from (Lopez & Fortney 2014) are shown for 95% and 98% core mass fraction, 6.2 Gyr (orange).

4.8 Discussion

By combining *TESS* space-based photometry with HARPS high-precision radial-velocity measurements, along with additional high-sensitivity ground-based photometric observations, we were able to confirm a short period, hot Neptune-like planet orbiting the nearby metal-rich G8V star TOI-132. The planet was found to have an orbital period of only 2.1 days, a radius of $3.42^{+0.13}_{-0.14}$ $R_{\oplus}$, and mass of $22.40^{+1.90}_{-1.92}$ $M_{\oplus}$, implying a density and equilibrium temperature of $3.08^{+0.44}_{-0.46}$ g cm^{-3} 1395^{+52}_{-72} K, respectively.

In Fig. 5.12 we can see that TOI-132 b is located in an underpopulated region of the mass-radius diagram. Of the relatively small number of known Neptune-like planets with well constrained properties, TOI-132 b stands out as bridging the gap between 100% water worlds and more typical Neptunes that have atmospheric mass fractions of ∼10%. The planet likely more closely resembles NGTS-4 b (West et al. 2019), which is shown in the figure despite the relatively high uncertainties measured for the planetary parametsers, or TOI-824 b (Burt et al. 2019, private communication). These three planets appear to have similar masses and radii, giving rise to similar densities and bulk compositions, which might indicate they share similar formation histories.

Moreover, it is interesting to mention the planet K2-100 b from the *K2* mission Mann et al. (2017). Recently characterized by (Barragán et al. 2019b), the planet consists of a young, inflated Neptune on a short period around a G-type star. TOI-132 b falls within the evolutionary range of K2-100 b after 5 Gyr. This may indicate in the past TOI-132 b could have shared similar characteristics to that of K2-100 b, and at some point given the strong stellar irradiation on TOI-132 b could have caused atmospheric loss we see in the present. Hence, TOI-132 b is an interesting target for atmospheric transit spectroscopy, to check for evidence of ongoing atmospheric loss through a wind.

While TOI-132 b is not as extreme in some respects as the recently discovered, first ultra hot Neptune LTT 9779 b (Jenkins et al. 2019), it is placed right at the edge of the Neptune desert. The survival of the planet's atmosphere can likely be understood based on its large core mass, and also the incompatibility with being composed of either 100% rock or water. This would imply that, at the present time, TOI-132 b could maintain some significant gaseous atmosphere. We employed a 1-D thermal evolution model (Lopez & Fortney 2014), and for an Earth-like rocky core we find a best-fit current day atmospheric mass fraction of $4.3^{+1.2}_{-2.3}$% gas, which can be retained with an initial envelope fraction of ∼ 9% at 10 Myr. We note here that rocky core likely consists of a combination of rock and iron even if the relative core mass fraction is not clear. Moreover, these results are model-dependent rather than being directly constrained by the data.

With the *Gaia* parameters from Table 4.1, we calculated the star's Galactic space motion. We used the `IDL` routine `calc_uvw`, based upon Johnson & Soderblom (1987) and the local standard of rest from Coşkunoğlu et al. (2011), we obtained (U,V,W)=(18.4 ± 0.2, -32.6 ± 0.4, 16.5 ± 0.4) km s^{-1}. Per the methodology of Reddy et al. (2006), this corresponds to a 98% probability that TOI-132 belongs to the Galactic thin disk, which is consistent with the relatively high [Fe/H] we measured for the star.

The relatively high metallicity of the host star can also help to explain the large core mass fraction of the planet. Such metal-rich disks can quickly build up high-mass cores that can accumulate large fractions of gas before the disk is dispersed on timescales of ∼5−10 Myrs (Baraffe et al. 2010; Mulders 2018). Indeed, we may expect more cores to have been formed in this process, possibly

influencing the migration history of TOI-132 b, and therefore future precision radial-velocity measurements should be sought to search for the presence of a more rich planetary system.

Chapter 5

A 55-day period dense Neptune transiting the bright star HD 95338

Based on the results published in Díaz, M. R., et al., *The Magellan/PFS Exoplanet Search: A 55-day period dense Neptune transiting the bright (V=8.6) star HD 95338*, 2020, MNRAS, 496, 4330.

In this chapter we introduce HD 95338 b, a super-Neptune planet detected using precision RVs as part of the Planet Finder Spectrograph (PFS; Crane et al. 2006, 2008, 2010) long term planet search project, and which we found to transit after analyzing the *TESS* lightcurve. HD 95338 b is the first single-transit planet candidate from TESS discovered with a period larger than 27 days (the time baseline of the TESS data series). HD 95338 was also observed by the Transiting Exoplanet Survey Satellite (*TESS*), and we identify a clear single transit at the period corresponding to the signal detected in the radial velocity data. Follow-up observations with HARPS also confirm the presence of the periodic signal in the combined data. A Markov Chain Monte Carlo period search on the velocities allows strong constraints on the expected transit time, matching well the epoch calculated using *TESS*. A joint fit model yields an absolute mass of $39.43^{+6.04}_{-4.13} M_\oplus$ and a radius of $3.98^{+0.09}_{-0.08}\ R_\oplus$ which translates to a density of $3.41^{+0.56}_{-0.40}$ g cm^{-3} for the planet. Given the planet mass and radius, structure models suggest it is fully composed of ice. HD 95338 b is one of the most dense Neptune planets yet detected, indicating a heavy element enrichment of ∼90% ($\sim 35\, M_\oplus$). This system presents a unique opportunity for future follow-up observations that can further constrain structure models of cool gas giant planets.

5.1 Spectroscopic Observations

High-precision Doppler measurements of HD 95338 were acquired using PFS mounted on the 6.5 m Magellan II (Clay) telescope at Las Campanas Observatory, and the High Accuracy Radial velocity Planet Searcher (HARPS; Pepe et al. 2002b) installed on the ESO 3.6 m telescope at La Silla Observatory.

5.1.1 PFS

Observations were carried out using PFS between February 26 2010 and May 25 2018, as part of the Magellan Exoplanet Long Term Survey (LTS). PFS uses an iodine cell for precise RV measurements and it delivers a resolving power of R ∼80,000 in the iodine region when observing with the 0.5"×2.5" slit. Iodine-free template observations were acquired with the 0.3"×2.5" slit at a resolving power of R ∼127,000. 52 observations were acquired using an average of 540 s of exposure time yielding a mean radial velocity uncertainty of 1.13 m $s^{-1}$and a median SNR∼144.

PFS was upgraded with a new CCD detector in 2017. The new CCD is a 10k×10k sensor and has smaller pixels, which improves the line sampling in the spectra. In addition, regular LTS stars are now observed using the 0.3"×2.5" slit, therefore improving the resolution. The data using this new setup is labeled as PFS2 and includes 31 observations. For this upgraded setup, the mean exposure time used was 485 s for each observation giving rise to a mean radial velocity uncertainty of 0.87 m $s^{-1}$for a median SNR∼74. The radial velocities are computed with a custom pipeline following the procedure outlined by Butler et al. (1996). They are listed in Table 5.1 and 5.2.

The spectral wavelength range in PFS covers the Ca II H & K lines, enabling the possibility of deriving S-indices to monitor the stellar chromospheric activity. S-indices are derived using the prescription outlined by Baliunas et al. (1996) and Boisse et al. (2011). In general, authors determine their S-index errors based on photon noise on the CCD (Boisse et al. 2011; Lovis et al. 2011; Jenkins et al. 2017). In our case, however, doing so can grossly underestimate the real error, reporting $< 1\%$ or smaller, as they are probably dominated by instrumental systematics (e.g., wavelength calibration, normalization errors). To avoid any bias to unrealistic error estimation we assumed a homogeneous 5% errorbar estimated from the RMS of the S-index series.

5.1.2 HARPS

Eleven observations using HARPS were acquired between May 24 2018 and April 6 2019 from program IDs 0101.C-0497, 0102.C-0525 and 0103.C-0442 (PI: Díaz), in order to confirm the signal found in PFS data and also to constrain the orbital parameters of the planet candidate. The observations were carried out using simultaneous Thorium exposures with a fixed exposure time of 900 s reaching a mean signal-to-noise ratio of ∼67 at 5500 Å. We re-processed the observations with the TERRA software (Anglada-Escudé & Butler 2012), where a high S/N template is constructed by combining all the observations that pass a threshold S/N cutoff, and then the RVs are computed by a χ^2-fitting process relative to this template. The mean radial velocity uncertainty we get from this analysis is ∼0.89 m s^{-1}. TERRA also provides a computation of the S-indices and their uncertainties. These along with the RVs are listed in Table 5.3.

Table 5.1: PFS1 Radial Velocities of HD 95338. This table is published in its entirety in the machine-readable format. A portion is shown here for guidance regarding its form and content.

BJD (- 2450000)	RV (m s^{-1})	σ RV (m s^{-1})	S (dex)	σ S (dex)
5253.72066	1.806	1.191	0.2450	0.012
5256.80073	3.796	1.186	0.1867	0.012
5342.53484	-2.873	1.114	0.3596	0.012
5348.50146	0.620	1.317	0.2815	0.012
5349.52059	-1.081	1.371	0.2713	0.012
5588.85377	2.115	0.988	0.1724	0.012
5663.60446	5.616	1.178	0.1918	0.012
5959.79501	-3.994	1.019	0.2402	0.012
6284.83957	-6.118	0.836	0.2481	0.012
6291.83583	-7.558	0.829	0.1590	0.012
6345.74970	-6.404	1.179	0.2418	0.012
6355.71078	-2.553	1.206	0.3401	0.012
...	...	...	...	...

Table 5.2: PFS2 Radial Velocities of HD 95338. This table is published in its entirety in the machine-readable format. A portion is shown here for guidance regarding its form and content.

BJD (- 2450000)	RV (m s^{-1})	σ RV (m s^{-1})	S (dex)	σ S (dex)
8471.81505	5.205	0.931	0.1644	0.008
8471.82063	3.733	0.892	0.1659	0.008
8473.82297	2.519	0.918	0.1690	0.008
8473.82677	2.613	0.910	0.1705	0.008
8474.83964	2.712	0.869	0.1770	0.008
8474.84350	1.512	0.839	0.1654	0.008
8475.84374	1.324	0.751	0.1586	0.008
8475.84752	0.202	0.784	0.1609	0.008
8476.82523	-2.224	0.797	0.1631	0.008
8476.82897	1.295	0.785	0.1571	0.008
8479.84682	-3.814	0.813	0.1623	0.008
...	...	...	...	...

Table 5.3: TERRA Radial Velocities of HD 95338

BJD (- 2450000)	RV (m s^{-1})	σ RV (m s^{-1})	S (dex)	σ S (dex)
8262.52210	-2.347	0.963	0.1568	0.0016
8263.58809	-2.716	0.555	0.1642	0.0011
8264.56962	-2.820	0.775	0.1637	0.0014
8265.60191	-2.412	0.677	0.1672	0.0012
8266.54165	-4.199	1.105	0.1520	0.0018
8429.84914	0.0	0.706	0.1580	0.0011
8430.83705	1.651	0.712	0.1606	0.0009
8576.69728	12.654	1.156	0.1584	0.0016
8577.79238	14.113	1.479	0.1504	0.0023
8578.71982	11.102	0.853	0.1564	0.0013
8579.70958	11.115	0.790	0.1605	0.0012

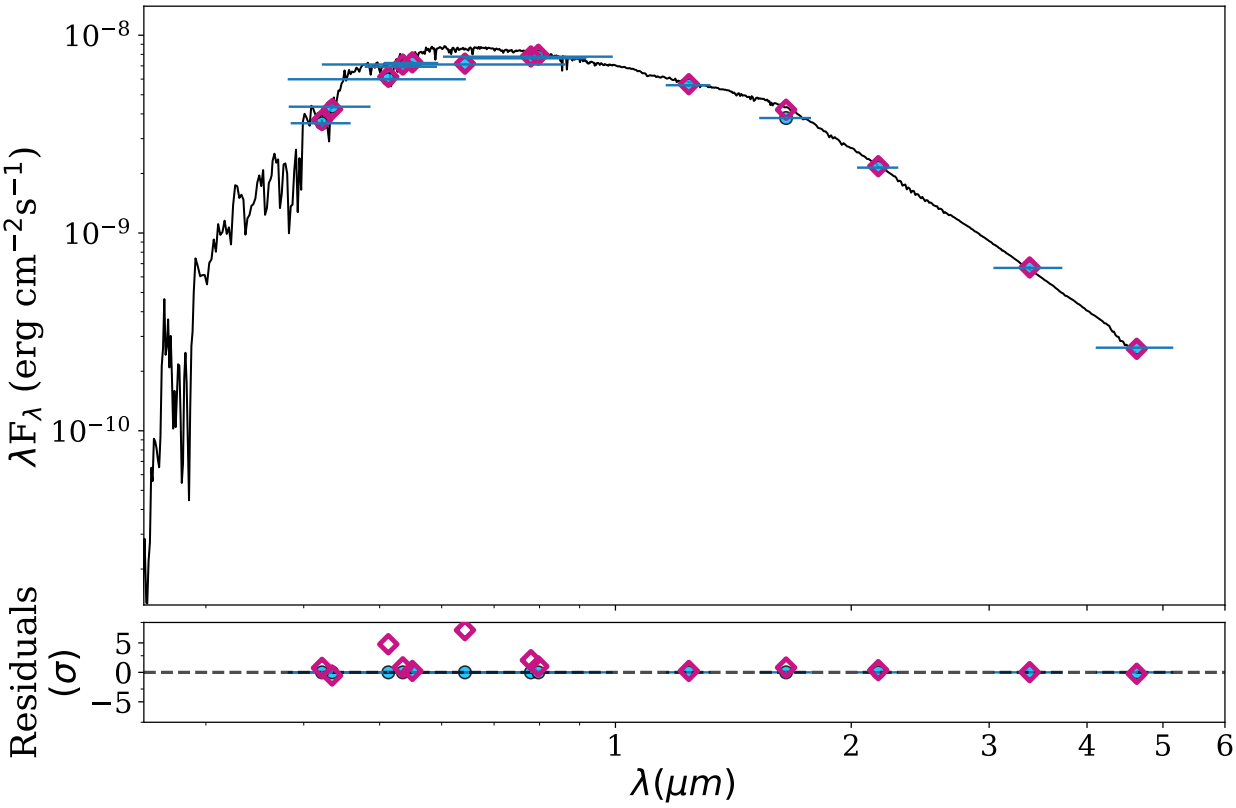

Figure 5.1: Top: best fitting BT-Cond SED model. Blue points are the photometry and magenta diamonds are the synthetic photometry. Horizontal error bars show the width of the filter bandpass. Bottom: Residuals of the fit, normalized to the photometry errors.

5.2 Stellar Parameters

We derived [Fe/H], $T_{\rm eff}$, age, mass, radius, log$g$ and $v$sini using the spectral classification and stellar parameter estimation package `SPECIES` (Soto & Jenkins 2018), previously used in, e.g, Díaz et al. (2018); Díaz et al. (2020a). In short, `SPECIES` derives $T_{\rm eff}$, log g, [Fe/H] and microturbulence by measuring the equivalent widths (EWs) of a list of neutral and ionized iron lines, and then using `MOOG` (Sneden 1973b) to solve the radiative transfer equation in the stellar interior, along with ATLAS9 model atmospheres (Castelli & Kurucz 2004). The adopted values for the atmospheric parameters are those for which no correlation is found between the individual iron abundance and the line excitation potential, nor the reduced EWs (EW/λ), and the average abundance for the FeI and FeII lines is the same. The EWs used in this work were measured by fitting Gaussian-shaped profiles to the absorption lines through the `EWComputation`[1] module in `SPECIES`. Details of the fitting procedure will appear in Soto et al. in prep. We produced a high signal-to-noise, stacked spectrum from HARPS observations to be used for the precise computation of the EWs. Physical parameters like mass and age are found by interpolation through a grid of MIST models (Dotter 2016), using the `isochrones` Python package (Morton 2015). Finally, macroturbulence and rotation velocity were computed using temperature relations and fitting synthetic profiles to a set of five absorption lines (see Soto & Jenkins 2018 for more details).

Then we performed a Spectral Energy Distribution (SED) fit to publicly available catalog photometry shown in Table 5.4 using the values found by `SPECIES` as priors.

The SED fit was done with `ARIADNE`, a Python tool designed to automatically fit archival photometry to atmospheric model grids. `Phoenix v2` (Husser et al. 2013), `BT-Settl`, `BT-Cond` (Allard et al. 2012), `BT-NextGen` (Hauschildt et al. 1999), Castelli & Kurucz (2004) and Kurucz (1993) stellar atmosphere models were convolved with different filter response functions, $UBVRI$; 2MASS $JHK_{\rm s}$ (Skrutskie et al. 2006); SDSS *ugriz*; WISE $W1$ and $W2$; Gaia G, RP and BP (Gaia Collaboration et al. 2016, 2018); Pan-STARRS *girwyz*; Strömgren uvby; GALEX NUV and FUV; *TESS*; *Kepler*; and NGTS to create 6 different model grids. We then model each SED by interpolating the model grids in $T_{\rm eff}$ − log g−[Fe/H] space. The remaining parameters are distance, radius, extinction in the V band, and individual excess noise terms for each photometry point in order to account for possible underestimated uncertainties or variability effects. We set priors for $T_{\rm eff}$, log g, and [Fe/H] from the `SPECIES` results, for the radius we took Gaia DR2 radius values as prior, for the distance we used the *Gaia* parallax as priors (after applying the -52.8±2.4 μas correction from Zinn et al. 2019) and then we treated it as a free parameter in the fitting routine. We limited the A_V to a maximum of 4.243 taken from the re-calibrated SFD galaxy dust map (Schlegel et al. 1998; Schlafly & Finkbeiner 2011). Each excess noise parameter has a zero mean Normal distribution as the prior, with the variance equal to five times the size of the reported uncertainty. We then performed the fit using `dynesty`'s nested sampler (Speagle 2019) to sample the posterior parameter space, obtaining the Bayesian evidence of each model and the marginalized posterior distribution for each fitted parameter as a by-product. Finally we averaged the posterior samples of each model, weighting each sample by its normalized evidence. To plot the SED, we selected the model grid with the highest evidence to calculate the synthetic photometry and overall model (Figure 5.1). We note the residuals from Figure 5.1 are normalized to the error of the photometry. In the case of precise photometry, e.g. *Gaia*, the residuals show a relatively high scatter. A more detailed explanation of the fitting procedure, accuracy, and precision of `ARIADNE` can be found in Vines & Jenkins (2020).

[1] Available at `https://github.com/msotov/EWComputation`

Table 5.4: Stellar Parameters of HD 95338

Parameter	Value	Source
TESS Name	TIC 304142124	
R.A. (J2000)	10:59:26.303	SIMBAD
Dec. (J2000)	-56:37:22.947	SIMBAD
TESS	7.8436±0.0006	ExoFOP[a]
H	6.729±0.037	2MASS
J	7.098±0.024	2MASS
Ks	6.591±0.017	2MASS
V	8.604±0.012	Simbad
B	9.487±0.013	Simbad
G	8.3821±0.0003	*Gaia*
RP	7.8017±0.0013	*Gaia*
BP	8.8464±0.001	*Gaia*
$W1$	6.553±0.071	Wise
$W2$	6.578±0.023	Wise
Parallax (mas)	27.0553±0.0499	Gaia, Zinn et al. (2019)
Distance (pc)	$36.97^{+0.02}_{-0.03}$	This work
Spectral type	K0.5V	This work (`ARIADNE`)
Mass ($M_\odot$)	$0.83^{+0.02}_{-0.02}$	This work (`ARIADNE`)
Radius ($R_\odot$)	$0.87^{0.04}_{0.04}$	This work (`ARIADNE`)
Age (Gyr)	5.08 ±2.51	This work (`SPECIES`)
A_V	$0.073^{+0.012}_{-0.015}$	This Work (`ARIADNE`)
Luminosity ($L_\odot$)	0.49±0.01	Anderson & Francis 2012
$T_{\rm eff}$ (K)	5212^{+16}_{-11}	This work (`SPECIES`)
[Fe/H]	0.04±0.10	This work (`SPECIES`)
log g	4.54± 0.21	This work (`SPECIES`)
v sin i (km s^{-1})	1.23 ± 0.28	This work (`SPECIES`)
$v_{\rm mac}$ (km s^{-1})	0.97±0.41	This work (`SPECIES`)

[a] `https://exofop.ipac.caltech.edu/tess/`

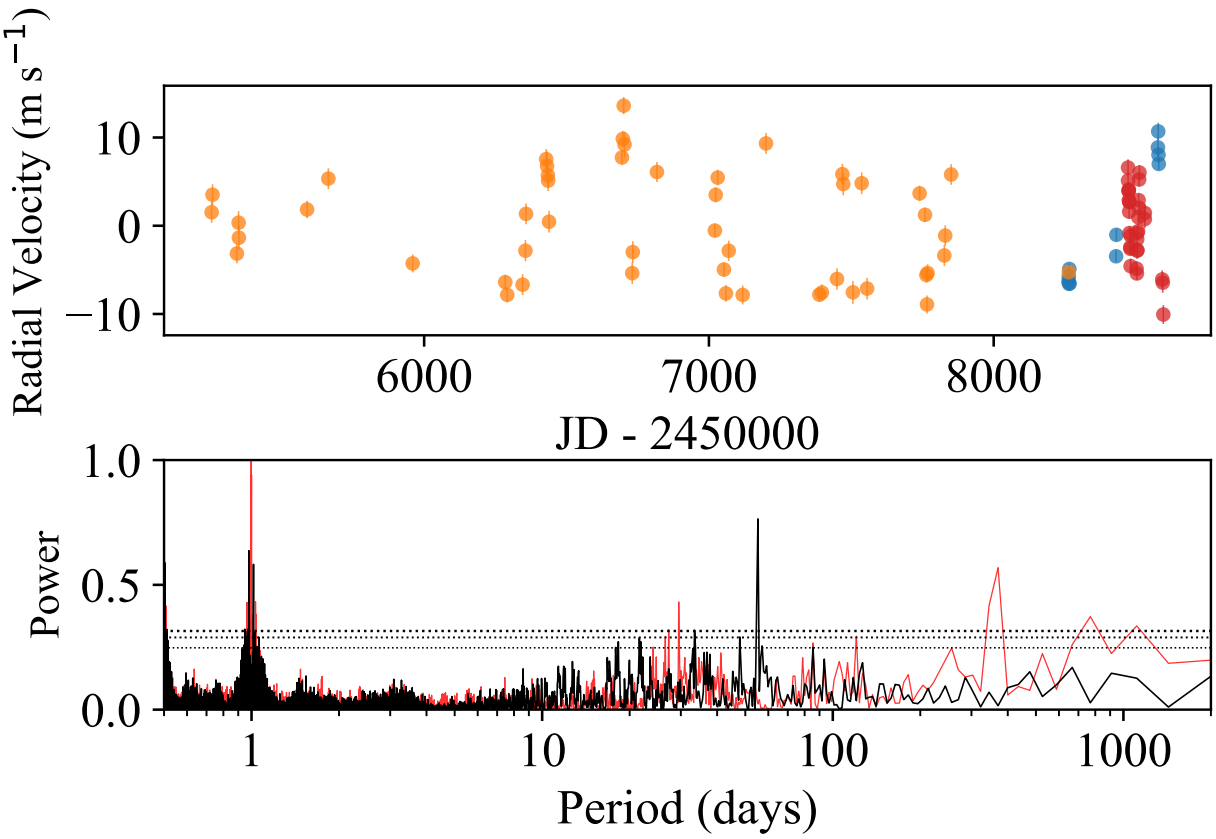

Figure 5.2: Top: Radial velocity time series for HD 95338 obtained with PFS1 (orange), PFS2 (red) and HARPS (blue). Bottom: GLS periodogram for the combined radial velocities. Each data set has been corrected by their respective velocity zero-point, estimated from the mean of the time series. Horizontal lines, from bottom to top, represent the 10, 1 and 0.1% significance thresholds levels estimated from 5000 bootstraps with replacement on the data. The periodogram in red shows the window function for the time series.

5.3 Detection from Radial Velocities

We began examining the radial-velocity data by using the traditional periodogram analysis approach to look for any periodicities embedded in the data. We used the generalized version (Zechmeister & Kürster 2009) of the Lomb-Scargle periodogram (Lomb 1976; Scargle 1982, hereafter GLS). Figure 5.2 shows the initial RV-only analysis where the signal at 55-days is clearly identified from the combined radial velocities. From this analysis we informed the following modeling process.

We modeled the radial velocities of HD 95338 following the same procedure defined in Tuomi et al. (2014b) and performed in Jenkins & Tuomi (2014) and Díaz et al. (2018) with some slight variations in our model. We define the global model as follows:

$$y_{\mathrm{i},j} = \hat{y}_{\mathrm{i},j} + \varepsilon_{\mathrm{i},j} + \eta_{\mathrm{i},j} \ , \tag{5.1}$$

where

$$\hat{y}_{\mathrm{i},j} = \gamma_j + f_k(t_\mathrm{i}) \tag{5.2}$$

is the deterministic part of the model composed of an offset γ_j for data set j and the Kepelerian component

$$f_k(t_\mathrm{i}) = \sum_{m=1}^{N_p} K_m[\cos(\omega_m + \nu_m(t_\mathrm{i})) + \mathrm{e}_m \cos(\omega_m)] \ , \tag{5.3}$$

which is a function that describes a m-Keplerian model with K_m being the velocity semi-amplitude, ω_m argument of periapsis of the star's orbit with respect to the barycenter, ν_m is the true anomaly at the time of the planetary transit and e_m is the eccentricity for the m-th planet. ν_m is also a function of the orbital period and the mean anomaly $M_{0,m}$, measured at time T_0=2455253.72066.

The stochastic component in the radial velocity data is modeled using a moving average (MA) approach,

$$\eta_{\mathrm{i},j} = \sum_{l=1}^{q} \phi_{j,l} \ \exp\left\{\frac{|t_{\mathrm{i}-l} - t_\mathrm{i}|}{\tau_j}\right\}(v_{\mathrm{i}-l,j} - \hat{y}_{\mathrm{i}-l,j}) \ , \tag{5.4}$$

where $\phi_{j,l}$ represents the amplitude of the qth-order MA model, τ_j is the time scale of the MA(q) model for the j-th instrument. The range of τ_j is determined according to the data timespan and cadence. Thus $\tau_{\max} = t_{\max}$- $t_{\min}$, where $t_{\max}$ and $t_{\min}$ are the maximum and minimum value of the timespan of the combined set, respectively. Finally, $\tau_{\min}$=min$\{t_2 - t_1, t_3 - t_2, ..., t_N - t_{N-1}\}$, represents the minimum difference between two epochs and N is the total number of epochs. The white noise term in Equation 5.1 is denoted by $\varepsilon_{\mathrm{i},j}$, where we assume that there is an excess white noise (jitter) in each data set with a variance of σ_j such that $\varepsilon_{\mathrm{i},j} \sim \mathcal{N}(0, \sigma_\mathrm{i}^2 + \sigma_j^2)$, where σ_i and σ_j are the uncertainties associated with the measurement $y_{\mathrm{i},j}$ and jitter for the j-th dataset, respectively.

5.3.1 Posterior Samplings and Signal Detection

In order to estimate the posterior probability of the parameters in the model given the observed data we use Bayes' rule:

$$P(\theta \,|\, y) = \frac{P(y \,|\, \theta)\, P(\theta)}{\int P(y \,|\, \theta)\, P(\theta)\, \mathrm{d}\theta} \tag{5.5}$$

where $P(y \,|\, \theta)$ is the likelihood function and $P(\theta)$ corresponds to the prior. The denominator is a

normalizing constant such that the posterior must integrate to unity over the parameter space. For our model, we choose the priors for the orbital and instrumental parameters as listed in Table 5.5.

Table 5.5: Prior selection for the parameters used in the MA analysis

Parameter	Units	Prior Type	Range
Semi-amplitude	m s^{-1}	Uniform	$K \in [\,0, 100]$
Logarithmic Period	day	Uniform	$\ln P \in [\,\ln(1.1), \ln(10^6)]$
Eccentricity	-	$\mathcal{N}(0, 0.2)$	$e \in [0, 1)$
Long. of Peric.	rad	Uniform	$\omega \in [\,0, 2\pi]$
Mean Anomaly	rad	Uniform	$M_0 \in [\,0, 2\pi]$
Jitter	m s^{-1}	Uniform	$\sigma_J \in [0, 100]$
Smoothing time scale	day	Uniform	$\tau_j \in [\tau_{\min}, \tau_{\max}]$ (see text)
MA Amplitude	-	Uniform	$\phi_j \in [\,0, 1]$

For a given model, we sample the posterior through multiple tempered (hot) MCMC chains to identify the global maximum of the posterior. We then use non-tempered (cold) chains to sample the global maximum found by the hot chains. The procedure is similar to that previously done in Díaz et al. (2018) with the difference that here our MA model includes a correlated (red) noise component but it does not include explicit correlations with activity indicators because it would introduce extra noise although it might remove some activity signals (see, e.g. Feng et al. 2019). We explore the correlations between activity indices and radial velocities in Section 5.4. From the posterior samples, we infer the parameter at the mean value of the distribution and we report the uncertainties from the standard deviation of the distribution. This approach is also explained in detail in Feng et al. (2019). To select the optimal noise model, we calculate the maximum likelihood for a MA model using the Levenberg-Marquardt (LM) optimization algorithm (Levenberg 1944; Marquardt 1963).

We define the Bayes Factor (BF) comparing two given models, $\mathcal{M}_k$ and $\mathcal{M}_{k-1}$, as

$$\ln B_{k,k-1} = \ln P(y|\mathcal{M}_k) - \ln P(y|\mathcal{M}_{k-1}) \tag{5.6}$$

We calculate ln(BF) for MA($q+1$) and MA(q). If ln(BF)<5, we select MA(q), according to Equation 5.6. If ln(BF)≥ 5, we select MA($q+1$) and keep increasing the order of the MA model until the model with the highest order passing the ln(BF)≥ 5 criterion is found. Considering that the Bayesian information criterion (BIC) is a good criterion for signal selection (Kass & Raftery 1995; Feng et al. 2016), we convert BIC to BF according to the formula given by Feng et al. (2016).

Our MCMC runs gave rise to the posterior histograms shown in Figures 5.3 and 5.4, where the period, amplitude, and minimum mass (and the remaining orbital parameters) show Gaussian distributions centered on their respective mean values.

We used the posterior distribution for $T_{\rm peri}$, the eccentricity and the longitude of pericenter, ω, to predict the transit time of the orbit, since the eccentric anomaly is defined as $E = 2\arctan(\sqrt{(1-\mathrm{e})(1+\mathrm{e})}\tan(\nu/2))$, where $\nu = \pi/2 - \omega$ is the true anomaly. Then

$$T_c = \frac{M}{2\pi}P + T_{\rm peri} \tag{5.7}$$

where

$$M = E - \mathrm{e}\,sin(E) \tag{5.8}$$

From the posterior distributions for $T_{\rm peri}$ (see Figure 5.3) we obtain $T_c = 2458585.929 \pm 0.840$ which turns out to be well in agreement, within uncertainties, with the ephemeris from the *TESS* photometry, $T_{c,TESS} = 2458585.279$ (see Table 5.8). The posterior mean values for the radial velocity-only analysis are listed in Table 5.6. It is worth noting that the final value for the timescale of the red noise, τ_j, is not constrained for PFS2 as it did not converge to a unique solution. We choose the best MA(q) model based on 0-planet + MA(q) model comparison and thus q is determined based on the assumption that the time correlation in the RV data is totally noise, therefore q is typically larger than it should actually be. This is the reason why the amplitude and time scale of MA(q) models sometimes do not converge after adding Keplerian components which can explain the time correlation in the data better than stochastic red noise models such as MA. Although we can perform a selection of q and number of signals simultaneously, it would be a 2-dimensional model selection

and is thus time consuming. On the other hand, if a data set only contains white noise and signals, the Keplerian model will be favored against the MA model due to the advantage of simultaneous fitting. Compared to previous adoption of a single red noise model such as GP, our approach is more robust to overfitting or underfitting problems.

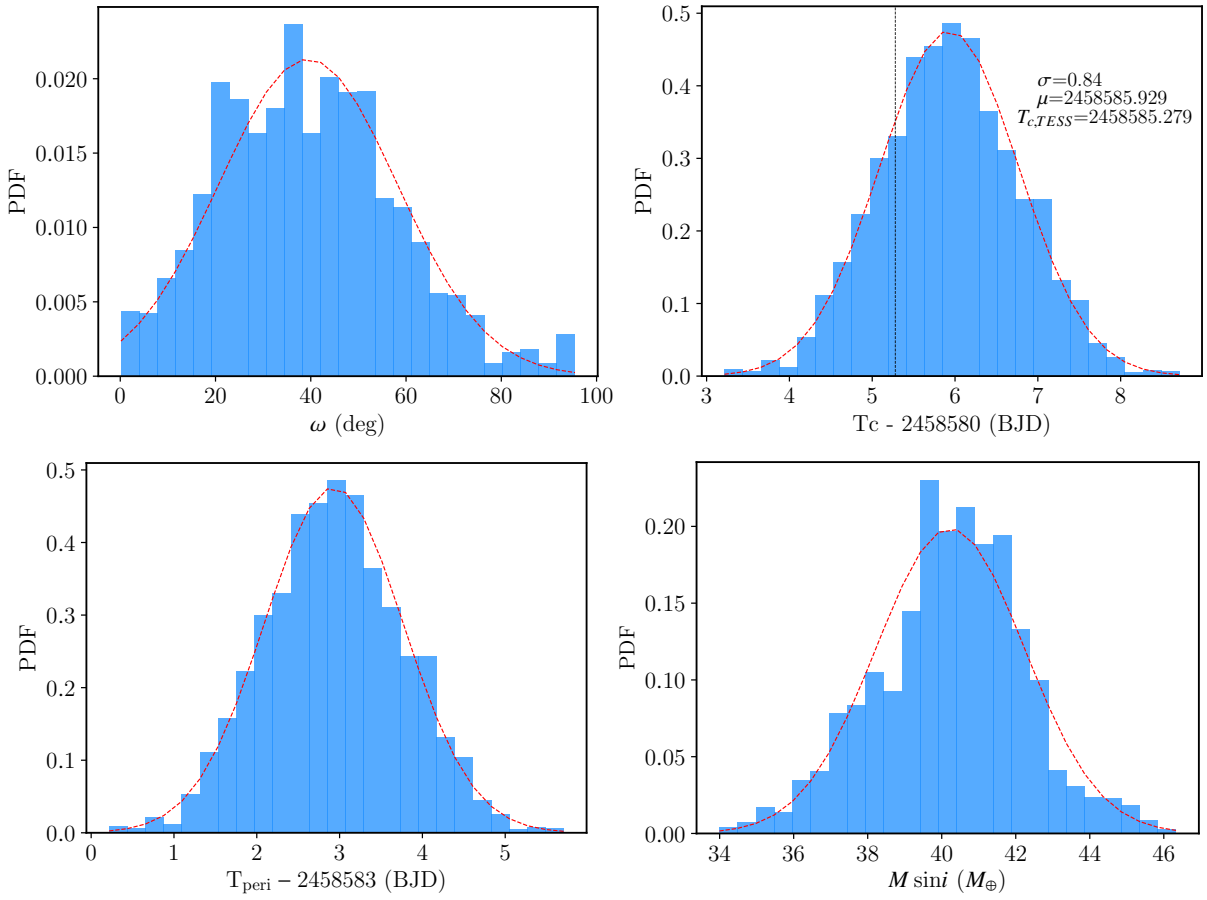

Figure 5.3: Posterior distributions of the orbital parameters ω, T_c, $T_{\rm peri}$ and minimum mass, respectively, obtained from our RV analysis. Dashed red lines on each plot show a Gaussian fit to the posterior distribution. T_c is derived from the time of pericenter passage values ($T_{\rm peri}$, see text). Vertical black dashed line represents the transit time from the *TESS* lightcurve. From the histogram we found a mean value of T_c = 2458585.929 and σ=0.84, which overlaps nicely with the transit time from the lightcurve, strongly suggesting both signals could originate from the same source.

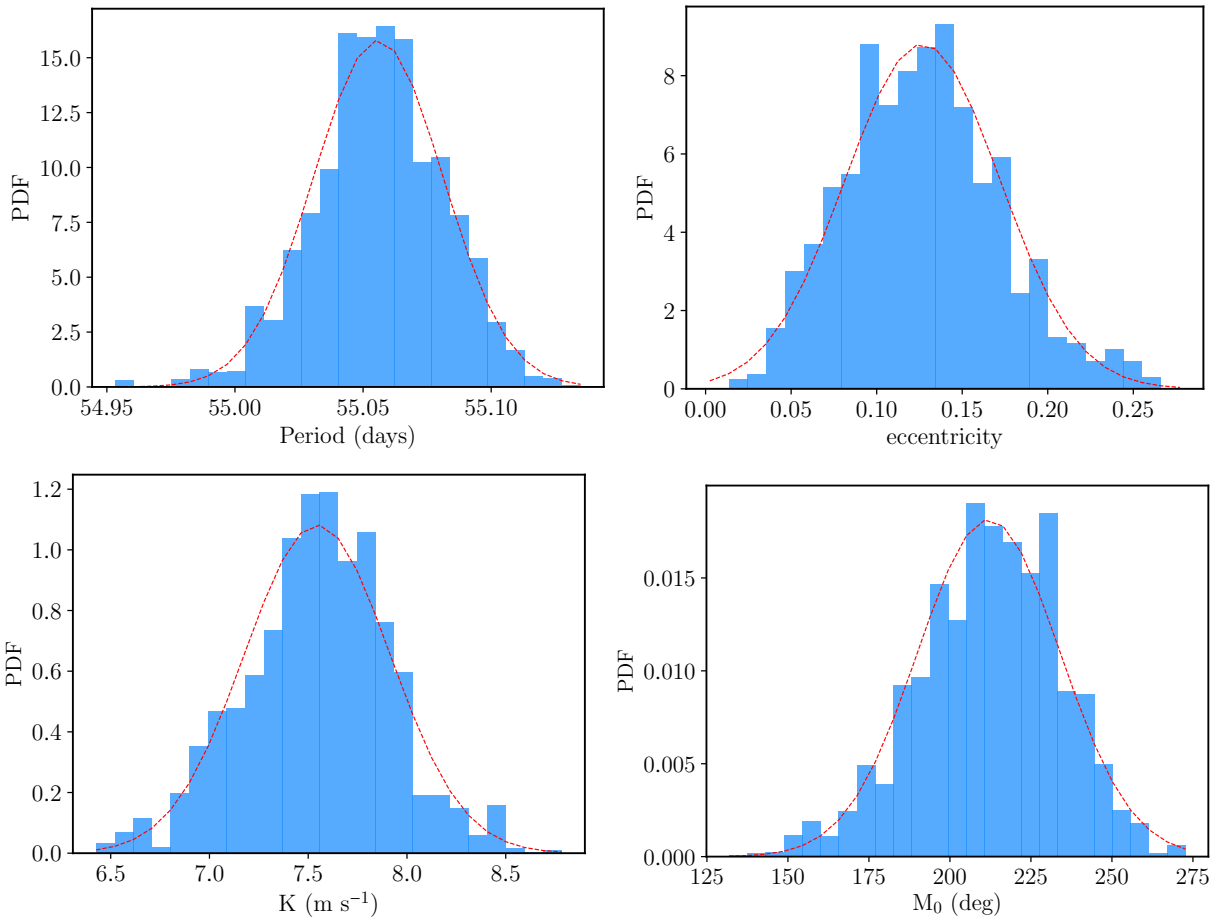

Figure 5.4: Posterior distributions of the orbital parameters P, e, K, M_0, respectively, obtained from our RV analysis. Dashed red lines on each plot show a Gaussian fit to the posterior distribution.

Table 5.6: Posterior for the parameters included in the RV-only analysis.

Parameter	Value
P (days)	55.056±0.025
$T_{\rm peri}$ (BJD - 2450000)	8585.2795±0.8384
K (m s^{-1})	7.54 ±0.37
e	0.127±0.045
ω (deg)	39.428 ± 18.719
M_0 (deg)	212.004±21.983
Msini ($M_\oplus$)	40.34±2.01
$\mu_{\rm PFS1}$ (m s^{-1})	0.316±0.584
$\sigma_{J,\rm PFS1}$ (m s^{-1})	1.725±0.818
$\phi_{\rm PFS1}$	0.457 ±0.426
ln$\tau_{\rm PFS1}$	3.18±1.10
$\mu_{\rm PFS2}$ (m s^{-1})	0.178±0.780
$\sigma_{J,\rm PFS2}$ (m s^{-1})	0.985±0.532
$\phi_{\rm PFS2}$	0.360 ±0.314
ln$\tau_{\rm PFS2}$	0.323±6.895
$\mu_{\rm HARPS}$ (m s^{-1})	0.796±0.938
$\sigma_{J,\rm HARPS}$ (m s^{-1})	1.80±0.87

Note: MA(1) applied to PFS. White noise applied to HARPS.

We note that additional tests were conducted using the Delayed Rejection Adaptive Metropolis algorithm (Metropolis et al. 1953; Haario et al. 2001, 2006), as previously done in Tuomi et al. (2014b) and Díaz et al. (2018) and we found the results were in full agreement with the MA approach within the uncertainties.

5.4 Stellar Activity and RV correlations

We computed the GLS periodogram of the combined S-indices from PFS1, PFS2 and HARPS (Figure 5.5). We do not find statistically significant periods from stellar activity matching the signal of the planet candidate (marked with a vertical line). However, we do see multiple peaks at ∼1, ∼29 and ∼150 days above the 1% significance threshold. The 1-day period is likely due to the frequency of the sampling in the observations, similarly the 29 d peak is close to the lunar period. The additional 150 d period could be related to a stellar magnetic cycle, but more data is needed to test this hypothesis. Figure **??** shows the correlations between the mean-subtracted activity indices in the Mt. Wilson system, S_{MW}, and the radial velocities: PFS1 (open triangles), PFS2 (black triangles) and HARPS (orange circles). We note the improvement in the scatter from PFS2 compared to PFS1; new activity indices are comparable to the scatter of those from HARPS, derived using the TERRA software. We see 4 points that are far off from the mean. We find the Pearson r correlation coefficients for PFS1, PFS2 and HARPS are 0.15, 0.38, -0.39, respectively, meaning no significant strong correlations are found ($|r| < 0.5$).

5.5 Photometry

5.5.1 TESS Photometry

HD 95338 was observed by *TESS*. We checked the target was observed using the Web *TESS* Viewing Tool (WTV[2]), as initially the target did not produce an alert on the *TESS* Releases website[3] where an overview table, alerts and downloadable data is available. We identified a single-transit in the *TESS* photometry containing data from Sector 10 using camera 3, observed between March 26th and April 22nd 2019.

We extracted the `PDCSAP_FLUX` 2-minute cadence photometry following the same procedures we recently used in Díaz et al. (2020a). The `PDCSAP_FLUX`, median-corrected photometry is shown in the top panel of Figure 5.7. We then applied a median filter to remove the lightcurve variability, in particular on both sides near the transit event. The final flattened lightcurve is shown in the lower panel of Figure 5.7 and it is the transit data used throughout all our analyses.

We note that the star is located in a relatively crowded field, as *Gaia* returns 12 sources within an angular separation of 1 arcmin. Given that the pixels in the *TESS* cameras are 21 arcsec wide, this could mean some of the sources would contaminate the aperture. However, the brightest nearby source is G ∼18 mag, which is 12 magnitudes fainter than HD 95338 ($G = 8.38$). Converted into flux, this companion is ∼7,000 times fainter than HD 95338. From a preliminary inspection and analysis of the light curve, we estimated a transit depth of ∼2000±500[4] ppm. Therefore, the difference in

[2] `https://heasarc.gsfc.nasa.gov/cgi-bin/tess/webtess/wtv.py`
[3] `https://tev.mit.edu/data/`
[4] https://exofop.ipac.caltech.edu/tess/target.php?id=304142124

flux would cause a depth of $\sim$ 100 ppm, which we find to be negligible compared to the transit depth.

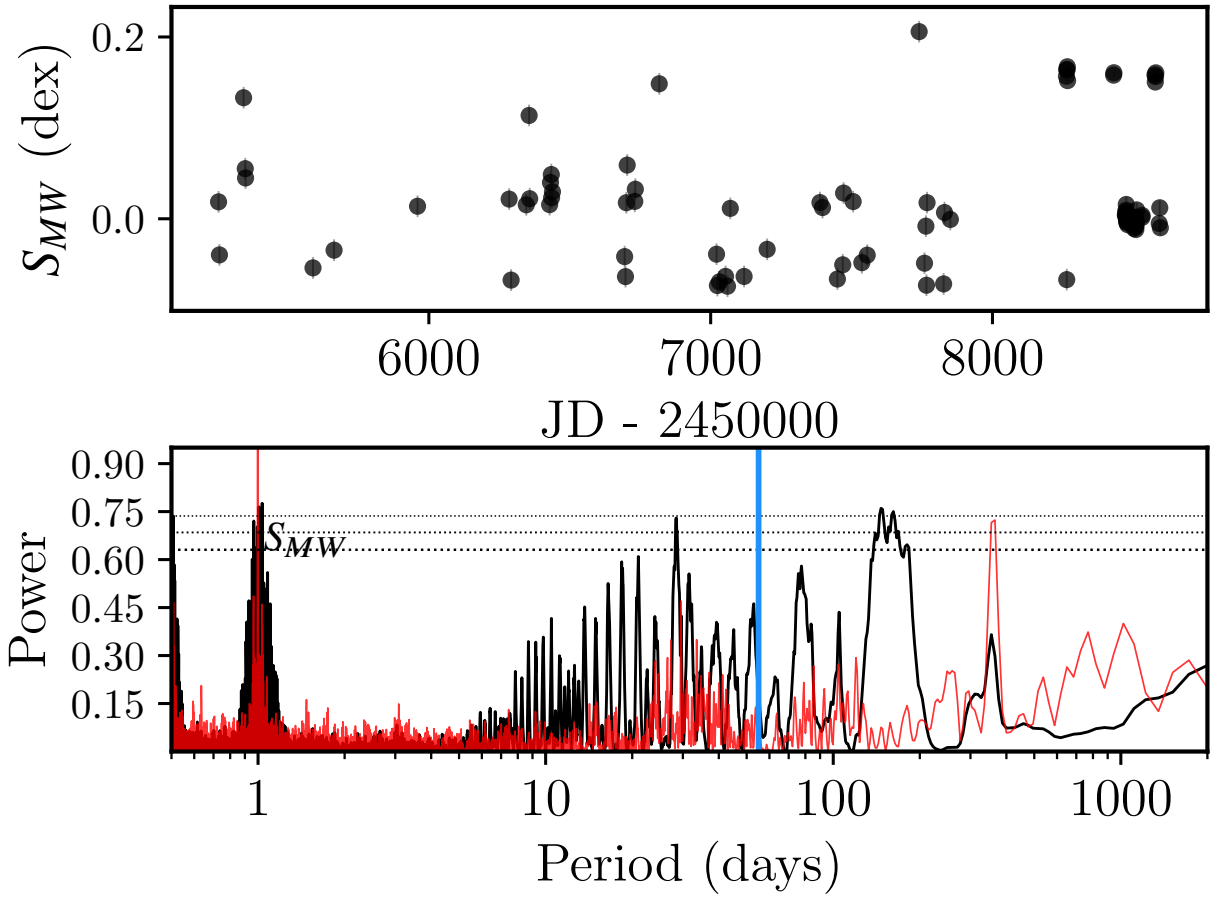

Figure 5.5: Top: Time series of combined, mean subtracted S-indices from HARPS, PFS1 and PFS2. Bottom: GLS Periodogram of the S-indices. Vertical line shows the position of the 55-day radial velocity signal. Horizontal lines, from bottom to top, represent the 10, 1 and 0.1% significance thresholds levels estimated from 5000 bootstraps with replacement on the data.

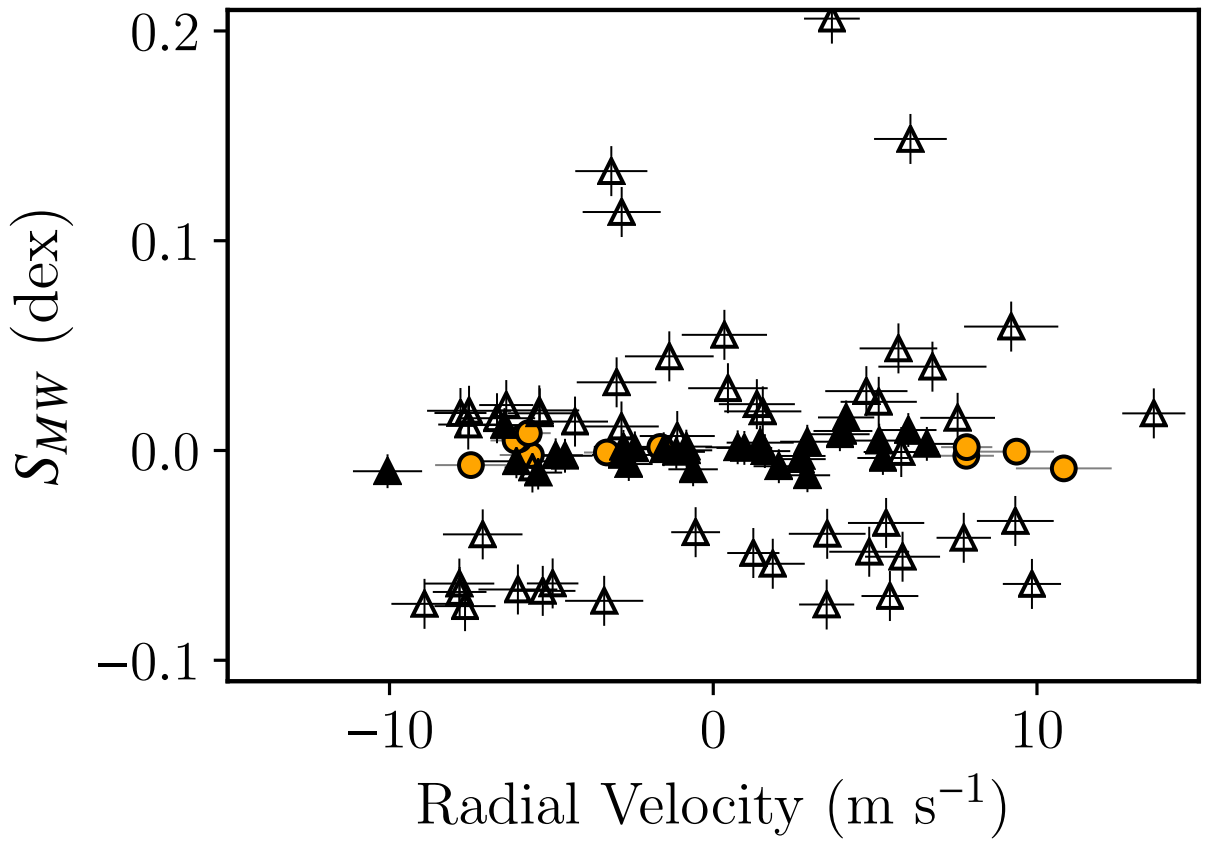

Figure 5.6: Radial velocity vs S-indices from HARPS (circles), PFS1(open triangles), PFS2 (black triangles).

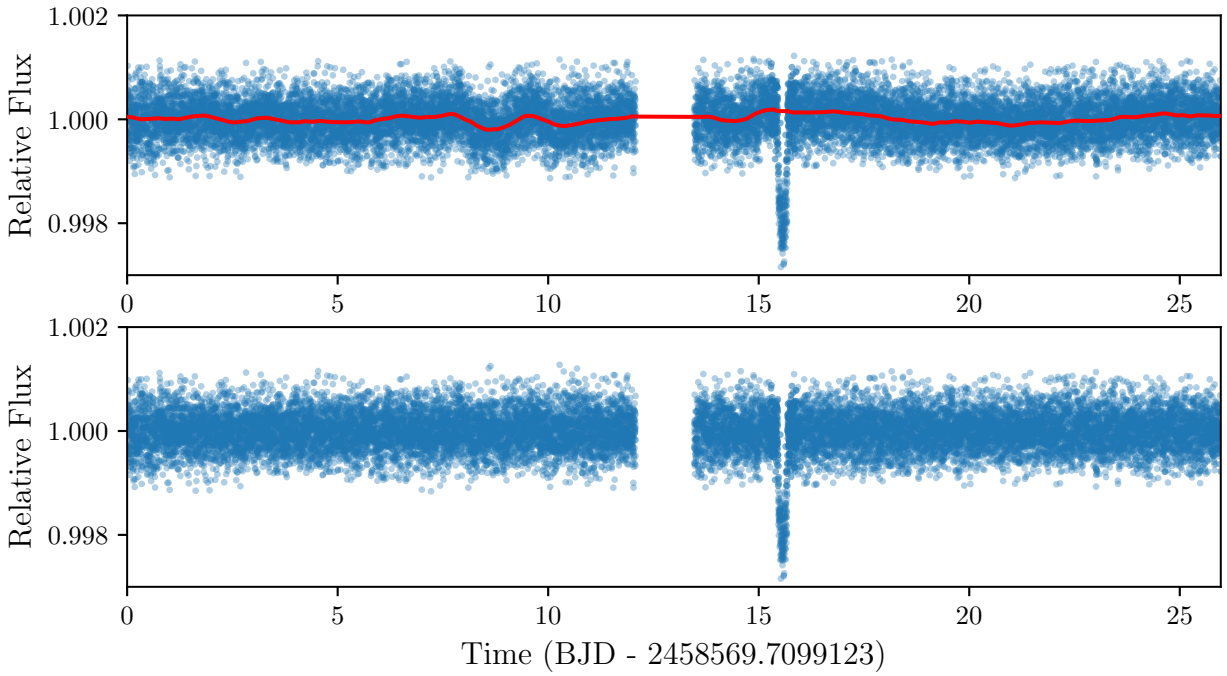

Figure 5.7: Top: `PDC_SAP` lightcurve for HD 95338 from *TESS* Sector 10 showing the single transit. Red solid curve on top of the photometry shows a median filter applied to remove variability. Bottom: Median filter corrected `PDC_SAP` TESS light curve for HD 95338.

Recent work by Sandford et al. (2019) have shown the use of single-transit lightcurves to estimate orbital periods based on precise parallaxes from Gaia. While their work focused on *K2* data, we can apply the same methodology to our *TESS* lightcurve, since we also know the transit depth, and we can calculate the scaled semi-major axis and stellar density from the combination of the `ARIADNE` results and the high resolution spectra. We recall equations 1 and 2 from Sandford et al. (2019):

$$P^2 = \frac{3\pi}{G}\left(\frac{a}{R_\star}\right)^3 \rho_\star^{-1} \tag{5.9}$$

$$\sigma_P = \frac{P}{2}\sqrt{\left(\frac{\sigma_{\rho_\star}}{\rho_\star}\right)^2 + \left(\frac{3\sigma\frac{a}{R_\star}}{\frac{a}{R_\star}}\right)^2} \tag{5.10}$$

which yield the orbital period (and the associated error) of a single transit using Kepler's third law and assuming circular orbits, where G is the gravitation constant, $(a/R_\star)$ corresponds to the scaled semi-major axis measured directly from the shape of the transit and $\rho_\star$ is the stellar density that must come from an independent analysis. In our case, we used the stacked spectra acquired with HARPS, and from our spectra classification analysis with `SPECIES` combined with the SED fit, we find a stellar density of $\rho_\star$=$1.68^{+0.45}_{-0.23}$ g cm^{-3}. We estimate $(a/R_\star)$= $58.06^{+1.39}_{-2.48}$ from the transit seen in the *TESS* lightcurve. Then, using equations (1) and (2) from from Sandford et al. (2019) we get an estimate for an orbital period of 47±9 days for the single transit observed by *TESS* being consistent within the uncertainties to the period of the signal found in the radial velocity data.

5.5.2 ASAS Photometry

In an attempt to search for additional sources of periodicity we used data from the All Sky Automated Survey (ASAS; Pojmanski 1997). Figure 5.8 shows the photometry time series consisting on 625 measurements from December 7th 2000 to December 3rd 2009. We selected the best quality data, flagged as "A" or "B". We used the GLS periodogram to search for signals after filtering the highest quality data from outliers, and found no statistically significant periods that could be attributed to the stellar rotation period, due in part to the size of the typical uncertainty in the ASAS photometry.

In order to address how often we could recover a prediction for the transit centroid, T_c, that has an uncertainty of 1.5% of the orbital period or better, just as we see for HD 95338 b, we simulated 10^6 systems with a single planet and random orbital parameters. We consider that all the random systems transit their host stars and we used flat priors for the distribution of longitude of pericenter, ω, and for the eccentricity. For the distribution of orbital periods we used the broken power law presented in Mulders et al. (2018), where the break occurs at P_b=10 days. For shorter periods the probability is written as $(P/P_b)^{1.5}$, while for longer periods the probability is unity. For each system, we generated the remaining orbital parameters according to standard equations for the orbital parameters, use these to predict T_c (see Section 5.3). We find that ∼9% of the systems sampled randomly fulfill this criterion.

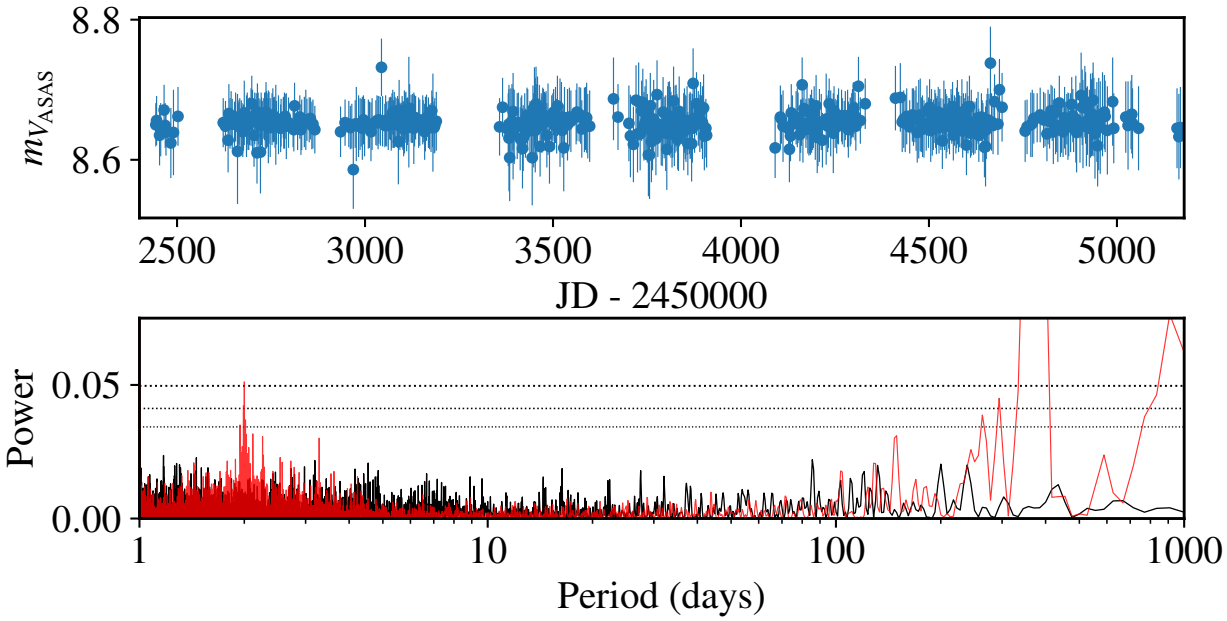

Figure 5.8: GLS periodogram of the ASAS V-band photometry. Horizontal lines mark the position of the 10,1 and 0.1% FAP threshold levels, from bottom to top, respectively. A peak close to ∼90 days is seen in the power spectrum, however it is below any FAP threshold and cannot be considered as statistically significant.

Table 5.7: Priors used on the joint analysis of HD 95338.

Parameter name	Prior	Units	Description
$\rho_\star$	$\mathcal{N}(1685{,}30)$	kg m^{-3}	Stellar density.
Parameters for planet b			
P_b	$\mathcal{J}(1, 100)$	days	Orbital Period.
$T_{c,b} - 2457000$	$\mathcal{U}(1000, 1100)$	days	Time of transit-center.
$r_{1,b}$	$\mathcal{U}(0, 1)$	—	Parametrization for p and b[1].
$r_{2,b}$	$\mathcal{U}(0, 1)$	—	Parametrization for p and b[1].
K_b	$\mathcal{U}(1, 100)$	m s^{-1}	Radial-velocity semi-amplitude.
e_b	$\mathcal{U}(0, 1)$	—	eccentricity.
ω_b	$\mathcal{U}(0, 359.)$	deg	argument of periastron.
Parameters for TESS			
$D_{\rm TESS}$	1.0 (Fixed)	—	Dilution factor for *TESS*.
$M_{\rm TESS}$	$\mathcal{N}(0, 1000)$	ppm	Relative flux offset for *TESS*.
$\sigma_{w,\rm TESS}$	$\mathcal{J}(0.1, 100)$	ppm	Extra jitter term for *TESS* lightcurve.
$q_{1,\rm TESS}$	$\mathcal{U}(0, 1)$	—	Quadratic limb-darkening parametrization.
$q_{2,\rm TESS}$	$\mathcal{U}(0, 1)$	—	Quadratic limb-darkening parametrization.
RV instrumental parameters			
$\mu_{\rm PFS1}$	$\mathcal{N}(0, 10)$	m s^{-1}	Radial velocity zero-point (offset) for PFS1.
$\sigma_{w,\rm PFS1}$	$\mathcal{J}(0.1, 10)$	m s^{-1}	Extra jitter term for PFS1 radial velocities.
$\mu_{\rm PFS2}$	$\mathcal{N}(0, 10)$	m s^{-1}	Radial velocity zero-point (offset) for PFS2.
$\sigma_{w,\rm PFS2}$	$\mathcal{J}(0.1, 10)$	m s^{-1}	Extra jitter term for PFS2 radial velocities.
$\mu_{\rm HARPS}$	$\mathcal{N}(0., 10)$	m s^{-1}	Radial velocity zero-point (offset) for HARPS.
$\sigma_{w,\rm HARPS}$	$\mathcal{J}(0.1, 10)$	m s^{-1}	Extra jitter term for HARPS radial velocities.

[1]We used the transformations from Espinoza (2018).

Table 5.8: Planetary Properties for HD 95338 b

Property	Value
Fitted Parameters	
$\rho_\star$ (kg m^{-3})	$1686.537^{+29.810}_{-29.993}$
P (days)	$55.087^{+0.020}_{-0.020}$
T_c (BJD - 2450000)	$8585.2795^{+0.0006}_{-0.0006}$
a/R_*	$64.676^{+0.381}_{-0.384}$
b	$0.430^{+0.070}_{-0.113}$
K (m s^{-1})	$8.17\ ^{+0.42}_{-0.39}$
i_p (deg)	$89.57^{+0.09}_{-0.05}$
e	$0.197^{+0.029}_{-0.024}$
ω (deg)	$23.42^{+11.53}_{-11.99}$
Derived Parameters	
M_p ($M_\oplus$)	$42.44^{+2.22}_{-2.08}$
R_p ($R_\oplus$)	$3.89^{+0.19}_{-0.20}$
a (AU)	$0.262^{+0.002}_{-0.002}$
ρ_p (g cm^{-3})	$3.98^{+0.62}_{-0.64}$
T^1_{eq} (K)	385^{+17}_{-17}
$\langle F \rangle$ ($\times 10^7$ erg s^{-1} cm^{-2})	1.01±0.03
Instrumental Parameters	
M_{TESS} (ppm)	$-0.0000027^{+0.0000028}_{-0.0000027}$
$\sigma_{w,TESS}$ (ppm)	$1.836^{+12.323}_{-1.570}$
$q_{1,TESS}$	$0.389^{+0.109}_{-0.073}$
$q_{2,TESS}$	$0.848^{+0.108}_{-0.183}$
μ_{PFS1} (m s^{-1})	$0.77^{+0.36}_{-0.35}$
$\sigma_{w,PFS1}$ (m s^{-1})	$2.31^{+0.32}_{-0.28}$
μ_{HARPS} (m s^{-1})	$3.83^{+0.59}_{-0.56}$
$\sigma_{w,HARPS}$ (m s^{-1})	$1.61^{+0.54}_{-0.40}$
μ_{PFS2} (m s^{-1})	$-1.01^{+0.27}_{-0.28}$
$\sigma_{w,PFS2}$ (m s^{-1})	$1.30^{+0.30}_{-0.26}$

[1]Estimated using a Bond albedo of 0.5.

If the agreement between the RV prediction and transit T_c found for HD 95338 is just a statistical fluke, then this means there are more planets in the system, since another body must give rise to the transit. The probability of 9% does not consider this possibility. For that to be the case, we should also normalize by the fraction of Neptunes that are found in multiple systems. Although this value is uncertain, and may actually be ∼100%, we can at least estimate it using a literature search. To do this, we retrieved the number confirmed Neptunes with known companions detected by the transit method by *Kepler/K2* from the `exoplanet.eu`[5] catalog in a mass range between 10 and 45 $M_\oplus$. We find that the number of these multi-systems is 19 out of a total of 65, which corresponds to a fraction of ∼29%. This leads to a final probability of ∼3%, meaning it is highly unlikely that we have observed the configuration we find for HD 95338 b if the orbital parameters are randomly distributed. Even if Neptunes are indeed found to exist exclusively in multi-planet systems, there is still a 91% probability that the RV detected companion and the *TESS* detected companion are the same object.

5.6 Joint Analysis

We performed a joint fit of the photometry and radial velocities (Tables 5.1 to 5.3) using the `juliet` package (Espinoza et al. 2019a) in order to estimate the orbital parameters for the system. To model the photometry `juliet` uses the `batman` package (Kreidberg 2015) while the radial velocities are modeled using `radvel` (Fulton et al. 2018). We then sampled the parameter space using the `dynesty` nested sampler (Speagle 2019) to compute posterior samples and model evidences. The parameters for the joint model were set according to Table 5.7. We treated the eccentricity as a free parameter motivated by our finding from the RV-only analysis suggesting the eccentricity was different from zero. The resultant value was in agreement with the one from our previous analysis. The RV semi-amplitude prior was chosen to be flat between 1 and 100 to explore a wider range of amplitudes and not only values centered around the semi-amplitude found in the RV-only analysis. The jitter terms for PFS1, PFS2 and HARPS, were set using a Jeffreys prior over two orders of magnitude (0.1 to 10 m s^{-1}), resulting in excess RV noise of 2.3, 1.3 and 1.6 m s^{-1}, respectively. For the orbital period we used a Jeffreys prior over two orders of magnitude, from 1 to 100 days. The time of transit (T_c) was derived from the time of pericenter pasage ($T_{\rm peri}$) as discussed in Section 5.3.1. However, we also chose an uninformative prior using the whole range of the radial velocity baseline.

For the photometry parameters we used the efficient sampling for the transit depth (p) and impact parameter (b) described in Espinoza (2018) that allows only physically plausible values in the (b,p) plane to be sampled via the r_1 and r_2 coefficients according to the description of Kipping (2013) for two parameter laws. As a result we obtained a planet mass of $42.44^{+2.22}_{-2.08}\,M_\oplus$, consistent with a super-Neptune, with a radius of $3.89^{+0.19}_{-0.20}\,R_\oplus$ that translates to a relatively high density of $3.98^{+0.62}_{-0.64}$ g cm^{-3} for this planet. We note here we did not use GPs nor MA as in the radial velocity-only analysis, so the residuals shown in 5.9 (right) are really the full residuals from a pure Keplerian model including instrumental jitter.

[5] `http://exoplanet.eu/catalog/`

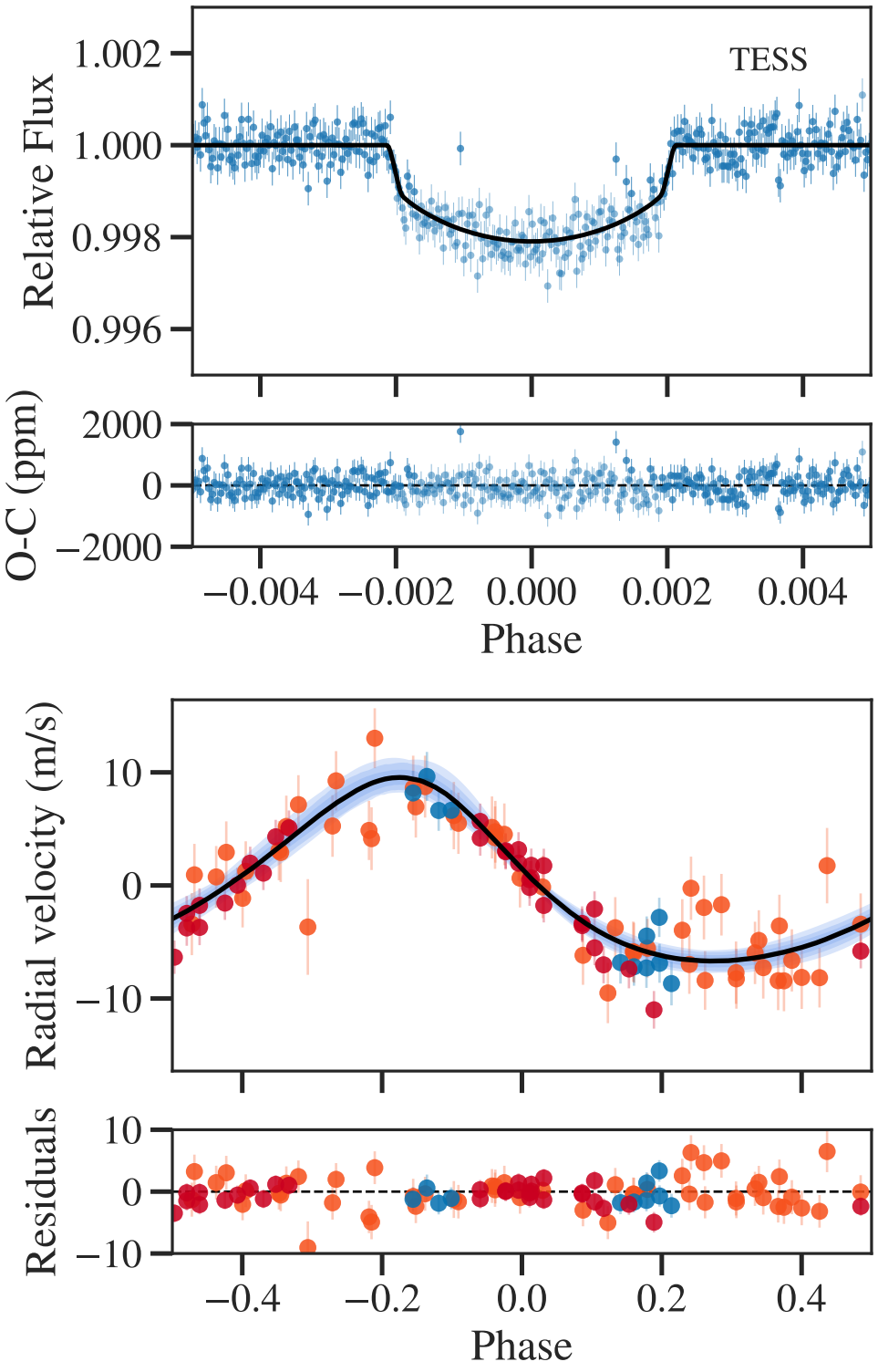

Figure 5.9: Top: TESS lightcurve phased-folded to the period of 55 days. Solid line is the model for the transit. Bottom panel shows the residuals. Bottom: Phased-folded radial velocities from PFS1 (orange), HARPS (blue) and PFS2 (red) where the jitter has been added to the errobars. Solid black line represents the Keplerian model from the joint fit with `juliet`. The orbital parameters for the system are listed in Table 5.8.

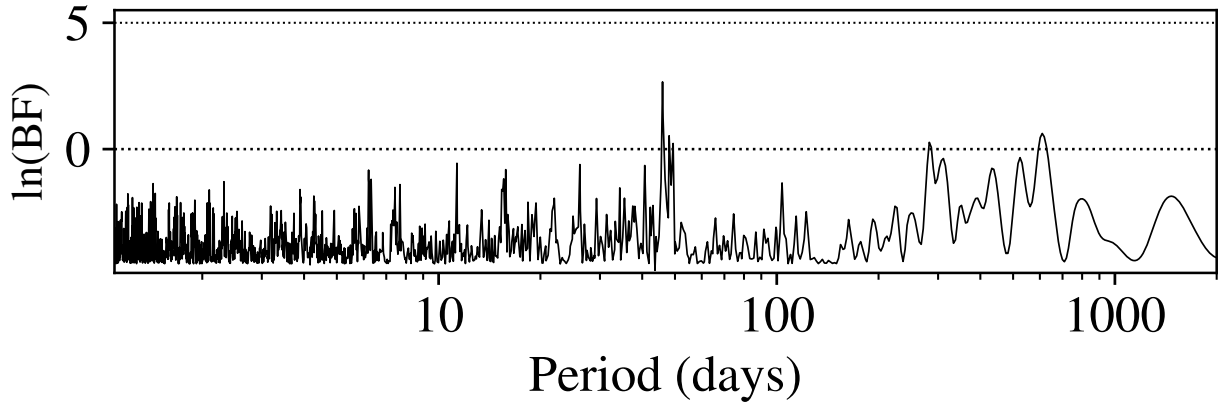

Figure 5.10: Bayes Factor periodogram of the residuals for the 1-planet model from our joint fit with `juliet`. No statistically significant signals are seen after subtracting the 55-day period. There is a peak in the power spectrum around signal around 46 days, however it is below our detection threshold ln(BF)>5.

5.7 Additional Signals

We searched for additional signals by analyzing the residuals from the 1-planet fit using same MA approach described in Section 5.3. Figure 5.10 shows the Bayes Factor Periodogram (BFP; Feng et al. 2017a) of the residual radial velocities for a 1-planet model. For this data, we do not find evidence for additional statistically significant signals present in the system after removing the 55-day planet signal. However, we do see a periodic signal at ∼46 days in the residual BFP, but we cannot reach any conclusion at this moment as the signal is below the detection threshold of ln(BF)>5 to be considered as significant. It can be related to the activity of the star, based on what we see in the periodogram analysis of the stellar activity indicators where we see some hints of periodicities around 30-40 days. Additional spectroscopic data will help to confirm or rule out additional signals.

5.8 Discussion

To better understand the composition of HD 95338 b, we have constructed interior structure models matched to its observed mass, radius, and orbital parameters. These models are explained in detail in Thorngren et al. (2016); briefly, they solve the equations of hydrostatic equilibrium, conservation of mass, and the material equation of state to determine the radius of a well-mixed planet. The equations of state (EOS) used were Chabrier et al. (2019) for H/He and a 50-50 ice-rock mixture from ANEOS (Thompson 1990) for the metals. Giant planets gradually cool by radiating away the residual heat left over from their initial formation, which we regulated using the atmosphere models of Fortney et al. (2007) to evolve the planets through time. Finally we used the Bayesian retrieval framework from Thorngren & Fortney (2019) to infer the bulk metallicities consistent with the planet parameters. The planet is cool enough that no anomalous heating effect should be present. The composition is consistent with that of ice (Figure 5.12), which is to say a mixture of ammonia, water, and methane without regard for the actual state of matter. Indeed, the ices in this planet would be mostly supercritical fluids, with possibly plasma near the core, and maybe a small amount of gaseous water in the atmosphere. The only solid material would be iron and rocks.

Our models show that to reproduce the planet's high bulk density ($\rho_{\rm p}$= $3.98^{+0.62}_{-0.64}$ g cm^{-3}), a metallicity of Z=0.90±0.03 was required (see Figure 5.11). As such, it is among the most metal rich planets of this mass range, and raises questions about how the planet formation process can gather so much metals without also accreting more H/He. While extreme, this is not truly an outlier: other planets in this mass range are also found to have high metallicities (see Thorngren et al. 2016), including Kepler-413 b ($M_{\rm p} = 0.21\,M_{\rm J}$, $Z \simeq 0.89$, Kostov et al. 2014) and K2-27 b ($M_{\rm p} = 0.09\,M_{\rm J}$, $Z \simeq 0.84$, Van Eylen et al. 2016). It could be that these highly metallic, and massive planets, were formed through collisions with other worlds after the proto-planetary disk had dispersed, stripping the planet of gas whilst enriching it with further metals. Indeed the results here imply that the heavy element enrichment for HD 95338 b is of order $\sim 38\,M_{\oplus}$. It is important to note that the radius measurement of this planet is sufficiently precise that modeling uncertainties are larger than statistical uncertainties. These principally include uncertainties in the EOS, the interior structure of the planet (core-dominated vs well mixed), and the rock-ice ratio of the metals. However, these uncertainties do not endanger the qualitative conclusion that the planet is extremely metal-rich, and changes would often lead to an even higher inferred Z.

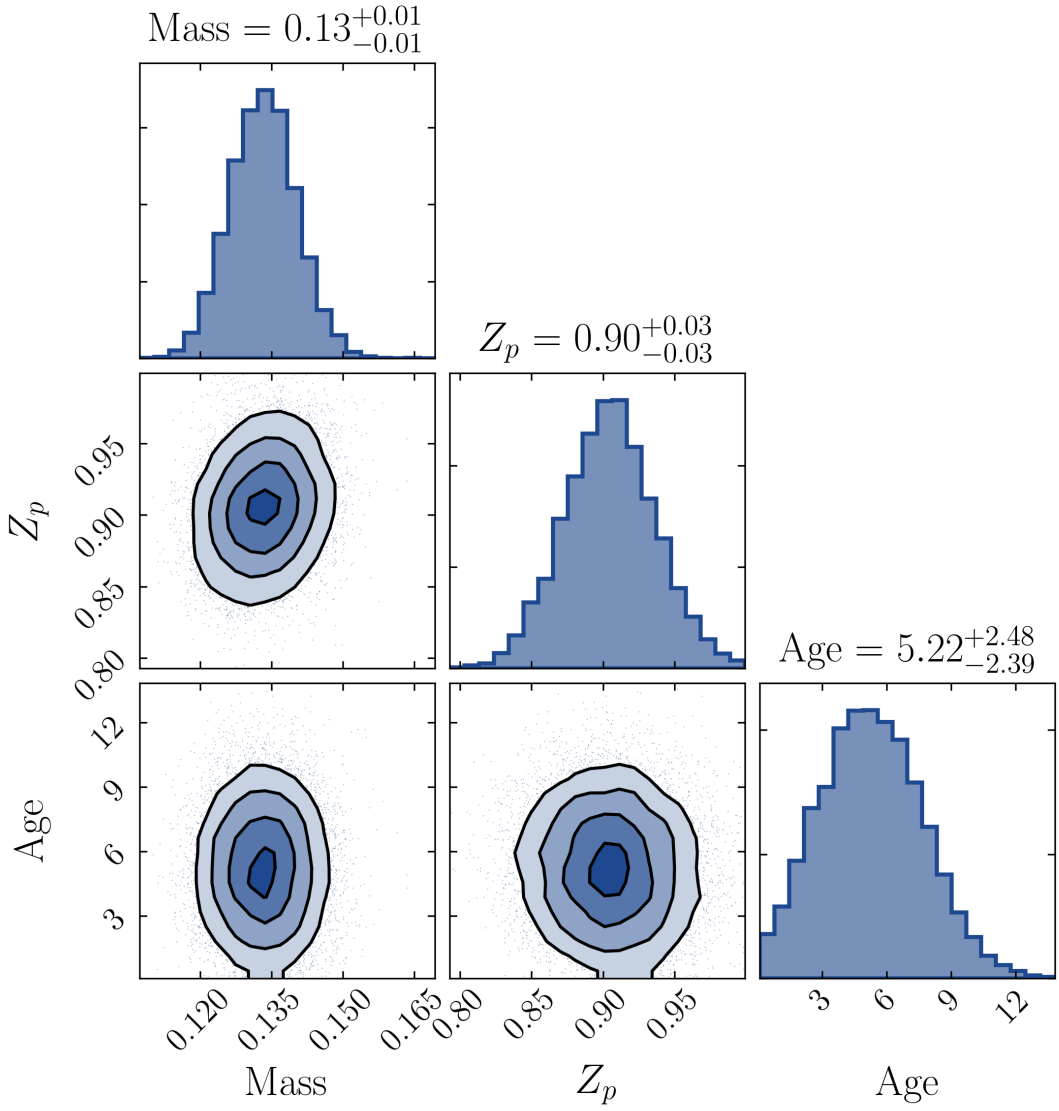

Figure 5.11: Corner plot showing the posteriors of heavy element content derived from the Bayesian retrieval framework described in Thorngren & Fortney (2019).

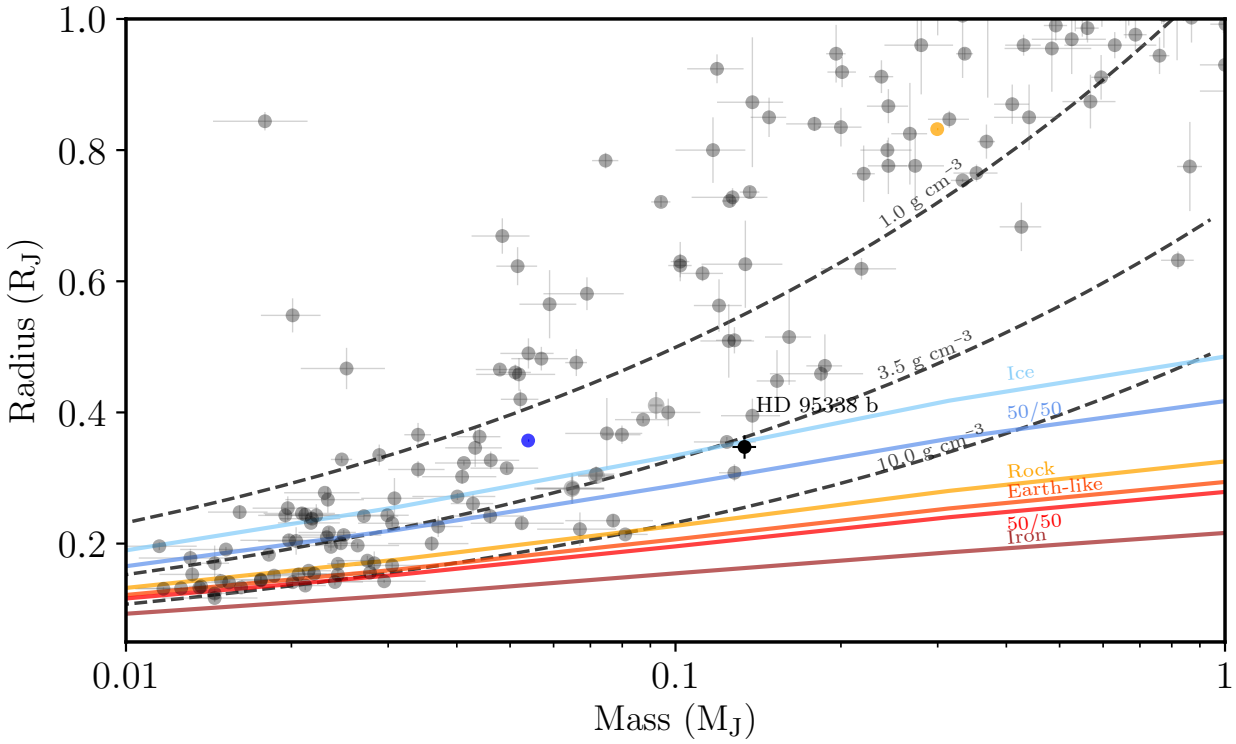

Figure 5.12: Mass-radius diagram. Gray circles represent confirmed exoplanets from `TEPcat` (Southworth 2011) that have radius measurements with a precision of 20% or better. Neptune (blue) and Saturn (yellow) are included for comparison. Three iso-density curves are represented by the grey dashed lines. Composition models are from Fortney et al. (2007), and are shown by the coloured and labelled curves. The observed and derived parameters of HD 95338 b place this planet being consistent with an ice world (see text).

Chapter 6

Summary and conclusions

Through the application of generalized Lomb-Scargle periodograms and tempered MCMC samplings, we conclude that there is a strong periodic signal in the radial velocities of the quiescent and slow rotating K dwarf HD 26965. The evidence presented in Chapter 2, can be interpreted as the Doppler signal induced on the star by an orbiting planet. Our best solution explains these variations by the presence of a low-mass, super-Earth planetary candidate that has a minimum mass of 6.92 ± 0.79 $M_{\oplus}$ orbiting the host star with a period of 42.364 ± 0.015 days and at a distance of 0.215 ± 0.008 AU. The periodogram analysis of V-band photometry from ASAS does not show any significant periodic signal in the data. However, since the amplitude of the signal is small ($\sim$1.5 m s^{-1}), the precision of the data is not sufficient to detect the signal within the noise of the photometry.

Further periodogram analysis of the stellar activity indicators does not show statistical evidence supporting a chromospheric origin for the periodic variations in the radial velocities, although we have found correlations between the radial velocities and the activity indices from the different spectrographs that might deviate even from linear relationships. However, when we analyze the independently acquired chromospheric calcium S-indices from the Mt. Wilson HK project, and after removing two long-period activity cycles, we find evidence for the rotation of the star closely matching the period of the radial velocity detected signal.

Regarding this last point, we note that although it is important to properly include activity correlations into any global model of radial velocity data, which when done for this data set we find a higher statistical probability for the given Keplerian model supporting the planetary signal, if there are statistically significant correlations between activity indicators and the velocity measurements, then additional external activity indicators should be acquired, where possible. Also, moving away from linear correlation models between current activity indices and the radial velocities may be necessary, particularly if the data suggests more complex models, such as quadratics, might be favored. In any case it is clear that the inclusion of multiple sources of external data that also rule out possible magnetic cycles and rotation periods as the source of any radial velocity signal, can help to maintain the lowest false-positive rate for any given Doppler survey.

In summary, despite all the evidence favoring a Doppler signal present in this multi-instrument radial velocity data set, the methods described in this section do not seem to be able to disentangle weak planetary signals from residual photospheric noise, at least when the orbital periods are close

to the rotation period of the star and there are correlations present between the velocities and the measured activity indicators. One possible explanation to the multiple periods found in this study and the ones previously reported in the literature is that we could be measuring the effects of differential rotation on the star.

In Chapter 3 we presented a straightforward methodology to derive iodine-free spectra directly from observations taken through an iodine cell for high resolution spectrographs. This method has successfully been implemented for observations carried out with PFS, HIRES and UCLES. We are currently working on the implementation for other spectrographs that use the iodine cell method, such as APF, UVES and CHIRON.

Although the results shown in herein consider only the well-studied star τ Ceti, we have successfully tested the implementation of this algorithm on other stars with different spectral types, producing similar results when the spectra are of a high quality (high signal-to-noise).

The method works well for most of the stars with F, G and K spectral types, which constitute the bulk population of stars for most spectra types. Stars of spectral type M are currently not supported, but we plan to integrate a module to derive iodine-free spectra for these objects, particularly since they represent ∼15% of the sample we currently monitor as part of the PFS Exoplanet Search.

One particular disadvantage of the implementation presented here is that it currently relies upon the acquisition of a high-quality template (high signal to noise, good weather conditions) as the smallest flaw in the template is carried to the iodine-free spectrum, giving rise to large residuals for a small number of chunks. In any case, if the template observation is good, deriving 1% or better iodine correction is possible with this method.
Derivation of spectral activity indices is the subject of future work. In particular, the case of line bisectors that will be more affected by the asymmetries in the LSF.

In Chapter 4 we have presented the *TESS* discovery of a Neptune-sized planet transiting the G-type star TOI-132 near the edge of the so-called Neptune desert. Confirmation of this candidate comes from high precision HARPS spectroscopic confirms the reality of the transiting planet with a ∼2.11 d orbital period, which when combined with the stellar mass of 0.97 $M_{\odot}$, provides a planetary absolute mass of $21.90^{+1.39}_{-1.46}$ $M_{\oplus}$. Additional ground-based photometry and speckle images provide evidence of the planetary nature of TOI-132 b, ruling out possible blends and stellar companions within the aperture. Modeling the *TESS* light curve returns a planet radius of $3.571^{+0.111}_{-0.121}$ $R_{\oplus}$, yielding a density of $2.651^{+0.299}_{-0.323}$ g cm^{-3}.

Structure models suggest that the planet can have a rocky core, retaining an atmospheric mass fraction of $4.3^{+1.2}_{-2.3}$%. TOI-132 b stands as a *TESS* Level 1 Science Requirement candidate, which aims to precisely determine the masses for 50 transiting planets smaller than $4R_{\oplus}$. Therefore, future follow-up observations will allow the search for additional planets in the TOI-132 system, if any, and also will help to constrain the low-mass planet formation and evolution models, key to better understanding the Neptune desert.

In Chapter 5, we presented the discovery of a dense Neptune-like planet, that is currently the longest period planet known to transit a star brighter than $V = 9$. Moreover, it is the first single transit confirmed planet from the *TESS* mission. It orbits the quiescent early-K star, HD 95338, and was originally detected using long-term radial velocity measurements carried out as part of the Magellan/PFS Exoplanet Survey for 10 years. Additional radial velocity data from HARPS help

to further constrain the period and orbital parameters of the candidate. Examination of publicly available *TESS* photometry shows a single transit event observed in Sector 10.

We used a Moving Average model via MCMC samplings to estimate the best solution for a 1-planet model on the combined radial velocities from PFS and HARPS. From our orbital parameters we estimated the transit time, $T_c = 2458585.929 \pm 0.84$ and found it to be consistent within the errors with the observed transit by *TESS*, $T_{c,TESS} = 2458585.279$, strongly suggesting both signals originate from the same source, and adding credibility to the reality of the planetary nature of the object.

After performing a joint model fit combining the radial velocities and the photometric measurements, we find the planet has a radius of $R_{\rm p}$=$3.89^{+0.19}_{-0.20}\,R_\oplus$ and a mass of $M_{\rm p}$=$42.44^{+2.22}_{-2.08}\,M_\oplus$, giving rise to an anomalously high density for this planet of $\rho_{\rm p}$= $3.98^{+0.62}_{-0.64}$ g cm^{-3}.

Planet structure models place HD 95338 b as being consistent with an ice world based on its mass and radius. From our Bayesian retrieval framework we estimated the heavy element content to be $Z = 0.90 \pm 0.03$, which translates to $\sim 38\,M_\oplus$. Such a high metallic value requires additional modeling efforts to explain and therefore follow-up observations are crucial to arrive at a better understanding of the properties of the planet and also to further constrain models for how such a world could form in the first place. Moreover, the study of spin-orbit alignment of the planet with respect to the star via Rossiter-McLaughlin observations could provide some insights on the past history of the system such as interaction with companions and migration.

Bibliography

Allard, F., Homeier, D., & Freytag, B. 2012, Philosophical Transactions of the Royal Society A: Mathematical, Physical and Engineering Sciences, 370, 2765

Aller, A., Lillo-Box, J., Jones, D., Miranda, L. F., & Barceló Forteza, S. 2020, A&A, 635, A128

Alonso-Floriano, F. J., Sánchez-López, A., Snellen, I. A. G., et al. 2019, A&A, 621, A74

Anderson, E., & Francis, C. 2012, Astronomy Letters, 38, 331

Anglada-Escudé, G., & Butler, R. P. 2012, ApJS, 200, 15

Anglada-Escudé, G., & Tuomi, M. 2015, Science, 347, 1080

Anglada-Escudé, G., Arriagada, P., Vogt, S. S., et al. 2012, ApJL, 751, L16

Anglada-Escudé, G., Tuomi, M., Gerlach, E., et al. 2013, A&A, 556, A126

Anglada-Escudé, G., Amado, P. J., Barnes, J., et al. 2016a, Nature, 536, 437

Anglada-Escudé, G., Tuomi, M., Arriagada, P., et al. 2016b, ApJ, 830, 74

Armstrong, D. J., Lopez, T. A., Adibekyan, V., et al. 2020, Nature, 583, 39

Arriagada, P. 2011, ApJ, 734, 70

Arriagada, P., Butler, R. P., Minniti, D., et al. 2010, ApJ, 711, 1229

Babcock, H. W. 1961, ApJ, 133, 572

Bakos, G. Á., Csubry, Z., Penev, K., et al. 2013, PASP, 125, 154

Baliunas, S., Sokoloff, D., & Soon, W. 1996, ApJL, 457, L99

Baraffe, I., Chabrier, G., & Barman, T. 2010, Reports on Progress in Physics, 73, 016901

Baranne, A., Queloz, D., Mayor, M., et al. 1996, A&AS, 119, 373

Barden, S. C., Ramsey, L. W., & Truax, R. J. 1981, Publications of the Astronomical Society of the Pacific, 93, 154. https://doi.org/10.1086/130795

Barragán, O., Gandolfi, D., & Antoniciello, G. 2019a, MNRAS, 482, 1017

Barragán, O., Aigrain, S., Kubyshkina, D., et al. 2019b, MNRAS, 490, 698

Baskin, N. J., Knutson, H. A., Burrows, A., et al. 2013, ApJ, 773, 124

Batalha, N. M., Rowe, J. F., Bryson, S. T., et al. 2013, ApJS, 204, 24

Beaugé, C., & Nesvorný, D. 2013, The Astrophysical Journal, 763, 12

Benítez-Llambay, P., Masset, F., & Beaugé, C. 2011, Astronomy and Astrophysics, 528, A2

Bevington, P. R., & Robinson, D. K. 2003, Data reduction and error analysis for the physical sciences

Birkby, J. L., de Kok, R. J., Brogi, M., et al. 2013, MNRAS, 436, L35

Black, D. C. 1980, SSRv, 25, 35

Black, D. C. 1981, in NASA Conference Publication, Vol. 2156, NASA Conference Publication, ed. J. Billingham, 163–176

Boisse, I., Bonfils, X., & Santos, N. C. 2012, A&A, 545, A109

Boisse, I., Bouchy, F., Hébrard, G., et al. 2011, A&A, 528, A4

Borucki, W. J., Koch, D., Basri, G., et al. 2010, Science, 327, 977

Bouchy, F., Pepe, F., & Queloz, D. 2001, A&A, 374, 733

Bouchy, F., Udry, S., Mayor, M., et al. 2005, A&A, 444, L15

Bourrier, V., Lecavelier des Etangs, A., Dupuy, H., et al. 2013, A&A, 551, A63

Brahm, R., Jordán, A., Bakos, G. Á., et al. 2016, AJ, 151, 89

Brahm, R., Espinoza, N., Jordán, A., et al. 2019, AJ, 158, 45

Brewer, J. M., Giguere, M., & Fischer, D. A. 2014, PASP, 126, 48

Brogi, M., Giacobbe, P., Guilluy, G., et al. 2018, A&A, 615, A16

Brown, T. M., Baliber, N., Bianco, F. B., et al. 2013, Publications of the Astronomical Society of the Pacific, 125, 1031

Buchhave, L. A., Latham, D. W., Johansen, A., et al. 2012, Nature, 486, 375

Burt, J., Feng, F., Holden, B., et al. 2021, AJ, 161, 10

Burt, J. A., Nielsen, L. D., Quinn, S. N., et al. 2020, AJ, 160, 153

Butler, R. P., & Marcy, G. W. 1996, ApJL, 464, L153

Butler, R. P., Marcy, G. W., Fischer, D. A., et al. 1999, ApJ, 526, 916

Butler, R. P., Marcy, G. W., Williams, E., et al. 1996, PASP, 108, 500

Campbell, B., & Walker, G. A. H. 1979, PASP, 91, 540

Casasayas-Barris, N., Pallé, E., Yan, F., et al. 2019, A&A, 628, A9

Castelli, F., & Kurucz, R. L. 2004, ArXiv Astrophysics e-prints, astro-ph/0405087

Cegla, H. M., Watson, C. A., Shelyag, S., Mathioudakis, M., & Moutari, S. 2019, ApJ, 879, 55

Ceillier, T., Tayar, J., Mathur, S., et al. 2017, A&A, 605, A111

Chabrier, G., Mazevet, S., & Soubiran, F. 2019, ApJ, 872, 51

Charbonneau, D., Brown, T. M., Latham, D. W., & Mayor, M. 2000, ApJL, 529, L45

Charbonneau, D., Brown, T. M., Noyes, R. W., & Gilliland, R. L. 2002, ApJ, 568, 377

Chen, G., van Boekel, R., Madhusudhan, N., et al. 2014, A&A, 564, A6

Chen, H., & Rogers, L. A. 2016, ApJ, 831, 180

Coşkunoğlu, B., Ak, S., Bilir, S., et al. 2011, MNRAS, 412, 1237

Collier Cameron, A., Ford, E. B., Shahaf, S., et al. 2021, MNRAS, 505, 1699

Collins, K. A., Kielkopf, J. F., Stassun, K. G., & Hessman, F. V. 2017, AJ, 153, 77

Courcol, B., Bouchy, F., & Deleuil, M. 2016, MNRAS, 461, 1841

Crane, J. D., Shectman, S. A., & Butler, R. P. 2006, in Proc. SPIE, Vol. 6269, Society of Photo-Optical Instrumentation Engineers (SPIE) Conference Series, 626931

Crane, J. D., Shectman, S. A., Butler, R. P., et al. 2010, in Proc. SPIE, Vol. 7735, Ground-based and Airborne Instrumentation for Astronomy III, 773553

Crane, J. D., Shectman, S. A., Butler, R. P., Thompson, I. B., & Burley, G. S. 2008, in Proc. SPIE, Vol. 7014, Ground-based and Airborne Instrumentation for Astronomy II, 701479

Curiel, S., Cantó, J., Georgiev, L., Chávez, C. E., & Poveda, A. 2011, A&A, 525, A78

de Mooij, E. J. W., López-Morales, M., Karjalainen, R., Hrudkova, M., & Jayawardhana, R. 2014, ApJL, 797, L21

Debosscher, J., Sarro, L. M., Aerts, C., et al. 2007, A&A, 475, 1159

Dekker, H., D'Odorico, S., Kaufer, A., Delabre, B., & Kotzlowski, H. 2000, in Society of Photo-Optical Instrumentation Engineers (SPIE) Conference Series, Vol. 4008, Optical and IR Telescope Instrumentation and Detectors, ed. M. Iye & A. F. Moorwood, 534–545

Díaz, M. R., Jenkins, J. S., Tuomi, M., et al. 2018, AJ, 155, 126

Díaz, M. R., Jenkins, J. S., Gand olfi, D., et al. 2020a, MNRAS, 252

Díaz, M. R., Jenkins, J. S., Feng, F., et al. 2020b, MNRAS, 496, 4330

Diego, F., Charalambous, A., C. Fish, A., & Walker, D. 1990, 1235

Dong, S., Xie, J.-W., Zhou, J.-L., Zheng, Z., & Luo, A. 2018, Proceedings of the National Academy of Science, 115, 266

Dotter, A. 2016, ApJS, 222, 8

Dotter, A., Chaboyer, B., Jevremović, D., et al. 2008, ApJS, 178, 89

Dragomir, D., Teske, J., Günther, M. N., et al. 2019, ApJL, 875, L7

Dumusque, X., Udry, S., Lovis, C., Santos, N. C., & Monteiro, M. J. P. F. G. 2011, A&A, 525, A140

Duncan, D. K., Vaughan, A. H., Wilson, O. C., et al. 1991, ApJS, 76, 383

Earl, D. J., & Deem, M. W. 2005, Phys. Chem. Chem. Phys., 7, 3910. http://dx.doi.org/10.1039/B509983H

Eastman, J. 2017, EXOFASTv2: Generalized publication-quality exoplanet modeling code, , , ascl:1710.003

Eastman, J., Gaudi, B. S., & Agol, E. 2013, PASP, 125, 83

Espinoza, N. 2018, Efficient Joint Sampling of Impact Parameters and Transit Depths in Transiting Exoplanet Light Curves, , , arXiv:1811.04859

Espinoza, N., & Jordán, A. 2016, MNRAS, 457, 3573

Espinoza, N., Kossakowski, D., & Brahm, R. 2019a, MNRAS, 490, 2262

Espinoza, N., Bayliss, D., Hartman, J. D., et al. 2016, The Astronomical Journal, 152, 108

Espinoza, N., Brahm, R., Henning, T., et al. 2019b, arXiv e-prints, arXiv:1903.07694

Esposito, M., Armstrong, D. J., Gandolfi, D., et al. 2019, A&A, 623, A165

Evans, J. W., & Michard, R. 1962, ApJ, 136, 493

Feng, F., Anglada-Escudé, G., Tuomi, M., et al. 2019, MNRAS, 490, 5002

Feng, F., Tuomi, M., & Jones, H. R. A. 2017a, MNRAS, 470, 4794

Feng, F., Tuomi, M., Jones, H. R. A., et al. 2017b, AJ, 154, 135

Feng, F., Tuomi, M., Jones, H. R. A., Butler, R. P., & Vogt, S. 2016, MNRAS, 461, 2440

Feng, F., Crane, J. D., Wang, S. X., et al. 2019, The Astrophysical Journal Supplement Series, 242, 25. http://dx.doi.org/10.3847/1538-4365/ab1b16

Figueira, P., Marmier, M., Bonfils, X., et al. 2010, A&A, 513, L8

Foreman-Mackey, D. 2016, The Journal of Open Source Software, 24, doi:10.21105/joss.00024. http://dx.doi.org/10.5281/zenodo.45906

Fortney, J. J., Marley, M. S., & Barnes, J. W. 2007, ApJ, 659, 1661

Frank, C., Kerber, F., Avila, G., et al. 2018, in Ground-based and Airborne Instrumentation for Astronomy VII, ed. C. J. Evans, L. Simard, & H. Takami, Vol. 10702, International Society for Optics and Photonics (SPIE), 2047 – 2056. https://doi.org/10.1117/12.2313484

Fridlund, M., Gaidos, E., Barragán, O., et al. 2017, A&A, 604, A16

Fulton, B. J., Petigura, E. A., Blunt, S., & Sinukoff, E. 2018, PASP, 130, 044504

Fulton, B. J., Petigura, E. A., Howard, A. W., et al. 2017, AJ, 154, 109

Gaia Collaboration, Prusti, T., de Bruijne, J. H. J., et al. 2016, A&A, 595, A1

Gaia Collaboration, Brown, A. G. A., Vallenari, A., et al. 2018, A&A, 616, A1

Gandolfi, D., Fossati, L., Livingston, J. H., et al. 2019, ApJL, 876, L24

Gangestad, J. W., Henning, G. A., Persinger, R. R., & Ricker, G. R. 2013, arXiv e-prints, arXiv:1306.5333

Gao, P., Plavchan, P., Gagné, J., et al. 2016, PASP, 128, 104501

García, R. A., Ceillier, T., Salabert, D., et al. 2014, A&A, 572, A34

Giles, H. A. C., Collier Cameron, A., & Haywood, R. D. 2017, MNRAS, 472, 1618

Gilks, W., Richardson, S., & Spiegelhalter, D. 1995, Markov Chain Monte Carlo in Practice, Chapman and Hall/CRC Interdisciplinary Statistics (Taylor and Francis). https://books.google.cl/books?id=TRXrMWY_i2IC

Gilliland, R. L., Morris, S. L., Weymann, R. J., Ebbets, D. C., & Lindler, D. J. 1992, PASP, 104, 367

Glebocki, R., & Gnacinski, P. 2005, VizieR Online Data Catalog, 3244

Goggans, P. M., & Chi, Y. 2004, AIP Conference Proceedings, 707, 59. https://aip.scitation.org/doi/abs/10.1063/1.1751356

Gray, R. O., Corbally, C. J., Garrison, R. F., et al. 2006, AJ, 132, 161

Griffin, R., & Griffin, R. 1973, MNRAS, 162, 243

Guerrero, N. M., Seager, S., Huang, C. X., et al. 2021, arXiv e-prints, arXiv:2103.12538

Haario, H., Laine, M., Mira, A., & Saksman, E. 2006, Statistics and Computing, 16, 339. http://dblp.uni-trier.de/db/journals/sac/sac16.html#HaarioLMS06

Haario, H., Saksman, E., & Tamminen, J. 2001, Bernoulli, 7, 223. http://projecteuclid.org/euclid.bj/1080222083

Halverson, S., Roy, A., Mahadevan, S., et al. 2015, ApJ, 806, 61

Hastings, W. K. 1970, Biometrika, 57, 97

Hatzes, A. P. 2002, Astronomische Nachrichten, 323, 392

Hauschildt, P. H., Allard, F., & Baron, E. 1999, The Astrophysical Journal, 629, 865

Haywood, R. D., Collier Cameron, A., Queloz, D., et al. 2014, MNRAS, 443, 2517

Heacox, W. D. 1986, AJ, 92, 219

Helled, R., Lozovsky, M., & Zucker, S. 2016, Monthly Notices of the Royal Astronomical Society, 455, L96

Henry, G. W., Marcy, G. W., Butler, R. P., & Vogt, S. S. 2000, ApJL, 529, L41

Hidalgo, D., Pallé, E., Alonso, R., et al. 2020, arXiv e-prints, arXiv:2002.01755

Hobson, M. P., & McLachlan, C. 2003, MNRAS, 338, 765

Hsu, D. C., Ford, E. B., Ragozzine, D., & Ashby, K. 2019, AJ, 158, 109

Huang, C. X., Burt, J., Vanderburg, A., et al. 2018, ApJL, 868, L39

Huang, C. X., Vanderburg, A., Pál, A., et al. 2020a, Research Notes of the American Astronomical Society, 4, 204

—. 2020b, Research Notes of the American Astronomical Society, 4, 206

Husser, T.-O., von Berg, S. W., Dreizler, S., et al. 2013, Astronomy & Astrophysics, 553, A6. http://arxiv.org/abs/1303.5632{%}0Ahttp://dx.doi.org/10.1051/0004-6361/201219058

Ivezic, Z., Connolly, A. J., VanderPlas, J. T., & Gray, A. 2014, Statistics, Data Mining, and Machine Learning in Astronomy: A Practical Python Guide for the Analysis of Survey Data (USA:

Princeton University Press)

Izidoro, A., Bitsch, B., Raymond, S. N., et al. 2021, A&A, 650, A152

Izidoro, A., Morbidelli, A., Raymond, S. N., Hersant, F., & Pierens, A. 2015, A&A, 582, A99

Jansson, P. A. 1984, Deconvolution: With Applications in Spectroscopy, With Applications in Spectroscopy (Academic Press). https://books.google.cl/books?id=QjpjPgAACAAJ

Jenkins, J. M. 2002, ApJ, 575, 493

—. 2017, Kepler Data Processing Handbook: Overview of the Science Operations Center, Tech. rep.

Jenkins, J. M., Twicken, J., Tenenbaum, P., et al. 2020a, in American Astronomical Society Meeting Abstracts, Vol. 235, American Astronomical Society Meeting Abstracts #235, 327.02

Jenkins, J. M., Chandrasekaran, H., McCauliff, S. D., et al. 2010, in Society of Photo-Optical Instrumentation Engineers (SPIE) Conference Series, Vol. 7740, Proc. SPIE, 77400D

Jenkins, J. M., Twicken, J. D., McCauliff, S., et al. 2016a, in Proc. SPIE, Vol. 9913, Software and Cyberinfrastructure for Astronomy IV, 99133E

Jenkins, J. S., Jones, H. R. A., Pavlenko, Y., et al. 2008, A&A, 485, 571

Jenkins, J. S., Pozuelos, F. J., Tuomi, M., et al. 2019, MNRAS, 490, 5585

Jenkins, J. S., & Tuomi, M. 2014, ApJ, 794, 110

Jenkins, J. S., Jones, H. R. A., Tinney, C. G., et al. 2006, MNRAS, 372, 163

Jenkins, J. S., Jones, H. R. A., Goździewski, K., et al. 2009, MNRAS, 398, 911

Jenkins, J. S., Murgas, F., Rojo, P., et al. 2011, A&A, 531, A8

Jenkins, J. S., Jones, H. R. A., Tuomi, M., et al. 2013, ApJ, 766, 67

—. 2016b, ArXiv e-prints, arXiv:1603.09391

—. 2017, MNRAS, 466, 443

Jenkins, J. S., Díaz, M. R., Kurtovic, N. T., et al. 2020b, Nature Astronomy, arXiv:2009.12832

Jensen, E. 2013, Tapir: A web interface for transit/eclipse observability, Astrophysics Source Code Library, , , ascl:1306.007

Jin, S., Mordasini, C., Parmentier, V., et al. 2014, ApJ, 795, 65

Johnson, D. R. H., & Soderblom, D. R. 1987, AJ, 93, 864

Jones, M. I., & Jenkins, J. S. 2014, A&A, 562, A129

Jones, M. I., Jenkins, J. S., Brahm, R., et al. 2016, A&A, 590, A38

Jordán, A., Brahm, R., Espinoza, N., et al. 2019, arXiv e-prints, arXiv:1911.05574

Kaltenegger, L., Segura, A., & Mohanty, S. 2011, ApJ, 733, 35

Kanodia, S., Stefansson, G., Cañas, C. I., et al. 2021, AJ, 162, 135

Kass, R. E., & Raftery, A. E. 1995, Journal of the American Statistical Association, 90, 773. https:

//www.tandfonline.com/doi/abs/10.1080/01621459.1995.10476572

Kipping, D. M. 2013, MNRAS, 435, 2152

Konopliv, A. S., Yoder, C. F., Standish, E. M., Yuan, D.-N., & Sjogren, W. L. 2006, Icarus, 182, 23

Kopparapu, R. K., Ramirez, R., Kasting, J. F., et al. 2013a, ApJ, 770, 82

—. 2013b, ApJ, 765, 131

Kossakowski, D., Espinoza, N., Brahm, R., et al. 2019, arXiv e-prints, arXiv:1906.09866

Kostov, V. B., McCullough, P. R., Carter, J. A., et al. 2014, ApJ, 784, 14

Kreidberg, L. 2015, PASP, 127, 1161

Kreidberg, L., Line, M. R., Bean, J. L., et al. 2015, ApJ, 814, 66

Kurucz, R. L. 1993, VizieR Online Data Catalog, 6039

Lambrechts, M., & Johansen, A. 2012, A&A, 544, A32

Lambrechts, M., & Lega, E. 2017, A&A, 606, A146

Lanotte, A. A., Gillon, M., Demory, B.-O., et al. 2014, A&A, 572, A73

Latham, D. W., Rowe, J. F., Quinn, S. N., et al. 2011, ApJL, 732, L24

Lecavelier des Etangs, A., Bourrier, V., Wheatley, P. J., et al. 2012, A&A, 543, L4

Leighton, R. B., Noyes, R. W., & Simon, G. W. 1962, ApJ, 135, 474

Levenberg, K. 1944, Quarterly of Applied Mathematics, 2, 164. http://www.jstor.org/stable/43633451

Li, J., Tenenbaum, P., Twicken, J. D., et al. 2019, PASP, 131, 024506

Lissauer, J. J., Ragozzine, D., Fabrycky, D. C., et al. 2011, ApJS, 197, 8

Lomb, N. R. 1976, Ap&SS, 39, 447

Lopez, E. D., & Fortney, J. J. 2013, ApJ, 776, 2

—. 2014, The Astrophysical Journal, 792, 1

Lopez, S., & Jenkins, J. S. 2012, ApJ, 756, 177

Lovis, C., Dumusque, X., Santos, N. C., et al. 2011, arXiv e-prints, arXiv:1107.5325

Lu, C. X., Schlaufman, K. C., & Cheng, S. 2020, AJ, 160, 253

Lundkvist, M. S., Kjeldsen, H., Albrecht, S., et al. 2016, Nature Communications, 7, 11201

Luque, R., Nowak, G., Pallé, E., et al. 2019, A&A, 623, A114

Mamajek, E. E., & Hillenbrand, L. A. 2008, ApJ, 687, 1264

Mann, A. W., Gaidos, E., Vanderburg, A., et al. 2017, AJ, 153, 64

Marcy, G. W., & Butler, R. P. 1992, PASP, 104, 270

—. 1996, ApJL, 464, L147

Marcy, G. W., Butler, R. P., Vogt, S. S., Fischer, D., & Liu, M. C. 1999, ApJ, 520, 239

Marcy, G. W., Isaacson, H., Howard, A. W., et al. 2014, ApJS, 210, 20

Marquardt, D. W. 1963, Journal of the Society for Industrial and Applied Mathematics, 11, 431. http://www.jstor.org/stable/2098941

Mathur, S., García, R. A., Régulo, C., et al. 2010, A&A, 511, A46

Matsumoto, Y., & Kokubo, E. 2017, AJ, 154, 27

Mayo, A. W., Rajpaul, V. M., Buchhave, L. A., et al. 2019, The Astronomical Journal, 158, 165. https://doi.org/10.3847%2F1538-3881%2Fab3e2f

Mayor, M., & Queloz, D. 1995, Nature, 378, 355

Mayor, M., Pepe, F., Queloz, D., et al. 2003, The Messenger, 114, 20

Mayor, M., Udry, S., Lovis, C., et al. 2009, A&A, 493, 639

Mazeh, T., Holczer, T., & Faigler, S. 2016, Astronomy and Astrophysics, 589, A75

McCully, C., Turner, M., Volgenau, N., et al. 2018, LCOGT/banzai: Initial Release, v0.9.4, Zenodo, doi:10.5281/zenodo.1257560. https://doi.org/10.5281/zenodo.1257560

McLaughlin, D. B. 1924, ApJ, 60, doi:10.1086/142826

Meléndez, J., Bedell, M., Bean, J. L., et al. 2017, A&A, 597, A34

Meschiari, S., Wolf, A. S., Rivera, E., et al. 2009, PASP, 121, 1016

Metropolis, N., Rosenbluth, A. W., Rosenbluth, M. N., Teller, A. H., & Teller, E. 1953, J. Chem. Phys. J. Chem. Phys. J. Homepage, 21, doi:10.1063/1.1699114. http://dx.doi.org/10.1063/1.1699114http://jcp.aip.org/resource/1/JCPSA6/v21/i6http://jcp.aip.org/http://jcp.aip.org/about/about{_}the{_}journalhttp://jcp.aip.org/features/most{_}downloadedhttp://jcp.aip.org/authors

Meunier, N., Lagrange, A. M., Borgniet, S., & Rieutord, M. 2015, A&A, 583, A118

Milbourne, T. W., Haywood, R. D., Phillips, D. F., et al. 2019, ApJ, 874, 107

Mira, A. 2001, Metron - International Journal of Statistics, 0, 231. https://ideas.repec.org/a/mtn/ancoec/2001316.html

Mordasini, C., Alibert, Y., Benz, W., & Naef, D. 2008, in Astronomical Society of the Pacific Conference Series, Vol. 398, Extreme Solar Systems, ed. D. Fischer, F. A. Rasio, S. E. Thorsett, & A. Wolszczan, 235

Morton, T. D. 2015, isochrones: Stellar model grid package, , , ascl:1503.010

Mulders, G. D. 2018, Planet Populations as a Function of Stellar Properties, 153

Mulders, G. D., Pascucci, I., Apai, D., & Ciesla, F. J. 2018, AJ, 156, 24

Mulders, G. D., Pascucci, I., Apai, D., Frasca, A., & Molenda-Zakowicz, J. 2016, ArXiv e-prints, arXiv:1609.05898

Murgas, F., Jenkins, J. S., Rojo, P., Jones, H. R. A., & Pinfield, D. J. 2013, A&A, 552, A27

Murgas, F., Astudillo-Defru, N., Bonfils, X., et al. 2021, A&A, 653, A60

Nascimbeni, V., Piotto, G., Pagano, I., et al. 2013, A&A, 559, A32

Nelson, B. E., Ford, E. B., & Rasio, F. A. 2017, AJ, 154, 106

Niedzielski, A., Goździewski, K., Wolszczan, A., et al. 2009, ApJ, 693, 276

Nowak, G., Niedzielski, A., & Wolszczan, A. 2010, in EAS Publications Series, Vol. 42, EAS Publications Series, ed. K. Gożdziewski, A. Niedzielski, & J. Schneider, 165–168

Noyes, R. W., Hartmann, L. W., Baliunas, S. L., Duncan, D. K., & Vaughan, A. H. 1984, ApJ, 279, 763

O'Toole, S. J., Tinney, C. G., & Jones, H. R. A. 2008, MNRAS, 386, 516

Owen, J. E., & Lai, D. 2018, Monthly Notices of the Royal Astronomical Society, 479, 5012

Owen, J. E., & Wu, Y. 2013, ApJ, 775, 105

Palle, E., Nowak, G., Luque, R., et al. 2019, A&A, 623, A41

Paneque-Carreño, T., & Jenkins, J. S. 2019, A&A, Submitted

Pavlenko, Y. V., Jenkins, J. S., Jones, H. R. A., Ivanyuk, O., & Pinfield, D. J. 2012, MNRAS, 422, 542

Pepe, F., Mayor, M., Galland, F., et al. 2002a, A&A, 388, 632

Pepe, F., Mayor, M., Rupprecht, G., et al. 2002b, The Messenger, 110, 9

Pepe, F., Cristiani, S., Rebolo, R., et al. 2020, arXiv e-prints, arXiv:2010.00316

Pepe, F. A., Cristiani, S., Rebolo Lopez, R., et al. 2010, in Proc. SPIE, Vol. 7735, Ground-based and Airborne Instrumentation for Astronomy III, 77350F

Perryman, M. 2011, The Exoplanet Handbook (Cambridge University Press), doi:10.1017/CBO9780511994852

Persson, C. M., Fridlund, M., Barragán, O., et al. 2018, A&A, 618, A33

Persson, C. M., Csizmadia, S., Mustill, A. e. J., et al. 2019, A&A, 628, A64

Petigura, E. A., Howard, A. W., & Marcy, G. W. 2013, Proceedings of the National Academy of Science, 110, 19273

Petigura, E. A., Marcy, G. W., Winn, J. N., et al. 2018, AJ, 155, 89

Piskunov, N., & Valenti, J. A. 2017, A&A, 597, A16

Pizzolato, N., Maggio, A., Micela, G., Sciortino, S., & Ventura, P. 2003, A&A, 397, 147

Pojmanski, G. 1997, 47, 467

Queloz, D. 1995, Symposium - International Astronomical Union, 167, 221–229

Queloz, D., Henry, G. W., Sivan, J. P., et al. 2001, A&A, 379, 279

Quirrenbach, A., Amado, P. J., Caballero, J. A., et al. 2016, in Society of Photo-Optical Instrumentation Engineers (SPIE) Conference Series, Vol. 9908, Ground-based and Airborne Instrumentation for Astronomy VI, ed. C. J. Evans, L. Simard, & H. Takami, 990812

Raftery, A. E., & Lewis, S. M. 1992, Statistical Science, 7, 493. http://www.jstor.org/stable/2246100

Rajpaul, V., Aigrain, S., Osborne, M. A., Reece, S., & Roberts, S. 2015, MNRAS, 452, 2269

Rajpaul, V., Aigrain, S., & Roberts, S. 2016, MNRAS, 456, L6

Raychaudhuri, P. 1972, Ap&SS, 18, 425

Raymond, S. N., & Morbidelli, A. 2022, in Astrophysics and Space Science Library, Vol. 466, Astrophysics and Space Science Library, ed. K. Biazzo, V. Bozza, L. Mancini, & A. Sozzetti, 3–82

Reddy, B. E., Lambert, D. L., & Allende Prieto, C. 2006, MNRAS, 367, 1329

Ribas, I., Tuomi, M., Reiners, A., et al. 2018, Nature, 563, 365

Ricker, G. R., Winn, J. N., Vanderspek, R., et al. 2015, Journal of Astronomical Telescopes, Instruments, and Systems, 1, 014003

Rivera, E. J., Laughlin, G., Butler, R. P., et al. 2010, ApJ, 719, 890

Rivera, E. J., Lissauer, J. J., Butler, R. P., et al. 2005, ApJ, 634, 625

Roberts, G. O., Gelman, A., & Gilks, W. R. 1997, Ann. Appl. Probab., 7, 110. http://dx.doi.org/10.1214/aoap/1034625254

Robertson, P., Mahadevan, S., Endl, M., & Roy, A. 2014, Science, 345, 440

Robertson, P., Roy, A., & Mahadevan, S. 2015, ApJL, 805, L22

Rosenblatt, F. 1971, Icarus, 14, 71

Rossiter, R. A. 1924, ApJ, 60, doi:10.1086/142825

Saar, S. H. 1998, in Astronomical Society of the Pacific Conference Series, Vol. 154, Cool Stars, Stellar Systems, and the Sun, ed. R. A. Donahue & J. A. Bookbinder, 211

Saar, S. H., & Donahue, R. A. 1997, ApJ, 485, 319

Saar, S. H., & Osten, R. A. 1997, MNRAS, 284, 803

Salz, M., Czesla, S., Schneider, P. C., & Schmitt, J. H. M. M. 2016, A&A, 586, A75

Sandford, E., Espinoza, N., Brahm, R., & Jordán, A. 2019, Monthly Notices of the Royal Astronomical Society, 489, 3149. https://doi.org/10.1093/mnras/stz2348

Santerne, A., Díaz, R. F., Almenara, J. M., et al. 2015, MNRAS, 451, 2337

Santos, A. R. G., García, R. A., Mathur, S., et al. 2019, ApJS, 244, 21

Santos, N. C., Mortier, A., Faria, J. P., et al. 2014, A&A, 566, A35

Scargle, J. D. 1982, ApJ, 263, 835

Schlafly, E. F., & Finkbeiner, D. P. 2011, Astrophysical Journal, 737, doi:10.1088/0004-637X/737/2/103

Schlegel, D. J., Finkbeiner, D. P., & Davis, M. 1998, ApJ, 500, 525

Schuler, S. C., Vaz, Z. A., Katime Santrich, O. J., et al. 2015, ApJ, 815, 5

Schwarzschild, K., & Villiger, W. 1906, ApJ, 23, 284

Seager, S., & Mallén-Ornelas, G. 2003, ApJ, 585, 1038

Skrutskie, M. F., Cutri, R. M., Stiening, R., et al. 2006, AJ, 131, 1163

Smith, J. C., Stumpe, M. C., Van Cleve, J. E., et al. 2012, PASP, 124, 1000

Sneden, C. A. 1973a, PhD thesis, THE UNIVERSITY OF TEXAS AT AUSTIN.

—. 1973b, PhD thesis, THE UNIVERSITY OF TEXAS AT AUSTIN.

Soto, M. G., & Jenkins, J. S. 2018, A&A, 615, A76

Sousa, S. G., Santos, N. C., Israelian, G., Mayor, M., & Monteiro, M. J. P. F. G. 2007, A&A, 469, 783

Southworth, J. 2011, MNRAS, 417, 2166

Speagle, J. S. 2019, arXiv e-prints, arXiv:1904.02180

Speagle, J. S., & Barbary, K. 2018, dynesty: Dynamic Nested Sampling package, Astrophysics Source Code Library, , , ascl:1809.013

Spronck, J. F. P., Fischer, D. A., Kaplan, Z. A., Schwab, C., & Szymkowiak, A. 2013, Publications of the Astronomical Society of the Pacific, 125, 511. https://doi.org/10.1086/670814

Stassun, K. G., Collins, K. A., & Gaudi, B. S. 2017, AJ, 153, 136

Stassun, K. G., Corsaro, E., Pepper, J. A., & Gaudi, B. S. 2018a, AJ, 155, 22

Stassun, K. G., & Torres, G. 2016, AJ, 152, 180

—. 2018, ApJ, 862, 61

Stassun, K. G., Oelkers, R. J., Pepper, J., et al. 2018b, AJ, 156, 102

Steenbeck, M., & Krause, F. 1969, Astronomische Nachrichten, 291, 49

Steinmetz, T., Wilken, T., Araujo-Hauck, C., et al. 2008, Science, 321, 1335. https://science.sciencemag.org/content/321/5894/1335

Stumpe, M. C., Smith, J. C., Catanzarite, J. H., et al. 2014, PASP, 126, 100

Suárez Mascareño, A., Faria, J. P., Figueira, P., et al. 2020, A&A, 639, A77

Szabó, G. M., & Kiss, L. L. 2011, The Astrophysical Journal, 727, L44

Thompson, S. L. 1990, doi:10.2172/6939284

Thorngren, D., & Fortney, J. J. 2019, ApJL, 874, L31

Thorngren, D. P., Fortney, J. J., Murray-Clay, R. A., & Lopez, E. D. 2016, ApJ, 831, 64

Tinney, C. G., McCarthy, C., Jones, H. R. A., et al. 2002, MNRAS, 332, 759

Tokovinin, A., Fischer, D. A., Bonati, M., et al. 2013, PASP, 125, 1336

Tokovinin, A., Mason, B. D., Hartkopf, W. I., Mendez, R. A., & Horch, E. P. 2018, AJ, 155, 235

Torres, G., Andersen, J., & Giménez, A. 2010, A&A Rv, 18, 67

Tuomi, M. 2012, A&A, 543, A52

Tuomi, M., & Anglada-Escudé, G. 2013a, A&A, 556, A111

—. 2013b, A&A, 556, A111

Tuomi, M., Anglada-Escudé, G., Gerlach, E., et al. 2013a, A&A, 549, A48

Tuomi, M., Anglada-Escude, G., Jenkins, J. S., & Jones, H. R. A. 2014a, ArXiv e-prints, arXiv:1405.2016

Tuomi, M., & Jones, H. R. A. 2012, A&A, 544, A116

Tuomi, M., Jones, H. R. A., Barnes, J. R., Anglada-Escudé, G., & Jenkins, J. S. 2014b, MNRAS, 441, 1545

Tuomi, M., Jones, H. R. A., Jenkins, J. S., et al. 2013b, A&A, 551, A79

Tuomi, M., Jones, H. R. A., Butler, R. P., et al. 2019, arXiv e-prints, arXiv:1906.04644

Turnbull, M. C. 2015, ArXiv e-prints, arXiv:1510.01731

Turner, J. D., de Mooij, E. J. W., Jayawardhana, R., et al. 2020, ApJL, 888, L13

Twicken, J. D., Caldwell, D. A., Davies, M., et al. 2018, in American Astronomical Society Meeting Abstracts, Vol. 232, American Astronomical Society Meeting Abstracts #232, 120.04

Udry, S., & Mayor, M. 2008, in Astronomical Society of the Pacific Conference Series, Vol. 398, Extreme Solar Systems, ed. D. Fischer, F. A. Rasio, S. E. Thorsett, & A. Wolszczan, 13

Ulrich, R. K. 1970, ApJ, 162, 993

Valencia, D., Guillot, T., Parmentier, V., & Freedman, R. S. 2013, ApJ, 775, 10

Valencia, D., Sasselov, D. D., & O'Connell, R. J. 2007, ApJ, 665, 1413

Valenti, J. A., Butler, R. P., & Marcy, G. W. 1995, PASP, 107, 966

Valenti, J. A., & Fischer, D. A. 2005, ApJS, 159, 141

Valenti, J. A., & Piskunov, N. 1996a, A&AS, 118, 595

—. 1996b, A&AS, 118, 595

Van Eylen, V., Agentoft, C., Lundkvist, M. S., et al. 2018, MNRAS, 479, 4786

Van Eylen, V., Albrecht, S., Gandolfi, D., et al. 2016, AJ, 152, 143

Van Eylen, V., Albrecht, S., Huang, X., et al. 2019, AJ, 157, 61

van Leeuwen, F. 2007, A&A, 474, 653

VanderPlas, J. T. 2018, The Astrophysical Journal Supplement Series, 236, 16. https://doi.org/10.3847%2F1538-4365%2Faab766

Venturini, J., & Helled, R. 2017, ApJ, 848, 95

Vines, J. I., & Jenkins, J. S. 2020, in prep

Vines, J. I., Jenkins, J. S., Acton, J. S., et al. 2019, MNRAS, 489, 4125

Vogt, S. S. 2002, in Astronomical Society of the Pacific Conference Series, Vol. 270, Astronomical Instrumentation and Astrophysics, ed. F. N. Bash & C. Sneden, 5

Vogt, S. S., Butler, R. P., Rivera, E. J., et al. 2010, ApJ, 723, 954

Vogt, S. S., Allen, S. L., Bigelow, B. C., et al. 1994, in Proc. SPIE, Vol. 2198, Instrumentation in Astronomy VIII, ed. D. L. Crawford & E. R. Craine, 362

Vogt, S. S., Radovan, M., Kibrick, R., et al. 2014, PASP, 126, 359

von Braun, K., Boyajian, T. S., Kane, S. R., et al. 2012, ApJ, 753, 171

von Paris, P., Gratier, P., Bordé, P., & Selsis, F. 2016, A&A, 587, A149

Walker, G. A. H., Shkolnik, E., Bohlender, D. A., & Yang, S. 2003, PASP, 115, 700

West, R. G., Gillen, E., Bayliss, D., et al. 2019, Monthly Notices of the Royal Astronomical Society, 486, 5094

Wheatley, P. J., West, R. G., Goad, M. R., et al. 2017, Monthly Notices of the Royal Astronomical Society, 475, 4476. https://doi.org/10.1093/mnras/stx2836

Wheatley, P. J., West, R. G., Goad, M. R., et al. 2018, Monthly Notices of the Royal Astronomical Society, 475, 4476

Wildi, F., Pepe, F., Chazelas, B., Curto, G. L., & Lovis, C. 2010, in Ground-based and Airborne Instrumentation for Astronomy III, ed. I. S. McLean, S. K. Ramsay, & H. Takami, Vol. 7735, International Society for Optics and Photonics (SPIE), 1853 – 1863. https://doi.org/10.1117/12.857951

Wilson, O. C. 1978, ApJ, 226, 379

Winn, J. N. 2010, arXiv e-prints, arXiv:1001.2010

Winn, J. N., Matthews, J. M., Dawson, R. I., et al. 2011, ApJL, 737, L18

Wise, A. W., Dodson-Robinson, S. E., Bevenour, K., & Provini, A. 2018, ArXiv e-prints, arXiv:1808.09009

Wolszczan, A., & Frail, D. A. 1992, Nature, 355, 145

Wright, J. T. 2005, PASP, 117, 657

—. 2018, Radial Velocities as an Exoplanet Discovery Method, ed. H. J. Deeg & J. A. Belmonte, 4

Wright, J. T., & Eastman, J. D. 2014, PASP, 126, 838

Wright, J. T., Marcy, G. W., Butler, R. P., & Vogt, S. S. 2004, ApJS, 152, 261

Wright, J. T., Upadhyay, S., Marcy, G. W., et al. 2009, ApJ, 693, 1084

Wyttenbach, A., Ehrenreich, D., Lovis, C., Udry, S., & Pepe, F. 2015, A&A, 577, A62

Yee, S. W., Petigura, E. A., & von Braun, K. 2017, ApJ, 836, 77

Zechmeister, M., & Kürster, M. 2009, A&A, 496, 577

Zechmeister, M., Kürster, M., Endl, M., et al. 2013, A&A, 552, A78

Zeng, L., Sasselov, D. D., & Jacobsen, S. B. 2016, ApJ, 819, 127

Zeng, L., Jacobsen, S. B., Sasselov, D. D., et al. 2019, Proceedings of the National Academy of Sciences, 116, 9723. https://www.pnas.org/content/116/20/9723

Zhao, L., Fischer, D. A., Brewer, J., Giguere, M., & Rojas-Ayala, B. 2018, AJ, 155, 24

Zinn, J. C., Pinsonneault, M. H., Huber, D., & Stello, D. 2019, ApJ, 878, 136